

Structural and Spectroscopic studies of transition metal based Multiferroics and Oxides

By

Harishchandra Singh

Enrolment Number: PHYS03201004011

**Raja Ramanna Centre for Advanced Technology
Indore-452013, India**

*A thesis submitted to the
Board of Studies in Physical Sciences*

In partial fulfillment of requirements for the Degree of

DOCTOR OF PHILOSOPHY

of

HOMI BHABHA NATIONAL INSTITUTE

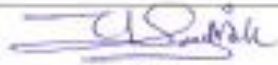
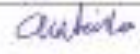
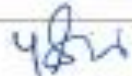
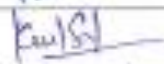
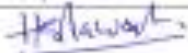
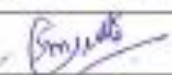


October 2015

Homi Bhabha National Institute

Recommendations of the Viva Voce Committee

As members of the Viva Voce Committee, we certify that we have read the dissertation prepared by Shri Harishchandra Singh entitled "Structural and spectroscopic studies on transition metal based oxides and multiferroics" and recommend that it may be accepted as fulfilling the thesis requirement for the award of Degree of Doctor of Philosophy.

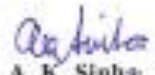
Chairman – Dr. P. A. Naik		Date: 23/5/2016
Guide / Convener – Dr. A. K. Sinha		Date: 23/5/2016
External Member – Dr. N. P. Lalla	23/5/16	Date: N.P. Lalla
Examiner – Dr. Yogesh Singh		Date: 23/5/16
Member 1 – Dr. K. S. Bindra		Date: 23/5/16
Member 2- Dr. H. S. Rawat		Date: 23/05/2016
Member 3- Dr. Aparna Chakrabarti	Aparna Chakrabarti	Date: 23.05.2016
Member 4- Dr. S. M. Gupta		Date: 23/5/16
Member 5- Dr. S. K. Dixit	S. K. Dixit	Date: 23/5/16

Final approval and acceptance of this thesis is contingent upon the candidate's submission of the final copies of the thesis to HBNI.

I hereby certify that I have read this thesis prepared under my direction and recommend that it may be accepted as fulfilling the thesis requirement.

Date: 23/5/16

Place: RRCAT, Indore

 23/5/16
A. K. Sinha
Guide

STATEMENT BY AUTHOR

This dissertation has been submitted in partial fulfillment of requirements for an advanced degree at Homi Bhabha National Institute (HBNI) and is deposited in the Library to be made available to borrowers under rules of the HBNI.

Brief quotations from this dissertation are allowable without special permission, provided that accurate acknowledgement of source is made. Requests for permission for extended quotation from or reproduction of this manuscript in whole or in part may be granted by the Competent Authority of HBNI when in his or her judgment the proposed use of the material is in the interests of scholarship. In all other instances, however, permission must be obtained from the author.



Harishchandra Singh

DECLARATION

I, hereby declare that the investigation presented in the thesis has been carried out by me. The work is original and has not been submitted earlier as a whole or in part for a degree/diploma at this or any other Institution/University.



Harishchandra Singh

DEDICATIONS

I dedicate this thesis to...

MY MOTHER

Abstract

The thesis reports investigation of structural and spectroscopic properties of transition metal based magneto-electric multiferroic systems and their correlation with the magnetic as well as ferroelectric properties. Low structural symmetry systems Co_3TeO_6 (CTO) and Mn doped CTO (CMTO) have been synthesised using an optimized solid state reaction route and their growth mechanism has been studied. Further, Cobalt is found to exist in mixed oxidation states of +2 and +3, which gives rise to the possibilities of both ferromagnetic (FM) and antiferromagnetic (AFM) interactions, in CTO. With the help of low magnetic field magnetization, it is established that CTO show short range FM interactions in addition to reported AFM interactions, the so called Griffiths Phase (GP). We have observed five AFM transitions, which are understood to be due to four Co-O-Co networks corresponding to five crystallographically in-equivalent lattice sites of Co. Experimental observations of spontaneous polarization as well as spontaneous magnetization and magneto-dielectric coupling (representing spin lattice coupling in this system) have been reported in CTO, for the first time.

Further, Mn doping in CTO increases the critical temperature (below which the samples attain AFM interactions) substantially. In this work, the reason for the increase in AFM transition temperature is attributed to decreased TM-O bond lengths as well as maximum average TM charge states for a specific concentration of Mn. The observance of robust FM interactions (below 185 K) in CMTO systems shows supersession on increasing the magnetic fields. The FM transitions are limited to short range length scales and are embedded in long range AFM matrix (GP similar to the case of CTO). GP is found to be much more robust (compared to CTO), in the sense that it shows up to much higher magnetic fields and higher temperatures. The thesis is organized in five chapters. The Introduction chapter describes the importance and status (before this thesis) of the present work. In chapter 2, synthesis method and characterization techniques have been described. An important contribution of this chapter is establishment of X-ray absorption near edge structure (XANES) spectroscopy technique for study of phase concentration of Co_3O_4 and CoO in a mixed phase samples. Chapter 3 and 4 covers the main results of the thesis along with discussion on results. In the final chapter, conclusion of this work and scope for future work has been listed.

Publications:

(i) In refereed journal :

1. *Observation of high spin mixed oxidation state of cobalt in ceramic Co_3TeO_6 ;*
Harishchandra Singh, H. Ghosh, T.V. Chandrasekhar Rao, A. K. Sinha, P. Rajput
Journal of Applied Physics (2014) 116, 214106 (1-7).
2. *Structural investigations on $\text{Co}_{3-x}\text{Mn}_x\text{TeO}_6$; ($0 < x < 2$); High temperature ferromagnetism and enhanced low temperature anti-ferromagnetism;*
Harishchandra Singh, A. K. Sinha, H. Ghosh, M. N. Singh, Parasmani Rajput, C. L. Prajapat, M. R. Singh, G. Ravikumar
Journal of Applied Physics (2014) 116, 074904 (1-9).
3. *Spectroscopic and structural studies of isochronally annealed cobalt oxide nanoparticles;*
Harishchandra Singh, A. K. Sinha, M.N. Singh, P. Tiwari, D.M. Phase, S. K. Deb
Journal of Physics and Chemistry of Solids (2014) 75, 397-402.
4. *Short range ferromagnetic, magnetoelectric and magneto-dielectric effect in ceramic multiferroic Co_3TeO_6 ;*
Harishchandra Singh, H. Ghosh, T. V. Chandrasekhar Rao, G. Sharma, J. Saha, and S. Patnaik
Journal of Applied Physics (2016) 119, 044104.
5. *Griffith like robust ferromagnetism in $\text{Co}_{3-x}\text{Mn}_x\text{TeO}_6$; ($x = 0.5, 1$ and 2);*
Harishchandra Singh, H. Ghosh, C. L. Prajapat, G. Ravikumar;
Material Research Bulletin, (2016) 80, 273.
6. *Insight into the growth reaction mechanism of ceramic Co_3TeO_6 : Synchrotron structural and thermal analysis;*
Harishchandra Singh, A. K. Sinha, S. M. Gupta, M. N. Singh, H. Ghosh;
Journal of the American Ceramic Society: in press

(ii) Conferences :

1. *Synthesis and structural characterization of $\text{Co}_{3-x}\text{Mn}_x\text{TeO}_6$; ($0.3 \leq x \leq 2$) solid solutions using Synchrotron Source;*

Harishchandra Singh, A. K. Sinha, Haranath Ghosh, M. N. Singh, A. Upadhyay
International Conference on Advanced Functional Materials (ICAFM), 19th - 21th Feb,
(2014). Thiruvananthapuram, Kerala, India.

2. *Investigation of Co-Co networks in ceramic multiferroic Co_3TeO_6 from structural study;*

Harishchandra Singh, A. K. Sinha, Haranath Ghosh, M. N. Singh, A. Upadhyay
AIP Conf. Proc. (2015) **1665**, 060021-22.

3. *Negative magneto-dielectric coupling in ceramic multiferroic Co_3TeO_6 ;*

Harishchandra Singh, G. Sharma, Haranath Ghosh, S. Patnaik, A. K. Sinha
International European Meeting on Ferroelectricity-EMF 2015, 28th June - 3rd July (2015).
University of Porto, Portugal.

iii) **Publications (not included in the thesis):**

1. *Origin of giant dielectric constant and magnetodielectric study in $Ba(Fe_{0.5}Nb_{0.5})O_3$ nano-ceramics;*

P. K. Patel, K. L. Yadav, **Harishchandra Singh**, and A. K. Yadav
Journal of Alloys and Compounds (2014) **591**, 224-229.

2. *Effect of Zn doping on the magneto-caloric effect and critical constants of Mott insulator MnV_2O_4 ;*

P. Shahi, **Harishchandra Singh**, A. Kumar, K. K. Shukla, A. K. Ghosh, A. K. Yadav, A. K. Nigam, and Sandip Chatterjee
AIP Advances **4**, (2014) 097137 (1-10).

3. *Air annealing effects on lattice structure, charge state distribution, and room temperature ferrimagnetism in $Co_{2.25}Fe_{0.75}O_4$;*

M. R. Panda, R. N. Bhowmik, **Harishchandra Singh**, M. N. Singh, and A. K. Sinha
Mat. Res. Exp. (2015) **2**, 036101 (1-11).

ACKNOWLEDGEMENTS

This thesis work is the part of research that has been done since I came to RRCAT. When I look back, I realize that I have worked with a great number of people whose contribution in assorted ways to the research and the making of the thesis deserved special mention. It is a pleasure to convey my gratitude to all of them.

It is a great honor and privilege to express my deep sense of gratitude to my Ph.D. guide Dr. Anil K. Sinha, at the successful completion of my thesis work. He infused enthusiasm at every step of research work. He has a cool temperament that certainly benefits a person working with him. I feel invigorated at every moment on recalling the words of inspirations received from him. Discussion with him was always very fruitful. He taught me to think at basic level for every problem. I thank him for his expertise shown in guiding my work and the willingness to share his knowledge and experience. His profound practical skills, immense knowledge and critical but valuable remarks led me to do a good research. I especially thank him for his prompt reading and careful critique of my thesis.

I sincerely give special gratitude to Dr. Haranath Ghosh for fruitful discussions and suggestions time to time. He has infused many ideas that helped me a lot in growing up in the field of science. I am greatly indebted to him for his support, trust, guidance and encouragement throughout these years. He has greatest professional influence on my development as a researcher. He pushed me to develop my weaknesses and exploit my strengths. His courage to tackle new and difficult problems is admirable. Thanks are also due to Dr. Haranath Ghosh for performing the first principles total energy calculations on one of the studies samples.

I sincerely thank Dr. S. M. Gupta for his continuous discussion during the thesis work. I grew up in the field of growth taking help from his ideas. He owns a great quality to sort out the experimental difficulties with many exciting ideas that eventually helped me in reaching the targets while this thesis works. He has a great ability to keep the person motivated. He is keen for a chat about interesting things in physics and is always very encouraging. He has always helped me as a friend and scientist as well.

I am very grateful to Dr. P. D. Gupta, Director RRCAT for his continual help during my stay at RRCAT for PhD training. I am extremely thankful to Dr. P. A. Naik, Head ISUD for his constant encouragement. I also thank him for his full support at every step of my Ph.D training. I am grateful to Dr. S. M. Oak and Dr. P. A. Naik (Chairman-C3), Dr. N. P. Lalla (External member), UGC DAE CSR Indore and all members of C3-Doctoral Committee for their constructive motivation and guidance.

I am thankful to Dr. P. S. Anil Kumar, IISc Bangaluru, India and Dr. Y. Singh, IISER Mohali for reviewing this thesis work.

I sincerely thank our HBNI Ph.D. coordination committee members specially Dr. G. S. Lodha, Dr. S. B. Roy, Dr. Arup Banerjee and Dr. S. K. Deb for their continuous care and help during the Ph. D. course. I also thank our HBNI cell at RRCAT to provide all the necessary support especially during my Ph. D. course work. I thank HBNI committee for providing us various sports facilities at guest house. I also thank HBNI committee members, RRCAT for urging us to celebrating Ph.D. day.

I thank BL-12 group members specially Mr. M. N. Singh for the help in learning the operation of angle dispersive X-ray diffraction (ADXRD) beamline, at every step. He is very supportive. I used to call him at both the day and night for the help required during the

measurements. He never said no to me. I have also shared my happiness and sorrow with him. I also thank Mr. Ashok Kumar for his continuous support since I joined Ph.D. program in HBNI, RRCAT. I thank Dr. Archana Sagdeo for her useful guidance as a senior group member and for providing lab source XRD set-up. I also thank Dr. Pooja Gupta and Mr. Anuj Upadhyay for their constant help during the course.

I am very thankful to Dr. S. N. Jha for providing support during PhD work and allowing me to use EXAFS beam-line as well as other facilities. I am extremely thankful to Dr. Tapas Ganguly, Dr. Sanjay Rai for their various help and suggestions during the course of my Ph.D. training. I thank Dr. Aparna Chakrabarti for inviting us for dinner on several occasions at her home along with the help that she has provided. I also thank Dr. C. Kamal. I had fruitful discussion over various topics with him. I cherish my interactions and discussions with him. Thanks are also due to all members of ISUD.

I thank Dr. Kevin Jorissen (University of Washington) for providing JFEFF software and fruitful discussion on the XANES analysis using JFEFF.

I thank Dr. T. V. Chandrasekhar Rao for providing magnetic property measurements data and discussions during the work. I also thank C.L. Prajapat and Dr. G. Ravikumar for the magnetic measurements. Thanks are due to Mr. Ashok Kumar Yadav, for his help in EXAFS measurements at Scanning EXAFS beamline. I thank Dr. A. Sundaresan and B. Rajeswaran for initial magnetic measurements. I am also thankful to Dr. C. Mukherjee for performing the gold coating on Cobalt oxide nanoparticles samples for SEM measurements. I thank Mrs. Pragya Tiwari for performing SEM measurements. I would like to thank Dr. S. Patnaik, JNU New Delhi for help in Dielectric and Polarization measurements. I would also like to thank RRCAT Glass Blowing Section's members for their continuous help during my

Ph.D. work. Thanks are due to Dr. D. M. Phase and Mr. A. D. Wadikar, UGC DAE CSR Indore for help in XPS measurements. I am indebted to members of Indus operation crew without whom it would have not been possible to do the experiments on Indus-2. I am also grateful to all the professors/associate professors who have taught us during 1st year course work.

Above all, it would have not been possible for me to achieve this milestone in my research career without encouragement and support from my all family members who have dreamed and prayed for my all around success.

It would be grateful for me to thank my M.Sc. batch mates: Ashok, Samar, Gyaneshwar, Piyush, Rajiv, Vikas and childhood friends: Anand, Divakar.

My time at RRCAT was made enjoyable in large part due to my PhD friends, MTech students who have become a part of my life. We had valuable research discussions. We together had enjoyed small trips and parties. Playing volleyball with them was quite refreshing after spending whole day in the lab.

I sincerely thank all the persons who have helped and supported me directly or indirectly in the course of this research work.

Contents

Contents	i
Synopsis	iii
List of Figures	xi
List of Tables	xix

Chapter 1: Introduction

1.1. Multiferroics	5
1.2. Combining magnetism and ferroelectricity	6
1.2.1. <i>Type I Multiferroics</i>	7
1.2.2. <i>Type II (Magnetic) Multiferroics</i>	9
1.3. Applications and recent trends in Multiferroics	12
1.4. Issues and Motivation of the present work	14
1.5. Organization of the Thesis	16

Chapter 2: Experimental Details

2.1. Introduction	17
2.2. Synthesis	17
2.2.1. <i>Solid State Reaction Route</i>	17
2.2.2. <i>Wet Chemical Route</i>	19
2.3. Thermal Analysis	20
2.4. An overview of Indus-2 and the Beamline used for the present work	20
2.5. X-Ray Diffraction	22
2.6. X-Ray Absorption Near Edge Structure Spectroscopy	29
2.7. X-ray Photoelectron Spectroscopy	34
2.8. Scanning Electron Microscopy	36
2.9. Dielectric Constant and pyroelectric current (Polarization) Measurements	37
2.10. Magnetization Measurements	39
2.11. Demonstration of structural and spectroscopic techniques to study oxides	41
2.11.1. <i>X-ray Absorption Near Edge Structure Spectroscopy analysis</i>	42
2.11.2. <i>X-ray Photoelectron Spectroscopy analysis</i>	47
2.11.3. <i>Synchrotron X-ray diffraction analysis</i>	50

Chapter 3: Cobalt Tellurate (Co₃TeO₆; CTO)

3.1. Two step solid state synthesis of CTO	58
3.1.1. Introduction	58
3.1.2. Results and Discussion	59
3.1.2.1. <i>Growth and its structural correlation</i>	59
3.1.2.2. <i>X-ray Photoelectron spectroscopic analysis</i>	71
3.1.3. Conclusions	73
3.2. Observation of high-spin mixed oxidation state of cobalt in CTO	75
3.2.1. Introduction	75
3.2.2. Results and Discussion	78
3.2.2.1. <i>X-ray Absorption Near Edge Structure Spectroscopy</i>	78
3.2.2.2. <i>High field DC Magnetization study</i>	83
3.2.2.3. <i>First principles study</i>	86
3.2.2.4. <i>In the search for the origin of Co³⁺</i>	89

3.2.3.	Conclusions	91
3.3.	Magneto-electric and Magneto-dielectric properties of CTO	93
3.3.1.	Introduction	93
3.3.2.	Results and Discussion	94
	3.3.2.1. <i>Low field DC Magnetization Study</i>	94
	3.3.2.2. <i>Structural investigation for the insight into the magnetism</i>	96
	3.3.2.3. <i>Bifurcation between FC and ZFC magnetization curves</i>	100
	3.3.2.4. <i>Investigation of Magneto-Electric and Magneto-Dielectric effect</i>	105
3.3.3.	Conclusions	110
Chapter 4: Mn doped Co₃TeO₆		
4.1.	Structural and Spectroscopic Characterizations on Co_{3-x}Mn_xTeO₆	115
4.1.1.	Introduction	115
4.1.2.	Results and Discussion	116
	4.1.2.1. <i>Synchrotron X-ray diffraction study</i>	116
	4.1.2.2. <i>X-ray Absorption Near Edge Structure study</i>	126
4.1.4.	Conclusions	130
4.2.	Magnetic Properties of Co_{3-x}Mn_xTeO₆; (x = 0.5, 1 & 2)	132
4.2.1.	Introduction	132
4.2.2.	Results and Discussion	133
	4.2.2.1. <i>Magnetic behavior of Co_{3-x}MnxTeO₆ (x = 0.5, 1 and 2)</i>	133
	4.2.2.2. <i>Structural insight for the observed magnetic behavior</i>	141
4.2.3.	Conclusions	144
Chapter 5: Conclusions and Future work		147
References		153

SYNOPSIS

Structural and spectroscopic studies play vital role in transition metals (TMs) based Multiferroics (MFs) and Oxides. This is because TM and their complexes (TM surrounded by oxygen) exhibit variety of structures and properties due to the unique nature of outer shell *d*-electrons of TM. These (partially filled $3d^1$ to $3d^9$ orbitals of first row TM atoms) electrons not only influence structural and spectroscopic (electronic) properties, but also the magnetic properties of TM based compounds. Key features behind the variations in the aforementioned properties of TM based compounds are the crystal field splitting (Δ_{cf} : of the degenerate 3d orbitals) and coulomb correlation (U : between two electrons in the same orbital). In addition to these, charge state of the TM and type of interactions between the TM ions also lead to variation in the properties. Electrons in transition metal oxides (TMOs) manifest themselves in many different ways leading to interactions among charge, spin, lattice and orbital degrees of freedom. One of the current interesting implications of such interactions among these degrees of freedom is magneto-electric (ME) MFs,¹ which exhibits two fundamental ferroic (magnetic and ferroelectric (FE)) orders coupled in the same phase. ME-MF materials show enormous applicability in spintronics, next generation low power- non-volatile memory storage devices and in solar cells etc.²⁻⁵ Stabilization of ferroelectricity and magnetism in a single phase material is quite difficult due to the demand of two mutually exclusive requirements. Magnetic ordering requires localization of electrons in partially filled d shells and is usually seen in TM showing metallic behavior. Conversely, electrical polarization requires a structural distortion of the lattice, which occurs from empty d shells, and thus FE materials tend to be insulators. This is not the only constraint; the simultaneous occurrence of both the orders is also prohibited from symmetry considerations. The electrical polarization needs the lack of inversion centre, whereas, the magnetic order requires

lack of time reversal. Although, the coexistence of ferroelectricity with magnetism was initially considered to be one of the rarest of rare phenomena, the evolution of strongly cross-coupled response in various materials with spontaneous polarization and magnetization has changed the existing scenario drastically. The path that MF community adopts is to induce ferroelectricity in a compound, either by breaking the inversion symmetry (BIS) or by using some other mechanisms.¹ Depending on the mechanism, responsible for the origin of ferroelectricity, MF materials can be classified into two types, type I (proper) and type II (improper). In type I MFs, ferroelectricity and magnetism have separate mechanisms and the coupling strength between the two is weak, although the individual strengths are significant. On the other hand, in type II MFs, both the magnetic and ferroelectric orders have a common mechanism *i.e.* one can induce the other. Such materials exhibit intrinsic magnetic structures, which are responsible for BIS and hence for electrical polarization. Due to the large coupling between the electric and magnetic orders, these materials are extremely important from technological point of view. In order to utilize ME-MF materials with full potential, there remain a number of issues, which need to be addressed. Besides, understanding the mechanism of coupling of these ferroic orders, enhancing the coupling strength, designing and finding new MFs are some of the frontline research activities.

In the quest of finding new and better performing materials, Cobalt Tellurate (Co_3TeO_6 ; CTO) has been found to have favourable characteristics.⁶ CTO (belonging to A_3TeO_6 family; A = Mn, Ni, Cu, Co) shows very interesting structural as well as low temperature magnetic properties.⁶⁻¹¹ Single crystal CTO crystallizes in monoclinic (C2/c) crystal symmetry. The interest in CTO is due to its low temperature type II MF properties. In addition, the monoclinic crystal structure with multiple magnetic transitions at low temperatures makes CTO very

interesting. Origin and understanding of each transition have its own challenge due to the complex crystal as well as magnetic structure of CTO.⁶⁻¹¹ There exists substantial amount of work on CTO, however, there are some issues, which are still under debate. Issues discussed below form the basis for the work, presented in this thesis.

Single phase synthesis and understanding its zero magnetic field behaviour remains a challenging issue in ceramic as well as single crystal CTO.¹²⁻¹³ In addition, there are no reports showing all the five (~ 34 K, 26 K, 21 K, 17.4 / 18 K and 16 K) magnetic transitions in one ceramic or single crystal CTO sample. Different groups have reported mainly two transitions ($T_{N1} \sim 26$ K and $T_{N2} \sim 18$ K) along with few other transitions noted above.⁶⁻¹⁰ This may be attributed to the difference in the method of sample preparation adopted by different groups. Further, no report discusses growth mechanism of CTO, in details. We provide, for the first time, a two step solid state reaction growth mechanism for the preparation of ceramic CTO, which shows all the five transitions, in a single phased material.

As per earlier reports on single crystal / ceramic CTO, only Co^{2+} ions occupy five different crystallographic positions as tetra, square-pyramidal and three inequivalent octahedral sites.¹¹ Further, very large variations are observed in Co-O bond distances. It has been reported that largest bond distance is almost double to that of the smallest one. In this scenario, observance of only Co^{2+} ions in these varying coordinations is difficult to appreciate. One possibility to arrange such a polyhedral mixing with a range of bond lengths can be through mixed valence ions. However, to the best of our knowledge, there is no report on the presence of Co^{3+} in (either single crystal or ceramic) CTO. In our work, we have used Synchrotron X-ray Diffraction (SXR), X-ray Absorption Near Edge Spectroscopy (XANES) and high field DC

magnetization in corroboration with first principle calculations to show the presence of high spin mixed oxidation state of Co in ceramic CTO, for the first time.

In literature, there have been theoretical predictions¹⁴ about the spontaneous weak magnetization as well as the spontaneous polarization. The experimental proof for the weak magnetization has been put forward with domain structure observed in Second Harmonic Generation measurements.¹⁴ The experimental observation of the spontaneous zero field polarization remains yet to be confirmed. We measure temperature and magnetic field dependent magnetization, dielectric constant and polarization to show the possibility of the spontaneous polarization and magnetization below 18 K in ceramic CTO. Measurements show the above two effects in our sample (at zero magnetic field). Temperature dependent DC magnetization reveals complicated magnetic structures and signature of all the magnetic phases observed earlier in neutron diffraction studies are retained in present ceramic CTO.

Wang et al.,⁹ have observed four magnetic transitions and ascribed two of them to two magnetic networks Co1-Co4 and Co2-Co3-Co5 using neutron diffraction studies. To explain all the magnetic transitions, there might be a possibility of other magnetic networks, which the authors have not mentioned. We have analyzed the room temperature SXRD data using Rietveld refinement and VESTA (a 3D visualization software) for our ceramic as well as reported data of single crystal CTO. It is important to note that we have observed two additional structural networks Co1-Co5 and Co2-Co3-Co4, which we attribute to the observed magnetic transitions. Through this, we propose four structural networks, which may be related to the observed multiple magnetic transitions.

Furthermore, to enhance the coupling strength and the transition temperature (at which the MF transitions take place) in CTO, researchers have tried doping Co site with several

transition metals such as Cd, Fe and Mn etc. Out of these, only Mn doped CTO (CMTO) results in the enhancement of transition temperature, below which MF properties are observed. On the other hand, other dopants lead to lower transition temperatures. As mentioned earlier, CTO is a low symmetry ($C2/c$) type II multiferroic at low temperatures, which shows complex magnetic structure with a sequence of antiferromagnetic (AFM) transitions. Mn_3TeO_6 (MTO), on the other hand, crystallizes in higher symmetry ($R\bar{3}$) and is a type I multiferroic. Surprisingly, MTO also shows similar AFM transition temperatures, as is observed in the case of CTO. MTO and CTO show main AFM transitions at around 23 K and 26 K, respectively. In contrast, Mn doping in CTO enhances the AFM transition temperature to ~ 40 K; even when the AFM transition temperatures of the end members are much lower.¹⁵⁻¹⁶ Not only the reason behind the enhancement in the transition temperature is not discussed in literature, but also no evidence of FM interaction has been reported. To address these issues, we have carried out room temperature SXRD and Mn as well as Co K- edge XANES studies on Mn doped CTO samples. These results have been used to explain magnetic properties of the samples.

Thesis Outline

This thesis comprises of five chapters and contents of each chapter are discussed briefly in the following:

1. Introduction

This chapter describes fundamentals of MF, their importance and proposed application in various fields. From application point of view, merits / demerits of type I and type II MFs are discussed. Current status of knowledge and issues pertaining to CTO and Mn doped CTO are pointed out.

2. Experimental techniques

This chapter describes the details of characterization techniques used in the present thesis.

Experimental aspects of X-ray diffraction and X-ray absorption measurements and their data interpretation procedures are elaborated. Details of diffraction and absorption beamlines used in this work have been given. In addition, X-ray photoelectron spectroscopy (XPS) and XANES spectroscopy have been discussed in detail. Other experimental techniques used for magnetic, dielectric and polarization measurements have also been described, in brief. Further, utilization of structural and spectroscopic tools to study oxides is described, wherein XANES, XPS and SXRD measurements have been carried out on Cobalt oxide nanoparticles to determine the phase composition.

3. Cobalt Tellurate (Co_3TeO_6 : CTO)

This chapter is divided into three sections. Section 3.1 describes a two steps solid state reaction route for the synthesis of monophasic CTO. Thermo-gravimetric data along with SXRD measurements have been used to optimize synthesis parameters like concentration of reactants, single/double step calcination times and temperatures to get single phase CTO. Co and Te core level XPS spectra on the single phasic CTO indicate possible mixed oxidation states of Co (i.e. Co^{2+} and Co^{3+}) and +6 oxidation state of Te, respectively. Section 3.2, therefore, is focused on the determination of charge and spin states of Co in CTO. We find coexistence of high spin Co^{3+} and Co^{2+} in ceramic CTO. These conclusions are established using XANES, high field DC magnetization and first principle calculations. Relative concentrations of Co^{3+} and Co^{2+} in CTO have been estimated by Co K edge XANES measurements using interpolation of absorption edge energies of CoO, CoF_3 and Co metal foil standards, whereas the spin state of these ions have been obtained by the analysis of pre-edge part of XANES spectrum. First principle calculations also show the most favourable total energy for the above mentioned configuration of Co ions in CTO. Observed magnetic moment could be explained using high spin states of Co^{3+} and Co^{2+} .

Section 3.3 presents the observation of magneto-electric and magneto-dielectric couplings in ceramic CTO using temperature and magnetic field dependent DC magnetization, dielectric, pyroelectric and polarization measurements. Observation of all the five magnetic transitions and their possible correlations with room temperature structural analysis are discussed. Observance of short range ferromagnetic interactions has been attributed to Co^{3+} -O- Co^{2+} networks. Further, following various reports,¹⁷⁻¹⁹ we present several interesting observations from magnetic field dependent dielectric constant data such as spontaneous polarization, presence of ferromagnetic correlation below T_{N2} , possible spin-phonon coupling and magneto-dielectric effect in this system for the first time. These observations also lead to believe that CTO contains weak ferromagnetic nano regions embedded in AFM matrix, the so called Griffiths phase. Finally, combined dielectric and pyroelectric current (polarization) measurements are utilized to comment on the spontaneous symmetry breaking even in the absence of magnetic field.

4. Mn doped Co_3TeO_6 (CMTO)

This chapter is divided into two sections. Preparation, structural as well as spectroscopic characterizations of $\text{Co}_{3-x}\text{Mn}_x\text{TeO}_6$; ($0 < x \leq 2$) solid solutions have been discussed in Section 4.1. Phase diagram obtained from the two phase Rietveld refinement of SXRD data indicate mixed symmetries i.e. monoclinic ($C2/c$) and rhombohedral ($R\bar{3}$) for $x < 0.5$, and only $R\bar{3}$ symmetry for $x \geq 0.5$. Further, it shows increase in lattice parameters as well as average transition metal - oxygen (Co/Mn-O) bond lengths for $x \geq 0.5$, attaining a minimum value at $x = 0.5$. Co and Mn K-edge XANES spectra reveal that both Co and Mn are in mixed oxidation states of +2 and +3. Relative ratios of $\text{Co}^{3+}/\text{Co}^{2+}$ and $\text{Mn}^{3+}/\text{Mn}^{2+}$ (obtained from XANES data) decrease with increasing x (for $x \geq 0.5$) with a maximum value at $x = 0.5$. These structural and spectroscopic evidences have been used to propose possible interpretation of observed as well as reported

magnetic behaviour of CMTO. Section 4.2 not only supports the above interpretation but also presents CMTO as the potential magnetic materials having very high temperature ferromagnetic correlations, low temperature enhanced AFM interactions and their coexistence. This is demonstrated through detailed magnetization studies.

5. Summary and Future Scope

In this chapter, summary and major conclusions of the thesis are described. We show that the existence of Co^{3+} and Co^{2+} in ceramic CTO does not diminish multiferroic properties observed earlier in single crystal, but actually enhances some of the observables like ME-MF behaviour, magneto-dielectric effect and Griffiths phase. Mn Doped CTO results in near room temperature short-range robust ferromagnetic as well as long range low temperature enhanced antiferromagnetic correlations. Issues which could not be attempted or concluded are described, in brief. Possible ways to resolve these issues have also been discussed, as future work.

References:

- ¹H. Schmid, *Ferroelectrics* **162**, 317 (1994); D. Khomskii, *Physics* **2**, 20 (2009).
- ²R. Nechache, et al., *Nature Photonics* **9**, 61 (2015).
- ³W. Wang, J. Zhao, W. Wang et al., *Phys. Rev. Letts.* **110**, 237601 (2013).
- ⁴I. N. Apostolova, A. T. Apostolov, et al., *J. Appl. Phys.* **113**, 203904 (2013).
- ⁵W. Kleemann, *Physics* **2**, 105 (2009); J. F. Scott, *NPG Asia Materials* **5**, e72 (2013).
- ⁶M. Hudl, R. Mathieu, S. A. Ivanov, M. Weil, et al., *Phys. Rev. B* **84**, 180404(R) (2011).
- ⁷W. H. Li, C. W. Wang, D. Hsu, C. H. Lee et al., *Phys. Rev. B* **85**, 094431(2012).
- ⁸S. A. Ivanov, R. Tellgren, C. Ritter, et al., *Mater. Res. Bull.* **47**, 63 (2012).
- ⁹C. W. Wang, C. H. Lee, C. Y. Li, et al., *Phys. Rev. B* **88**, 184427 (2013).
- ¹⁰J. L. Her, C. C. Chou, Y. H. Matsuda, et al., *Phys. Rev. B* **84**, 235123 (2011).
- ¹¹R. Becker, M. Johnsson, H. Berger, *Acta Crystallogr. C* **62**, i67 (2006).
- ¹²N. V. Golubko, V. Yu. Proidakova, et al., *Bull. Russ. Acad. Sci.: Phys.* **74**, 724 (2010).
- ¹³J. Sikac and L. Jenskysky, *Collection Czechoslov. Chern. Commun.* **45**, 2489 (1980).
- ¹⁴P. Toledano, V. Carolus, M. Hudl, et al., *Phys. Rev. B* **85**, 214439 (2012).
- ¹⁵R. Mathieu, S. A. Ivanov, P. Nordblad and M. Weil, *Eur. Phys. J. B* **86**, 361 (2013).
- ¹⁶S. A. Ivanov, R. Mathieu, P. Nordblad, et al., *Mater. Res. Bull.* **50**, 42 (2014).
- ¹⁷G. Lawes, T. Kimura, C.M. Varma, et al., *Progress in Solid State Chemistry* **37**, 40 (2009).
- ¹⁸A. K. Singh, D. Jain, V. Ganesan, A. K. Nigam, S. Patnaik, *Europhysics Lett.* **86**, 57001 (2009).
- ¹⁹Q. Zhang, K. Singh, F. Guillou, C. Simon, Y. Breard, et al., *Phys. Rev. B* **85**, 054405 (2012).

List of Figures:

Chapter 1

Fig. 1.1. Pictorial illustration of TM's d level splitting in (a) octahedral and b) tetrahedral crystal fields. Representation of corresponding coordination geometries is also shown. Crystal field stabilization energy (CSFE), for both the cases, where $n(t_{2g})$ and $n(e_g)$ – are the number of electrons occupying the respective energy levels, is mentioned. 2

Fig. 1.2. Distortion from the regular octahedra (b) due to strong electric field of octahedral anions generally changes its structure via higher symmetry to lower symmetry through elongation in any of the three crystallographic directions. Representative elongations along z direction (a) and y directions (c) have been shown. Crystal field parameters would be different for each case, where Δ_D and Δ_R for distorted and regular octahedra, respectively. 3

Fig. 1.3. Interaction among three degrees of freedom of an electron in a lattice i.e. charge, spin and orbital, results in ME MF that combines properties of ferroelectrics (due to charge) and magnets (due to spin). Hysteresis along with switching behaviour, displayed by ferromagnets and ferroelectrics mutually control magnetic response with an electric field and modification of polarization by magnetic field leading to the basis for making 4-state logic devices. 5

Fig. 1.4. Modulated spin structures, (a) sinusoidal, where magnitude of the magnetic moment changes along the propagation axis (arrow). (b), (c) The same remains constant in helicoidal and cycloidal spin configuration cases, only rotation axis changes. In (b), the rotation axis coincides with the propagation axis, while they are perpendicular in (c). In (d) and (e), which are longitudinal and transverse conical spin spirals, the spins rotate on a cone (not in a plane but), leading to a macroscopic magnetization. 9

Fig. 1.5. The Dzyaloshinskii-Moriya (DM) interaction's mechanism (a) Dependence of superexchange interaction between neighboring spins on their bond angle and hence on the displacement \mathbf{x} of oxygen ions, which results in the minimization of DM interaction energy for fixed bond angles adjusted by oxygen displacement. (b) In zig-zag chains, vector $\mathbf{D}_{ij} = \mathbf{x} \times \mathbf{r}_{ij}$ alternates in sign leading to a homogeneous shift of the negative ions with respect to the positive ions, which results in macroscopic polarization. (c) Collinear 11

spin structure with $\uparrow - \uparrow - \downarrow - \downarrow$ spin configuration breaks inversion symmetry and hence induces the electrical polarization.

Chapter 2

- Fig. 2.1.** Schematic to understand XRD mechanism through Bragg reflection by lattice planes of a crystalline sample. For XRD pattern, path difference between reflected rays by adjacent lattice planes must be integral multiple of wavelength. 23
- Fig. 2.2.** Optical layout of BL-12. 24
- Fig. 2.3.** Photograph of 1st experimental station consisting of several components. 25
- Fig. 2.4.** Photograph of the 2nd experimental station with its various components. 25
- Fig. 2.5.** (a) Shows 2D intensity data as found at Image Plate for LaB₆ NIST standard, (b) shows Rietveld refinement of the same LaB₆ 1D pattern and (c) shows a typical view of the refined structure form Rietveld refinement. 26
- Fig. 2.6.** Schematic illustration of X-ray absorption spectrum. 29
- Fig. 2.7.** Various modes of XANES measurements depending on the sample's conditions and requirements. I and IC in different subscript represent photon beam intensity and ionization chambers, respectively. 32
- Fig. 2.8.** (a) Instrumental setup of X-ray photoelectron spectroscopy (XPS) and (b) A typical XPS spectrum: survey scan of Co₃O₄ nanoparticles. Inset shows enlarge part of the same. 34
- Fig. 2.9.** Schematic layout of pyroelectric current measurements setup. Switches labeling represent electrical connection to be made for measurements. Switch 1 for poling process, 2 for electrical shortening and switch 3 for final step of measurements. 38
- Fig. 2.10.** Schematic of vibrating sample magnetometer (VSM). The detection coil assembly is wound in a second-order gradiometer configuration with oppositely wound detection coils. 39
- Fig. 2.11.** Schematic of typical SQUID magnetometer used for magnetization measurements. Detection coils, SQUID-input coils and the connecting wires are the parts of a closed superconducting loop acting as a flux transformer, where the detection coils are connected to the SQUID-input coil, which is inductively coupled to the SQUID sensor. 40
- Fig. 2.12.** SEM images of three samples, (a) H1, (b) H2 and (c) H4. 41

Fig. 2.13. Normalized Co K-edge XANES spectra for all the samples H1 to H4, along with CoO (H0) and Co₃O₄ (H5) standards. Vertical shifting has been done for the sake of clarity. Features in the XANES spectra are marked with P (Pre-edge), A (Main edge), W (White line) and B. Energy calibration has been done using Co metal foil XANES spectra. 42

Fig. 2.14. Demonstration that the identification of features in XANES spectra does not alter the conclusion of the analysis, wherein variations of transition energies as a function of cobalt oxides NP samples have been shown. Numbers in the X axis represent H0 to H5. 44

Fig. 2.15. Linear Combination Fitting (LCF) for all the samples H1 to H4 using cobalt K-edge XANES spectra. Raw data points are shown by black (+) and solid lines (red) denote LCF fit to the data. Fractions of standards CoO (shown by blue dash dot) and Co₃O₄ (shown by magenta dash) are used for LCF. 45

Fig. 2.16. Normalized core level XPS spectra of Co 2*p* and O 1*s* (*right inset*) for all the samples (H1 to H4). 47

Fig. 2.17. Oxygen 1*s* XPS spectra of cobalt oxide nanoparticle samples H1 to H4 fitted with Shirley background and two Lorentzian-Gaussian peaks (I, II). 49

Fig. 2.18. Synchrotron X-Ray diffraction patterns recorded at room temperature from cobalt oxide nanoparticle samples (H1 to H4). 50

Fig. 2.19. Reitveld refined Synchrotron X-Ray diffraction patterns for all the samples. Red dots represent the raw data, and solid black lines are the fit obtained by the Rietveld refinement. The blue and magenta line beneath the pattern records the Bragg positions and difference between the observed and calculated patterns, respectively. 51

Chapter 3

Fig. 3.1. SXRD patterns of TeO₂, Co₃O₄ and their mixture at room temperature. 59

Fig. 3.2. DTA/TGA curves for Co₃O₄ + TeO₂ mixture. Thermal analysis indicates four step reaction assigned as I, II, III and IV. Inset shows 1st derivative of TGA curve showing anomaly at ~500 °C (region I). 60

Fig. 3.3. The stoichiometric ground mixture at 500 °C indicates initialization of a new phase (CoTeO₄) along with unreacted initial reactants. Calcination at 600 °C, on the other hand, corresponds to CoTeO₄ as major phase. 61

Fig. 3.4. Stabilization of CoTeO₄ along with various other phases, as we increase the calcinations temperature from 600 °C to 800 °C, all these phases are get converted to the 62

final compound Co_3TeO_6 .

Fig. 3.5. No change in TeO_2 phase at $700\text{ }^\circ\text{C}$ for 2 hrs calcinations, which excludes the possibilities of TeO_3 , Te_2O_5 or Te_4O_9 leading to the stability against its oxidation or reduction. 63

Fig. 3.6. SXRD data showing no change in Co_3O_4 phase at $700\text{ }^\circ\text{C}$ for 2 hrs calcinations. This excludes the possibilities of their oxidizing agents like CoO and Co_2O_3 during calcinations process. 63

Fig. 3.7. Shows comparisons of single step and double step calcinations (see text for details). 65

Fig. 3.8. (a) A high resolution Synchrotron X-ray Diffraction measurement is used to probe monophasic CTO, (b) shows the corresponding impurity, which is Co_3O_4 , (c) Rietveld refinement is used to estimate concentration of impure Co_3O_4 phase. 67

Fig. 3.9. Simulated and observed Synchrotron X-Ray Diffraction patterns recorded at room temperature ($\lambda = 0.9480\text{ \AA}$) for ceramic CTO sample. 68

Fig. 3.10. Polyhedral view (a-b plane) of the ceramic CTO clearly signifies the octahedral, pentahedral and tetrahedral sites of Co, and octahedral sites of Te. 68

Fig. 3.11. (a) Normalized core level XPS spectra of Co $2p$, satellite (ss) peaks nearby main peaks confirms the mixed oxidation state of Co in CTO, (b) normalized core level XPS spectra of Te $3d$, binding energy 587.3 eV and 576.8 eV positions of the main peaks confirm the +6 oxidation state of Te and (c) Oxygen $1s$ XPS spectra CTO sample fitted with Shirley background and two Lorentzian- Gaussian peaks acquired with Al $K\alpha$ source. 71

Fig. 3.12. Polyhedra of our ceramic CTO as compared to single crystal CTO show marginal distortion in the corresponding $\text{CoO}_6/\text{CoO}_5/\text{CoO}_4$ and TeO_6 polyhedra leading to shorter typical bond distances of Co/Te-O. 77

Fig. 3.13. Edge step normalized Co K-edge XANES spectra of CTO, Cobalt oxide standards (CoO and CoF_3) and Co metal foil. Co foil is used for photon energy calibration. 78

Fig. 3.14. LCF fit of ceramic CTO using CoO and CoF_3 standard samples (main panel) and inset shows linear dependence of oxidation states as a function of energy obtained from derived formula. 80

Fig. 3.15. Te L₃ edge XANES spectra of CTO along with Te standards. 80

Fig. 3.16. Edge step normalized Co-K edge XANES spectra of ceramic CTO sample 81 showing pre edge structure at around 7709 eV (main panel). CoF₃ and CoO are used as the source for high spin Co³⁺ and Co²⁺, respectively (left inset). Various pre edge features namely A1, A2 and A3 has been shown for the sake of clarify (left inset). Gaussian peak fitting has been used to analyze the crystal field splitting between the e_g and t_{2g} states of Co cations after careful background subtraction (see right inset).

Fig. 3.17. High field DC magnetization under ZFC/FC protocol indicates 83 antiferromagnetic behavior akin to that of single crystal CTO. Curie-Weiss fit to FC data is shown in right inset. Left inset shows the corresponding Neel temperatures (T_{N1} and T_{N2}) through the second derivative of MFC. Effective magnetic moment (μ_{eff}) has been calculated through the relation: $\mu_{\text{eff}} = \sqrt{8C} \mu_{\text{B}}$ per.

Fig. 3.18. (A) Graphical representation of Co₃TeO₆ crystal structure where only Co - O 87 bonding is shown (red solid ball is the oxygen) and (B) Representative angles (in degree) between Co-O-Co are shown, which can modify the nature of super-exchange interaction (e. g., $\angle \text{Co} - \text{O} - \text{Co} \geq 120^\circ$ AFM type and weak FM type otherwise). These are employed in first principles calculations. Various orientations are used for clear visual presentation.

Fig. 3.19. SXRD patterns of CTO synthesized in air, argon and vacuum atmosphere, 90 indicating the only novel route for CTO synthesis. Dash represents multiphase CTO for vacuum ad argon case.

Fig. 3.20. Co K edge XANES spectra of CTO synthesized in air, argon and vacuum 91 atmosphere, indicates same Co valency.

Fig. 3.21. ZFC and FC Magnetization vs temperature curves taken under 100 Oe. Inset 95 shows the 1st derivative of FC curve.

Fig. 3.22. 1st derivative of DC magnetization data at 5 Oe (shown in the inset), which 95 shows clear signature of all magnetic transitions, especially at 16 K.

Fig. 3.23. Schematic drawing of the proposed Co-Co spins arrangements, for our ceramic 98 CTO, through layer A, B, C and D, respectively. These layers are Co2-Co3-Co5 (a), Co1-Co4 (b), Co2-Co3-Co4 (c) and Co1-Co5 (d), respectively. The Co ions lie in the ac plane, as in the earlier case of Wang et al.,.

Fig. 3.24. Similar schematic drawing of the proposed Co-Co spins arrangements, for single crystal CTO through layer A, B, C and D, respectively. These layers are Co2-Co3-Co5 (a), Co1-Co4 (b), Co2-Co3-Co4 (c) and Co1-Co5 (d), respectively. 99

Fig. 3.25. It shows the magnetization difference of the corresponding FC and ZFC mode. 101

Fig. 3.26. Thermal dependence of inverse susceptibility (H/M) data of ceramic CTO taken at magnetic field of 100 Oe. 102

Fig. 3.27. Magnetic hysteresis loop measurement at 5 K and 300 K. 103

Fig. 3.28. This shows power law behavior of inverse susceptibility (H/M) data. 103

Fig. 3.29. Low field Magnetization data, both in ZFC and FC mode, taken subsequently at 100 Oe, 500 Oe and 1000 Oe. It clearly shows the suppression of deviation, as indicated by vertical arrows and insets. 104

Fig. 3.30. Dielectric constant vs temperature profile at different magnetic fields. Inset shows the error bar of one of the representative dielectric data taken at 5 T. 105

Fig. 3.31. Dielectric constant showing change in peak position towards lower temperature with the increase in magnetic field. 107

Fig. 3.32. Measured pyroelectric current as a function of temperature in the presence of 0, 3 and 5 T external field (poling field = 6.6 kV/cm). 108

Fig. 3.33. Electrical polarization derived from pyroelectric current is plotted as a function of temperature in the presence of 0, 3 and 5 T external field. 108

Chapter 4

Fig. 4.1. Synchrotron X-ray diffraction patterns of $x = 0.0, 0.1, 0.2, 0.3, 0.5, 1$ and 2 compositions possessed either mixed ($C2/c$ and $R\bar{3}$) symmetry ($0.1, 0.2, 0.3$) or pure $R\bar{3}$ symmetry ($0.5, 1.0, 2.0$). Here $x = 0$ corresponds to pure CTO ($C2/c$) phase. 116

Fig. 4.2. Synchrotron XRD patterns of $Co_{3-x}Mn_xTeO_6$ with only $x = 0.0, 0.05, 0.25$ and 0.5 . Inset shows SXRD patterns for $x = 0.3, 0.4$ and 0.5 for q around ~ 4.8 , indicating mix phase behavior below 0.5 . 117

Fig. 4.3. (a) CTO, (b) MTO crystal structures with $C2/c$ and $R\bar{3}$ symmetries, respectively. Red smaller circles represent oxygen atoms, blue and magenta circles represent Co and Mn atoms, respectively, while the large dark yellow circles show Te atomic positions (a, b, c axes are as indicated) . Arrow in (b) shows a particular transition metal in oxygen environment. 118

Fig. 4.4. Two phase Rietveld refinement for the composition $x =$ (a) 0.1, (b) 0.2, (c) 0.25 119
and (d) 0.3, wherein C2/c and $R\bar{3}$ with their corresponding structural parameters have
been taken as inputs. Red circle represent raw data, black solid line the Rietveld fit, blue
vertical bar the Bragg reflections and zigzag magenta line the difference between
observed and calculated intensities.

Fig. 4.5. Phase diagram obtained from Rietveld Refinement on the SXRD data as a 120
function of Mn concentration indicates mixed phases of C2/c and $R\bar{3}$ for $x < 0.5$, while
pure $R\bar{3}$ phase for $x \geq 0.5$. Enlarge data shows the representative error bar.

Fig. 4.6. (a) Variations of lattice parameters through volume per formula unit of C2/c 120
phase and (b) $R\bar{3}$ phase as a function of Mn concentrations for $x < 0.5$, error bars are
within the symbols. Connecting solid lines are shown just to guide the eye.

Fig. 4.7. Rietveld refinement of SXRD patterns for $x = 0.5, 1$ and 2 indicates the pure $R\bar{3}$ 121
phase.

Fig. 4.8. (a) Variations of $R\bar{3}$ phase lattice parameters and (b) average transition metal- 123
oxygen bond distances as a function of Mn concentration for $x \geq 0.5$ along with $x = 0.3$
within the error bars.

Fig. 4.9. Octahedral distortions for $x = 0.5, 1.0$ and 2.0 , obtained from Rietveld refined 124
structure, clearly showing bond length (in Å) variations. Distortions in the bond distances
can also be seen in the bond angles (O-TM-O) which vary from 75.8 to 73.4° in upper
part and from 108.2 to 106.6° in the lower part as we go from $x = 0.5$ to $x = 2.0$. This
particular TM has been shown by arrow in Fig. 4.3 (b).

Fig. 4.10. Edge step normalized XANES spectra at Co K edge, which show gradual shift 126
of main edge energy indicating increase of Co^{2+} concentration (right inset) with increase
in Mn concentration using maxima in the first derivative of normalized absorption and the
corresponding charge proportion (left inset).

Fig. 4.11. Edge step normalized XANES spectra at Mn K edge for $x = 0.1$ and the 128
corresponding LCF fit (right inset) along with gradual shift of main edge (raising edge)
energy, via maxima in the first derivative, which indicates increase of Mn^{2+} concentration
with increase in Mn concentration (left inset).

Fig. 4.12. Te L_3 edge XANES spectra of $x = 0.5$ sample (main panel), showing +6 129
oxidation state of Te in the corresponding solid solution. Here we have used two

standards reference samples, TeO_2 for Te^{4+} state and $\text{Te}(\text{OH})_6$ for Te^{6+} oxidation states, respectively. Inset show 1st derivative for $x = 0.5, 1.0$ and 2.0 as a function of energy, indicating the same +6 oxidation state of Te in all the samples.

Fig. 4.13. (a), (b), (c) Low magnetic field DC magnetization in ZFC/FC protocol for $x = 0.5, 1.0$ and 2.0 indicates enhanced AFM transition (45 K, 40 K and 30 K) followed by induced ferromagnetic ordering at around 185 K. Insets show the dm/dT to assign exact Curie temperature. 134

Fig. 4.14. (a), (b), (c): Corresponding magnetic hysteresis (M/H) measurements at 300 K and 25 K for all samples signify the paramagnetic behavior at room temperature and FM like at low temperature. 135

Fig. 4.15. FM correlations is manifested through the CW fit of the inverse magnetic susceptibility (H/M) data for CMTO ($x = 0.5, 1$ and 2) solid solutions, inset enlarge the linear part. Data has been offset along Y-axis for clarity. 137

Fig. 4.16. Magnetization difference curves as a function of temperature for CMTO ($x = 0.5, 1$ and 2) show additional transitions at 118 K, 112 K and 83 K, respectively. 137

Fig. 4.17. Representative hysteresis loop for CMTO; $x = 0.5$ at 180 K, 150 K and 100 K. 138

Fig. 4.18. Deviation of H/ M curve from the CW law, the upper inset shows the enlarge data for $x = 2$. Main panel data is shifted in Y axis for clarity, corresponding values are not shown. 139

Fig. 4.19. Very high magnetic field χ (H/M) and χ^{-1} curves for CMTO, which signifies another characteristic of GP. The CW fit indicates absence of GP at 50 kOe. 140

Fig. 4.20. Unaltered values of T_N at various magnetic fields for CMTO ($x = 0.5, 1$ and 2). 140

Fig. 4.21. (a) Polyhedral view along (010), (b) layered structure (side view from b -axis) of Mn/Co ions, (c) equilateral triangular arrangements (top view along b axis) of Mn/Co ions located at different layers, and (d) network type of structure through oxygen along c -axis (a-b plane). 142

List of Tables:

Table 2.1. Major Parameters of Indus-2.	21
Table 2.2. Beam Parameters at BL-12.	24
Table 2.3. Features of the Huber-5020 diffractometer.	25
Table 2.4. Details of the Image plate setup.	25
Table 2.5. Phase compositions obtained from Rietveld refinement on SXRD data and LCF on XANES data of cobalt oxide nanoparticles samples H1 to H4 are tabulated, along with refined cell parameters.	52
Table 3.1. Rietveld refined lattice parameters and atomic positions of Co_3TeO_6 at room temperature.	69
Table 3.2. Comparison of lattice parameters of present ceramic CTO with the earlier reports.	69
Table 3.3. Most relevant interatomic distances (\AA) in our ceramic CTO in comparison to the single crystal CTO.	70
Table 3.4. Binding energies (in eV) for Co $2p$ ($2p_{1/2}$ and $2p_{3/2}$) and Te $3d$ reported in literature along with our results. O/T denotes the octahedral and tetrahedral coordination, respectively.	72
Table 3.5. Total energies of all possible antiferromagnetic and ferromagnetic spin configurations for the coexistence of Co^{2+} and Co^{3+} in Co_3TeO_6 . The energies have been tabulated with respect to the energy of $\text{Co}^{2+}\text{-O-Co}^{2+}$ antiferromagnetic spin arrangement (Co^{2+} as 100%) as reference. The lowest-energy spin arrangement is given by $\text{Co}^{2+}\text{-O-Co}^{2+}$. AFM+GKA as shown in the table for the respective concentration of Co^{3+} .	80
Table 4.1. Results of the Rietveld refinement of the crystal structure of the Mn doped CTO samples (here $x = 0.5, 1.0$ and 2.0 only) at room temperature using Synchrotron X-ray powder diffraction data using $R\bar{3}$ space group.	122
Table 4.2. Effective Bohr magneton (μ_{eff}) and λ values for both GP and PM phase obtained from fitted parameters (observed through CW fit) and modified CW law for CMTO. Maximum errors in μ_{eff} and λ are 0.06 and 0.005, respectively.	137

Chapter 1

Introduction

Materials with new functionalities and improved performances are key drivers of innovation. Current examples of such materials are transition metal (TM) based Oxides¹ and Multiferroics (MFs).²⁻³ These materials show potential applications in many fields like medical,⁴⁻⁶ spintronics,⁷⁻⁹ memory storage devices,¹⁰⁻¹⁴ solar cells¹⁵⁻¹⁶ etc.¹⁷⁻¹⁹ and thus are fundamentally important²⁰⁻²². Oxide complexes of TMs (TM surrounded by oxygen) exhibit variety of structures and properties due to unique nature of their outer shell *d*-electrons.²³ TMs are elements with partially filled *d* ($3d^1$ to $3d^9$) orbitals and exhibit relatively narrow *d* bands. Some implications, of having such features in TMs, are as follow. Overlap of substantially higher level broader band (e.g. 4*s* band of Vanadium (V)) with the entire *d* band results in an occupied (4*s*) band giving rise to metallic conductivity of (V) TMs.²⁴⁻²⁵ In TMOs (e.g. Vanadium oxide), on the other hand, completely filled 2*p* orbitals of oxygen anions form the valence band and partially filled 3*d* orbitals form the conduction band. Because of the bonding/anti-bonding splitting between the 2*p* and 4*s* bands, the cationic 4*s* band is several eVs above the 3*d* band (and completely empty at zero temperature) leading to insulating / semiconducting behaviour.²⁴⁻²⁵ The TM's 3*d* band is therefore responsible for all the electronic and magnetic properties in TM based compounds.^{1-3,20-23} Due to the pivotal role of 3*d* orbitals, we briefly describe the underlying fundamentals of TMOs in the following:

In TMOs, electrons manifest themselves in many different ways as they interact strongly not only with each other but also experience the crystal field potentials of the surrounding.^{23,24} Fig. 1.1 describes crystal field splitting (Δ) of 3*d* orbital under tetrahedral and octahedral crystal field potentials of anions environment around TM. These are the common types of polyhedral coordinations, where Δ is generally larger in the octahedral case (see Fig. 1.1). Under such potential, the electron in 3*d* orbitals of the TM prompts splitting of degenerate 3*d* orbitals into

two sub-orbitals, i) triply degenerate t_{2g} (d_{xy} , d_{yz} , and d_{xz} with spatial distributions along xy , yz , and xz) and ii) doubly-degenerate e_g ($d_{x^2-y^2}$ and d_{z^2} orbitals with spatial distribution along the coordinate axes). A comparison of the energy scales corresponding to Δ and coulomb interaction (U , also known as Hubbard repulsive energy) play major role in deciding a range of properties in TMOs, e.g. the spin states (low, intermediate or high) of the TM ions.²³ For instance, in the case of Fe^{3+} ($3d^5$) in oxygen octahedra, wherein larger Δ compared to U results in filling of lower orbital (t_{2g}) followed by e_g orbital and hence giving only one unpaired spin, indicating its low spin state.²³ Whereas, larger Δ in case of Co^{2+} ($3d^7$) in octahedral configuration results in its high spin state.²³ These two cases result in different magnetic moments and hence different magnetic properties in the corresponding compounds.

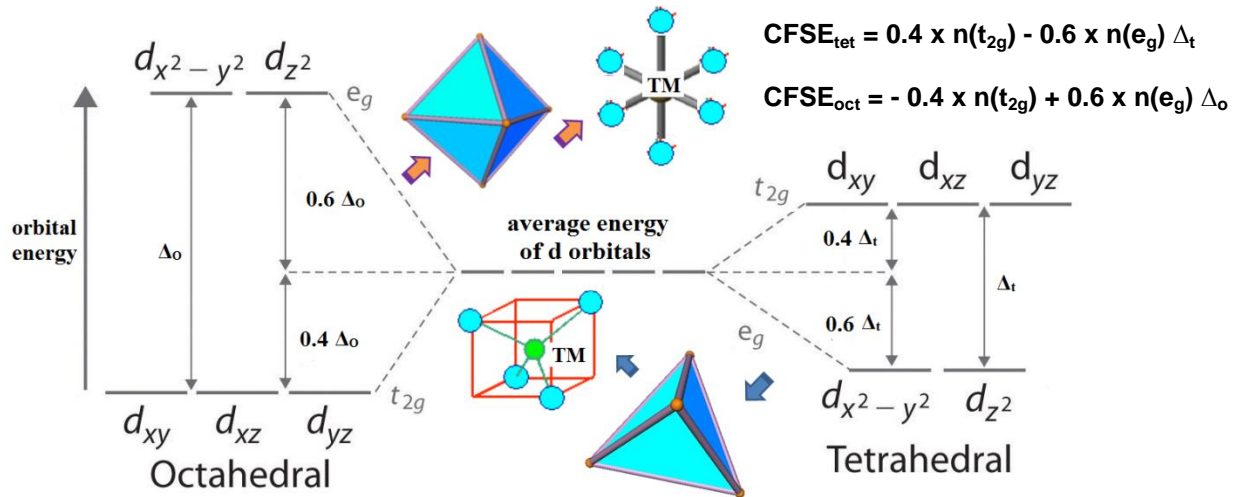


Fig. 1.1. Pictorial illustration of TM's d level splitting in (a) octahedral and b) tetrahedral crystal fields. Representation of corresponding coordination geometries is also shown. Crystal field stabilization energy (CFSE), for both the cases, where $n(t_{2g})$ and $n(e_g)$ – are the number of electrons occupying the respective energy levels, is mentioned.

Lifting of the degeneracy of d orbitals not only gives information on the variation in the magnetic properties but also may explain structural (phase transition) and spectroscopic (electronic) properties. In the presence of strong crystal field of octahedral/tetrahedral anions, the

regular polyhedra of cations either changes its structure from higher symmetry (cubic) to lower symmetry (tetragonal/orthorhombic) or distort through John Teller (JT) distortion (to be discussed in the next paragraph).^{23,24,26-27} Fig. 1.2 describes the distortion of regular polyhedra through elongation in any of the three crystallographic directions. This effect may lead to ferroelectric behaviour at the cost of the breaking of inversion symmetry (BIS).^{23,24,26-27} Furthermore, t_{2g} to e_g transition ranging between 1.8 eV to 3.1 eV (i.e. in the visible region) may explain electronic (the color) property.²⁸ Crystal field also provides significant splitting effects in square-pyramidal and trigonal-prismatic crystal symmetries.²³⁻²⁴

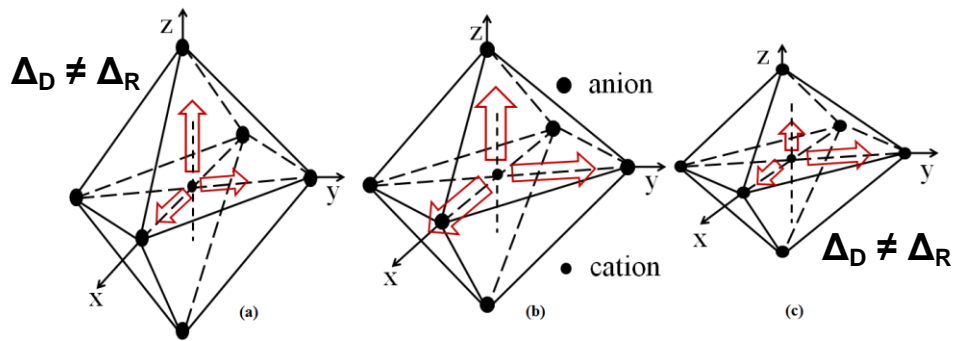


Fig. 1.2. Distortion from the regular octahedra (b) due to strong electric field of octahedral anions generally changes its structure from higher symmetry to lower symmetry through elongation in any of the three crystallographic directions. Representative elongations along z direction (a) and y directions (c) have been shown. Crystal field parameters would be different for each case, where Δ_D and Δ_R for distorted and regular octahedra, respectively.

In the following, we discuss the interplay of lattice and electron energies towards the magnetic interaction, which is also another implication of crystal field potential. This interaction is due to the combined effect of competition among crystal field, Hund's coupling and Pauli's exclusion principle. This interaction results in other interesting concepts such as JT distortion, super-exchange and double exchange mechanisms.^{23,26-27} JT distortion is a structural distortion due to the interaction between lattice and orbital energy. It is un-even occupation of electrons in a

degenerate set of orbitals, which creates un-even forces to distort the structure, thereby lowering both the symmetry and the energy of the system. For example, in TMOs, when two apical O atoms in an octahedron move toward the central atom, the d_z^2 orbital shifts to higher energies as compared to $d_{x^2-y^2}$ orbital, thus lifting the degeneracy of these orbitals. Out of the three known modes of octahedral distortion (breathing, basal plane and stretching modes), typical JT like distortion along z and y axes are shown in Fig. 1.2. Moreover, apart from the direct exchange between TM ions, two indirect exchange interactions through intervening oxygen namely the super-exchange and the double exchange have also been proposed to explain observed magnetic behaviour in a number of TMOs.²⁷ Double exchange prefers ferromagnetic (FM) interaction, while super-exchange may result in FM or antiferromagnetic (AFM) interaction, which depends on the electron configuration of the magnetic ions, the angle of interaction and the type of TM-O-TM bonding.²⁹⁻³⁰ The outcome of magnetic interactions in most of the TMOs can often be predicted from Goodenough-Kanamori-Anderson (GKA) rules.²⁹⁻³⁰

The phenomena discussed above are the result of coupling among charge, spin, lattice and orbital degrees of freedom.^{1,23} One of the most interesting examples in this category is the coupling between (ferro) electric and magnetic orders²⁻³ in insulating TMOs. This is also the main subject of this thesis. Structural and spectroscopic techniques have been used to understand the interaction and coupling between these two (electric and magnetic) orders. Attention has also been drawn for the correlation among structural, spectroscopic and MF (magnetic, dielectric and electronic) properties in TM based MFs. Usually, electricity and magnetism are coupled through Faraday's and Ampere's laws,³⁰⁻³¹ however, this coupling in insulators (where no electric current flows) is non-trivial.^{3,33} This coupling was observed for the first time in Cr_2O_3 , due to the broken inversion and the time reversal symmetries.³⁴⁻³⁵ The large electrical polarization in BiFeO_3 and

the magnetic control on electrical polarization in TbMnO_3 have triggered intense research in the field of MFs.³⁶⁻³⁷ An additional outcome of this coupling (between electric and magnetic orders) is the magneto-dielectric effect,³⁸⁻³⁹ wherein dielectric constant gets modified by magnetic field / magnetic ordering, indicating spin-phonon coupling. Although, such electric and magnetic orders are mutually exclusive in a single phase material, recent observations on various materials establish magneto-electric (ME) MFs as the future material.^{1,40} Remaining part of this chapter describes two types of ME couplings followed by proposed mechanisms explaining these couplings. The purpose and the motivation of this thesis are mentioned at the end of this chapter (section 1.4).

1.1. Multiferroics

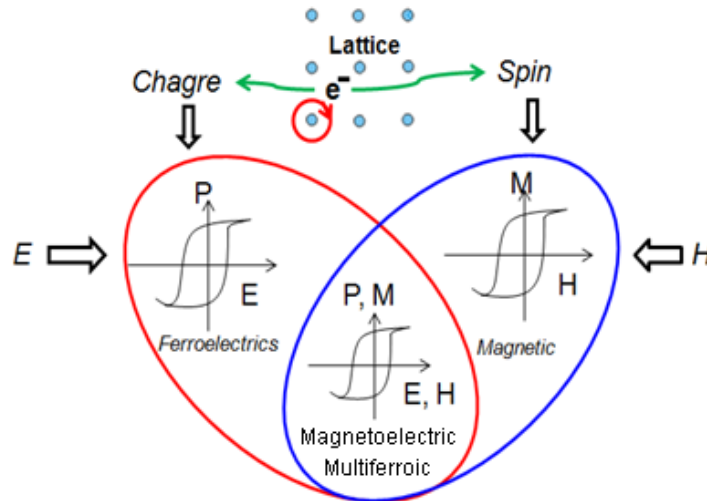


Fig. 1.3. Interaction among three degrees of freedom (charge, spin and orbital) of an electron in a lattice, results in ME MF that combines properties of ferroelectrics (due to charge) and magnets (due to spin). Hysteresis along with switching behaviour, displayed by ferromagnets and ferroelectrics mutually control magnetic response with an electric field and modification of polarization by magnetic field leading to the basis for making 4-state logic devices.

Single phase compounds and multiphase composites, which possesses simultaneously two or more primary ferroic orders viz. ferroelectric, ferromagnetic, ferroelastic and ferrotoroidic, are

called MFs.²⁻³ ME MF materials contains only two fundamental ferroic (magnetic and ferroelectric) orders in the same phase (Fig. 1.3). From application point of view, the coupling between these two ferroic orders is more important. For example, possibility of controlling magnetization by applying electric field or controlling polarization by applying magnetic field, in a single phase materials, is of great technological importance.⁴¹⁻⁴⁵ Magnetism and ferroelectricity (FE), as independent phenomena, are rather well studied in condensed matter physics. The stabilization of FE and magnetism in a single phase is quite difficult due to demand of two mutually exclusive requirements.^{3,33} The magnetic ordering requires localization of electrons into partially filled d shells and is usually seen in TMs leading to the metallic behavior. Conversely, FE (and hence electrical polarization) requires structural distortion of the lattice occurring usually from empty d shells, and ferroelectric materials tend to be insulators.^{3,41} This is not the only constraint, as simultaneous occurrence of magnetic and electric orders is also prohibited from symmetry considerations. Electrical polarization needs the lack of the inversion center whereas, magnetic order requires lack of time reversal.^{33,41} Although, the coexistence of FE with magnetism was initially considered as one of the rarest of rare phenomena, the evolution of strongly cross-coupled response of various materials with the spontaneous polarization and the spontaneous magnetization in the absence of external field has changed the existing scenario drastically.^{2-3,34-40}

1.2. Combining magnetism and ferroelectricity

A compound having transition metal provides magnetic ordering. But inducing FE in the same phase is not trivial.^{3,33,41} The path that MF community adopts is to induce ferroelectricity in a compound (consisting of magnetic elements), either by BIS or by using some other

mechanism.^{3,41} On the basis of microscopic mechanism for the origin of FE, the MF materials can be classified into two types, the type I (proper) and type II (improper) MFs.

1.2.1. Type I Multiferroics

In type I MF, appearance of FE and magnetism have separate mechanisms and thus the coupling strength between the two is weak, although the individual strengths can be quite significant.⁴⁰

These materials usually exhibit large polarization, and the ferroelectric transition is usually observed at higher temperature than that of the magnetic transition.⁴⁰ Depending on mechanisms, common examples of single phase type I MF materials are BiFeO_3 ,^{34,60} Fe_3O_4 ⁴⁶⁻⁴⁸ and YMnO_3 ⁴⁹⁻⁵⁰, which exhibit lone pair, charge order and geometrical frustration mechanisms, respectively.

In BiFeO_3 , FE occurs due to lone pair electron (Bi's). These electrons (also called the dangling bonds because they are always unsatisfied in chemical reactions) are highly polarizable and therefore lead to favorable condition for FE. Similar mechanism is observed for BiMnO_3 and PbVO_3 , where Bi^{3+} and Pb^{2+} , respectively play major role in the origin of the electrical polarization.⁴⁰ The co-valency of Bi/Pb-O bonds create electric dipoles (with certain admixture of oxygen p orbitals) along the corresponding bonds. On the other hand, magnetism in these compounds originates from the B site (Fe, Mn, V) consisting of unfilled 3d orbitals with uncompensated spins. In these cases, the magnetic and ferroelectric properties are decoupled and corresponding transition temperatures are far apart from each other.⁴⁰ It is also important to note that FE observed in these compounds is different from those of the conventional perovskite ferroelectric, which is of displacive nature.⁵¹

Charge order (CO),⁴⁶ often observed in transition metal compounds, occurs when the valence of TM is not distributed equally on a particular crystal site. The average valence of that particular site, in most cases, has non integral value. Consequently, below the temperature at which charge

ordering occurs: i) charges start to localize on the particular sites at the cost of other sites, which were previously equivalent and ii) the appearance of super-lattice due to symmetry lowering.⁴⁶ One of the famous examples, where a charge order has been reported, is magnetite Fe_3O_4 (AB_2O_4). Below the Verwey-transition ($T_V = 120\text{K}$), Fe ions at the B site start to arrange into Fe^{2+} and Fe^{3+} and lead to FE ordering.⁴⁷⁻⁴⁸ However, this does not necessarily mean that mixed valence configuration will always lead to spatial inversion symmetry breaking.⁴⁷⁻⁴⁸ It may happen that the mixed valency of TM leads to the weakening and strengthening of alternate TM-O bonds resulting in net dipole moment and hence the polarisation.⁴⁷⁻⁴⁸ Similar to the earlier case, magnetism originates from the presence of localized spins of electrons (partially filled d shells) of TM ions.

Lastly, we consider the case of geometrically frustrated type I ME MF, as observed in YMnO_3 .⁴⁹⁻⁵⁰ FE in YMnO_3 has nothing to do with magnetic Mn^{3+} ions or its JT nature. It occurs by an accidental by-product (frustration of MnO_5 polyhedra and distortion in Y-O bonds) due to the tendency of close packing. Close packing in normal ABO_3 (where A ions are in 6-fold and B ions are in 12-fold coordination) perovskite occurs through tilting and rotation of BO_6 octahedra. This may also lead to structural transition like cubic to orthorhombic. However, in YMnO_3 (where Mn ions exist in 5-fold and Y ions are in 7-fold coordinations), tilting of MnO_5 block with Mn at the center, provide two down Y-O bonds and one up Y-O bond, resulting in net dipole moment.⁵⁰ This leads to loss of inversion symmetry and thus results in FE, wherein dipole moments are formed by Y-O pairs. The remaining requirement of ME MF i.e. magnetism in the same phase originates from the presence of localized electrons of d shells of Mn, as in earlier two cases.

1.2.2. Type-II (Magnetic) Multiferroics

In type II MFs, FE and magnetism are dependent phenomena i.e. one can induce the other.³⁵ Such materials exhibit intrinsic certain magnetic structures, which are responsible for BIS and hence for the electrical polarization.³⁵ Due to large coupling, these materials are extremely important from technological point of view.³⁵ In the following, we discuss various mechanisms for the development of ferroelectric order (as a result of BIS) on magnetic transitions, in some details.

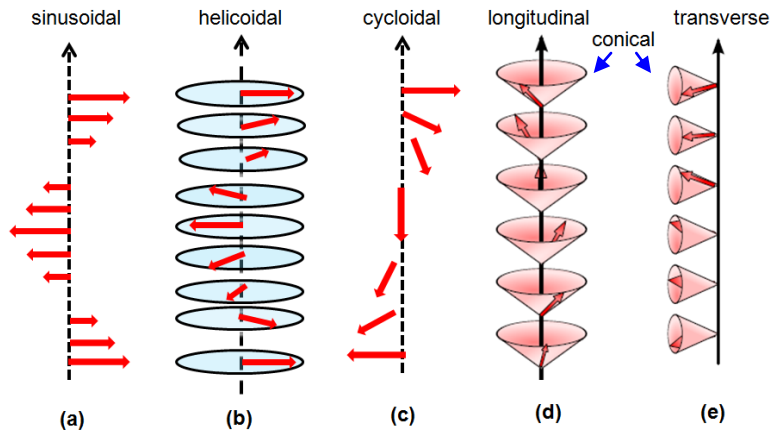


Fig. 1.4. Modulated spin structures, (a) sinusoidal, where magnitude of the magnetic moment changes along the propagation axis (arrow). (b), (c) The same remains constant in helicoidal and cycloidal spin configuration cases, only rotation axis changes. In (b), the rotation axis coincides with the propagation axis, while they are perpendicular in (c). In (d) and (e), which are longitudinal and transverse conical spin spirals, the spins rotate on a cone (not in a plane), leading to a macroscopic magnetization.

There are certain modulated magnetic orders different from well known FM and AFM orders, which play important role in strong ME coupling.^{41,52} These spin structures are sinusoidal, helical, cycloidal, conical etc. All these may be grouped under spin spirals and are shown in Fig. 1.4. The spin-spiral structures result from *magnetic frustration*,⁴¹ a situation in which no spin arrangement exists that simultaneously fulfils all exchange paths. As a result, a compromise spin structure is obtained, which only partially fulfils these paths. Spin-spiral structures are formed

for certain geometric arrangements of spins and relative strengths of the exchange paths. Different spiral arrangements are possible (Fig. 1.4), out of these only few can induce FE.⁴¹

The best known mechanism for the generation of a ferroelectric polarization is through a spin spiral structure based on the Dzyaloshinskii-Moriya (DM) interaction.^{41,53} The antisymmetric D-M interaction is the relativistic correction to the usual superexchange interaction and its strength is proportional to the spin-orbit coupling. This interaction favors non-collinear spin ordering, viz. spiral spin ordering. Once it produces the spiral state the lattice reacts (relaxes) to it by the magnetoelastic effect or exchange striction (minimizes energy) and that causes the atomic shifts or ferroelectric polarization. This is an antisymmetric contribution to the Hamiltonian due to spin-orbit coupling,

$$H_{DM} \propto \vec{D} \cdot \left(\begin{array}{c} \vec{S}_i \times \vec{S}_j \\ \vec{S}_i \quad \vec{S}_j \end{array} \right)$$

where, \mathbf{S}_i and \mathbf{S}_j are neighboring spins and \mathbf{D} is the *Moriya vector*. The vector \mathbf{D} can be expressed as $\mathbf{D}_{ij} = \mathbf{x} \times \mathbf{r}_{ij}$. Here, \mathbf{r}_{ij} is the vector connecting spins \mathbf{S}_i and \mathbf{S}_j and \mathbf{x} is the displacement of an intermediate oxygen ion from the connection line, which mediates the super-exchange between spins (Fig. 1.5 (a)). Magnetically induced FE in spin spirals works exactly the other way round. It is therefore also called the *inverse* DM interaction.^{41,53} The inverse effect is nothing but the efforts of the lattice degrees of freedom to repair the damage done by the D-M interaction. If a spin spiral is present and the oxygen atoms are not fixed, the displacement \mathbf{x} can be changed to minimize the DM energy term (Fig. 1.5 (b)).

An alternative explanation for the magnetic structure induced polarization is through spin current model⁵⁴ (i.e. $\mathbf{P}_{ij} \propto \gamma \times \mathbf{e}_{ij} \times (\mathbf{S}_i \times \mathbf{S}_j)$), for a pair of neighboring spins $\mathbf{S}_i, \mathbf{S}_j$ with the unit vector \mathbf{e}_{ij} connecting them. Here, γ is a constant, which depends on the spin-orbit coupling and super-

exchange interactions. These types of spin spiral structures have been proposed for rare earth manganites (e.g. TbMnO_3).³⁵ The paraelectric phase, in these cases, is characterized by sinusoidal spins network ($\mathbf{S}_i \times \mathbf{S}_j = 0$), whereas, ME phase is explained through spin current model having finite values of polarization with spin spiral ($\mathbf{S}_i \times \mathbf{S}_j \neq 0$) network. According to Katsura et al.,⁵⁴ the spin current induced between non-collinearly coupled spins displaces the oxygen atom, sandwiched between the two moments (TMs), through electron lattice interaction. This causes BIS leading to the ferroelectric nature.

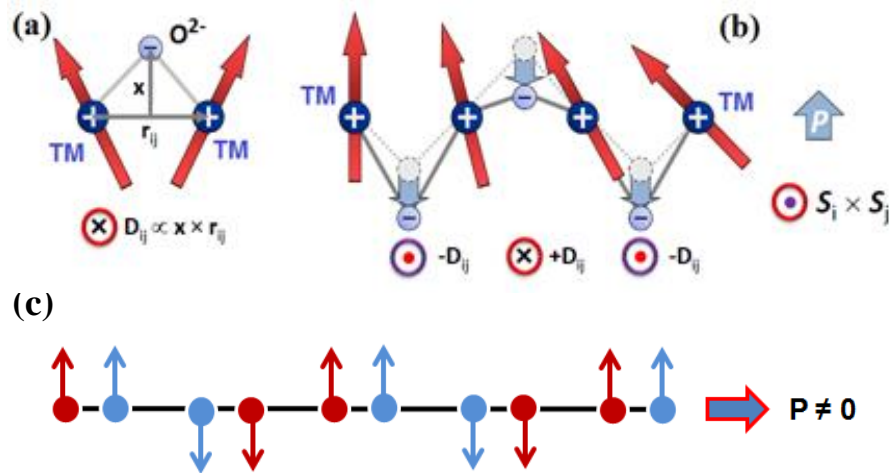


Fig. 1.5. The Dzyaloshinskii-Moriya (DM) interaction's mechanism, (a) Dependence of superexchange interaction between neighboring spins on their bond angle and hence on the displacement \mathbf{x} of oxygen ions, which results in the minimization of DM interaction energy for fixed bond angles adjusted by oxygen displacement. (b) In zig-zag chains, vector $\mathbf{D}_{ij} = \mathbf{x} \times \mathbf{r}_{ij}$ alternates in sign leading to a homogeneous shift of the negative ions with respect to the positive ions which results in macroscopic polarization. (c) Collinear spin structure with $\uparrow - \uparrow - \downarrow - \downarrow$ spin configuration breaks inversion symmetry and hence induces the electrical polarization.

In contrast to the spin spiral magnetic structure, collinear magnets consist of spins arranged in Ising chain ($\uparrow - \uparrow - \downarrow - \downarrow$), which is shown in Fig. 1.5 (c), BIS occurs through the Heisenberg-like symmetric exchange term.⁴¹ This specific type of spin arrangement is adopted by the stabilization of FM interaction between nearest neighbour and strengthening of AFM interaction over next nearest neighbours. These arrangements of spins (i.e. $\uparrow - \uparrow$ and $\downarrow - \downarrow$) can lead to in-

equivalent interatomic forces that result in magneto-striction based FE.⁴¹ Due to an exchange-striction,⁴¹ the distortion of ferro and antiferro bonds ($\uparrow-\uparrow$ and $\uparrow-\downarrow$) is different and thus the material (whether one have dissimilar or identical magnetic ion) becomes ferroelectric, as also predicted by theoretical calculations.⁵⁵ One more mechanism of ferroelectricity in a collinear magnet is the “electronic” ferroelectricity, which has been seen in frustrated magnets.⁵⁶

1.3. Applications and recent trends in Multiferroics

ME MFs have attracted great attention due to their promising potential applications.^{4-20,34-45} FM materials have been widely used in the field of data storage because of their property of switchable spontaneous magnetization by an external magnetic field.⁵⁷ Similar property of FE is applied in ferroelectric random access memory (FeRAM) for computers and radio frequency identification (RFID).⁸ In ME MF, four degrees of ferroic order work simultaneously that enables the possibility of four stage logic realization in a single phase device.⁵⁸⁻⁶³

Current field of data storage devices consist of two types of non-volatiles memories, FeRAM and magneto resistive random access memory (MRAM).^{14,64} MRAM has the advantage of very large density of memory elements along with a handicap in high writing energy. It has similar access time and endurance compared to FeRAM. In order to combine the respective advantages of FeRAM and MRAM, the second character i.e. magnetism of ME MF needs to be coupled. Through this, one can switch P by H or M by E using the concept of ME effect. Development of ME random access memory (MERAM), which is one of the potential applications of ME MF, saves the writing energy by using low write voltages and also keeps the advantage of MRAM.^{14,64} Some of proposed applications of ME MF materials are magnetic sensors, microwave devices, transformers and gyrators.⁶⁵⁻⁶⁸

Another impressive application of ME MF is in the field of Spintronics.^{7-9,40,69} In conventional electronics, information is encoded by the electron charge. In spintronics, the electron spin is used as an additional degree of freedom to perform logic operations and store information etc. Spintronics exploit the spin-dependent electronic properties of magnetic materials and semiconductors.⁴⁰ In spintronics, magnetism is used to control an electric current. Due to the large power consumption and heating in conventional electronics, spintronics have triggered significant interest in MFs for their potential to reduce the energy consumption while also adding functionality to the device.

Further, very recently, ME MF materials, in thin film form, have been found to be promising materials in solar cells.^{15,70} The key features of the same are their efficient ferroelectric polarization driven carrier separation and above-bandgap generated photo-voltage. Nechache et al.¹⁵ developed a multilayer structures of $\text{Bi}_2\text{FeCrO}_6$ with a graded bandgap, for the first time, which provides non-negligible photocurrent (20 mA cm^{-2}) and power conversion efficiency (PCE) of 8.1%.¹⁵ The two combined breakthroughs i.e. efficient carrier separation and above bandgap voltage, are a result of long range ordering of the cations Fe and Cr. This leads to the reduction of the absorption edge (optical band gap) from approximately 2.5 eV (of the parent compositions with Fe or Cr) to an impressive 1.5 eV (where maximum PCE is expected), through the charge transfer mechanism between Fe and Cr. Actually, in $\text{Bi}_2\text{FeCrO}_6$, the ferroelectricity (and hence polarization) is driven mostly by Bi^{3+} results in the internal electric field, which control the charge transfer between Fe and Cr via O, leading to the tuning of the bandgap by controlling the cationic ordering of Fe and Cr.

It is clear from the above discussion that ME MF materials have been proposed to be of importance in various applications. The issues with further applications of ME MF materials are

the lack of strong ME effect and their functioning at / near room temperature. Recently Vaz et al.,⁷¹ suggest a way for solving these issues using MF composites (out of scope for this work).

1.4. Issues and Motivation of the present work

The subject matter of this thesis work, as mentioned above, is studies on structural and spectroscopic properties of TM based MFs and Oxides, owing to their frontier research activities⁷²⁻⁷³. We have chosen Cobalt oxide, Cobalt tellurate (Co_3TeO_6 : CTO) and Mn doped Co_3TeO_6 (CMTO). The interest in CTO⁷⁴⁻⁸⁶ is due to its low temperature type II MF properties and monoclinic crystal structure with multiple magnetic transitions. One of the structural issues with CTO is variety of polyhedral configurations of divalent Co ions (Co^{2+}), which is usually not feasible.⁸⁷⁻⁸⁹ Further, in order to enhance the coupling strength and the magnetic transition temperature, in CTO, we have studied Mn doped CTO ($\text{Co}_{3-x}\text{Mn}_x\text{TeO}_6$: CMTO). Here, both the end members (Co_3TeO_6 and Mn_3TeO_6 : MTO) belong to the A_3TeO_6 family; (A = Mn, Ni, Cu, Co),⁷⁶ and are improper and proper MFs, respectively. Although, substantial amount of work have been reported on CTO⁷⁴⁻⁸⁶ and CMTO⁹⁰⁻⁹⁴, there are several issues, still under debate.

1) Single phase synthesis⁸³⁻⁸⁶ and reported large variations in its intrinsic low magnetic field magnetic behaviour⁷⁷⁻⁸² remain a challenging issue in ceramic as well as single crystal CTO. In addition, to the best of our knowledge, none of the reports discuss growth mechanism of ceramic CTO.

2) There is no experimental report which shows all the five magnetic transitions ~ 34 K, 26 K, 21 K, 17.4 K and 16 K in a particular ceramic or single crystal CTO.⁷⁷⁻⁸⁰ Origin and the understanding of each magnetic transition is also an important issue.

3) Literature suggests only Co^{2+} ions in CTO, which occupies five different crystallographic positions as tetra, square-pyramidal and three octahedral sites.⁷⁴⁻⁸⁰ Such variety of polyhedral

configurations with divalent (Co^{2+}) ions are usually not feasible.⁸⁷⁻⁸⁹ One possible way to arrange such polyhedral mixing is through mixed valence ions. However, there are no reports about the presence of additional valency like Co^{3+} in (either single crystal or ceramic) CTO and thus needs to be explored.

4) Theoretical work predicts spontaneous weak magnetization as well as spontaneous polarization.⁸² The former one is consistent with domain structure observed in the Second Harmonic Generation measurements.⁸² The experimental observation of the spontaneous zero field polarization remains a subject of debate.

5) Moreover, magneto-dielectric,³⁸⁻³⁹ an important observation in the field of type II MFs, which deals generally with the response of dielectric constant under magnetic field, and hence spin phonon coupling has not been observed in any of the earlier reports.

6) In order to enhance the coupling strength and temperatures in CTO, researchers have tried doping Co site with several transition metals such as Cd, Fe and Mn etc.⁹⁰⁻⁹⁴ Out of these, only Mn doped CTO results in the enhancement of transition temperature.⁹¹⁻⁹² Mn doping in CTO enhances the AFM transition temperature to ~ 40 K, which is 26 K for CTO and 23 K for MTO.⁹¹⁻⁹² Not only the structural origin of this enhancement is missing, but also no evidence of FM interaction is observed.

We have made an attempt to understand the growth mechanism of CTO (synthesized through a novel two step solid state reaction route).⁹⁵ In order to address above mentioned issues (numbered as 2-5), extensive structural as well as spectroscopic studies with their probable correlation with magnetic and dielectric properties of CTO have been carried out.⁹⁵⁻⁹⁹ Temperature and magnetic field dependent magnetic, dielectric and polarization measurements are performed and analyzed to address above mentioned issues in CTO. Furthermore, to address

the issues in Mn doped CTO samples (described in paragraph numbered 6, above), we have carried out room temperature Synchrotron X-ray Diffraction (SXRD) and TM K- edge X-ray Absorption Near Edge Structure (XANES) studies, described in chapter 4. Detailed structural as well as spectroscopic studies have been used to establish a correlation between these information and the observed as well as reported enhancement in the AFM transition temperature and the high temperature robust ferromagnetism (not reported so far), in CMTO.¹⁰⁰⁻¹⁰²

1.5. Organization of the Thesis

Work of this thesis is organized as follows: Details of the instruments and experimental set-up used for various characterizations of samples; along with synthesis procedures are discussed in chapter 2. Utilization of XANES measurements for the study of phase concentration of a multiphase sample is established for cobalt oxide nanoparticles¹⁰³⁻¹⁰⁵. Chapter 3 is divided into three sections. In these sections, we have discussed the growth mechanism of CTO (Section 3.1), charge and spin states of Cobalt in CTO (Section 3.2) and their probable correlation to magneto-electric and magneto-dielectric properties (Section 3.3). Chapter 4 is divided into two sections. Preparations and characterizations of CMTO are discussed in the first section. The second section provides structural explanation to the observed magnetic behaviour of CMTO. Conclusions and proposed future work are discussed in chapter 5.

Chapter 2

Experimental techniques

2.1. Introduction

In this chapter, synthesis procedure and characterization techniques have been described. Since, the optimization of synthesis of samples are interrelated to the characterization steps, hence details of synthesis process are discussed in results and discussion section (chapter 3 for CTO and chapter 4 for CMTO). We only briefly mention about the synthesis procedure in this chapter. Structural details in relation with growth of these materials have been covered into the results and discussion part of chapters 3 and 4. For structural and spectroscopic characterizations (and their correlation with magnetic, dielectric and electronic properties), which are the main subject work of this thesis, Angle Dispersive X-ray Diffraction (ADXRD) beamline (BL-12)¹⁰⁶ has been used extensively along with scanning EXAFS beamline (BL-09)¹⁰⁷ at Indus synchrotron source¹⁰⁸⁻¹⁰⁹. X-ray diffraction and X-ray absorption techniques along with some details of Indus-2 synchrotron source are discussed followed by brief discussion on the dielectric and the magnetic measurement set-ups.

2.2. Synthesis

For the preparation of bulk ceramic CTO and CMTO, the solid-state reaction (SSR) route has been utilized. Cobalt oxide nanoparticles (NPs) have been prepared by the wet chemical route¹⁰³.

2.2.1. Solid State Reaction Route

The SSR (also called solid state diffusion, i.e. the movement and transport of atoms in solid phases) is the simplest and most widely used method for the preparation of polycrystalline samples. Four steps namely, i) Weighing and mixing, ii) Calcination, iii) Shaping or Pelletization and iv) Sintering, are used in the SSR route. Solids (powder form) do not react at room temperature over normal time scales and is necessary to heat them at much higher temperatures (often > 1000 °C) in order for the reaction to occur at an appreciable rate. In the SSR technique,

chemical reactants are taken in required stoichiometric or (sometimes) off- stoichiometric ratio and mixed thoroughly. After mixing, solid mixtures are heat treated at higher temperature (called calcination) for several hours with intermediate grindings. As a main element of a SSR route, a resistively heated quartz tube furnace system has been utilized for the present work. Shaping or pelletization of samples is preferred since it increases the area of contact between the grains. Finally, sintering has been done to increase the density. The factors on which the feasibility and rate of a SSR resides are reaction conditions, structural properties of the reactants, surface area of the solids, their reactivity and the thermodynamic free energy change associated with the reaction. The synthesis procedure for CTO and CMTO is given in the forthcoming paragraphs. CTO is synthesized using conventional SSR route. The reactants used are of analytical grade i.e. Co_3O_4 (Alpha Aesar 99.7 %) and TeO_2 (Alpha Aesar 99.99 %). The mentioned reactants are taken in stoichiometric as well as off- stoichiometric ratios and mixed thoroughly using Shaker mixture (TURBULA @- T 2 F) for 6 hrs. Obtained mixtures have been calcined at different temperatures and for different time in order to get single phasic CTO in an optimized condition. In the process of CTO preparation, stoichiometric as well as off- stoichiometric ratios of Co_3O_4 and TeO_2 has been considered for optimizing the growth. Optimization parameters include calcination time, calcination temperature, single step and double step calcination process etc. Optimized parameters suggest non-stoichiometric reactants (with 5% excess of TeO_2) and a two step calcinations procedure are essential for synthesis of single phase CTO sample. Firstly, the ground (non-stoichiometric) oxide mixture is heated at 700 °C for 10 hrs and then re-calcined at 800 °C for ~ 25 hrs, as a second step. For each step of calcination and sintering (~ 850 °C for 2hrs), the pellets are made by applying 2 tons of hydrostatic force.

$\text{Co}_{3-x}\text{Mn}_x\text{TeO}_6$; ($x = 0.0, 0.05, 0.1, 0.2, 0.25, 0.3, 0.4, 0.5, 1, \text{ and } 2$) are also synthesized via conventional SSR route. The reactants used are of analytical grade Co_3O_4 (Alpha Aesar 99.7 %), Mn_3O_4 (obtained from high purity MnO_2 : Alpha Aesar 99.999%) and TeO_2 (Alpha Aesar 99.99 %). We have used the same synthesis route, as in the case of CTO, which involves non-stoichiometric reactants (5% excess TeO_2) and a two step calcinations procedure. Firstly, the ground oxide mixture is heated at $700\text{ }^\circ\text{C}$ for 10 hrs and then re-calcined at $800\text{ }^\circ\text{C}$ for ~ 25 hrs as a second step. Different calcination times for different Mn concentrations are required for single phase synthesis. Calcination time of ~ 25 to 30 hrs for $x < 1$ and 48 hrs for $x \geq 1$ are used. For each step of calcination and sintering ($\sim 850^\circ\text{C}$ for 2hrs), the pellets are made by applying 2 tons of force. Volume compression in all the pellets for $x < 0.2$ and no volume change for $x > 0.5$ has been observed, on calcination. In the composition range $0.2 \leq x \leq 0.5$, volume expansion like behavior has been observed. Anomalous changes in volume of pellets after calcination might be due to large variation in the densities of CTO ($\sim 1400\text{ gm/cm}^3$) and MTO (720 gm/cm^3).

2.2.2. Wet Chemical Route

Cobalt oxide NPs are synthesized using wet chemical route.¹⁰³⁻¹⁰⁴ The reactants used are cobalt nitrate $\text{Co}(\text{NO}_3)_2 \cdot 6\text{H}_2\text{O}$ as a precursor, 2-Pyrrolidone as solvent, oleic acid and trioctylphosphine oxide (TOPO) as surfactants. The purpose of TOPO and oleic acid is to control of size and shape of the NPs. The chemicals used are of analytical grade and are procured from Sigma Aldrich. 0.5 g (1.72 mM) $\text{Co}(\text{NO}_3)_2 \cdot 6\text{H}_2\text{O}$ is dissolved in 25 mL (0.33 M) 2-pyrrolidone. 2 mL (6.2 mM) oleic acid and 2.4 g (6.2 mM) trioctylphosphine oxide are mixed with the above solution at 50°C and stirred for 30 minutes. The reaction takes place in two steps. After heating at $50\text{ }^\circ\text{C}$ and stirring the mixture for ~ 30 minutes, the solution has changed to pink color. This indicates the completion of the first phase. The solution is heated in air at $200\text{ }^\circ\text{C}$ for 1 hour and a black

solution is observed. The solution is then cooled to the room temperature and is diluted with methanol. Black powder is separated from the solution using centrifuge. The powder is dried at 65 °C for about 10 hours in the oven. The base sample (as grown) is further annealed at various temperatures from 300 °C to 800 °C for ~ 2 hrs in air. For the proposed work, we have chosen four samples 1) H1: as grown, 2) H2: annealed at 300 °C for 2 hours, 3) H3: annealed at 500 °C for 2 hours, and 4) H4: annealed at 800 °C for 2 hours.

2.3. Thermal Analysis

In order to understand the underlying growth reaction mechanism of CTO during SSR synthesis, thermal analysis of the mixed starting ($\text{Co}_3\text{O}_4+\text{TeO}_2$) powder is carried out. Thermal analyses, such as differential thermal analysis (DTA) and thermo-gravimetric analysis (TGA) of the oven-dried powder are carried out in a thermal analyzer (Perkin Elmer, Pyris Diamond) at a heating rate of 10 °C / min. DTA measures the temperature difference and shows a peak to the endothermic or exothermic direction depending on the type of reaction e.g. DTA takes upturn peak during oxidation i.e. exothermic reaction. TGA measures changes in mass of the sample with change in temperature e.g. change in mass during oxidation.

2.4. An overview of Indus-2 and the Beamline used for the present work

Laboratory X-ray source, where X-rays are produced through high energy beam of electrons falling on high Z materials, has immense importance. However, its low flux as well as spectral brightness or brilliance (flux per unit area of the radiation source per unit solid angle of the radiation cone per unit spectral bandwidth) remain experimental/technological limitation. This limitation is overcome by the synchrotron storage ring, wherein, electron or positron bunches continuously circulate at a fixed energy for periods up to many hours and results in synchrotron radiation (SR) emission. Material characterizations using X-rays have been greatly benefited by

the advent of SR sources. SR has several properties, which makes it more advantageous over laboratory X-rays. SR gives about 4 orders of magnitude higher photon flux, higher brilliance and most importantly, tunability in the X-ray region. Due to higher photon flux, one can afford to lose intensity in order to monochromatize X-rays with narrower energy spread (leading to higher energy resolution in structural and spectroscopic analysis). Also because of higher brilliance, the experiments are performed faster and with improved signal to noise ratio. In addition, tunability of the SR enables not only spectroscopic (response of a system as a function of energy) analysis but also multi-wavelength anomalous dispersion analysis quickly and conveniently.

Indus-2, the only Indian third generation SR source, is a 2.5 GeV and 200 mA current SR source having critical wavelength of 1.98 Å (for the radiation from bending magnets).¹⁰⁸⁻¹⁰⁹ Electrons are injected into a booster cum storage ring (circumference ~ 172.47 m) at 550 MeV and accelerated to 2.5 GeV, where the beam is kept stored for several hours. A set of 4 RF cavities with an operating frequency of 505.812 MHz provides the required energy for beam acceleration from 550 MeV to 2.5 GeV. Major parameters of Indus-2 source are summarized in Table 2.1.

Table.2.1. Major Parameters of Indus-2.	
Circumference	172.47 m
Injection Energy	550 MeV
Final Energy	2.5 GeV
Beam current	200 mA
Critical wavelength	1.98 Å (Bending Magnet)
Emittance	58 nmrad
Brightness	1.02×10^{14} (photons s^{-1} mm^{-2} bandwidth$^{-1}$)
Lifetime	18 hrs (at 100 mA current)

Depending on diverse purpose and requirements such as fundamental, medical and industrial, several beamlines (BLs) have been commissioned.¹⁰⁸⁻¹⁰⁹ These BLs are designed to operate either in hard X-rays (~5 - 25 keV) or soft X-rays (~100 eV to ~1500 eV) regions. Important components in a typical BL are slits, pre mirror, monochromator (crystal or grating), post mirror and the experimental station. The hard X-ray BLs are designed with double crystal monochromators (DCM), while the soft X-rays with grating monochromators.¹⁰⁸⁻¹⁰⁹ In addition, pre and post-mirror facilitate collimation or focusing of the X-ray beam, required for the operation of BL in high resolution or high flux modes, respectively. To avoid contamination of the reflecting surfaces of the optical elements and also to minimize scattering of photons by air, the BL has to be operated in high vacuum conditions with pressures of the order of 10^{-8} mbar, for hard X-ray BL. For soft X-ray BL, ultra high vacuum (UHV) of 10^{-9} mbar is required to facilitate windowless operation of the beamlines. In the following, we discuss the experimental techniques used in the present thesis, in some details.

2.5. X-Ray Diffraction

X-ray Diffraction (XRD)¹¹⁰⁻¹¹¹ has been a well-established technique in the field of structural investigation. Electrons in a crystal (a regular array of atoms) scatter X-rays. Since, the atoms are arranged in regular pattern, the scattered waves from the atoms exhibit definite phase relationship and interfere, giving rise to constructive and destructive interference.

In order to understand the underlying mechanism, Bragg has derived XRD equation (2.1) using Fig. 2.1, which is known as Bragg's law.

$$2 d_{hkl} \sin \theta = n \lambda, n = 1, 2, 3... \quad (2.1)$$

Bragg has considered consecutive parallel planes with the lattice spacing d , which is irradiated by incident radiation at incident angle θ . The path difference for rays reflected from adjacent

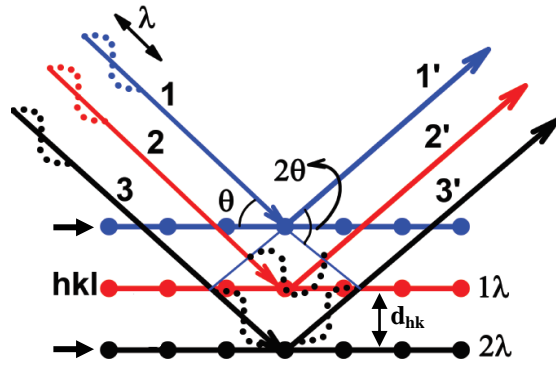


Fig. 2.1. Schematic to understand XRD mechanism through Bragg reflection by lattice planes of a crystalline sample. For XRD pattern, path difference between reflected rays by adjacent lattice planes must be integral multiple of wavelength.

planes is $2d \sin \theta$. These rays interfere constructively when the path difference is an integral multiple of wavelength λ . Bragg law, given by equation 2.1 gives only the space group information. Information about the basis/positions and types of atom at the lattice points is obtained by relative intensities of Bragg peaks. The intensity of a Bragg peak with miller indices (hkl) is given by

$$I_{hkl} \propto |F_{hkl}|^2; \quad (2.2)$$

F_{hkl} is the structure factor, which is defined as:

$$F_{hkl} = \sum_i f_i e^{2\pi i(hu_i + kv_i + lw_i)} \quad (2.3)$$

where, f_i is the atomic form factor of the i^{th} atom in the unit cell. u_i , v_i , w_i are the atomic (fractional) positions of the i^{th} atom in the unit cell. Summation is performed over the entire atoms in the unit cell. The proportionality includes the multiplicity for that family of reflections and other correction factors like absorption, geometrical factors, temperature dependence and polarization factors etc. As the temperature increases, peak intensity (or Bragg peaks) will decrease since spacing of the planes will not be correctly defined.

In this work, we have carried out synchrotron X-ray diffraction measurements using ADXRD beamline (BL-12)¹⁰⁶ at Indus-2 SR source¹⁰⁸⁻¹⁰⁹. BL-12 consists of pre and post mirrors and Si (111) based double crystal monochromator (DCM). The first optical element is a platinum coated Si pre-mirror which is plane and bendable in the form of a cylinder. This mirror is used for vertical focusing/collimation of the X-ray beam. DCM is the second optical element of the beamline and is used for monochromatization of photon beam. A pair of crystals is used in DCM for dual purpose of fixed exit of the beam, when energy is changed and also for suppression of higher order harmonics. The second crystal of the DCM, in the present optical design, is also used for the sagittal focusing of the beam. For high energy resolution, Si (311) crystal pair is also available which require approximately 3 days for being replaced and aligned. The third optical element is a platinum coated bendable post mirror used for vertical focusing of the beam. Optical layout and major parameters of ADXRD beamline are given in Fig. 2.2 and Table 2.2, respectively.

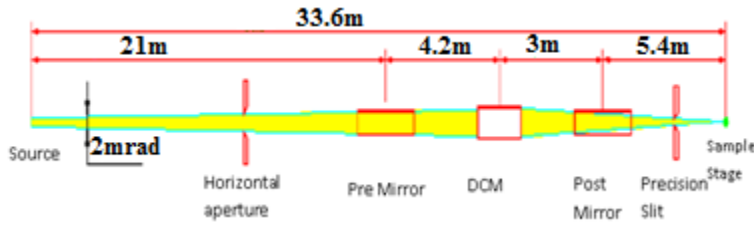


Fig. 2.2. Optical layout of BL-12.

Table 2.2. Beam Parameters at BL-12.

➤ Spectral Range: 5-22 keV
➤ Energy Resolution: 7000 (E/ΔE) at Cu K-edge
➤ Flux: 10 ¹⁰ photons/sec at 10keV
➤ Beam Size: 0.7mm (H) x 0.5mm (V)
➤ Angular Resolution ~ 0.018° /0.025°

BL-12 consists of two experimental stations in tandem. The adoptive optics allows us to focus the beam at one or the other experimental station. The first experimental station is a six circle diffractometer (Huber 5020) with scintillation point detector (Radicon). A photograph along with major specifications of the set-up is shown in Fig. 2.3 and Table 2.3, respectively.

Experimental station I: Huber-5020

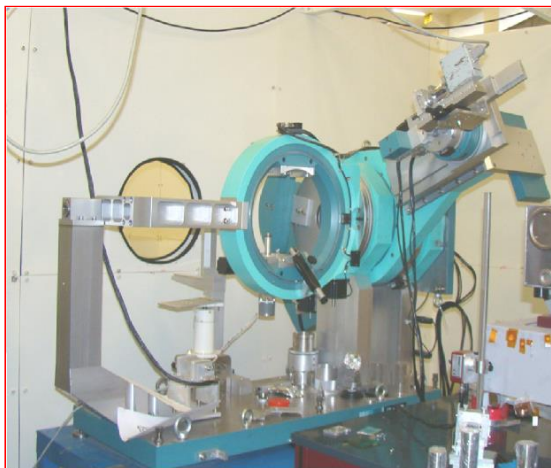


Fig. 2.3. Photograph of 1st experimental station consisting of several components.

Table 2.3. Features of the Huber-5020 diffractometer.

Angular range	0 – 100°
Sample environment	1. Air, Powder sample with provision for sample rotation 2. High temperature (up to 800K)
Higher order suppression	Possible with detuning of the second crystal
Various scan modes	1. θ -2 θ scan 2. detector scan 3. rocking curve scan 4. φ and χ scans
Incident flux monitoring	On line measurement using Ionization Chamber
q Range	4.66 \AA^{-1} - 14.74 \AA^{-1}
Angular Resolution	15 arc sec (single crystal in rocking curve) (and 0.018 degree for powder LaB ₆ (NIST))

Experimental station II: Image plate area detector



Fig. 2.4. Photograph of the 2nd experimental station with its various components.

Table 2.4. Detail features of the Image plate setup.

Diameter	345mm
Sample environment	1. Air 2. High pressure (Diamond anvil cell based) 3. Low Temperature (3K – 450K).
Higher order suppression	Possible with detuning of the second crystal
Sample mounting	Powder sample in a capillary with provision for sample rotation - Powder sample sandwiched between kapton sheets
q Range	up to 14.74 \AA^{-1}
Angular Resolution	0.025 degree (2σ in 2θ)

The second experimental station is Image plate area detector (Mar 345 Dtb). It consists of a pair of movable cross slits and two ionization chambers, for the alignment of the incident beam on the axis of the area detector. A photograph along with its main features is shown in Fig. 2.4 and Table 2.4, respectively. It may be mentioned that most of the Synchrotron XRD measurements included in this thesis have been carried out using the Image plate area detector.

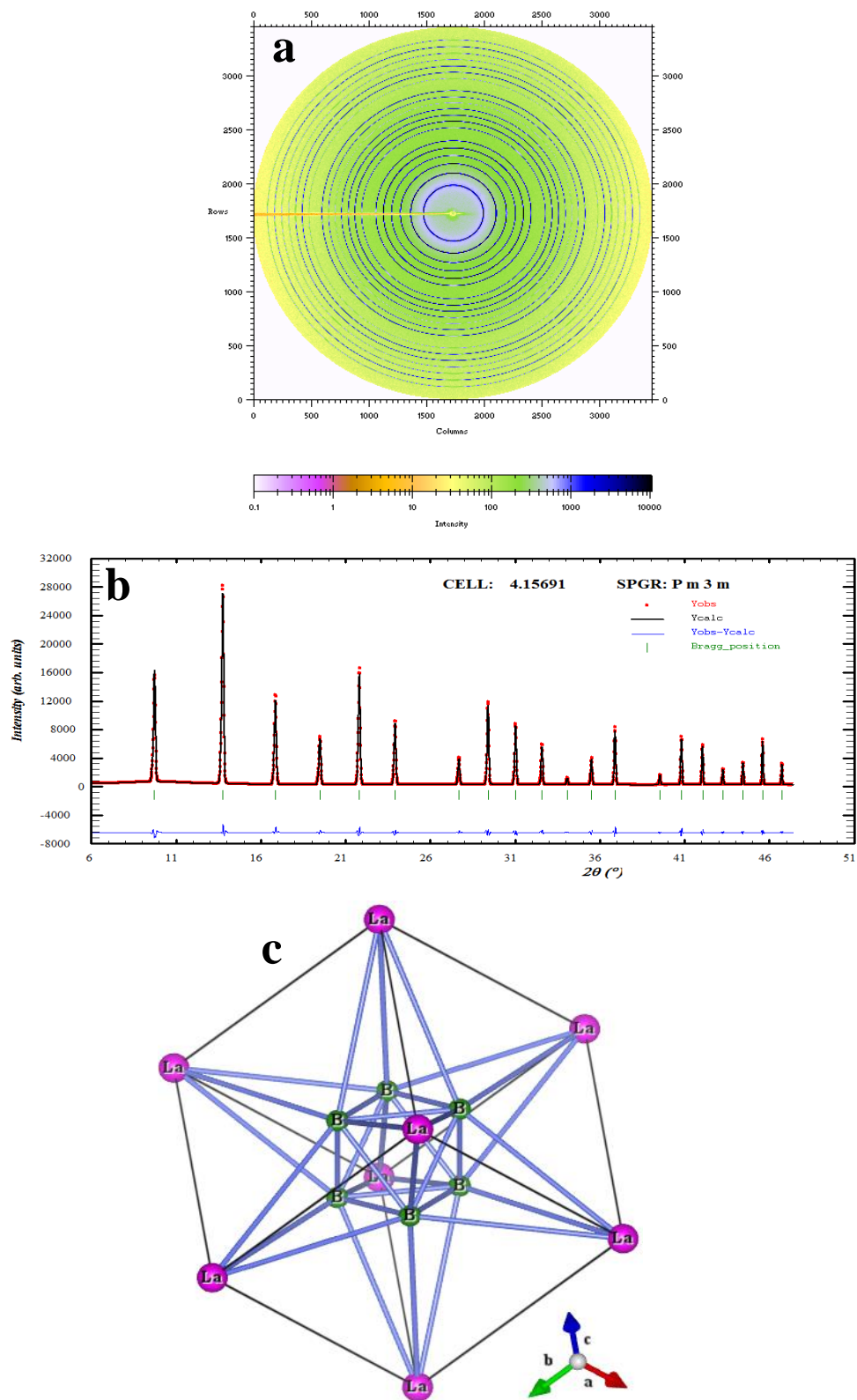


Fig. 2.5. (a) Shows 2D intensity data as found at Image Plate for LaB₆ NIST standard, (b) shows Rietveld refinement of the same LaB₆ 1D pattern and (c) shows a typical view of the refined structure form Rietveld refinement.

The XRD pattern obtained on the Image Plate is in the form of circular rings (2D pattern). These rings are converted into conventional intensity versus 2θ [I (2 θ) -1D] pattern using Fit2D software¹¹². A NIST standard (LaB₆) is used to get accurate values of (i) incident X – ray wavelength and (ii) D (distance between the sample and the detector). This value of wavelength was used for refinement of sample’s XRD patterns using Rietveld method.¹¹³ Apart from the powder samples on Image Plate, we have also performed High resolution SXRD measurements on diffractometer to resolve multiphase issue in CTO (to be discussed in Chapter 3). More details on each components of BL-12 can be found elsewhere.^{103,106,107-109} Fig. 2.5 (a) shows 2D intensity data as found in Image Plate for LaB₆ NIST standard. The data is reduced to I (2 θ) form, as shown by Fig. 2.5 b, using Fit2D software discussed above. This 1D intensity data along with its corresponding structure’s information has been used as input for Rietveld refinement. Fig. 2.5 (b) also shows theoretically obtained data points (circles) using FullProf¹¹³. In Fig. 2.5 (c), refined structure from Rietveld refinement is shown to find its atomic positions (Wyckoff), bonding, angle, polyhedral rotation or tilting etc. Synchrotron XRD provides the structural information like crystal symmetry, space group, lattice parameters, Wyckoff site distribution etc. Response of these parameters in extreme condition like temperature, pressure provide the understanding of mechanism for their variations in various properties such as structural, magnetic, electronic and dielectric. Below we discuss Rietveld refinement in brief.

Rietveld method is a powerful tool for refining crystal-structure using X-ray and neutron powder diffraction data.¹¹³⁻¹¹⁶ Present work emphasizes Rietveld refinement on X-ray diffraction data. It calculates the intensity [\propto (structure factor)²] for each plane, based on the parameters given and fit this data to the observed data using least square fitting. The refinement program also allows

the user to change some of the parameters suitable for better agreement between experimental and calculated values.

For satisfactory fit between observed and calculated patterns, the following agreement factors are optimized, 1). R_F - structure factor, 2). R_p - profile, 3) R_{wp} - weighted profile, 4) R_{exp} - expected weighted profile and 5). R_B - Bragg factor. The goodness of fit (χ^2) of the pattern fitting is defined as:

$$\chi^2 = S^2 = \left[\frac{R_{wp}}{R_{exp}} \right]^2 = \left[\frac{S_Y}{(N-P)} \right] \quad (2.4)$$

where, N and P are the number of profile points and refined parameters, respectively. R_{wp} is the main factor, which determines the convergence of refinement and R_{exp} is used to check the fit data quality. For obtaining the accurate structural parameters, R_{wp} and R_{exp} should be as low as possible. Backgrounds, in all the refinement, are modeled either by a suitable polynomial or by interpolation of user defined data points. Among the various peak shape functions, the pseudo-Voigt is most widely used. Since the Rietveld analysis is essentially a refinement process, the parameters which are refined in the Rietveld method include structural parameters (positional coordinates, unit cell parameters and thermal parameters), sample parameters (strains, domain size, preferred orientation etc.), instrumental parameters (FWHM of the peaks due to diffraction geometry, shift of origin, background etc.) and the scale factor. One has to consider occupancy parameter, scale factor, zero correction, half-width parameters and isotropic thermal parameters during refinement.

Synthesized (CTO, CMTO and cobalt oxide NPs) samples are characterized by SXRD measurements at BL-12. SXRD measurements have been performed in Debye-Scherrer geometry for all the samples. In order to compare SXRD patterns of various samples (see section

3.1 of chapter 3 and section 4.1 of chapter 4), we have used I vs q ($= 4\pi \sin \theta / \lambda$) plots instead of I vs 2θ plot (in order to make the SXRD pattern wavelength (λ) independent), because the measurements have been done at different wavelengths.

2.6. X-Ray Absorption Near Edge Structure Spectroscopy

X-ray absorption spectroscopy (XAS) of a material is characterized by sharp increases in absorption at definite X-ray photon energies.¹¹⁷ These definite photon energies are characteristic of the absorbing element and its neighborhood. A typical XAS spectrum is divided into two regions with respect to edge energy (E_0), as shown in Fig. 2.6. The structures in the vicinity of the edge up to around 50 eV from the edge are referred as X-ray Absorption Near Edge Structure (XANES). The region of the spectrum from about 50 eV to 1000 eV is called Extended X-ray Absorption Fine Structure (EXAFS).

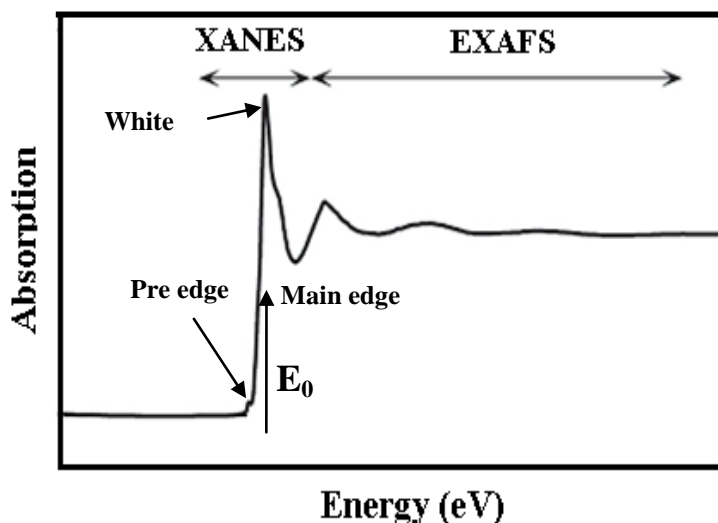


Fig 2.6. Schematic illustration of X-ray absorption spectrum.

In this work, XANES technique has been used extensively for the determination of charge states and spin states of elements (Co, Mn and Te) present in the studied (CTO, CMTO, cobalt oxide nanoparticles) samples. We have also proposed a method for estimating phase composition of

multiphase (cobalt oxide nanoparticles) materials using XANES. In the following, we discuss XANES technique and its measurement modes, in details.

K edge XANES spectrum is characterized by various features such as the main edge, the pre-edge, the white line as well as the near edge provide detailed information on the oxidation state, the coordination environment and the unoccupied DOS of the probed atom, respectively. However, the information on the coordination environment is an average of various possible coordinations. In XANES, we actually measure the probability that a deep-core electron will be promoted to an unoccupied bound or continuum state by the absorption of an incident X-ray photon. The absorption function measured by a core level absorption experiment is related to the transition rate of the photoelectron from some initial deep core state, $|i\rangle$, to a final state above the Fermi energy, $|f\rangle$. This transition rate is determined within the one electron and dipole approximations by Fermi's Golden Rule,

$$\mu \propto \sum_f |\langle f | \hat{\epsilon} \cdot \mathbf{r} | i \rangle|^2 \delta(\epsilon_f - \epsilon_i - \omega) \quad (2.5)$$

In this equation, $\hat{\epsilon} \cdot \mathbf{r}$ is the dipole operator for the incident electromagnetic wave on the system of atoms and electrons. First term in equation 2.5 is a dipole matrix element of the initial core state and the final state restricted to those final states, which are accessible by an incident photon of frequency ω . XANES spectra can be divided into two main regions: the pre-edge and the main edge.

Pre-edge region appears just below the main edge region and is caused by electronic transitions to empty bound states (see Fig. 2.6). Transition probability in this region is controlled by dipolar selection rules. For TM with partially empty d-orbitals, these features are visible owing to $1s \rightarrow 3d$ ($\Delta L=2$) transitions. The pre-edge features are relatively weak in intensity due to dipole-forbidden nature of these transitions. But the probability of their occurrence is nonzero (in the

case of TM oxide), because partially filled d-orbitals can hybridize with oxygen / anions p-orbitals. As a result, the intensity of these pre-edge features is weaker in comparison to absorption edge and enhances as the ligand environment is perturbed strongly, improving hybridization. In this way, pre-edge feature provides information of local geometry around the absorber (such as number of neighbors and ligand geometry).¹¹⁹⁻¹²¹ In addition, one can probe the spin state of that particular absorber on the basis of crystal field splitting (Δ), as discussed earlier in chapter 1. This feature reflects in the pre edge spectra as a result in the lifting of d orbitals degeneracy into e_g and t_{2g} orbitals due to crystal field of oxygen cage on TM. Several reports also suggest the determination of charge states using the pre-edge feature,¹¹⁹⁻¹²³ but mostly by main edge as discussed below.

When the incident photon energy is just sufficient to cause excitation of a core electron of the absorbing atom to empty states in continuum, there is a sharp increase in the absorption coefficient in the edge region (see Fig. 2.6). This transition is identified as 1s-4p (in the case of TM). However, it is still in debate about the accurate identification of this feature.¹²⁴⁻¹²⁸ Some of the authors have proposed this transition as 1s \rightarrow 4s, while others as 1s \rightarrow 4p transition.¹²⁴⁻¹²⁸ It may be mentioned here that, this identification does not change the interpretation of XANES spectra. The position of the absorption edge is closely related to the charge (oxidation) state on the absorbing metal ion. Higher the oxidation state of a metal, more is the positive charge (of the nucleus) experienced by the electron and thus more energy is required to excite an electron from an orbital. Hence, the position of the main edge blue shifts with increase in charge states. By measuring the edge position one can extract the information about the average valence state of the absorbing atom. The absorption edge is identified as the first inflection (maxima in first derivative) point or middle of the edge jump.

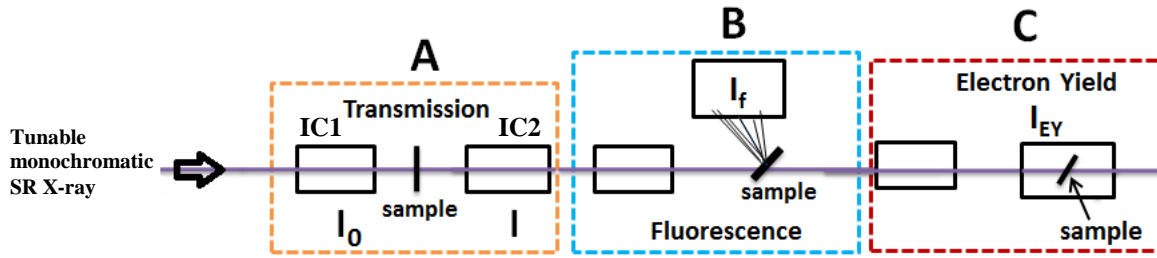


Fig. 2.7. Various modes of XANES measurements depending on the sample's conditions and requirements. I and IC in different subscript represent photon beam intensity and ionization chambers, respectively.

The XAS data can be collected in several modes: Transmission, Fluorescence and Total Electron yield (TEY), as shown in Fig. 2.7. The simplest and most popular mode is the transmission mode (Fig. 2.7: A), wherein the sample is placed between two identical ionization chambers (IC1 and IC2) to measure incident (I_0) and transmitted (I) intensities (X-ray flux), and absorption coefficient is obtained by the relation:

$$I / I_0 = \exp \{-\mu (E) \times x\} \quad (2.6)$$

where, x is the sample thickness and $E = hv$. Normalized $\mu (hv)$ vs hv is called XAS spectrum. To get the correct XAS spectrum, the edge jump in the spectrum is critical, which makes this mode more applicable only for samples with critical thickness or absorption. However, this mode cannot be used for samples, which are either too absorbing or too small in concentration. In such cases, in the former case the transmitted signal is too small, whereas, in the later case the edge jump is too weak, and cannot be relied upon.

For these samples, mainly two alternate modes, i) fluorescence and ii) total electron yield, are used. In fluorescence mode (Fig. 2.7: B), one measures the incident flux I_0 and the fluorescence X-ray's intensity, I_f , and absorption coefficient is obtained by the relation:

$$\mu(E) \propto I_f / I_0 \quad (2.7)$$

To measure the fluorescence, Vortex silicon drift detector (SDD) is used. Like other solid state X-ray detectors, SDDs measure the energy of an incoming photon by the amount of ionization it produces in the detector material. The major distinguishing feature of an SDD is the transversal field generated by a series of ring electrodes that causes charge carriers to 'drift' (concept allows significantly higher count rates) to a small collection electrode. Fluorescence mode is suitable for highly absorbing samples. However, this mode cannot be used with low Z materials, because the emitted photons lie in soft X-ray / VUV region, which gets absorbed in air. To overcome this problem, TEY detection mode (Fig. 2.7: C) is used. In TEY mode, we collect all the produced electrons and measure the drain current from the sample. It is not suitable for the highly insulating materials. Since probing depth of photoelectron is few nm, so experiments performed in the TEY mode are surface sensitive. Much larger escape lengths of photons in fluorescence mode, makes it more bulk sensitive as compared to TEY.

In this work, XANES measurements have been carried out at BL-12, both in transmission as well as fluorescence modes. Two ionization chambers (one for measuring incident flux and the second for measuring transmitted flux) have been used for data collection in transmission mode. We have also carried out some XANES measurements at Energy-Scanning EXAFS beamline (BL-09), in order to probe Te- L edge and K edges. BL-09 uses three ionization chambers, one for measuring incident flux, second for measuring transmitted flux and the third one for measuring XAS spectrum of a reference metal foil for energy calibration, for data collection in transmission mode. Rest of the experimental arrangement is the same as that of BL-12.

XANES measurements on the present (CTO, CMTO and cobalt oxide NPs) samples are carried out in transmission mode (for Co K-edge) and fluorescence mode (for Mn K-edge) at room temperature. The photon energy is calibrated by Co/Mn K-edge XANES spectra of standard

Co/Mn metal foils at 7709 / 6539 eV. Te L₃-edge XANES spectra has been recorded in transmission mode. In literature, average charge state of an ion has been obtained using XANES by linear extrapolation of edge energies of standards with known charge states in a sample. However, there is uncertainty in the slope of linear plot, in different reports. To establish the technique for the determination of charge state, we have taken a mixture of CoO and Co₃O₄ nanoparticles. The concentrations of the two phases were determined using XANES and also using XRD. A close match between the concentrations obtained by the two techniques, gives us confidence in average charge state obtained by XANES technique. The details of the proposed method are given in section 2.11 of this chapter.

2.7. X-ray Photoelectron Spectroscopy

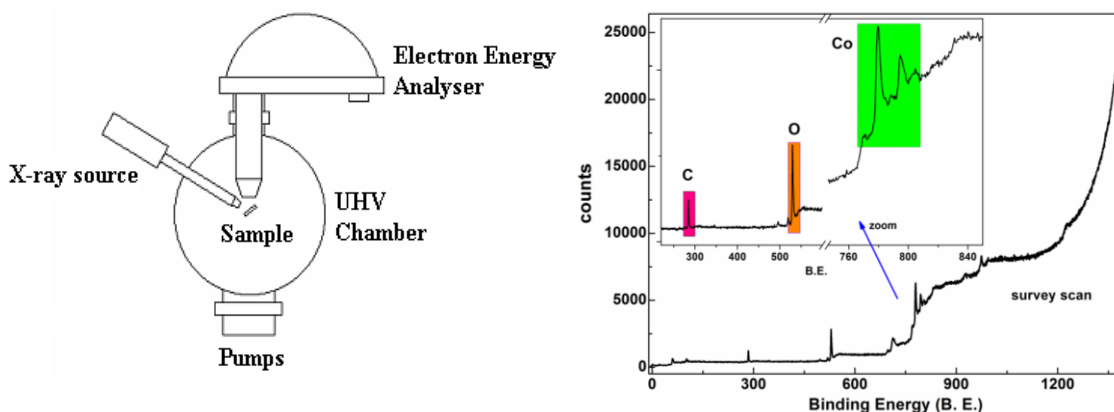


Fig. 2.8. (a) Instrumental setup of X-ray photoelectron spectroscopy (XPS) and (b) A typical XPS spectrum: survey scan of Co₃O₄ nanoparticles. Inset shows enlarge part of the same.

X-ray Photo-electron spectroscopy (XPS) is one of the most important methods to study the electronic structure of molecules, solids and surfaces.¹²⁹ In XPS, the kinetic energy distribution of the emitted photoelectrons from surface (escape depth ~ 5 – 10 nm) is analyzed to study electron binding energy (BE) and occupied electronic density of states of samples. The technique is based on the photoelectric effect. When the sample is irradiated with mono-energetic photon

of energy $h\nu$, it emits electrons from the sample surface. The kinetic energy of the emitted electron is given by

$$\text{K.E.} = h\nu - \text{B.E.} - \phi \quad (2.8)$$

where, $h\nu$ is the energy of the incident photon, B.E. is the binding energy of the emitted electron and ϕ is the work function of the spectrometer.

Schematic diagram of XPS set up is shown in Fig. 2.8 (a). In the present work, Omicron XPS system with monochromatic Al- $K_{\alpha 1}$ X-ray radiation (1486.6 eV, penetration depth $\sim 1 - 10$ nm) has been used for XPS measurements.¹³⁰ Survey scans are recorded over 0-1400 eV kinetic energies and then detailed scans are measured to determine the oxidation state of the elements of interest. In Fig. 2.8 (b), typical XPS spectrum for the cobalt oxide sample is presented in order to understand the analysis procedure. The XPS spectra are the plot of number of emitted electrons per energy interval versus their B.E. / kinetic energy. Since each element produces a characteristic set of XPS peaks at characteristic binding energies, one can identify directly the elements present on the surface of any material. These characteristic peaks of an element in the spectra correspond to the electrons emitting from its core levels, viz., 1s, 2s, 2p, 3s, etc. In XPS, the number of detected electrons corresponding to each characteristic peak is related to the amount of that particular element present within the area (volume) of the sample being irradiated. One can easily identify the chemical state of any element by knowing the exact peak position, peak separation and other spectral features such as satellite feature etc. In this measurement, ultra-high vacuum is required to increase the mean free path of the electrons coming out of the sample surface and reaching the detector.

XANES and XPS are sensitive to bulk and surface of the samples, respectively. Information obtained are also complementary in the sense that XPS gives information about occupied density

of states (DOS) below the Fermi level, whereas, XANES gives that for unoccupied DOS above the Fermi level.

2.8. Scanning Electron Microscopy

Electron microscopy is a versatile characterization technique to study the morphology, composition and texture of solid materials. Scanning electron microscopy (SEM) is used to analyze the same in the length scale ranging from few nanometers to hundreds of microns. The electrons are emitted from tungsten filament by thermionic emission process. Depending on the source, two types of SEM are commonly used. We have used field effect SEM, where field emission gun is used for emitting the electrons. The emitted electrons are accelerated by electric field in the energy range 1 keV to 30 keV. The beam is allowed to pass through electromagnetic lenses that focus it to form a nanometer sized electron probe. This probe scans on the specimen for SEM characterization. As a result of beam-specimen interactions various signals are produced. Secondary electrons are used for morphological characterization, back scattered electrons give rise to z contrast and diffracted backscattered electrons are used to determine crystal structures and orientations of minerals. X-rays emission spectra of constituent atoms are used for elemental analysis-known as energy dispersive spectroscopy (EDS). The secondary electron image is equivalent to an optical image in the reflected geometry and used extensively for material characterization. In the present work, cobalt oxide NPs samples are characterized using Phillips microscope (model XL30CP) to investigate the typical size of NP. For SEM measurements, NPs are dispersed in methanol and are ultrasonicated for 15 mins. These particles are dispersed dropwise on cleaned Si wafer. The samples are then dried under lamp light. A 100 Å thick gold layer is deposited on the samples to nullify the charging effect while performing SEM.

2.9. Dielectric Constant and pyroelectric current (Polarization)

Dielectric constant (ϵ) can be determined by placing the specimen between the parallel conducting plates. When electric field is applied between the plates, the interactions are described by the complex relative permittivity (ϵ^*) of the material and is expressed mathematically as:

$$\epsilon^* = \epsilon' + j \epsilon'' \quad (2.9)$$

where: ϵ' and ϵ'' are dielectric constant and dielectric loss factor, respectively ($j = \sqrt{-1}$).

$$\epsilon' = C / C_0 \quad (2.10)$$

$$\tan (\delta) = \epsilon'' / \epsilon' \quad (2.11)$$

and value of C_0 can be estimated by the formula.

$$C_0 = \epsilon_0 A / d \quad (2.12)$$

Here ϵ_0 is the permittivity of free space ($8.854 \times 10^{-12} \text{ Fm}^{-1}$) and A represents the area of the parallel plates. The value of C_0 can be determined using equation 2.10. For the measurement, we paint both surfaces of dielectric specimen with conductive silver paste and two copper wires are connected at both surfaces of pellets to work as electrode. The two electrodes are connected to QUADTech 1920 Precision LCR Meter via electrical connection of VTI (variable temperature insert) of Cryogen free magnet system. We measured (only for CTO sample) dielectric constant as a function of temperature and magnetic field. The response of dielectric constant in a magnetic field is called magneto-dielectric (MD) and is defined through MD parameter as:

$$\text{MD} = \{ \epsilon (T, H) - \epsilon (T, 0) \} / \epsilon (T, 0) \quad (2.13)$$

The schematic set up for pyroelectric current measurements is shown in Fig. 2.9. The electric current is measured with sweeping temperature (called pyroelectric current) and expressed as

$$I_p = S \frac{dP}{dT} \frac{dT}{dt} \quad (2.14)$$

where P , T , I , S , t are electric polarization, temperature, electric current, area of electrodes of the sample and time, respectively. Here, P is obtained by an integration of the electric current as;

$$P = \frac{1}{S} \int dt I_p \quad (2.15)$$

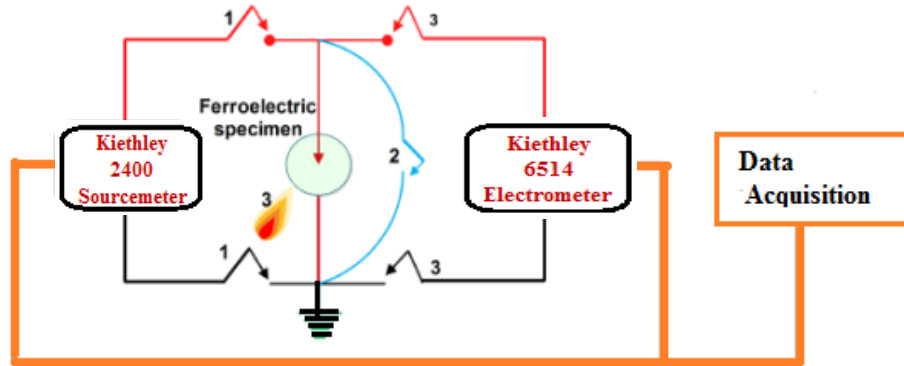


Fig. 2.9. Schematic layout of pyroelectric current measurements setup. Switches labeling represent electrical connection to be made for measurements. Switch 1 for poling process, 2 for electrical shortening and switch 3 for final step of measurements.

The electric current measured in an external magnetic field is called magneto-electric current. Before measuring pyroelectric current, both surface of the sample is painted with the conducting silver paste and two copper wires (of 42 gauzes) is attached to conducting surface of pellet. For poling process, the sample is cooled in presence of applied electric field (using two painted terminals). After completing poling process, two terminals are shorted for 15 minutes. Then, at the same temperature two terminals are connected to 6514 electrometer followed by wait for 15 minute. After this, the whole measurement is operated in remote mode, and the pyroelectric current is collected during the heating of pyroelectric specimen. The recorded current per unit area is integrated over time to convert pyroelectric current in polarization. Presently, only CTO sample has been considered for these particular measurements.

2.10. Magnetization Measurements

Magnetization measurements on the samples are performed using Vibrating Sample Magnetometer (VSM) and Superconducting Quantum Interference Device (SQUID) magnetometer (M/s. Quantum Design, model MPMS). The principle of magnetization measurements in these systems is based on the Faraday's law of electromagnetic induction, wherein, a voltage is induced in a conductor under a time-varying magnetic field. In VSM, on the other hand, the sample vibrates in a homogeneous magnetic field with small fixed amplitude and at a constant frequency (typically 20 - 40 Hz) against the stationary detection coils. This motion of the sample induces voltage (*emf*) in the detection coils, magnitude (voltage signal) of which depends on the magnetic moment of the sample, the amplitude and frequency of vibration of the sample as well as the distance of the sample from the detection coils. Further, the use of the lock-in technique provides accurate measurement of this voltage signal induced in the detection coils. A schematic consisting of main components in a typical VSM is shown in Fig. 2.10.

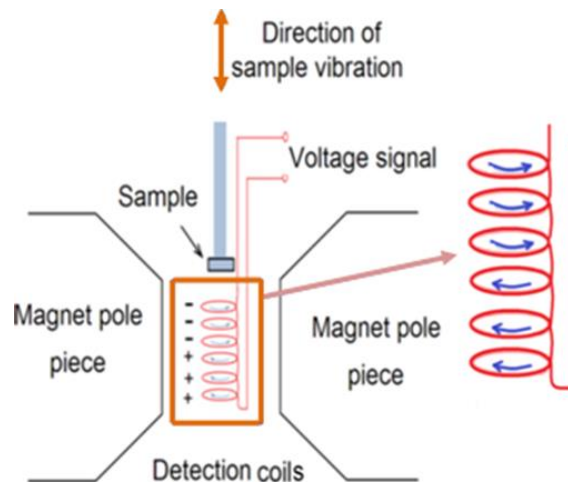


Fig. 2.10. Schematic of vibrating sample magnetometer (VSM). The detection coil assembly is wound in a second-order gradiometer configuration with oppositely wound detection coils.

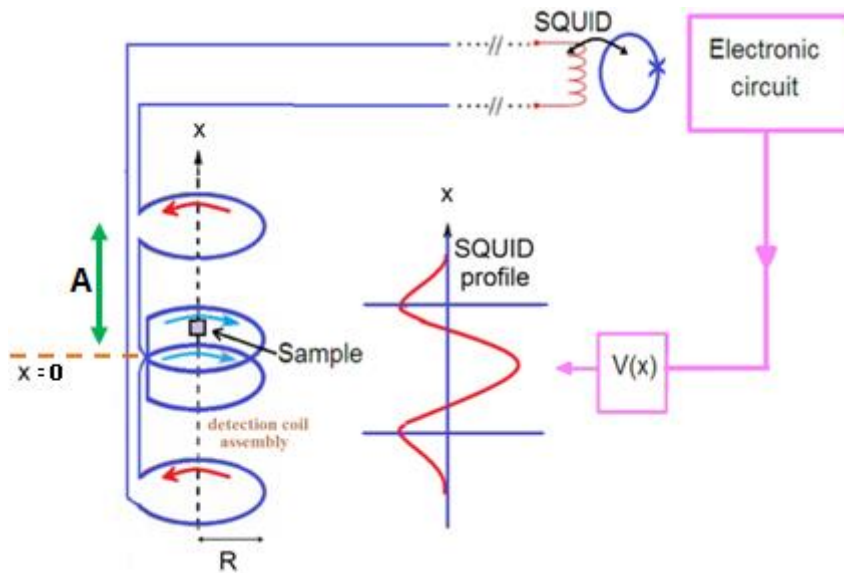


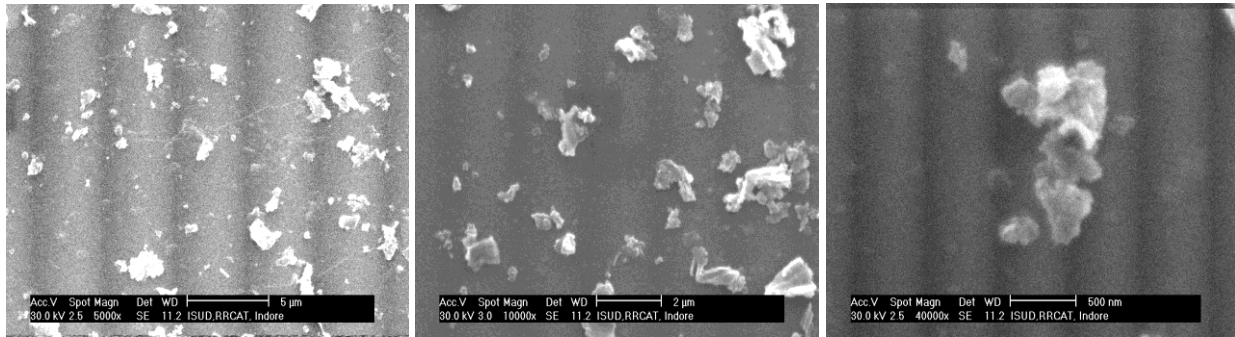
Fig. 2.11. Schematic of typical SQUID magnetometer used for magnetization measurements. Detection coils, SQUID-input coils and the connecting wires are the parts of a closed superconducting loop acting as a flux transformer, where the detection coils are connected to the SQUID-input coil, which is inductively coupled to the SQUID sensor.

The SQUID magnetometer is used for the magnetization measurement with higher sensitivity. It is basically a superconducting ring where two (in a dc-SQUID) Josephson junctions are inserted, where the principle is the magnetic flux linked with it is periodic (in the units of magnetic flux quantum, $\Phi_0 = h/2e$, where h is the Planck's constant and e is the electronic charge). For the magnetization measurement, the sample is moved in detection / superconducting coil, which is wound in a second-order gradiometer configuration (oppositely wound detection coils) in order to reject the contributions other than those coming from the sample as shown in Fig. 2.11. A superconducting magnet provides the magnetic field for the required measurements. The motion of the sample through the detection coil assembly changes the flux linked with the same detection coil assembly. Any change of flux linked with the detection coil assembly will result in a persistent current to flow through the closed superconducting loop to keep the total flux constant. The persistent current is proportional to the change in flux (linked with the detection

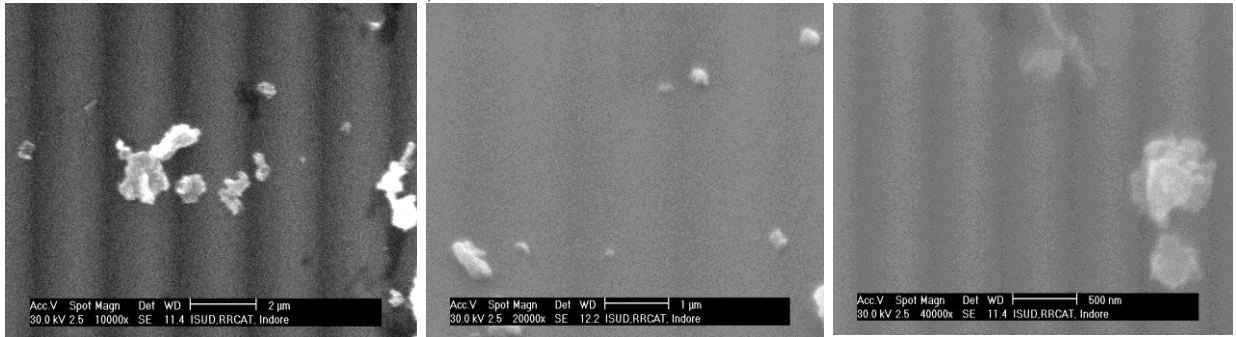
coil assembly) due to the motion of the sample. This persistent current produces a change in flux (which is also linked with the SQUID sensor). In the closed superconducting loop, the voltage signal across the SQUID sensor varies in accordance with the persistent current. One does not measure the current but rather the voltage across the SQUID output in a SQUID magnetometer.

2.11. Demonstration of structural and spectroscopic techniques to study oxides

a) as grown sample # H1



b) annealed at 300°C # H2



c) annealed at 800°C # H4

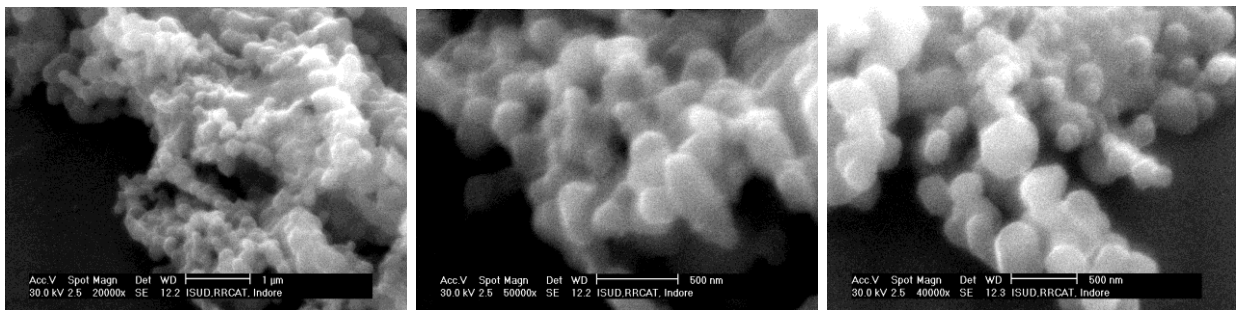


Fig. 2.12. SEM images of three samples, (a) H1, (b) H2 and (c) H4.

XANES, XPS and SXRD techniques are used to study as synthesized and isochronally annealed cobalt oxide nanoparticles grown using wet chemical route. In order to know the size of nanoparticles, all samples: as grown (H1), sample annealed at 300 °C (H2) and 800 °C (H4) are investigated using SEM. Fig. 2.12 (a), 2.12 (b), 2.12 (c) shows SEM images for as grown (H1), sample annealed at 300 °C (H2) and 800 °C (H4), respectively. The average size of the NP is ~ 180 nm (Fig. 2.12 (c)). SEM image clearly show how the annealing has led to the coalescence of nanoparticles (Fig. 2.12 (b)). In the case of as grown sample (2.12 (a)) and sample annealed at 300 °C (2.12 (b)), weak type II magnetic contrast is seen due to the some leakage field above the cobalt nanoparticles surface. This also verifies the Rietveld refinement results, which shows the presence of Co metallic nanoparticle phase in two samples H1 and H2 (to be discussed in subsection 2.11.3).

2.11.1. X-ray Absorption Near Edge Structure Spectroscopy analysis

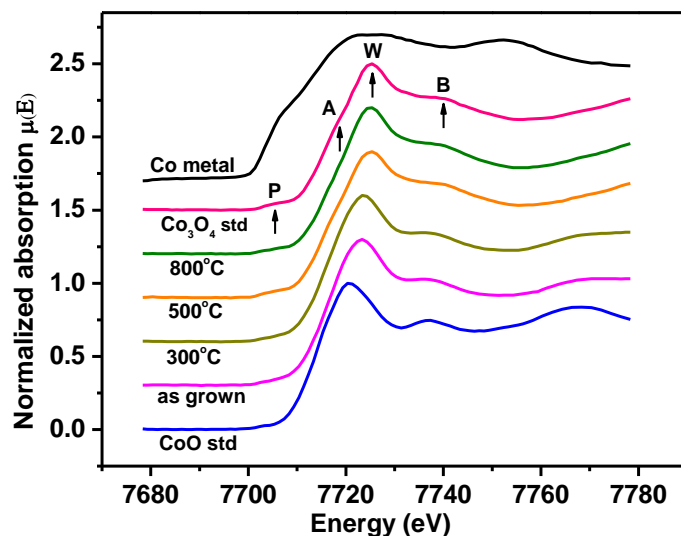


Fig. 2.13. Normalized Co K-edge XANES spectra of all the samples (H1 to H4) along with CoO (H0) and Co₃O₄ (H5) standards. Vertical shifting has been done for the sake of clarity. Features in the XANES spectra are marked with P (Pre-edge), A (Main edge), W (White line) and B. Energy calibration has been done using Co metal foil XANES

We have analyzed as grown and isochronally annealed cobalt oxide NP samples using XANES spectroscopy. Generally, XANES¹¹⁵ measurements (where absorption edge is being probed) are performed to study oxidation state, local surroundings and electronic states of specific metal site. However, in this work, XANES measurements (at Co K edge) on all the samples have been performed to investigate the composition of mixed phases of cobalt oxide. Fig. 2.13 shows the normalized Co K-edge XANES spectra of samples H1 to H4 along with the two standard samples CoO (H0) and Co₃O₄ (H5) with known oxidation states of Co. As shown in Fig. 2.13, XANES spectrum may be divided into four regions, namely, the pre edge (marked 'P'), the main edge (marked 'A'), white line (marked 'W') and the extended edge region (marked 'B'). All these regions correspond to different transition energies observed for that particular element in the compound. The pre edge corresponds to 1s→3d, a dipole forbidden (quadrupole) transition, is allowed because of favored co-ordination environment of the absorbing atom. The main edge is attributed to 1s→4s monopole transition, whereas the white line corresponds to dipole allowed 1s→4p transition.¹¹⁵ As discussed in earlier chapters, the notation of the main edge feature has some debates.¹²⁴⁻¹³⁰ Although, identification of the feature in the XANES spectra does not alter the overall conclusion of the analysis, demonstrated further in this section.¹⁰⁵ Main edge (rising edge) gives information about the oxidation state of the absorbing atom in the sample. This edge position shifts when the effective number of positive charges i.e. oxidation state changes resulting from 1s core hole shielding effects. In a sample with mixed oxidation state, the main edge is located in between the edge positions of the two. Using Linear Combination Fitting (LCF), which is based on the proposed empirical linear combination formula, one can quantitatively estimate the concentrations of the two phases in the sample.

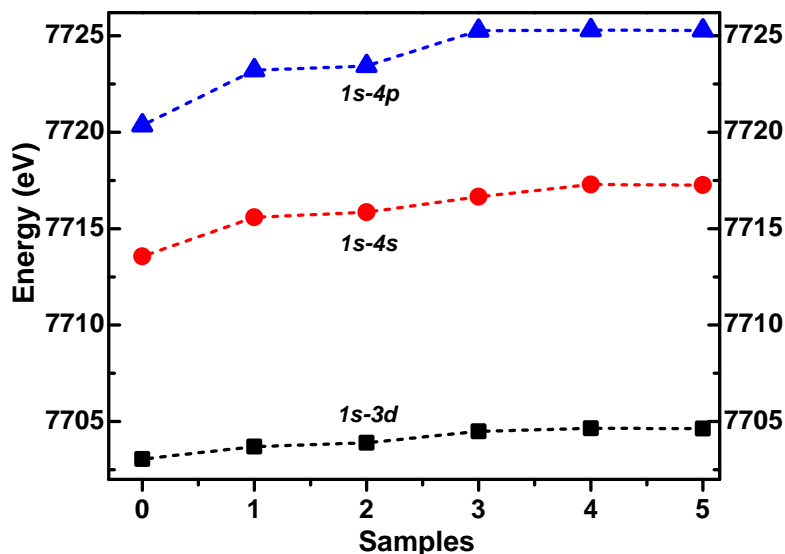


Fig. 2.14. Demonstration that the identification of features in XANES spectra does not alter the conclusion of the analysis, wherein variations of transition energies as a function of cobalt oxides NP samples have been shown. Numbers in the X axis represent H0 to H5.

For the same, a detailed qualitative as well as quantitative (using software Athena)¹⁰⁵ XANES analysis has been done. For the analysis, we have used XANES spectra of two standard samples CoO and Co₃O₄ along with Co metal foil to calibrate the photon energy (Fig. 2.13). Quantitative phase composition analysis has been done using LCF method. The position of main edge in XANES spectra for all the samples has been determined by the energy corresponding to ~ 0.5 absorption in the normalized XANES spectra. From Fig. 2.13, XANES spectrum of sample H0 (CoO) shows a minor pre edge peak, which signifies octahedral configuration of O around Co in agreement with literature. On the other hand, significant pre edge peak is observed for standard sample H5 (Co₃O₄) and is attributed to tetrahedral configuration of O around Co. This makes dipole forbidden 1s→3d (quadrupole) transition possible with the mixing of O 2p and Co 3d orbitals. In our samples, a visible pre edge feature for sample H1 is observed (Fig. 2.13). The intensity of the pre edge becomes more prominent with the increase in the annealing temperature indicating larger tetrahedral component. In addition, for the samples H1 to H4, the energy

positions of the main edge peak (marked A, Fig. 2.13) shifts towards higher energies with the increase in the annealing temperature. Both these observations indicate increase in average oxidation state with the increase in annealing temperature. Increase in the average oxidation state clearly indicates the increase in Co_3O_4 phase.

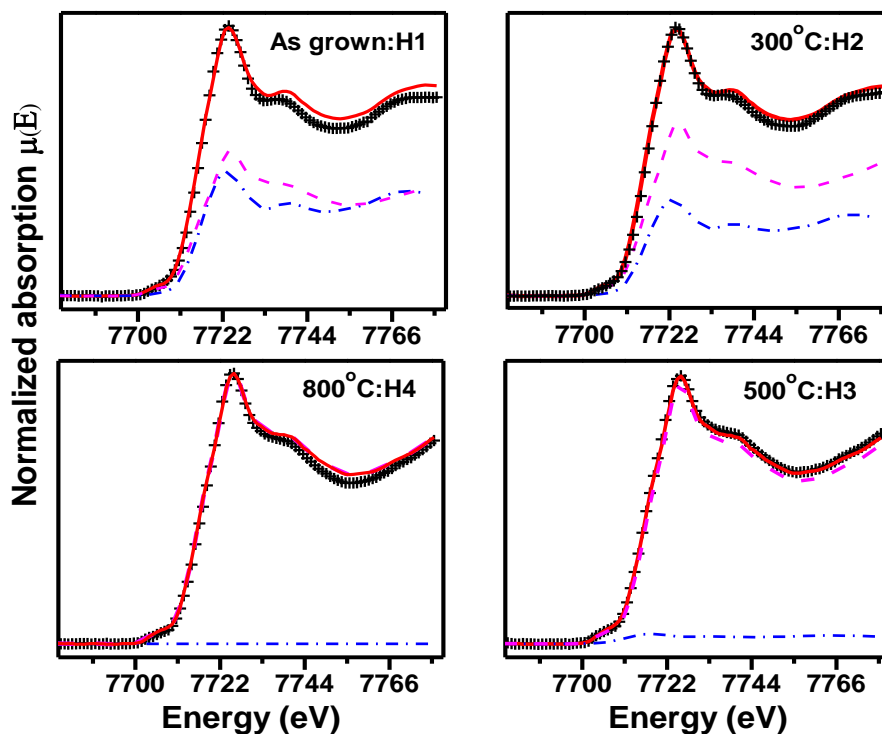


Fig. 2.15. Linear Combination Fitting (LCF) for all the samples H1 to H4 using cobalt K-edge XANES spectra. Raw data points are shown by black (+) and solid lines (red) denote LCF fit to the data. Fractions of standards CoO (shown by blue dash dot) and Co_3O_4 (shown by magenta dash) are used for LCF.

We have summarized and plotted the energy positions of $1s \rightarrow 3d$, $1s \rightarrow 4s$ and $1s \rightarrow 4p$ transitions for all the samples H0 to H5 in Fig. 2.14. For the two standard oxides, the main edge transition energy for Co_3O_4 is blue shifted ~ 3.7 eV as compared to CoO. The main edge energies of the NP samples H1 to H3 are found to be intermediate between the two standard oxide samples, whereas that of sample H4 is the same as that of Co_3O_4 . This indicates mixed phase behavior of samples H1 to H3. Further, white line positions for the standard samples indicate that Co_3O_4 peak is also

blue shifted (~ 4.9 eV) with respect to the CoO. Feature marked as B (extended edge region) occurs due to the surrounding environment of the absorbing atom. This feature is similar for the samples H3, H4 and H5 suggesting almost similar kind of surrounding environments for sample H3 and H4 as compared to standard H5. Whereas, the same feature for sample H0 is quite sharp. This indicates different kind of environment for Co in the sample H0 as compared to samples H3, H4. This feature for samples H1 and H2 is intermediate. Based on above analysis, we find that as grown sample together with sample annealed at 300°C are in the mixed phases of CoO and Co_3O_4 . The demonstration that the identification of features in XANES spectra does not alter the conclusion of the analysis can be seen in Fig. 2.14, wherein variations of transition ($1s \rightarrow 3d$, $1s \rightarrow 4s$ and $1s \rightarrow 4p$) energies as a function of cobalt oxides NP samples indicate almost similar behaviour. All these observations indicate that annealing at higher temperatures lead to the transformation of CoO to Co_3O_4 phase.¹⁰⁵

To confirm the above qualitative results, quantitative phase composition analysis using LCF method on XANES data has been done. LCF works on least square fit algorithm and use the XANES spectra of selected standards to determine the composition of an unknown sample. The basic principle of this method is based on the additive nature of absorption from each chemical state or species in the samples. LCF method fits the unknown sample as a linear combination of standards according to their valance states. Here, the pure phase of CoO (H0) and Co_3O_4 (H5) are used as standards. The normalized μ (E) data obtained for all the samples have been fitted by the linear combination of the normalized μ (E) data of standard samples. The experimental data and the best fit obtained are presented in Fig. 2.15. The goodness-of-fit is judged by Residual and Chi-square value. Percentages of phases in as grown and annealed samples are obtained

from the fit and are tabulated in Table 2.5, along with the composition obtained using two phase Rietveld refinement on SXRD data (to be discussed later in section 2.11.3).

2.11.2. X-ray photoelectron Spectroscopy analysis

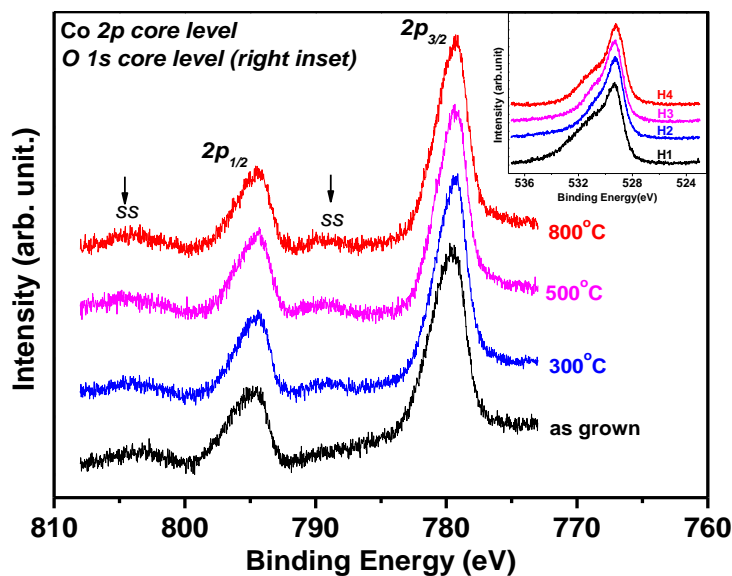


Fig. 2.16. Normalized core level XPS spectra of Co $2p$ and O $1s$ (right inset) for all the samples (H1 to H4).

XANES measurements (performed in transmission mode) described above are bulk sensitive measurements. In the case of TMO NPs, it is not uncommon to get a core shell structure; in which core and shell have different phases. Therefore, it is important to discuss surface characterization of as grown (H1) and annealed samples (H2 to H4) using a surface sensitive technique like XPS. Main peak for CoO and Co₃O₄ phases lie within very narrow range (within the instrumental resolution limit). Hence, the two phases couldn't be distinguished based on their main peak positions. However, one can distinguish different phases (CoO and Co₃O₄) in the case of Co-NP by noting the difference in the positions of the satellite peak with respect to the main peak. Satellite peak position for CoO is nearly 5-7 eV higher than its main peak, whereas, that for Co₃O₄ it is nearly 8-10 eV higher. There are few reports, which differentiate these two phases by using the intensity of satellite peak.¹⁰⁵ XPS spectra of as grown (H1) and annealed samples

(H2 to H4) are shown for Co 2*p* edge (Fig. 2.16) and O 1*s* edge (inset in the Fig. 2.16), respectively. Peak analyses are carried out using carbon peak at 284.6 eV as reference. Co 2*p* spectra for as grown sample (H1) show Co 2*p*^{1/2} and Co 2*p*^{3/2} main peaks at 795.2 eV and 779.9 eV, respectively with broad satellite peaks. Occurrence of broad satellite peak may be because of superposition of 2 or 3 peaks, to be discussed further. Binding energies (BE) of both the main peaks are red shifted by ~ 0.4 eV with increase in the annealing temperatures (samples H2 to H4). Further, separation between the satellite and the main peak positions increases with the increase in annealing temperature. No shake-up satellite peaks (in between the two main peaks) for as grown samples (H1) is observed indicating Co³⁺ in octahedral cage on the surface of NPs. Whereas, annealed samples show clear but subdued satellite peaks. The satellite peak for Co 2*p*^{1/2} and Co 2*p*^{3/2} peaks are shifted by (9.3 ± 0.1) eV and (10.2 ± 0.1) eV, respectively from their main peaks for sample H4. Further, the values of the peak shift increases slightly with the increase in annealing temperature. This clearly indicates that the concentration of Co₃O₄ phase increases with increase in annealing temperature. These results are in agreement with XANES results. The separation between the main and the satellite peaks (about 10 eV) are slightly higher than the values (8.5 eV (*p*^{1/2}) compared to 8.8 eV (*p*^{3/2})) reported for bulk/thin film/epitaxial Co₃O₄. Satellite peaks are attributed to crystal field splitting for Co²⁺ 3*d*⁷ energy states in tetrahedral crystal field environment. We believe that this is a significant result because it shows larger crystal field splitting for NPs compared to that in the bulk. The separation between Co 2*p*^{1/2} and Co 2*p*^{3/2} main peaks lie within 15.3 ± 0.1 eV (not shown) for all the samples H1 to H4. This suggests that the spin-orbit multiplet separation is not sensitive to ionic valence state of cobalt in the cobalt oxides.

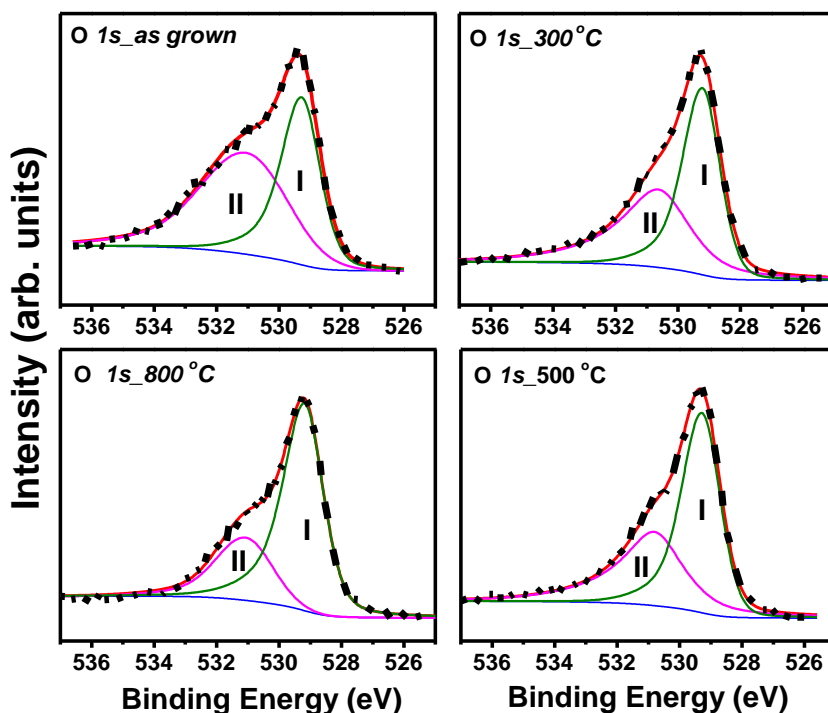


Fig. 2.17. Oxygen *1s* XPS spectra of cobalt oxide nanoparticle samples H1 to H4 fitted with Shirley background and two Lorentzian-Gaussian peaks (I, II).

Oxygen (O) *1s* peaks for samples H2 to H4 are almost same at 529.3 ± 0.1 eV (Fig. 2.17). Based on O *1s* binding energy, we rule out any appreciable charging effect in our data and no manipulation in the energy axis has been done to nullify charging effect. Following the earlier observations,¹²⁹⁻¹³¹ the photoelectron spectral features of O*1s* peak at $\sim 529.3 \pm 0.1$ eV for the sample H4, may indicates the presence of Co_3O_4 phase, in agreement with the XANES result. Analyses of O *1s* core level XPS peak for all samples are carried out after removing the Shirley background using XPSPEAK 4.1. Further, minimum numbers of Gaussian-Lorentzian peaks are used to account the XPS spectra. Oxide peak corresponds to 529.3 ± 0.1 eV position for all the samples (H1 to H4). The second peak observed at ~ 531.6 eV is attributed to the adsorbed hydroxyl group.¹²⁹⁻¹³¹ This peak shifts to slightly higher value in position and lower value in FWHM on annealing (H2 to H4). The position (FWHM) values are: 530.6 eV (2.4) for H2, 530.8 eV (2.2) for H3 and 531.1 eV (2.0) for H4 and 531.1 eV (3.1) for as grown (H1) sample. Fits for

samples H1 to H4 are shown in Fig. 2.17. The intensity ratios (area under the peak) of the peak I and peak II are 0.81 (H1), 1.13 (H2), 1.39 (H3) and 2.65 (H4). Based on our analysis¹⁰⁵, we have inferred that concentration of Co_3O_4 increases and adsorbed hydroxyl group decreases with the increase in annealing temperature, in agreement with XANES result.

2.11.3. Synchrotron X-ray diffraction analysis

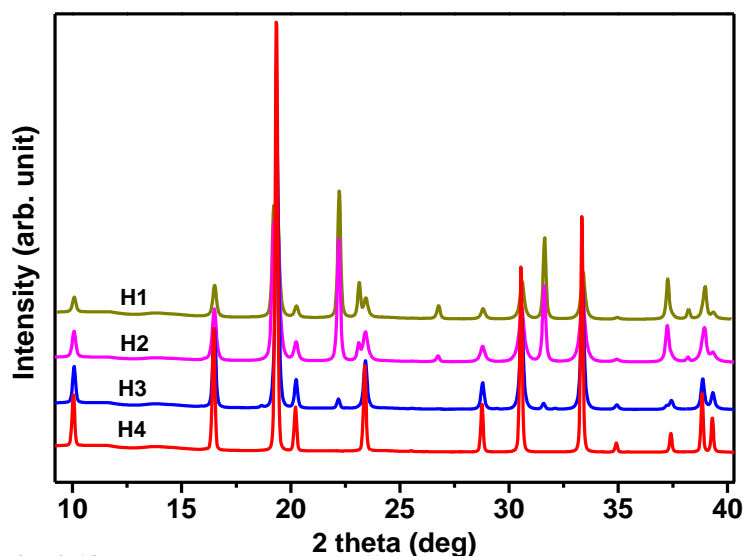


Fig. 2.18. Synchrotron X-Ray diffraction patterns recorded at room temperature from cobalt oxide nanoparticle samples (H1 to H4).

In subsection 2.11.1, we have applied XANES technique to estimate the phase concentration of a mixed phase of CoO and Co_3O_4 ; for the first time. A straightforward way of estimating the phase composition is Rietveld refinement on SXR data. We describe the SXR data analysis in the following, in an attempt to estimate the phase concentration of CoO and Co_3O_4 phases and its comparison with those obtained from XANES data. Fig. 2.18 shows the observed experimental data for H1 to H4. Initially, two phase (CoO and Co_3O_4) Rietveld refinement for all the samples (H1 to H4) have been done. Composition, unit cell parameters, Wyckoff positions and peak profile parameters etc. have been used as the refinable parameters. The crystal symmetries are

Fd3m (Co_3O_4) and Fm3m (CoO). In case of samples H1 and H2, we are not able to fit the data reasonably using two phase refinement. Some extra peaks have been observed in the SXRD patterns. These extra peaks correspond to Co metallic phase in the sample confirmed by JCPDS database (PDF # 150806).

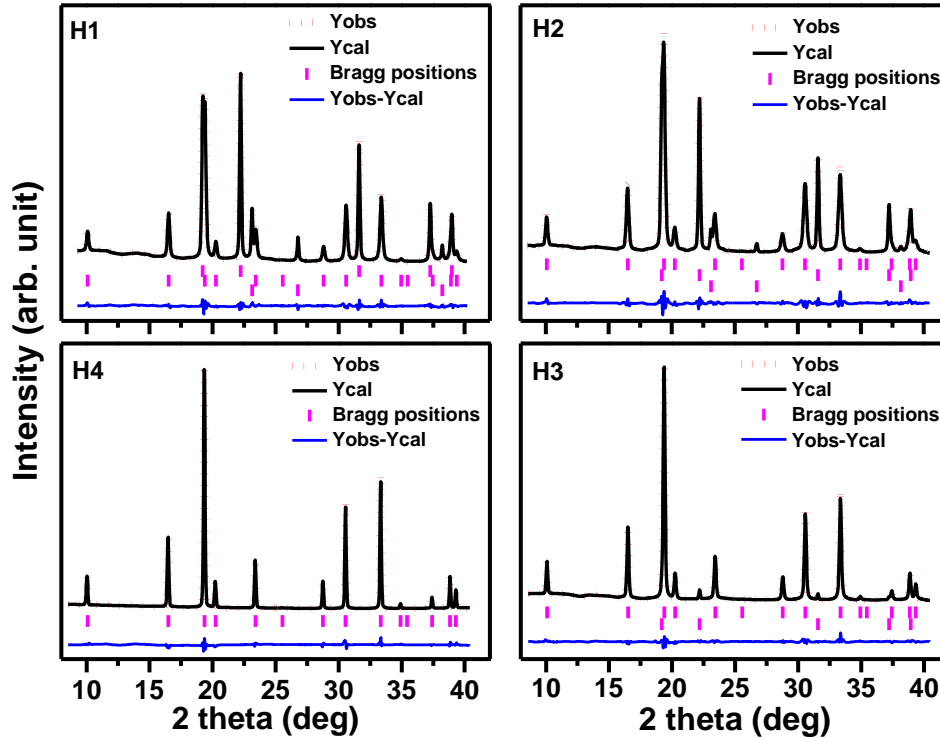


Fig. 2.19. Reitveld refined Synchrotron X-Ray diffraction patterns for all the samples. Red dots represent the raw data, and solid black lines are the fit obtained by the Rietveld refinement. The blue and magenta line beneath the pattern records the Bragg positions and difference between the observed and calculated patterns, respectively.

Variations particularly in sample H1 and H2 can be understood by three phase Rietveld refinement. Co with space group Fm3m is used as the third phase. Analysis shows that Co metallic phase is present with concentration of ~ 6 % and ~ 2 % in the sample H1 and H2, respectively. This is in agreement with the presence of weak type II magnetic contrast as observed in SEM for these two samples. This also leads to some discrepancy between SXRD and

XANES results for these two samples. Two phase Rietveld refined data for H3 and H4 and three phase Rietveld refined data H1 and H2 are shown in Fig. 2.19.

Table 2.5. Phase compositions obtained from Rietveld refinement on SXR D data and LCF on XANES data of cobalt oxide nanoparticles samples H1 to H4 are tabulated, along with refined cell parameters.

Sample No.	Annealing Temp (°C)	Phases present	Composition obtained		Cell parameter (Å)
			XRD	XANES	
H1	As grown	CoO	43.59	46.3	4.2502(3)
		Co ₃ O ₄	49.56	53.7	8.0635(2)
H2	300 °C	CoO	33.16	35.9	4.2528(1)
		Co ₃ O ₄	65.16	64.1	8.0686(2)
H3	500 °C	CoO	3.20	3.7	4.2561(4)
		Co ₃ O ₄	96.80	96.3	8.0697(3)
H4	800 °C	CoO	0.0	0.0	N. A.
		Co ₃ O ₄	100	100	8.0761(3)

Phase compositions for all the samples obtained from Rietveld analysis suggest that as grown sample (H1) and sample annealed at 300 °C (H2) are in mixed phase of Co, CoO, and Co₃O₄. For samples H3 and H4, we have found that CoO phase oxidized to Co₃O₄ in agreement with XANES results. Rietveld refinement results for all the samples are summarized in Table 2.5 along with the phase concentration obtained from XANES analysis. We find reasonably good agreement (within 4 %) between the compositions obtained from SXR D and XANES analysis.

It is important to note that a sharp jump of Co₃O₄ concentration is observed for sample annealed at 500 °C compared to 300 °C (Table 2.5). This may be because oxidation of Co metallic phase to CoO or Co₃O₄ is a two step process. First step corresponds to transition from Co to CoO and in the second step CoO transforms to Co₃O₄. Atomic structural changes and diffusion processes during the chemical transformation of Co to CoO and then to Co₃O₄ has also been reported. CoO

stabilizes via O in-diffusion by an indirect exchange mechanism through interstitial O and vacancies of certain type of Co sites from Co metallic NP phase. For Co_3O_4 , outward diffusion of Co is faster than the inward diffusion of O. It is also reported that even different phases of CoO (rocksalt or wurtzite) transform to spinel phase of Co_3O_4 in air during the oxidation with retention of the original crystal morphology. High temperature annealing improves the crystalline quality of NPs due to the rearrangement of cobalt cations and oxygen anions of CoO to the spinel Co_3O_4 phase. The phase compositions obtained through XANES data are compared with those obtained from Rietveld analysis on SXRD data. These values are found to be in good agreement.

Herein, quantitative phase compositions using Rietveld refinement (SXRD) and LCF (XANES) have been obtained. Both the methods are based on least square fit algorithm and require prior knowledge of the phases that exist in the sample. In the case of Rietveld refinement, one needs complete crystallographic information i.e. Wyckoff positions (fractional coordinates) of atom in the unit cell and unit cell parameters etc. for the corresponding phases. However, in case of LCF, only standard XANES spectra of all the phases are required. These standard spectra are used as combination for an unknown sample to obtain the composition depending on their chemical state. Therefore, XANES can also be a useful technique for quantitative phase composition analysis in the case of samples having complex structure, for which crystallographic information are not readily available.

To summarize, we have studied cobalt oxide NPs using synchrotron source. Qualitative analysis of XANES spectra of as grown and isochronally annealed samples of cobalt oxide NPs show that as grown together with sample annealed at $300\text{ }^\circ\text{C}$ are in mixed phase of CoO and Co_3O_4 . The phase concentration of Co_3O_4 increases with increase in annealing temperature at ambient.

Quantitative XANES analysis shows Co_3O_4 phase concentration increases from ~ 49 % in sample H1 to 100 % for sample H4. These results have been corroborated with Rietveld analysis on SXRD data. The composition obtained from the two methods is in reasonably good agreement. This suggests that XANES can be effectively used to study composition of mixed phase samples. XPS results indicate the increase in Co_3O_4 phase concentration on the surface, in agreement with the phase concentration for the bulk. This analysis established our procedure for the determination of average charge state of a sample, using XANES main edge analysis. We have used this procedure in chapters 3 and 4 for the determination of average charge state of Co and Mn in various samples.

Chapter 3

Cobalt Tellurate
(Co_3TeO_6 ; CTO)

As discussed in chapter 1 about the multiferroicity, their types and the possible mechanism for the development of the same, in detail. Besides understanding the mechanism of coupling of various ferroic orders and enhancing the strength of coupling among these ferroic orders, designing and finding new MF materials are some of the main concerns of MF researchers. CTO seems to have interesting characteristics, because of multiple magnetic transitions and type II multiferroicity.⁷⁵⁻⁸² The first Neutron diffraction study⁷⁶ on CTO indicates first-order multi- k phase transitions,⁸² with a sequence of three AFM phases (below 30 K) accompanied by ME effect.^{76,82} The in-commensurate (IC) AFM structure emerges at $T_{N1} = 26$ K (denoted as phase I), whereas the two commensurate AFM phases appear at 21 K (phase II) and $T_{N2} = 17.4$ K (phase III).^{76,82} In literature, there is disagreement in number of magnetic transitions in CTO. For example, Hudl et al.,⁷⁷ and Her et al.,⁷⁸ report two magnetic transitions (~ 18 K and 26 K) in addition to transitions at 34 K and 16 K, which the authors have not discussed. Wang et al.,⁸⁰ on the other hand, not only report IC nature of all these magnetic transitions but also discuss a total of four transitions at 26 K, 20 K, 18 K, and 16 K below 30 K. They also point out the probable origin of two magnetic transitions (26 K and 18 K) by studying chains in two Co-Co networks.⁸⁰ Theoretical Landau free energy analysis taking care of irreducible representations and monoclinic magnetic group symmetry suggests a strong magneto-elastic effect.⁸² The evolution of phase II from phase I take place through strong first order transition.⁸² This would also suggest a possible change in interatomic spacing causing first order transition, which may in turn influence exchange energy from phase I to phase II.⁸² A phenomenological explanation to the ME behaviour of CTO is also developed by Harris et al.⁸¹ In contrast, there is a smooth second order transition from phase II to phase III indicating no significant discontinuity in structural parameters.^{76,80,82} As theoretically explained,⁸² monoclinic symmetry of phase III ($2'$) permits

spontaneous weak magnetization as well as spontaneous polarization, where the later is due to a single spontaneous zero magnetic field polarization component P_y .⁸² Although, there exist plenty of works on CTO but there are certain issues, which are still under debate. In the following, detailed earlier observations along with issues and attempts have been described.

To get a clue on large variations in reported multiple magnetic transitions (seen in low magnetic fields), as discussed above, we synthesize ceramic CTO by two step calcination route (section 3.1). This also provides the explanation for the origin of its lowest symmetry structure in A_3TeO_6 family. We believe that synthesis process plays an important role in deciding the magnetic behavior in CTO.. To the best of our knowledge, none of the reports discuss growth reaction mechanism of CTO. Implication of this route of synthesis is discussed in section 3.2 and section 3.3 of this chapter.

From structural point view, synthesized single crystal CTO crystallizes in monoclinic ($C2/c$) crystal symmetry, in which only Co^{2+} ions occupy five different crystallographic positions as tetra, square-pyramidal and three octahedral sites.^{74,77-80} Co atoms possess very large variations in the typical Co-O bond distances; the smallest bond distances are almost half of the largest one. These informations, however, carries some basic concerns, which need to be addressed.⁸⁵⁻⁸⁷ For example, such a variety of polyhedral configurations and large variations in Co-O bond lengths of an ion with only 2+ valence, is difficult to comprehend. One possible way to arrange such a polyhedral mixing with a range of bond lengths is through mixed valence ions. However, to the best of our knowledge, no reports exist signifying the presence of Co^{3+} in (either single crystal or ceramic) CTO. In section 3.2 of this chapter, we have estimated average valence state of Co CTO, using XANES measurements. We have also commented on the spin state of Co ions in our ceramic CTO.⁹⁴

Further, as mentioned above: a) Understanding low magnetic field magnetic behaviour, remains a challenging issue.⁷⁷⁻⁸⁰ To the best of our knowledge, there is no experimental report which shows all the five magnetic transitions (~ 34 K, 26 K, 21 K, 17.4 K and 16 K) in a particular ceramic or single crystal CTO,⁷⁷⁻⁸⁰ b) In CTO, spontaneous weak magnetization as well as spontaneous polarization have been theoretically predicted.⁸², The former (weak magnetization) has been experimentally shown with domain structure observed in Second Harmonic Generation measurements.⁸² The experimental observation of the spontaneous zero field polarization has not been reported.^{77-80,82} c) Moreover, the magneto-dielectric effect,³⁸⁻³⁹ an important observation in the field of type II multiferroics, which deals generally with the response of dielectric constant under magnetic field indicating possible spin-phonon coupling,⁹⁹ which has not been observed in any of the earlier reports.

Attempts to solve these issues (discussed above in a), b) and c)), have been carried out in section 3.3 of this chapter.⁹⁵⁻⁹⁶. Our combined dielectric, pyroelectric and polarization measurements suggest that the ground state of CTO may possess spontaneous symmetry breaking even in the absence of magnetic field.⁹⁵

3.1. Two step solid state synthesis of ceramic CTO

This section describes the synthesis and structural investigations of CTO in order to probe the crystallographic aspects. A two-step solid state reaction route has been proposed to synthesize monophasic CTO. HR-SXRD has been used to optimize the synthesis parameters and ascertain purity in synthesized CTO. XPS study near Co K and Te L-edge show the possibility of mixed oxidation states of Co (i.e. Co^{2+} and Co^{3+}) and +6 valence state of Te, respectively.

3.1.1. Introduction

Mainly two routes of synthesis of CTO have been reported in literature: hydrothermal and solid state reaction.^{75,77-80,83-86} Different starting reagents like CoO, $Co(NO_3)_2 \cdot H_2O$, TeO_2 , $Te(OH)_6$, $H_2TeO_4 \cdot 2H_2O$ and TeO_3 have been used to synthesize CTO. Thermal decomposition of cobalt (II) tellurate-molybdates ($CoTeMoO_6$ and $Co_4TeMo_3O_{16}$) and amorphous cobalt tellurate ($CoH_4TeO_6 \cdot Co(OH)_2$) around 900 K for 24 hrs in air, have also been reported for CTO synthesis.⁸⁴ Different second phases like Co_5TeO_8 and $CoTeO_3$ are generally present in the calcined powder and in ceramic, which have been related to the loss of TeO_2 oxide during calcination/sintering at high temperature.^{83,85} Thermographic study of the CoO- TeO_2 system, heated in air, has revealed no oxidation to tellurate, unlike that observed in NiO- TeO_2 system.⁸⁴ Synthesis of CTO single crystal has also been reported by Becker et al.⁸⁶ using 3:2:1 ratio of $Co_3O_4 : TeO_2 : CoCl_2$ (or $PtCl_2$) through transport reaction method.

It is known that CTO decomposes spontaneously above 1100 K to CoO and TeO_2 , however, direct synthesis of the single phase CTO from CoO and TeO_2 below 1100 K seems difficult⁸³. Till now, no reaction mechanism has been proposed for the formation of CTO. Here we present, synthesis of single phase CTO using two step calcination and solid state reactions between

Co₃O₄ and TeO₂ in air at T < 1100 K. The sample, prepared using two step synthesis route, has been found to show better multi-ferroic properties.⁸⁶⁻⁸⁸

3.1.2. Results and Discussion

3.1.2.1. Growth and its structural correlation

Co₃TeO₆ is synthesized using conventional solid state reaction route using Co₃O₄ and TeO₂ reactants, as described briefly in chapter 2. Fig. 3.1 shows SXRD pattern of Co₃O₄, TeO₂ and their mixture at room temperature, in order to verify the purity of ingredients.

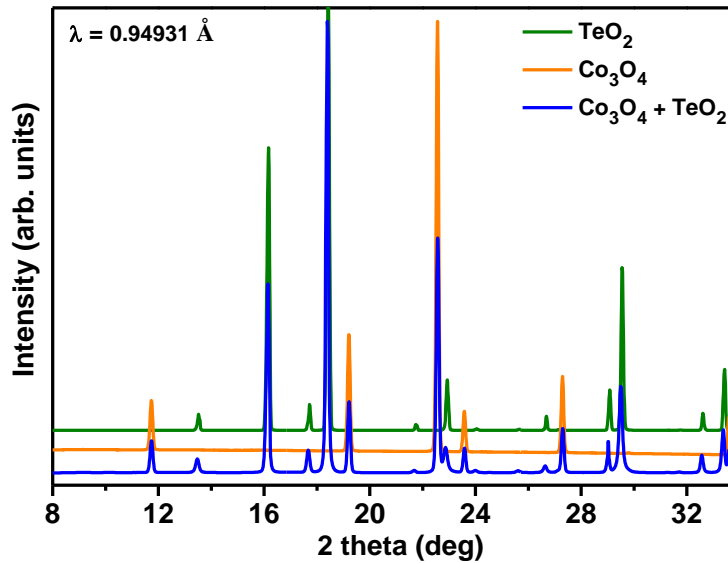


Fig. 3.1. SXRD patterns of TeO₂, Co₃O₄ and their mixture at room temperature.

Fig. 3.2 shows thermogravimetric curves (Differential thermal analysis (DTA) and Thermogravimetric analysis (TGA)). The thermogravimetric curves are divided into four regions marked as I, II, III and IV, as shown in Fig. 3.2. The region I, between 300 °C to 600 °C with a maximum (in DTA) around 480 °C (broad peak), corresponds to the oxidation of Te⁴⁺ to Te⁶⁺.



This oxidation reaction suggests weight gain during the calcination process, because of the incorporation of “O₂” in the chemical reaction (see Eq. 3.1). This oxidation and the corresponding weight gain depicted by broad hump in DTA and a jump in the first derivative of TGA are shown in the main panel and the inset of Fig. 3.2, respectively. The region II around 730 °C and the region III around 800 °C are due to intermediate phase formation and its transformation into the CTO phase, respectively. The temperature of region II also matches with melting point of TeO₂. In the last region IV above 900 °C, decomposition of the CTO phase into CoO and TeO₂ phase has been reported.⁸³

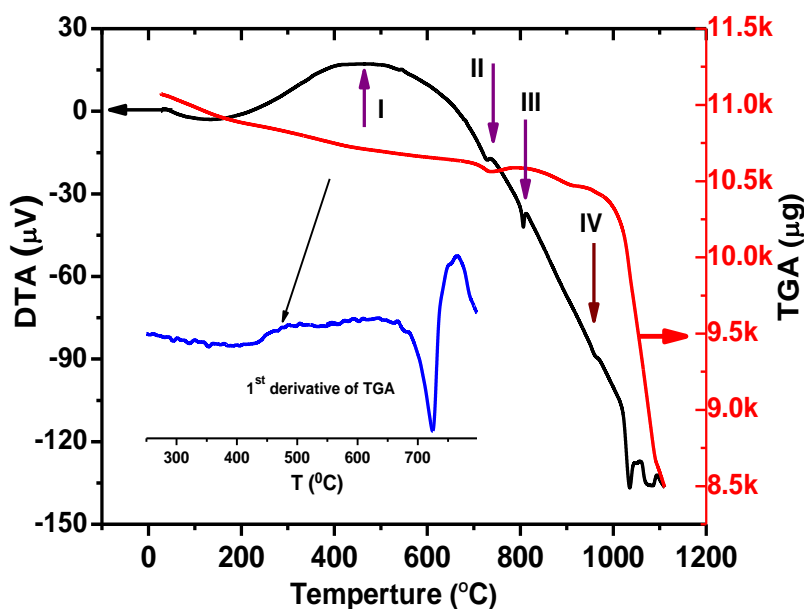


Fig. 3.2. DTA/TGA curves for Co₃O₄ + TeO₂ mixture. Thermal analysis indicates four step reaction assigned as I, II, III and IV. Inset shows 1st derivative of TGA curve showing anomaly at ~500 °C (region I).

Taking a clue from the thermal analysis of the reactants, we have chosen the temperatures for different steps of calcination. The reactant powders (Co₃O₄ and TeO₂) in stoichiometric amount are mixed thoroughly using ball mill and calcined at different temperatures ranging from 500 °C to 800 °C for a fixed time (12 hrs). Different calcined powders are labeled as CTO500, CTO600,

CTO650, CTO700 and CTO800. Fig. 3.3 compares SXRD patterns of the CTO500 and CTO600. Initiation of a new phase formation (marked by “●” in Fig. 3.3) has been noticed for CTO500 sample, which becomes major phase, when the mixed powder is calcined at 600°C (CTO600). All other extra peaks have been assigned to un-reacted starting reagents Co_3O_4 and TeO_2 . Rietveld refinement of CTO600 powder reveals the formation of an intermediate phase (CoTeO_4), which is of monoclinic ($P2_1/c$: $a \sim 6.192(3) \text{ \AA}$, $b \sim 4.671(3) \text{ \AA}$, $c \sim 5.567(2) \text{ \AA}$, $\beta \sim 124.07(2)^\circ$) symmetry.¹³¹ CoTeO_4 has also been reported previously with cubic space group [PDF#32-0318]. However, we get monoclinic CoTeO_4 phase with $P2_1/c$ symmetry, which is closer to the final compound CTO ($C2/c$).

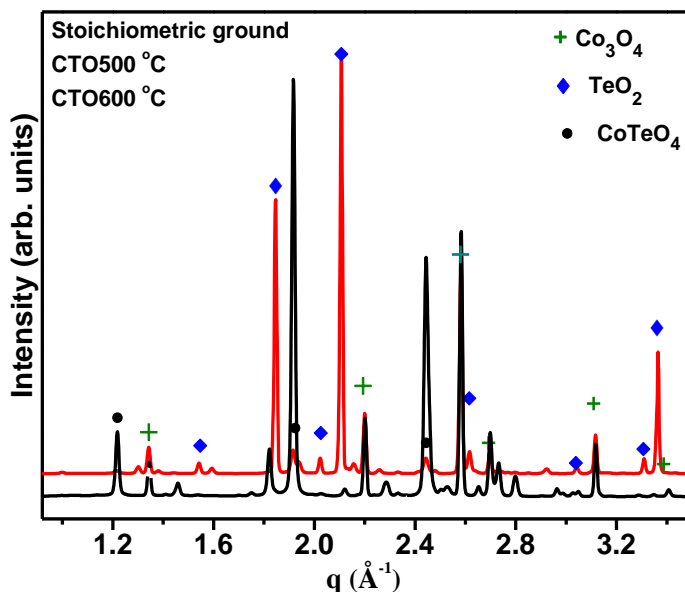


Fig. 3.3. The stoichiometric ground mixture at 500 °C indicates initialization of a new phase (CoTeO_4) along with unreacted initial reactants. Calcination at 600 °C, on the other hand, corresponds to CoTeO_4 as major phase.

Along with the intermediate phase (CoTeO_4), commencement of the CTO phase has also been noticed in CTO600 sample. Concentration of the CTO phase has been found to increase with further increase in the calcination temperatures. Fig. 3.4 compares the SXRD patterns of

CTO650, CTO700 and CTO800 samples. Phase analysis reveals that concentration of the CTO phase increases along with decrease in the CoTeO_4 phase with increasing calcination temperature. No peak corresponding to the CoTeO_4 phase has been noticed in CTO800 sample. Although, few extra peaks corresponding to Co_3O_4 have also been found in the SXRD pattern of CTO800 sample, which may be due to the loss of TeO_2 .

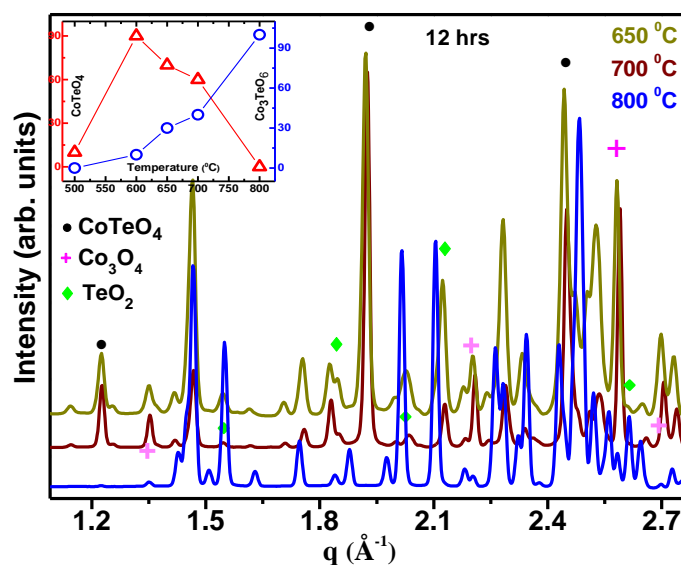


Fig. 3.4. Stabilization of CoTeO_4 along with various other phases, as we increase the calcinations temperature from 600 °C to 800 °C, all these phases are get converted to the final compound Co_3TeO_6 .

Based on the thermal and phase analysis, following reaction mechanism is suggested for the synthesis of CTO using Co_3O_4 and TeO_2 in the temperature regime 500 °C to 900 °C. We observed that it is not a single step process and complete via an intermediate CoTeO_4 phase, as can be seen in equation 3.1. This reaction mechanism is consistent with the oxidation and the corresponding weight gain observed in the thermal analysis plot, shown in Fig. 3.2. Here, the reactant TeO_2 and the intermediate product CoTeO_4 exhibit +4 and +6 oxidation states of Te, respectively.¹³¹ As can be seen in Fig. 3.3, the major unreacted phases i.e. Co_3O_4 may further react with CoTeO_4 to form Co_3TeO_6 in the following reactions:

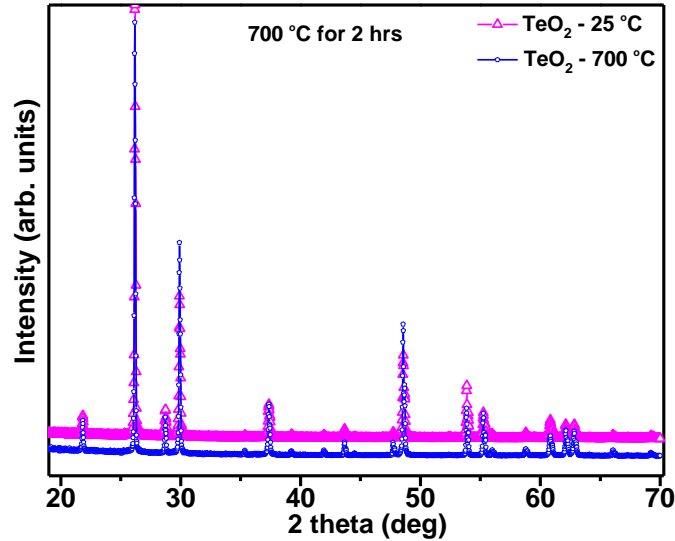
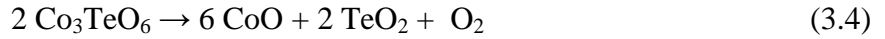


Fig. 3.5. No change in TeO₂ phase at 700 °C for 2 hrs calcinations, which excludes the possibilities of TeO₃, Te₂O₅ or Te₄O₉ leading to the stability against its oxidation or reduction.

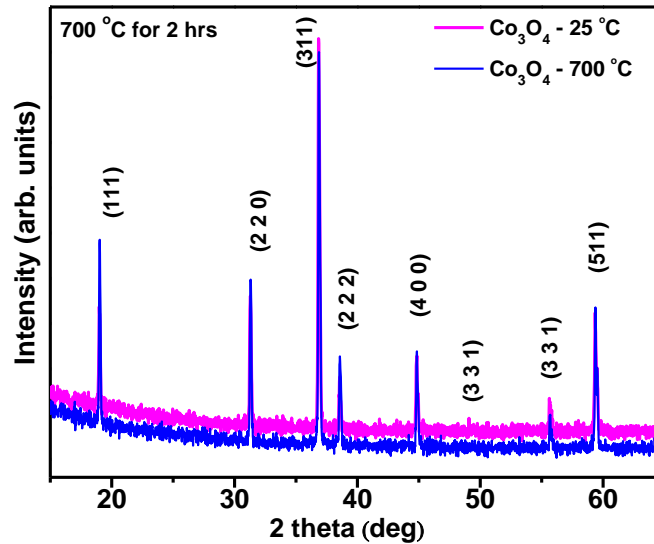


Fig. 3.6. SXRD data showing no change in Co₃O₄ phase at 700 °C for 2 hrs calcinations. This excludes the possibilities of their oxidizing agents like CoO and Co₂O₃ during calcinations process.

One can see from Figs. 3.3 and Fig. 3.4 that as we increase the calcination temperature from 500 °C to 800 °C, the intermediate CoTeO_4 phase is transformed to the final CTO product following equations 3.2 and 3.3. Equation 3.4 indicates decomposition of CTO above 900 °C. Inset of Fig. 3.4 shows variation of concentration of CoTeO_4 and Co_3TeO_6 phases against the calcination temperature.

The following equation has been used to calculate the concentrations of $\text{CoTeO}_4/\text{Co}_3\text{TeO}_6$ phases.

$$\% \text{ of } \text{CoTeO}_4/\text{Co}_3\text{TeO}_6 = I_{\text{CoTeO}_4/\text{Co}_3\text{TeO}_6} / (I_{\text{CoTeO}_4} + I_{\text{Co}_3\text{TeO}_6}) \times 100 \quad (3.5)$$

It has been reported that TeO_2 oxidizes to TeO_3 , Te_2O_5 or Te_4O_9 around ~ 650 °C - 700 °C.¹³²⁻¹³³ However, no such oxidation of TeO_2 has been observed, when TeO_2 is heated at 700 °C for 2 hrs. Similarly, no dissociation of Co_3O_4 into CoO and Co_2O_3 has been observed when the starting reagent Co_3O_4 is heated to 700 °C, as shown in Fig. 3.5 and Fig. 3.6. All these analyses are based on the single step synthesis in which the mixed ground powder is heated directly to the designed temperatures. Due to the large amount of unreacted Co_3O_4 phase in the last calcination stage (i.e. 800 °C), double step synthesis has also been attempted. We have chosen a two step process because TeO_2 is volatile (melting temperature ~ 730 °C) and hence we get unreacted Co_3O_4 phase along with CTO, in one step synthesis process. In two step process, mixed powder is first heated at 700 °C for 10-12 hours and then again at 800 °C for 20-24 hrs with intermittent mixing and grinding. We have optimized first step by taking several calcination temperatures ranging between 600 - 700 °C, wherein we find no change in the final product. Fig. 3.7 compares SXRD pattern of CTO synthesized using single and double step synthesis. One can clearly see that lower concentration of Co_3O_4 phase is present in the double step synthesis compared to that for the single step. To get a clue about how much Co_3O_4 phase is present in the two step CTO

synthesis, percentage of the Co_3O_4 phase has been calculated from the peak intensity of the most intense peaks in SXRD patterns.

Percentage of Co_3O_4 phase is calculated using the equation

$$\% \text{ of } \text{Co}_3\text{O}_4 \text{ phase} = [I_{\text{Co}_3\text{O}_4} / (I_{\text{Co}_3\text{TeO}_6} + I_{\text{Co}_3\text{O}_4})] \times 100 \quad (3.6)$$

where, $I_{\text{Co}_3\text{O}_4}$ and $I_{\text{Co}_3\text{TeO}_6}$ represent the highest peak intensities (area under the peak) corresponding to the Co_3O_4 and CTO phases, respectively. The above equation reveals a concentration of $\sim 15\text{-}18\%$ and $\sim 8\text{-}10\%$ Co_3O_4 phase for single and two step syntheses, respectively.

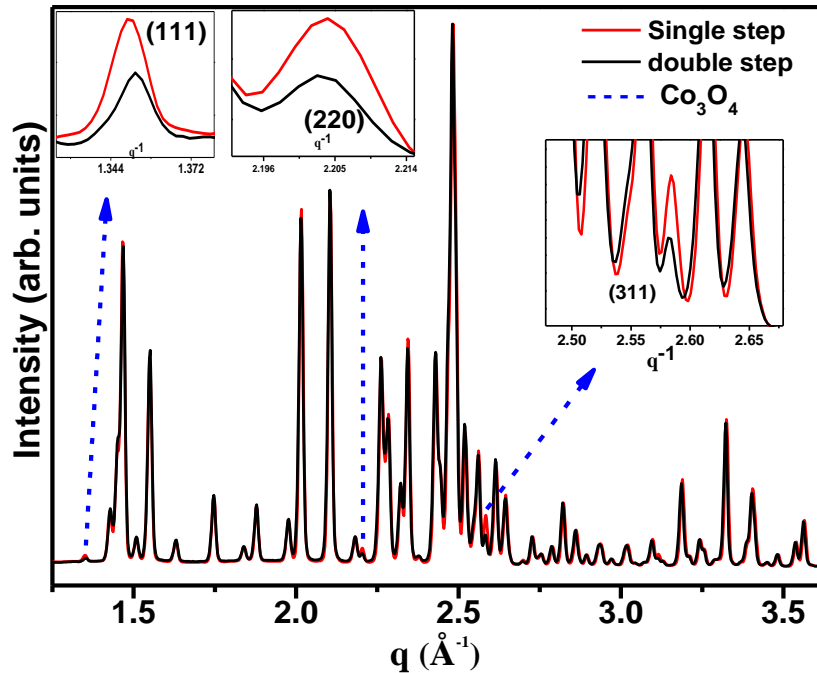


Fig. 3.7. Shows comparisons of single step and double step calculations.

It is important to note that the calcination temperature ($800\text{ }^\circ\text{C}$) is in between the melting points of TeO_2 ($735\text{ }^\circ\text{C}$) and Co_3O_4 ($890\text{ }^\circ\text{C}$), and the presence of the Co_3O_4 is due to the TeO_2 loss during calcination. To compensate the loss of TeO_2 , extra amount of the TeO_2 has been added in the stoichiometric amount of Co_3O_4 and TeO_2 powders. However, several reports have pointed

out the ambiguity in phase concentrations (due to different atomic numbers and symmetry of phases concern) calculated using the equation 3.7. Therefore, in order to know the accurate value of the Co_3O_4 phase concentration and hence the exact additional amount of TeO_2 , Rietveld refinement on SXR D data has been performed.

Fig. 3.8 (a) shows HR-SXR D patterns of the samples obtained using *stoichiometric (blue colour) and non- stoichiometric (red colour) reactant ratios*. One can clearly see that more Co_3O_4 phase is present in stoichiometric sample as compared to the non-stoichiometric one, as shown in Fig. 3.8 (b) (zoom part). Fig. 3.8 (c) shows two phases Rietveld refined SXR D patterns along with experimental and difference profiles. The same quantitative phase composition analysis using Rietveld Refinement on SXR D patterns gives $\sim 4\pm 1\%$ Co_3O_4 phase in the case of the two step CTO synthesis. To balance this loss in TeO_2 , extra TeO_2 has been added to complete the reaction. Fig. 3.8 compares the SXR D patterns of CTO, synthesized using stoichiometric (without extra TeO_2) and non-stoichiometric (with extra TeO_2) reactants. We find that, single phase CTO is synthesized when $\sim 5\%$ TeO_2 extra amount has been added in the stoichiometric amount of Co_3O_4 and TeO_2 . The mixed powder is first calcined in air at 700°C for 10 hrs and then again at 800°C for 24 hrs with intermediate mixing and drying steps. The above process has been repeated number of times to confirm the single phase CTO formation.

Detailed Rietveld analysis of the SXR D pattern reveals that monophasic CTO stabilized in monoclinic symmetry (space group: $C2/c$), in agreement with reported results on single crystal as well as powder CTO.⁷⁴⁻⁸⁰ The simulated pattern is shown in Fig. 3.9 along with observed experimental data. The room temperature refined crystallographic parameters obtained from the Rietveld refinement are summarized in Tables 3.1, 3.2 and 3.3. Insight into the structure of CTO (which contains five Co, two Te and nine O) indicates that crystallographically distinct Co

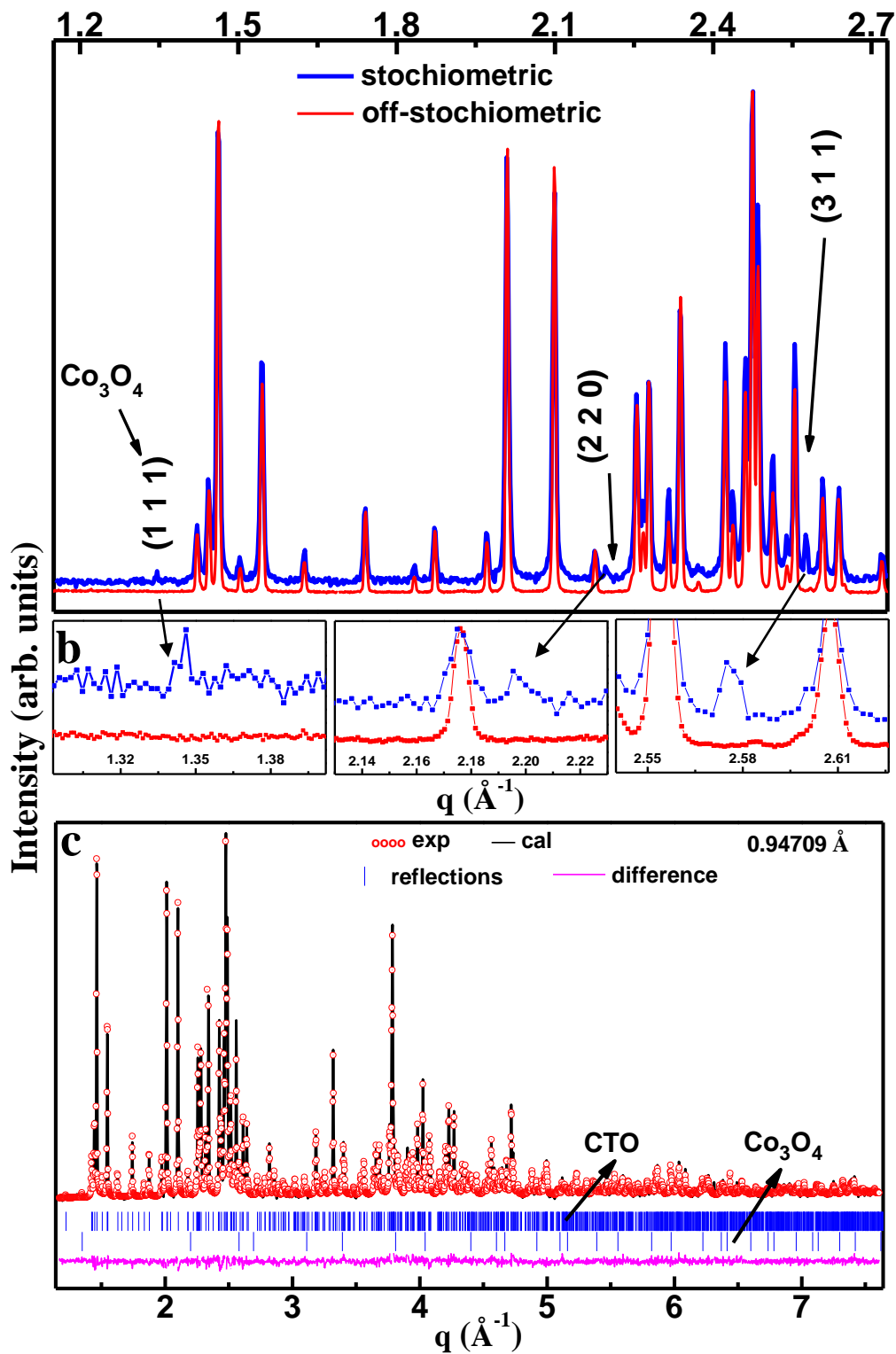


Fig. 3.8. (a) A high resolution Synchrotron X-ray Diffraction measurement is used to probe monophasic CTO, (b) shows the corresponding impurity, which is Co_3O_4 , (c) Rietveld refinement is used to estimate concentration of impure Co_3O_4 phase.

cations occupy 4e and 8f Wyckoff positions, Te 4b and 8f and all O 8f sites (Table 3.1). Both the Te ions occupy crystallographically different octahedral sites, whereas five Co ions occupy tetra, penta and octahedral sites as shown in Fig. 3.10.

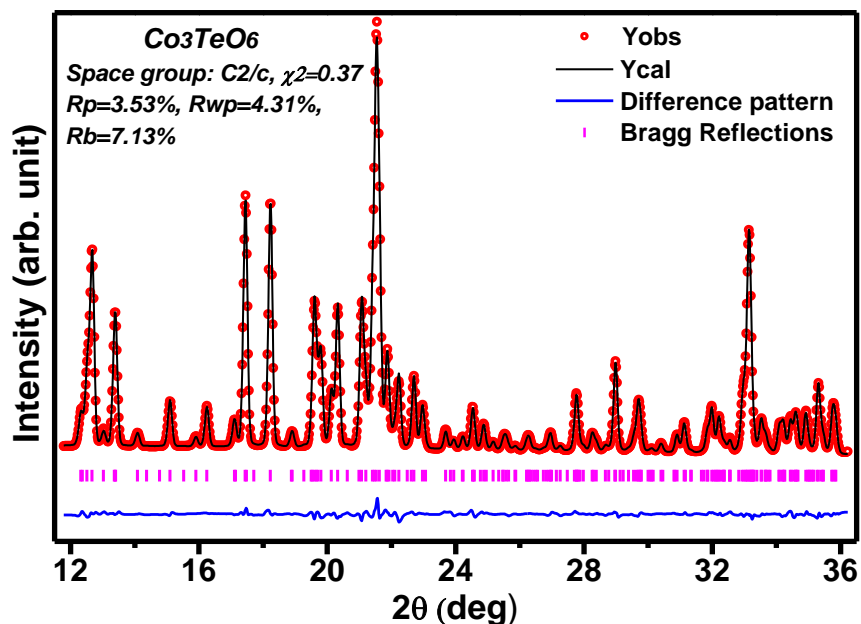


Fig. 3.9. Simulated and observed Synchrotron X-Ray Diffraction patterns recorded at room temperature ($\lambda = 0.9480 \text{ \AA}$) for ceramic CTO sample.

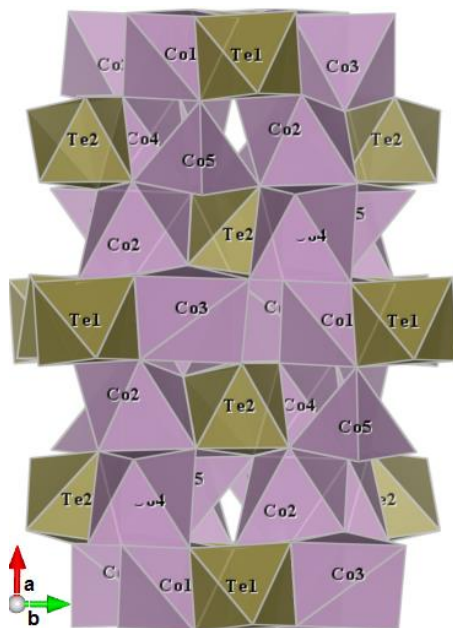


Fig. 3.10. Polyhedral view (a-b plane) of the ceramic CTO clearly signifies the octahedral, pentahedral and tetrahedral sites of Co, and octahedral sites of Te.

Table 3.1. Rietveld refined lattice parameters and atomic positions of Co_3TeO_6 at room temperature.

Co_3TeO_6 , $T = 300 \text{ K}$, $\chi^2 = 0.9983$; $R_{\text{wp}} = 4.31 \%$; $R_p = 3.53 \%$

$a = 14.8061(5) \text{ \AA}$, $b = 8.8406(3) \text{ \AA}$, $c = 10.3455(4) \text{ \AA}$, $\alpha = 90^\circ$, $\beta = 94.819(2)^\circ$, $\gamma = 90^\circ$

Atom	X	Y	Z
Co1	0.50000	-0.18278 (13)	0.25000
Co2	0.86205 (54)	-0.35713 (87)	0.23163 (65)
Co3	0.52150 (47)	-0.65706 (92)	0.04342 (54)
Co4	0.66890 (59)	-0.29106 (70)	0.05467 (67)
Co5	0.79836 (48)	-0.36092 (97)	0.57172 (67)
Te1	0.00000	0.50000	0.50000
Te2	0.66057 (23)	-0.49882 (59)	0.30046 (25)
O1	0.92542 (17)	-0.37621 (27)	0.55492 (20)
O2	0.58297 (19)	-0.33389 (40)	0.20480 (24)
O3	0.60095 (14)	-0.63851 (38)	0.19532 (22)
O4	0.75549 (15)	-0.54947 (30)	0.67236 (21)
O5	0.92948 (13)	-0.52162 (42)	0.34490 (18)
O6	0.58142 (14)	-0.48910 (35)	0.43810 (18)
O7	0.91876 (17)	-0.70289 (28)	0.55967 (24)
O8	0.73502 (18)	-0.34141 (43)	0.39372 (19)
O9	0.73099 (16)	-0.63739 (38)	0.38105 (21)

Table 3.2. Comparison of lattice parameters of present ceramic CTO with the earlier reports.

Sr. No.	a (Å)	b (Å)	c(Å)	β (°)	Ref.
1	14.8167	8.8509	10.3631	94.90	[13]
2	14.8014	8.8379	10.3421	94.83	[15]
3	14.7526	8.8139	10.3117	94.905	[17]
4	14.8113	8.8394	10.3589	94.834	[18]
5	14.8061	8.8406	10.3455	94.819	Our results [22,26,27]

Table 3.3. Most relevant interatomic distances (Å) in our ceramic CTO in comparison to the single crystal CTO.

Present CTO	Becker et al. ⁷⁴	Present CTO	Becker et al., ⁷⁴
Co-O	Co-O	Co-O	Co-O
Co5-O1 = 1.90824(7) Co5-O4 = 2.09208(6) Co5-O8 = 1.90407(6) Co5-O8 = 2.00313(7)	1.966 (4) 1.929 (3) 1.988 (4) 1.998 (3)	Co4-O4 = 2.20532(5) Co4-O7 = 1.85511(5) Co4-O2 = 2.12176(6) Co4-O9 = 2.18023(7) Co4-O4 = 2.20532(5) Co4-O7 = 1.85511(5)	2.131 (3) 2.282 (3) 1.982 (3) 2.389 (3) 2.065 (3) 2.030 (3)
Co3-O1 = 2.35588(6) Co3-O3 = 1.89226(6) Co3-O6 = 1.95899(5) Co3-O6 = 2.14707(6) Co3-O7 = 1.97877(5)	2.078 (3) 1.936 (3) 2.050 (3) 2.032 (4) 2.212 (3)	Co1-O1 = 2.274(8)×2 Co1-O2 = 1.9095(5)×2 Co1-O5 = 2.0614(5)×2	2.161 (3) 2.054 (3) 2.023 (3)
Co2-O3 = 2.11851(7) Co2-O4 = 1.83667(5) Co2-O5 = 2.07096(5)	1.963 (3) 2.008 (3) 2.023 (3)	Co2-O7 = 2.09548(7) Co2-O8 = 2.63144(8) Co2-O9 = 2.60085(6)	2.087 (4) 2.538 (4) 2.419 (3)
Te-O	Te-O	Te-O	Te-O
Te1-O1=1.68841(4)×2 Te1-O5=1.85095(6)×2 Te1-O7=2.27385(6)×2	1.951 (3) 1.908 (3) 1.938 (3)	Te2-O2=2.05289(5) Te2-O3=1.82849(5) Te2-O4=2.05713(6)	1.927 (3) 1.910 (3) 1.969 (3)
Te2-O6=1.91313(6)	1.927 (4)	Te2-O8=1.96798(5) Te2-O9=1.77183(4)	1.933 (3) 1.925 (3)

Rietveld refinement and corresponding results of valence bond sum calculations have also been done on SXRD data. The refined lattice parameters $a = 14.8061(5)$ Å, $b = 8.8406(3)$ Å, $c = 10.3455(4)$ Å, $\beta = 94.819(2)^\circ$, show marginal differences from earlier reports⁷⁴⁻⁸⁰ and are tabulated in Table 3.2. An important difference in our study lies in the typical bond distances of Co-O and Te-O (Table 3.3). In our samples, the Co-O bond lengths vary from 1.84 Å - 2.87 Å as compared to 1.97 Å - 2.93 Å reported earlier.^{74,76} In addition, the typical bond distance of Te-O ranges from 1.70 Å to 2.28 Å (in slightly more distorted TeO6 octahedra) as compared to that reported earlier from 1.88 Å - 1.98 Å.^{74,76} Among others, one of the possible causes for such a significant

difference in average bond distances (Co-O and Te-O), may be due to mixed valence of Co (to be discussed in next sub-section of this section). Structural analysis and visualization of structure have been done using VESTA software¹³⁴ on Rietveld refined structure. In addition, we also observe contraction of CoO₆ octahedra, CoO₅ pentahedra and/or CoO₄ tetrahedra as compared to the earlier reports. This might result in the shortening of the Co-O bond lengths accompanied by the variations in Te-O bond lengths.

We have also characterized the final single phase CTO sample using XPS, in order to get clue on average oxidation states of cations, as discussed below.

3.1.2.2. X-ray photoelectron spectroscopic analysis

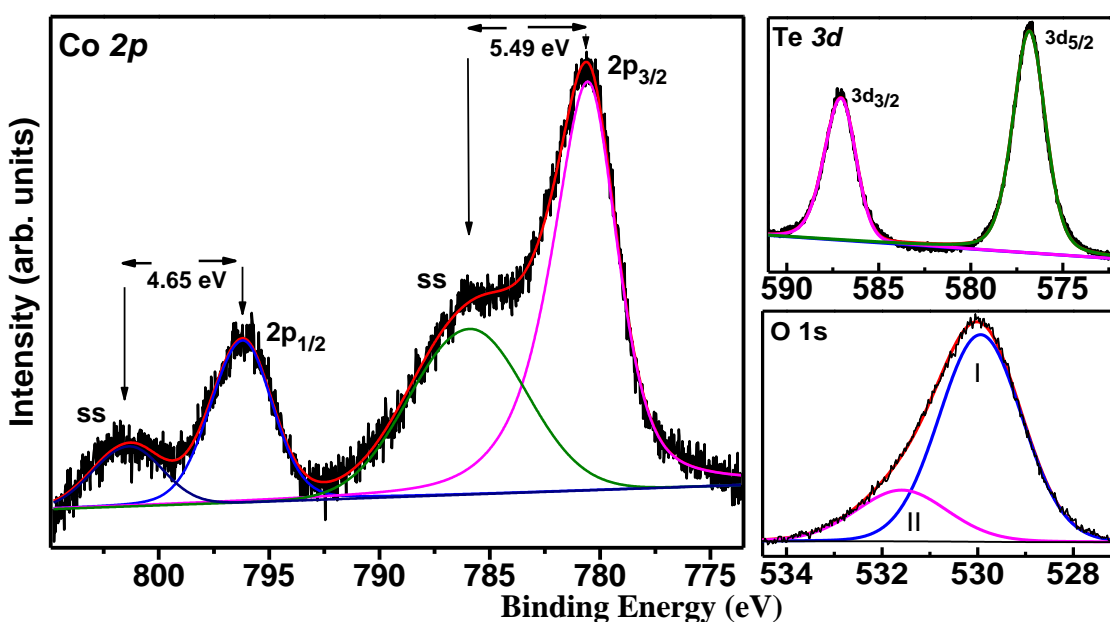


Fig. 3.11. (a) Normalized core level XPS spectra of Co 2*p*, satellite (ss) peaks nearby main peaks confirms the mixed oxidation state of Co in CTO, (b) normalized core level XPS spectra of Te 3*d*, binding energy 587.3 eV and 576.8 eV positions of the main peaks confirm the +6 oxidation state of Te and (c) Oxygen 1*s* XPS spectra CTO sample fitted with Shirley background and two Lorentzian-Gaussian peaks acquired with Al K α source.

In XPS¹²⁹ (details are given in chapter 2), main peak positions, peak separation and positions of other special features like shake up satellites, are used for the estimation of charge state of ions.

Also, shake up satellite gives information on oxygen cage geometry around the transition metal. Herein, we perform XPS measurements in order to check the oxidation states of Co and Te, which may give clue on microstructural variations as higher valence cations have smaller ionic radii. Figs. 3.11 (a), (b) and (c) show XPS spectra of prepared CTO sample for Co 2p, Te 3d and O 1s edges.

Table 3.4. Binding energies (in eV) for Co 2p ($2p_{1/2}$ and $2p_{3/2}$) and Te 3d reported in literature along with our results. O/T denotes the octahedral and tetrahedral coordination, respectively.

Sr. No.	Co 2p				Ref (No.)
	$2p_{3/2}$	ss	$2p_{1/2}$	ss	
1- Co ²⁺ (O/T)	780.5/780.7	786.4/789.5	796.3/796.0	803.0/804.5	[135-136]
Co ³⁺ (O)	779.6	---	794.5	----	[135-136]
2	780.05	784.70	795.80	801.29	CTO
Te 3d					
	$3d_{5/2}$		$3d_{3/2}$		
1	576.8	--	587.2	--	[137]
2	576.6	--	587.0	--	[138]
3	576.87	--	587.18	--	CTO

The photoelectron spectral features of oxygen (O) 1s peak for CTO sample falls at 529.9 ± 0.1 eV (I: oxide peak and II: adsorbed hydroxyl group).¹⁰³ This value is in agreement with the binding energy given earlier,^{103,135-136} showing negligible charging effect in our sample. Co 2p spectrum for CTO sample shows main Co $2p_{1/2}$ and Co $2p_{3/2}$ peaks at 780.1 eV and 795.8 eV, respectively, with significant satellite peaks. By using only the main peak positions, one can't probe accurately; the exact valence state of Co in the samples.¹³⁶ Satellite peak intensity along with their binding energy positions may identify the Co valence state. Reported values of Co 2p

binding energy and satellite peak positions are tabulated in Table 3.4 along with the experimentally observed values for our sample.

The satellite peaks for Co $2p^{1/2}$ and Co $2p^{3/2}$ peaks are shifted by (4.6 ± 0.1) eV and (5.5 ± 0.1) eV from their main peaks, respectively. Concerning the present case, only two ionic state of Co (+2 and +3) are stable and the values of their satellite peaks are tabulated in Table 3.4. From this table, one may see the mix valence behaviour of Co in the sample. The separation between Co $2p^{1/2}$ and Co $2p^{3/2}$ main peaks is about 15.7 ± 0.1 eV for CTO samples, which is rather insensitive to the valence state of Co. Therefore, spin-orbit multiplet separation cannot be used for the identification of ionic valence state of cobalt in cobalt based compounds.¹²⁴

Further, Te 3d peak position (FWHM) has been found to be at 576.8 (1.96) eV for $3d^{5/2}$ and at 587.2 (2.08) eV for $3d^{3/2}$, with spin orbit separation of 10.2 eV. The peak separation of 10.2 eV and no satellite peak indicate Te^{+6} .¹³⁷⁻¹³⁸ Table 3.4 compares peak positions of 3d peaks in CTO sample with those for Te^{+6} complexes, reported in literature.. We have also compared the binding energy position of Te^{+4} , which is not matching with our results indicating +6 charge state of Te in our sample. XPS analysis so far indicates the possibility of mixed valence Co and +6 oxidation states of Te in CTO sample.

3.1.3. Conclusions

To summarize this section, ceramic Co_3TeO_6 is synthesized via conventional solid state reaction route and possible reaction mechanism has been proposed. *Off-stoichiometric* Co_3O_4 and TeO_2 and two step calcination in air leads to single phase CTO. CTO structure crystallizes in monoclinic $C2/c$ space group in agreement with earlier reports of single crystal as well as ceramic CTO. Obtained structural parameters using Rietveld refinement shows slightly different lattice parameters from those reported in literature. Corresponding bond valence sum

calculations support all the crystallographic information reported earlier for the single crystal CTO. Noticeable differences between synthesized CTO and reported single crystal structures are observed through the variations in the average bond distances. We find wider variations in bond lengths of different Co and Te sites, which may be attributed to the mixed valence of Co in CTO. The conjecture is supplemented qualitatively by XPS results. Quantitative confirmation has been done using XANES measurements (to be discussed in section 3.2 of this chapter). Moreover, synthesis in different (oxygen reduced) atmospheric conditions will also be discussed.

3.2. Observation of high-spin mixed oxidation state of cobalt in CTO

This section describes the observation of coexistence of mixed oxidation states of Co (Co^{3+} and Co^{2+}) in our ceramic CTO. Co^{3+} and Co^{2+} ions are found to be in high spin states. XANES, high field DC magnetization and first principles ab-initio calculations have been used to study charge and spin states of Co in CTO. Finally, we have studied probable origin of Co^{3+} in CTO by synthesizing CTO in different atmospheric conditions.

3.2.1. Introduction

In continuation of previous section, which shows the signature of Co^{3+} in our synthesized CTO, a thorough study to investigate the possibility of additional charge state has been explored in this section. XPS study on our single phasic CTO suggests that Co may be in mixed oxidation states (Co^{3+} and Co^{2+}). However, literature suggests that only Co^{2+} ions occupy five different crystallographic positions as tetra, square-pyramidal and three octahedral sites in single crystal as well as ceramic CTO.⁷⁴⁻⁸⁰ Such polyhedral configurations with only one type of cations is difficult to appreciate,⁸⁷⁻⁸⁹ and thus leave the possibility of mixed valence cations.⁸⁷⁻⁸⁹ An interesting analogue is Co_3O_4 {i.e. $(\text{Co}^{2+})_{\text{tet}}[\text{Co}_2^{3+}]_{\text{oct}}\text{O}_4$ }, which possesses spatially inhomogeneous magnetic moments via Co^{2+} in tetrahedral sites and Co^{3+} in octahedral sites.¹³⁹ Due to the same, 3d electrons of Co ions experience different crystal fields, leading to different electronic/spin configurations.¹³⁹ The change in distribution of $\text{Co}^{2+}/\text{Co}^{3+}$ caused by various external sources like magnetic field, high pressure, temperature etc. have led to several other phenomena like diffusive charge transfer and very large effective magnetic moment, which make great interest in such systems.¹⁴⁰⁻¹⁴¹ As CTO shows features similar to those of spinel compounds, its low-temperature magnetic properties are likely to be very interesting, as observed in several reports⁷⁵⁻⁸². For example, Co^{3+} ions in octahedral coordinations prefer low spin state ($S=0$),

whereas the same may also show high spin state in same configuration as observed in several other cases.^{139,142} It may be also noted that Co^{3+} may exist in octahedral, tetrahedral or pentahedral site.¹⁴³⁻¹⁴⁴ As the strength of Hund's coupling and the crystal-field splitting are comparable for Co based compounds, the spin state of the cobalt ions are highly dependent on various factors like doping concentration, crystal structure, external magnetic field etc.¹⁴⁵ For example, magnetic field-induced spin-state transition state in $\text{Sr}_{1-x}\text{Y}_x\text{CoO}_{3-\delta}$ and a similar temperature induced spin state transition in $\text{La}_{2-x}\text{Sr}_x\text{CoO}_4$ are linked to low-to-intermediate spin (IS) and low-to-high spin (HS) state transitions of Co^{3+} , respectively.¹⁴⁶⁻¹⁴⁷

It is therefore important to investigate the charge and spin state of Co in our ceramic CTO, not reported so far. For this, we have performed XANES and high field DC magnetization measurements. The magnetization measurements combined with crystal field splitting obtained from XANES pre-edge analysis have indicated additional support for our interesting observations of mixed valence of Co (i.e. Co^{2+} and Co^{3+}), in our ceramic CTO. To ascertain the same, first principles simulations have also been carried out. Such observation of Co^{3+} oxidation state is a first step towards the experimental verification of some of the theoretical predications.⁸² For example, it is well known that the $\text{Co}^{2+}\text{-O-Co}^{2+}$ network gives rise to AFM correlations between Co ions through super-exchange interactions.⁷⁷⁻⁸⁰ Appearance of Co^{3+} ions in $\text{Co}^{2+}\text{-O-Co}^{2+}$ network can cause (a) structural distortion, (b) local FM interaction through double-exchange, (c) weakening of effective magnetic interaction between the Co^{2+} ions and (d) incommensurate (IC) AFM ordering.¹³⁹ For instance, a possible reason for the appearance of the IC-AFM order in Co_3O_4 is considered to be local structural modulations due to change in charge/spin state of Co ions.¹³⁹ This may also result in the larger effective magnetic moment as compared to that in single crystal (with only Co^{2+}). Through the present study, we show that the

existence of Co^{3+} and Co^{2+} in ceramic CTO does not diminish multiferroic property (to be discussed in section 3.3 of this chapter) observed earlier in single crystal, but actually enhances some of the observables.⁹⁶

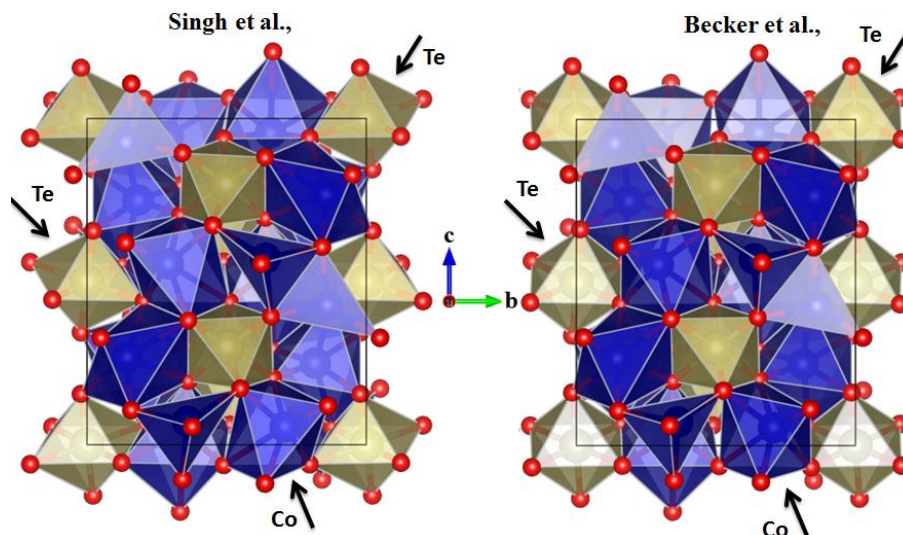


Fig. 3.12. Polyhedra of our ceramic CTO as compared to single crystal CTO show marginal distortion in the corresponding $\text{CoO}_6/\text{CoO}_5/\text{CoO}_4$ and TeO_6 polyhedra leading to shorter typical bond distances of Co/Te-O.

Structural analysis using Rietveld refinement on SXRD data leads to significant differences in bond distances (Co-O and Te-O) as compared to reported results on single crystal samples (Table 3.3). Herein, Co-O bond lengths vary from 1.84 (1) Å - 2.87 (1) Å as compared to 1.97 Å - 2.93 Å reported earlier.^{74,76,80} Also, Te-O bond lengths range from 1.70 (1) Å to 2.28 (1) Å (in slightly more distorted TeO_6 octahedra, and shown in Fig. 3.12) as compared to that reported earlier (1.88Å - 1.98Å).^{74,76,80} One of the possible causes for such a significant difference in average bond distances (Co-O and Te-O) may be due to the presence of Co^{3+} .¹⁴⁸ It may so happen that some of the Co sites are occupied by Co^{3+} instead of Co^{2+} , which may give rise to contraction of CoO_6 octahedra, CoO_5 pentahedra and/or CoO_4 tetrahedra.¹⁴⁸ This might result in the shortening of the Co-O bond lengths accompanied by the variations in Te-O bond lengths.

Experimental evidence for the observed micro-structural variations which are possibly due to the presence of Co^{3+} in addition to Co^{2+} in ceramic CTO, has been presented using XANES measurements. In the following, first we discuss XANES data in details followed by discussion on magnetization and first principles studies.

3.2.2. Results and Discussion

3.2.2.1. X-ray Absorption Near Edge Structure Spectroscopy

XANES, discussed in chapter 2, is an element specific spectroscopic tool, which provides information on oxidation state, local coordination around the absorbing atom and electronic structure including hybridization effect of orbitals.^{115,146} Fig. 3.13 shows edge step normalized XANES spectra of Co metal foil, CTO and cobalt oxide standards (for +2 and +3 oxidation states).

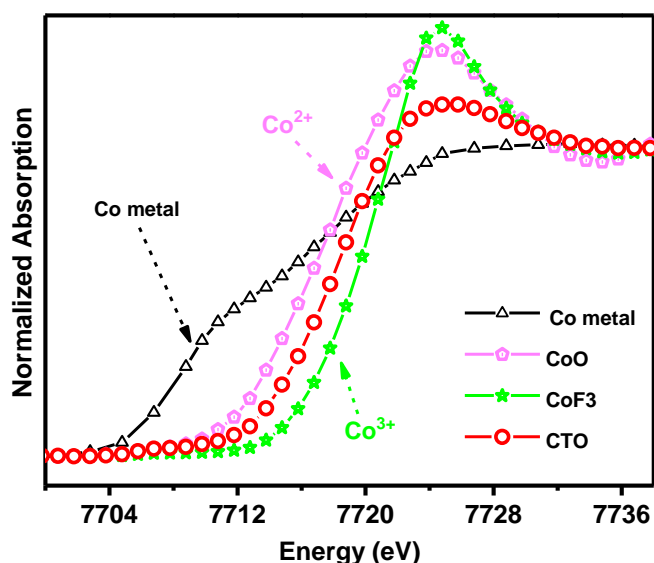


Fig. 3.13. Edge step normalized Co K-edge XANES spectra of CTO, Cobalt oxide standards (CoO and CoF_3) and Co metal foil. Co foil is used for photon energy calibration.

A typical TM K-edge XANES spectrum provides clue about the chemical shift and the nature of unoccupied density of states through the main ($1s-4p$) and pre ($1s-3d$) absorption edges,

respectively.^{115,149} In literature, the identification of the transition leading to the main edge (the shoulder) in XANES spectra has some controversy,^{115-122,149} as discussed in chapter 2. All the reports, however agree on the shoulder's sensitivity to the oxidation state of the absorbing atom. Energy position of the main absorption edge may be determined either as the energy corresponding to ~ 0.5 absorption or as the energy value of the maximum of first order differential spectrum. It gives oxidation state of the absorbing atom in the sample, as the main edge position shifts to higher energy due to core hole shielding effect with the increase in the average oxidation state. It is clear from Fig. 3.13 that the main edge corresponding to CTO is shifted towards higher energy side from that of the CoO standard. To understand the shift better, detailed analysis of XANES data is carried out. For this, we analyze XANES spectra of three different standard samples, viz Co metal foil, CoO and CoF₃ along with CTO, which are shown in Fig. 3.13. The spectra clearly show that the main edge position of CTO sample lies between those of CoO and CoF₃. This observation (blue shift in the energy edge position) indicates that Co in our CTO sample is not entirely in Co²⁺ state, in contrast to earlier reports,⁷⁴⁻⁸⁶ and suggests presence of Co³⁺. To calculate the concentration of Co²⁺ and Co³⁺, we use a simple linear combination formula, "Energy position of CTO sample = {Energy position of CoO $\times x$ + Energy position of CoF₃ $\times (1-x)$ } /100", where x is the calculated concentration of Co²⁺. The above formula has been derived by assuming a linear dependence of the chemical shift on the average valence.¹⁵⁰ In order to verify the same, we have plotted (shown in inset of Fig. 3.14) the energy positions of standard samples (Co metal foil, CoO and CoF₃) as a function of their known oxidation states (0, +2 and +3, respectively), which also verifies our observation. Experimentally obtained edge energy positions of CTO, CoO and CoF₃ together with aforementioned formula give relative concentration of Co²⁺ and Co³⁺ as 60% and 40%, respectively. One can also do the

same quantitative analysis by Linear Combination Fitting (LCF) on XANES data, using the software Athena.¹⁵¹ Experimental data and the best LCF fit are presented in Fig. 3.14. LCF fit also results $\text{Co}^{2+}/\text{Co}^{3+}$ ratio in CTO to be $\sim 60/40$, in agreement with the value obtained from the empirical formula used above.

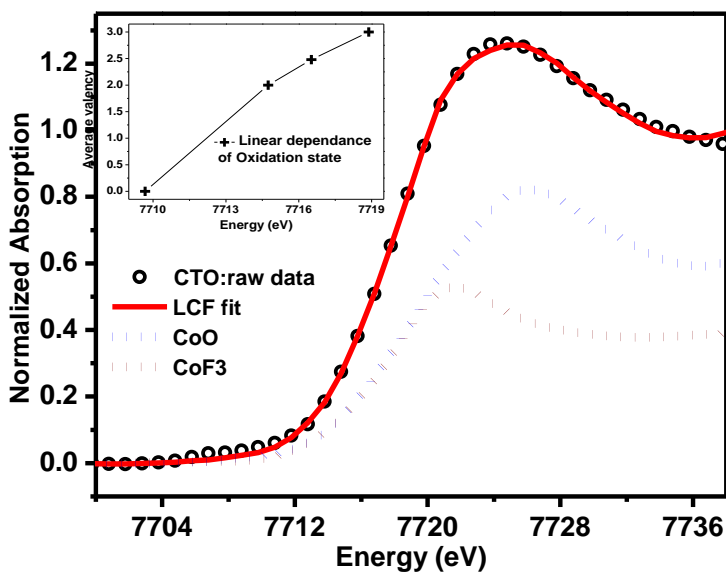


Fig. 3.14. LCF fit of ceramic CTO using CoO and CoF₃ standard samples (main panel) and inset shows linear dependence of oxidation states as a function of energy obtained from derived formula.

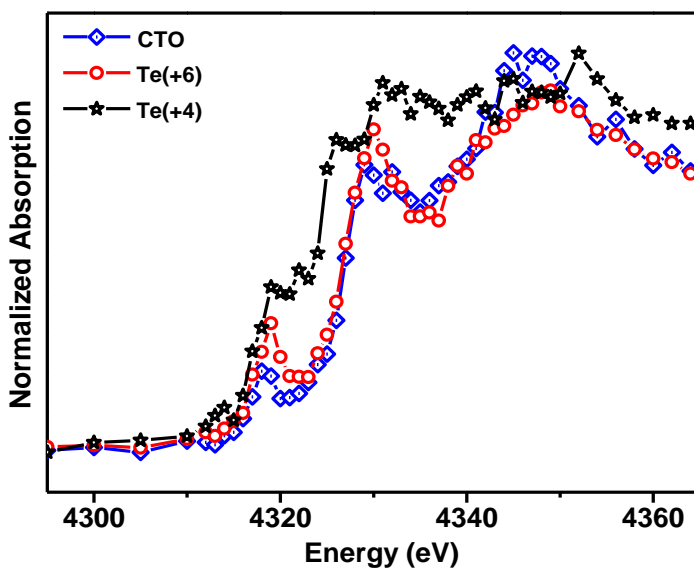


Fig. 3.15. Te L₃ edge XANES spectra of CTO along with Te standards.

From the above analysis, Co mix valency has been clearly established in our ceramic CTO sample. For the charge balance in Co_3TeO_6 , various additional possibilities arise. Te stabilizes in +6 and +4 or in the mixed states of these two, leading to mixed valence Co. However, our XPS data indicates +6 state of Te (see section 3.1). In order to verify the oxidation state of Te further, we have performed XANES measurements at Te L- edge. Fig. 3.15 shows the Te L- edge XANES spectrum along with their standards (Te^{4+} and Te^{6+} oxidation states). Comparison of Te L- edge XANES spectra with Te^{4+} and Te^{6+} standards clearly indicate Te^{6+} state in CTO. Other possibilities include oxygen excess¹⁷² and Co /Te vacancy.¹⁵³⁻¹⁵⁴ For example, observed mix valency of Co and +6 oxidation state of Te suggest oxygen non-stoichiometry in CTO, and will be further discussed in the last part of this section.

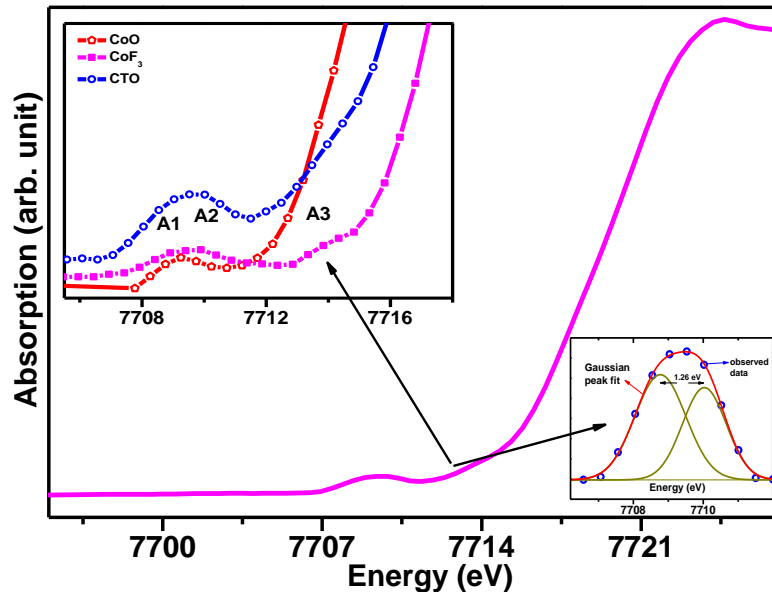


Fig. 3.16. Edge step normalized Co-K edge XANES spectra of ceramic CTO sample showing pre edge structure at around 7709 eV (main panel). CoF_3 and CoO are used as the source for high spin Co^{3+} and Co^{2+} , respectively (left inset). Various pre edge features namely A1, A2 and A3 has been shown for the sake of clarify (left inset). Gaussian peak fitting has been used to analyze the crystal field splitting between the e_g and t_{2g} states of Co cations after careful background subtraction (see right inset).

In order to estimate the contribution of TM ions to the magnetic moment, we need to know the charge state, spin state and orbital contribution of the ions. In the following, we estimate the spin state of Co^{3+} using pre edge feature of XANES spectrum. In literature,⁷⁵⁻⁸⁰ it has been proposed that Co^{2+} is in the high spin state. Followed by the observation of both Co^{2+} and Co^{3+} , we speculate the possible spin state of the observed Co^{3+} through the pre-edge study of XANES spectrum in our ceramic CTO. Figs. 3.16 (main panel and left inset) show the pre-edge structure below the main absorption line at around 7718 eV. The pre edge spectrum exhibits several features in the energy range 7708 eV to 7715 eV, denoted as A1, A2 and A3. Following earlier reports,¹⁵⁵⁻¹⁵⁷ we ascribe A1 and A2 to the 1s - 3d transitions into t_{2g} and e_g states, respectively. These transitions take place partly through direct quadrupolar transitions, and also a mixture of dipolar transitions to d - p hybridized molecular orbitals of Co (3d) and O (2p). We find that the crystal field splitting (the energy difference between the t_{2g} and e_g states) is of the order of 1.26 eV. This contradicts the possibility of low spin state of Co^{3+} in our sample, as in this case the expected crystal field splitting would be around 2.3 eV.¹⁵⁵⁻¹⁵⁷ The observed splitting (~ 1.2 eV) in our sample suggests high spin state of Co^{3+} . This splitting in the case of intermediate spin state of Co^{3+} has been reported to be 2.2 eV.¹⁵⁸ Furthermore, the splitting in the case of high spin Co^{2+} in CoO is 1.14 eV.¹⁵⁹ Therefore, the observed energy difference between A1 and A2 (shown in the right inset of Fig. 3.16, fitted with two Gaussian peaks after careful background subtraction) may correspond to the superposition of the high spin states of both the Co^{2+} and Co^{3+} .¹⁵⁵⁻¹⁵⁹ In literature, mixture of high spin states of Co^{3+} and Co^{2+} has also been reported for other compounds e.g. $\text{LaMn}_{1-x}\text{Co}_x\text{O}_3$ ($x = 0 - 1$).¹⁵⁵⁻¹⁵⁸

Furthermore, at higher energies, another broad feature (A3) at around 7714 eV is observed, which has been assigned to a ligand-to-metal charge transfer (LMCT) shake-down process.¹⁵⁵⁻¹⁵⁸

Shortening of bond lengths (as observed in section 3.1) in our ceramic CTO as compared to that in single crystal may also be due to charge transfer between Co^{2+} and Co^{3+} via oxygen. Our analysis so far assumes localized picture of t_{2g} and e_g states and hence have integral spins on oxygen. However, recent work by Medling *et al.*,¹⁶⁰ suggests that the localized picture may not be valid due to the interaction of e_g states with O-2p states. In contrast to the study of Medling *et al.*,¹⁶⁰ which concerns doping effect, our un-doped sample has intrinsic Co^{3+} and Co^{2+} occupying octahedral, tetrahedral and square pyramidal configurations, causing variations in the Co-O bond distances. Observation of high spin Co^{3+} in our ceramic CTO could affect the magnetic properties of the sample. In the following, we discuss the DC magnetization results and their correlation to the charge and spin states of TM ions in CTO.

3.3.2.2. High field DC Magnetization study

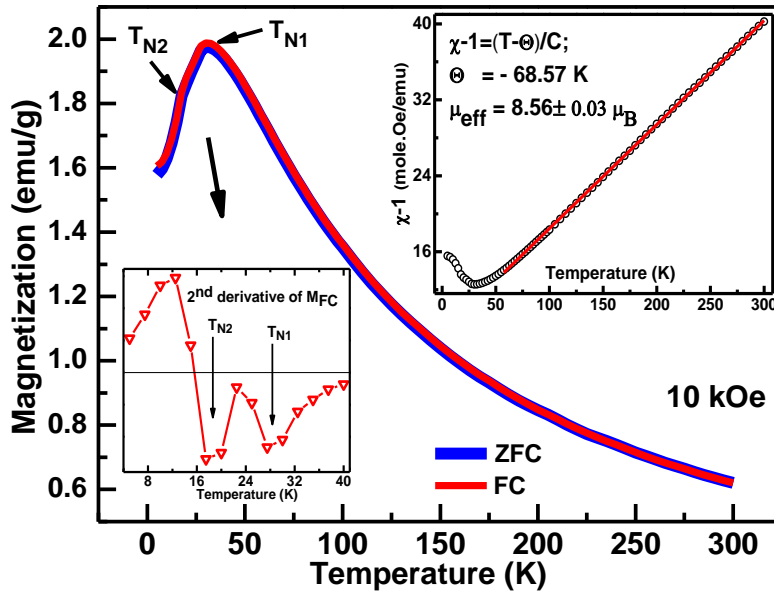


Fig. 3.17. High field DC magnetization under ZFC/FC protocol indicates antiferromagnetic behavior akin to that of single crystal CTO. Curie-Weiss fit to FC data is shown in right inset. Left inset shows the corresponding Neel temperatures (T_{N1} and T_{N2}) through the second derivative of M_{FC} . Effective magnetic moment (μ_{eff}) has been calculated through the relation: $\mu_{\text{eff}} = \sqrt{8C} \mu_B$ per *f. u.*

Fig. 3.17 shows magnetization on ceramic CTO under zero field cooled (ZFC) and field cooled (FC) conditions. DC magnetization of CTO has been recorded as a function of temperature under an applied constant magnetic field of 10 kOe. In FC, magnetic field is applied while cooling the sample from room temperature to lower temperatures, whereas, in ZFC, sample is cooled to lowest temperature in the first stage and then field is applied during the warming process. From the first look at the data, we find that the magnetic behavior is similar to that observed in single crystal studies, which includes two magnetic transitions at around 26 K (T_{N1}) and 18 K (T_{N2}) at high magnetic fields (> 1 Tesla).⁷⁸ Low field magnetization data, on the other hand, shows very complex magnetic behaviour and will be discussed in section 3.3 of this chapter. Left inset of Fig. 3.17 shows corresponding Neel temperatures (T_{N1} and T_{N2}) from the second derivative of M_{FC} curve in agreement with earlier reports. Her et al.,⁷⁸ mention typical tendency of these transitions as AFM and FM like, respectively through specific heat measurements under various magnetic fields on their single crystal CTO sample.⁷⁸

It is important to note from Fig. 3.17 that the measured magnetization of our ceramic CTO sample at 1 T is comparable to that reported in single crystal studies at 14 T⁷⁷. This shows our ceramic sample consists of improved magnetic properties compared to the reported magnetic properties for single crystal samples. To investigate the effect of the observation of Co^{3+} on magnetization, we analyze M vs T data in detail. The normal trend to analyses M vs T data is through Curie-Weiss (CW) fit, which may provide the nature of existing magnetic interactions, effective magnetic moment etc. The CW fit and the corresponding fit parameters of high temperature part of the dc magnetization data are shown in the right inset of Fig. 3.17. Fit shows negative value of Θ_{CW} (CW parameter) suggesting dominance of antiferromagnetic interactions in CTO, in agreement with earlier report.⁷⁸ Further, the effective magnetic moment (μ_{eff})

estimated from the CW parameter (obtained from CW fit) using $\mu_{eff}/f \cdot u = \sqrt{(8 C_{CW})}$ is 8.56 $\mu_B / f \cdot u$. This value is larger than that observed for single crystal studies $\sim 8.19 \mu_B / f \cdot u$. (or $\mu_{eff} = 4.73 \mu_B / \text{Co}^{2+} \text{ ion}$).⁷⁷⁻⁸⁰ In the present case, it is not feasible to assign μ_{eff} per Co^{2+} ions, because our XPS and XANES results indicate the presence of Co^{3+} . Therefore, we attribute the enhancement in the magnetic moment to the presence of Co^{3+} .

To investigate the observed enhancement in μ_{eff} , we calculate the C_{CW} parameter for Co^{3+} using the formula: $\mu_{eff}/f \cdot u = \sqrt{(8 C_{CW})}$. As mentioned above, μ_{eff} of CTO single crystal is $\sim 4.73 \mu_B / \text{Co}^{2+} \text{ ion}$ (orbital plus spin contributions), which results in $C_{CW}/(\text{Co}^{2+} \text{ ion}) = (4.73)^2 / 8 = 2.8$. Whereas, the experimental value of $C_{CW}/f \cdot u$ in our CTO is 9.16 (obtained through the CW fit, see Fig. 3.17). Assuming high spin state of Co^{2+} , we calculate the value of $C_{CW}/(\text{Co}^{3+} \text{ ion})$ using the following formula:

$$1.8 \times C_{CW}/(\text{Co}^{2+} \text{ ion}) + 1.2 \times C_{CW}/(\text{Co}^{3+} \text{ ion}) = 9.16$$

In this formula, we have divided the three cobalt of Co_3TeO_6 in to two parts 1.8 ($\sim 60\%$) Co^{2+} and 1.2 ($\sim 40\%$) Co^{3+} , respectively, as per the observations from LCF and XANES analyses. After simple calculations, we get $C_{CW}/(\text{Co}^{3+} \text{ ion}) = 3.43$, which corresponds to the magnetic moment of $5.24 \mu_B / \text{Co}^{3+} \text{ ion}$. This value of the magnetic moment is close to the magnetic moment of Co^{3+} ions in the high spin state (e.g, $\sqrt{4 \times S(S + 1) + L(L + 1)} \sim 5.48 \mu_B / \text{Co}^{3+} \text{ ion}$, where S and L are the spin and orbital angular momentum, respectively). Therefore, our magnetization and XANES results indicate the presence of Co^{2+} and Co^{3+} where both the ions favor high spin states in our CTO.

So far, we have established the coexistence of mixed valence states (Co^{2+} and Co^{3+}) of Co and their high spin states from the analysis of SXRD, XANES and high field magnetization data. However, some uncertainty remains in the indirect estimation of magnetic moment. Therefore, in

order to get a lowest energy and hence, most stable configuration, first principles calculations by taking Co^{2+} and Co^{3+} in various spin states (i.e. low and high for Co^{2+} and low, intermediate and high for Co^{3+}) have been carried out to further ascertain our findings.

3.2.2.3. *First principles study*

The first principles *ab-initio* calculations are performed using the CASTEP module of Material Studio 7.0 package¹⁶¹ that employs density functional theory using plane-wave pseudo-potential method. The first principles plane wave basis set calculations are performed within the generalized gradient approximation (GGA) using Perdew-Burke-Enzerhof (PBE) functional.¹⁶² Ultra-soft-pseudo-potentials, plane wave basis set with energy cut off of 380 eV and SCF tolerance of 10^{-6} eV/atom are used. Brillouin zone is sampled in the k space within Monkhorst-Pack scheme and grid size for SCF calculation is (2×4×2). During the first principles *ab-initio* simulations, the crystallographic details like lattice parameters, Wyckoff positions, etc. obtained from the Rietveld refined structure on room temperature SXRD data of CTO and is used as fixed input for the calculations. Fig. 3.18 shows the crystal structure (graphical view) of CTO along with some of Co – O – Co angles based on which GKA rule is applied. Large variations in bond lengths and bond angles corresponding to CTO indicate various possible interactions.²⁹⁻³⁰ The purpose of our simulations is to obtain a better understanding on the possible ground state configurations that justify the observed XANES and magnetization data. For example, whether the coexistence of Co^{2+} states with certain percentage of Co^{3+} (~ 40 % as emerges from XANES studies) is energetically favorable or not.

In order to ascertain the same, we have carried out single point total energy calculations using density functional theory (DFT) based on CASTEP code. Total energy calculations for all possible arrangements of Co^{2+} and Co^{3+} in terms of their spin states and magnetic alignments are

carried out; only some typical results have been tabulated in Table 3.5. The second column of Table 3.5 tabulates the nature of initial spin configuration between Co^{2+} (and/or Co^{3+}) ions via oxygen. The spin arrangement between Co^{2+} and Co^{3+} is also kept in AFM configurations. For 33 % of Co^{3+} in intermediate spin, an initial FM spin arrangement with Co^{2+} (high spin) resulted in unfavorable total energy, not included in the Table 3.5, suggesting long range FM state may be unlikely (but short range FM may not be overruled).¹⁶³ The third and fourth columns represent the crystallographic positions (Wyckoff sites) of Co^{2+} and Co^{3+} in CTO structure and their relative concentration, whereas the fifth and sixth columns indicate their spin states. Finally, the single point total energy is shown in the seventh column.

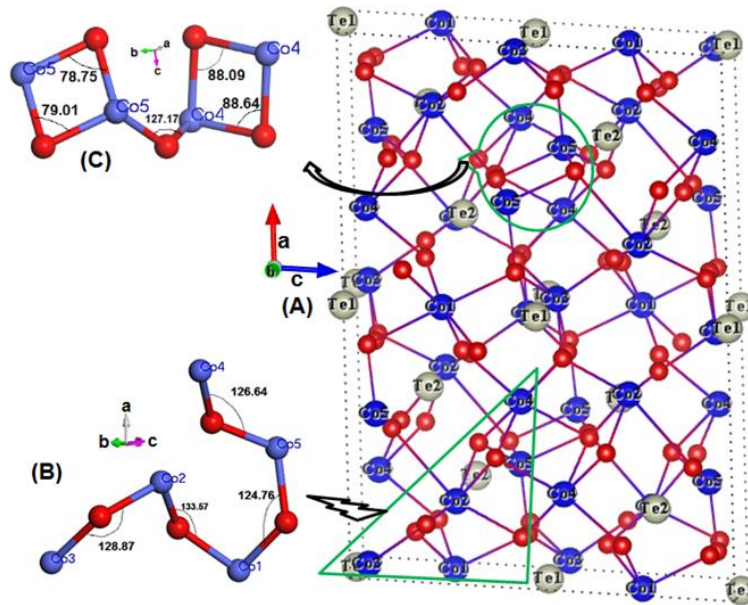


Fig. 3.18. (A) Graphical representation of Co_3TeO_6 crystal structure where only Co - O bonding is shown (red solid ball is the oxygen) and (B) Representative angles (in degree) between Co-O-Co are shown, which can modify the nature of super-exchange interaction (e. g., $\angle \text{Co} - \text{O} - \text{Co} \geq 120^\circ$ AFM type and weak FM type otherwise). These are employed in first principles calculations. Various orientations are used for clear visual presentation.

Table 3.5: Total energies of all possible antiferromagnetic and ferromagnetic spin configurations for the coexistence of Co^{2+} and Co^{3+} in Co_3TeO_6 . The energies have been tabulated with respect to the energy of Co^{2+} -O- Co^{2+} AFM spin arrangement (Co^{2+} as 100%) as reference. The lowest-energy spin arrangement is given by Co^{2+} -O- Co^{2+} : AFM+GKA as shown in the table for the respective concentration of Co^{3+} .

Sr. No.	Configurations	Co^{2+} (%)	Co^{3+} (%)	Spin state		Total relative Energy (meV)
				Co^{2+}	Co^{3+}	
1.	AFM Co^{2+} -O- Co^{2+}	100 ($Co_1, Co_2, Co_3, Co_4, Co_5$)	0.0	High	--	0
2.	AFM Co-O-Co	78 (Co_1, Co_2, Co_3, Co_4)	22 (Co_5)	High	Intermediate	-267.16
3.	AFM Co-O-Co	78 (Co_1, Co_2, Co_3, Co_4)	22 (Co_5)	High	Low	-316.31
4.	AFM Co-O-Co	78 (Co_1, Co_2, Co_3, Co_4)	22 (Co_5)	High	High	-305.18
5.	Co-O-Co AFM+GKA	67 (Co_2, Co_3, Co_4)	33 (Co_5, Co_1)	High	Intermediate	-381.51
6.	Co-O-Co AFM+GKA	67 (Co_2, Co_3, Co_4)	33 (Co_5, Co_1)	High	Low	-341.49
7.	Co-O-Co AFM+GKA	67 (Co_2, Co_3, Co_4)	33 (Co_5, Co_1)	High	High	-433.00
8.	Co-O-Co AFM+GKA	58 (Co_1, Co_4, Co_5)	42 (Co_2, Co_3)	High	Intermediate	-117.19
9.	Co-O-Co AFM+GKA	58 (Co_1, Co_4, Co_5)	42 (Co_2, Co_3)	High	Low	-450.32
10.	Co-O-Co AFM+GKA	58 (Co_1, Co_4, Co_5)	42 (Co_2, Co_3)	High	High	-529.89

Based on the earlier reports⁷⁴⁻⁸² on CTO, we have taken AFM arrangement between Co ions first. One may note that the configurations in which Co^{2+} is in high spin state in combination with high spin of Co^{3+} have favorable magnetic ground states. However, low or intermediate spin state of Co^{3+} may also be a possible magnetic ground state depending upon the amount of fractional presence of Co^{3+} and Co^{2+} . For example, for 78 % Co^{2+} and 22 % Co^{3+} , both the ground state energies for high spin – high spin and high spin – low spin are comparable. Energy calculations presented in Table 3.5 depend also on the fraction of Co^{3+} present, its neighboring spin configurations, etc. Note that Co^{2+} is in high spin state and is antiferromagnetically coupled via oxygen to another Co^{2+} . As per GKA rule,³⁰ some of the arrangements are also aligned ferromagnetically depending on the angle $\text{Co}^{2+}\text{-O} - \text{Co}^{2+}$ (above or below 120). Therefore, the configuration in which both Co^{2+} and Co^{3+} are in high spin states (Sr. No. 4, 7, 10) have the most favorable total energy for the observed concentration of Co^{2+} and Co^{3+} .

So far, we have discussed the evidence of Co^{3+} along with Co^{2+} in ceramic CTO using experimental observations and theoretical predictions. Emphasis on the search for the origin of the same is drawn in the next clause. One can easily guess from the result of the above analysis that possible outcome of mixed valence Co would be either anions non-stoichiometry (excess) or cations non-stoichiometry (vacancy).¹⁵²⁻¹⁵⁴

3.2.2.4. In the search for the origin of Co^{3+}

To investigate one of the possibilities, which is the most common in TM based oxides i.e. the possibility of oxygen excess, we have synthesized CTO in oxygen reduced (e.g. argon and vacuum) atmosphere in the optimized condition. In the argon atmosphere, tube furnace is first evacuated to 2×10^{-3} mbar pressure and then purged with argon for three times for few minutes each. The calcinations were carried out at constant flow of argon. For vacuum synthesis, pressed

pellet of ground mixture is sealed in a quartz ampoule at 7×10^{-6} mbar pressure and kept into the furnace. The ampoule with pellet was calcined in two steps (700 °C and 800 °C) without intermediate grinding, in the vacuum synthesis. Obtained samples are then characterized by SXRD and XANES techniques.

Fig. 3.19 shows SXRD patterns for CTO samples prepared under different atmospheric (air, argon and vacuum) conditions. SXRD patterns indicate that CTO synthesized in air results in monophasic CTO. Rest of the CTO samples have impurities; either Co_5TeO_8 (JCPDS # 20-0367) in the case of vacuum or $\text{Co}_2\text{Te}_3\text{O}_8$ (JCPDS # 89-4451), in the case of argon (see Fig. 3.19).

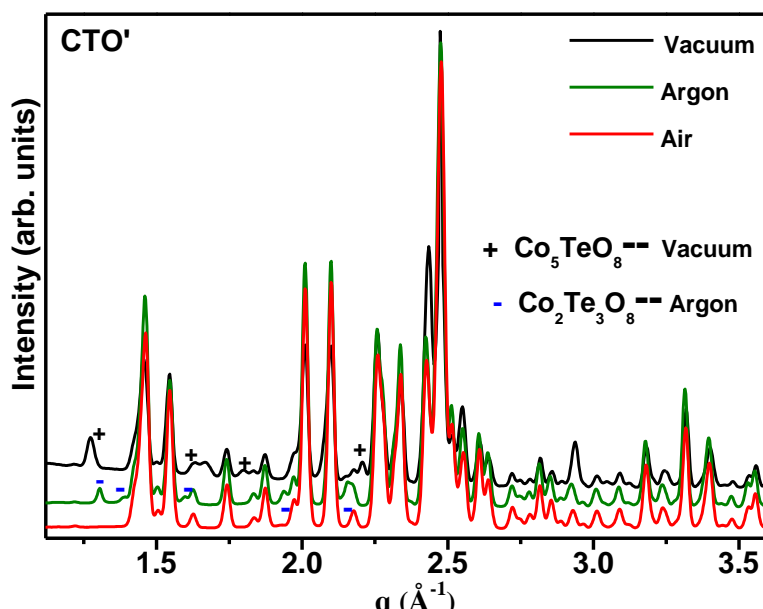
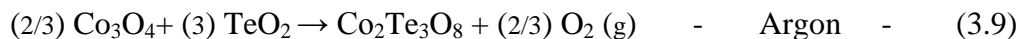


Fig.3.19. SXRD patterns of CTO synthesized in air, argon and vacuum atmosphere, indicating the only novel route for CTO synthesis. Dash represents multiphase CTO for vacuum and argon case.

We mention the possible reactions for the formation of impurities phases, as follow.



The other important observation from these samples is the same average valency of Co (within experimental error) in all the synthesized samples, as depicted by Co K edge XANES spectra (Fig. 3.20). Fig. 3.20 shows edge step normalized XANES spectra for all the samples synthesized under different atmospheric conditions (air, argon and vacuum). This actually complicates the cause of Co^{3+} in CTO. Based on all these studies, one may conclude that single phase of CTO forms only in air with two step calcinations. However, it is difficult to conclude the origin of Co^{3+} in CTO, suggesting the possibility of cations vacancy in our samples.

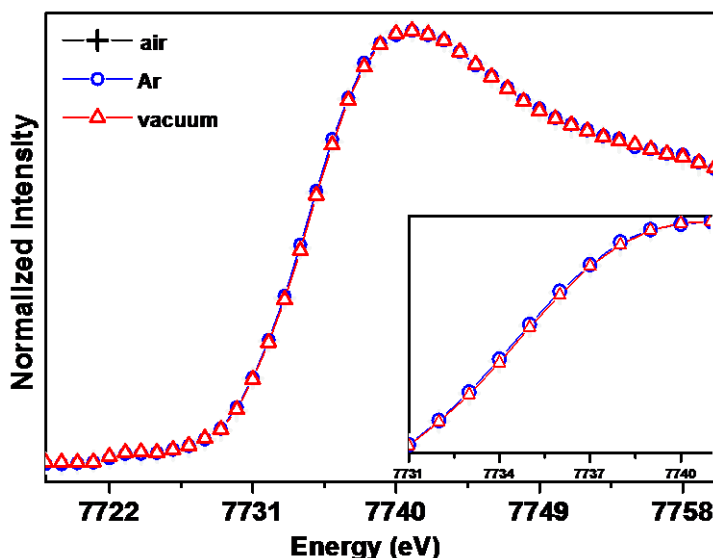


Fig. 3.20. Co K edge XANES spectra of CTO synthesized in air, argon and vacuum atmosphere, indicates same Co valency.

3.2.3. Conclusions

To conclude this section, we have evidenced the observation of Co^{3+} through XANES study, as also indicated earlier using XPS in section 3.1, of this chapter. Rietveld refinement of SXRD data recorded on ceramic CTO shows a noticeable deviation in typical Co-O bond distances when compared with other reports in literature, for single crystal as well as powder CTO. Observation of shorter bond lengths in our sample further supports the presence of Co^{3+} valence state. XANES spectra show coexistence of Co^{2+} and Co^{3+} with concentrations of 60 % and 40 %, respectively.

respectively. Magnetization measurements, with major magnetic transitions at ~ 26 K and ~ 18 K, show a large effective magnetic moment $\sim 8.56 \mu_B / f.u.$ obtained by Curie Weisse fit, indicating high spin Co^{3+} in agreement with XANES results. First principles based total energy calculations using CASTEP code support the experimental observation of high spin Co^{3+} in ceramic CTO. Consequences of Co^{3+} on the multiferroic properties of our ceramic CTO are discussed in the next section, where we show that the existence of Co^{3+} ions does not diminish any of the multiferroic properties seen earlier in powder as well as in single crystal CTO, but enhances some of the observables.⁹⁶⁻⁹⁷

3.3. Magneto-electric and Magneto-dielectric properties of CTO

This section describes magneto-electric and magneto-dielectric properties of ceramic CTO. Observation of all the magnetic transitions at low magnetic field and their possible structural correlations are discussed. Observed short range ferromagnetic interactions have been attributed to Co^{3+} -O- Co^{2+} network. Together with these, we present several interesting observations from magnetic field dependent dielectric constant data such as spontaneous electrical polarization, presence of ferromagnetic correlation below T_{N2} , possible spin-phonon coupling and magneto-dielectric effect in CTO. Finally, combined dielectric and pyroelectric current (polarization) measurements are utilized to comment on the spontaneous symmetry breaking in the absence of magnetic field.

3.3.1. Introduction

As discussed previously in the start of this chapter, single phase synthesis and the intrinsic low magnetic field magnetic behaviour of CTO remain under debate.⁷⁴⁻⁸⁶ The concern about this issue is due to its different magnetic behaviour at high and low magnetic fields.⁷⁵⁻⁸⁰ In section 3.2 of this chapter, we have discussed the high magnetic fields data, which shows only two AFM transitions $T_{N1} \sim 26$ K and $T_{N2} \sim 18$ K, in agreement with various reports on CTO.⁷⁷⁻⁷⁸ Low magnetic field data, on the other hand, shows different magnetic behaviour and thus are under debate.⁷⁶⁻⁸⁰ For example, there is no experimental report which shows all the five magnetic transitions (~ 34 K, 26 K, 21 K, 17.4 K and 16 K) in a particular ceramic or single crystal CTO. Different groups have reported different sets of magnetic transitions, including T_{N1} and T_{N2} .⁷⁵⁻⁸⁰ Assuming the origin of these variations in its synthesis part, we provide for the first time, the growth reaction mechanism of ceramic CTO in an attempt to solve this issue. Through this, we end up with monophasic and mixed valence CTO, as detailed in previous section 3.1 and 3.2.

Further, we have discussed the origin of low symmetry structure of CTO in A_3TeO_6 ($A = Mn, Ni, Cu, Co$)⁷⁶ family, where the other members of this family with $A = Mn, Ni$ show rhombohedral symmetry, while Cu_3TeO_6 shows cubic symmetry. Implications of such lower symmetry structure can be seen in its low temperature complex magnetic structure. As expected, due to high spin mixed valence state of Co in CTO, the magnetic behaviour may vary from the sample which has single +2 valence of Co, as reported in literature.⁷⁷⁻⁸⁰ Section 3.2 presents some of the advantages of having mixed valence Co in ceramic CTO as compared to its single crystal form.⁹⁶ In this section, we have studied low 5 Oe – 500 Oe) and high magnetic field (1 kOe-50 kOe) DC magnetization data in order to investigate its zero magnetic field magnetic behaviour along with its behavior on increasing the magnetic field.. Finally, attention has been drawn to show magneto-electric and magneto-dielectric couplings along with several intriguing observations in ceramic CTO. Following paragraphs describe magnetic behaviours at low magnetic field, their probable structural correlation and the presence of short range ferromagnetic interactions in CTO.

3.3.2. Results and Discussion

3.3.2.1. Low field DC Magnetization Study

Fig. 3.21 shows a representative low field (100 Oe) ZFC and FC magnetization curves (5 K to 80 K). No anomaly has been observed for $T > 80$ K, in agreement with literature. Starting from high temperature side, one can easily see a strong bifurcation between ZFC and FC curve at ~ 60 K, followed by various kinks below 60 K. In literature, these kinks are considered as magnetic transitions for CTO.⁷⁵⁻⁸⁰ To have an exact value of the kink, derivative (either first order or second order) with respect to temperature has been taken. These kinks are marked with arrows (see Fig. 3.21). In addition to the faint anomaly at ~ 16 K, we observe four main magnetic

transitions at around 34 K, 26 K, 21 K and 17.4 K (as shown by second derivative, the inset of Fig. 3.21), in agreement with single crystal studies.⁷⁵⁻⁸⁰ The bifurcation observed in ZFC and FC will be discussed in next paragraphs. As mentioned above (about the issue of five magnetic transitions), we show all the magnetic transitions (observed separately by various groups) in our single phase ceramic CTO.

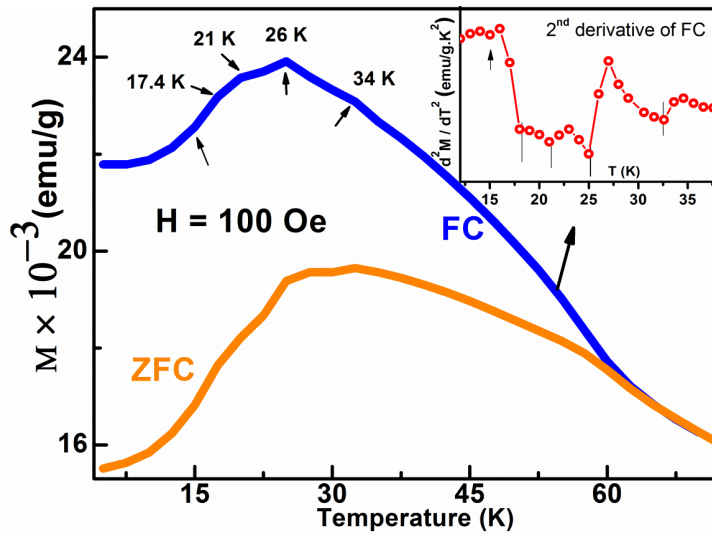


Fig. 3.21. ZFC and FC Magnetization vs temperature curves taken under 100 Oe. Inset shows the 1st derivative of FC curve.

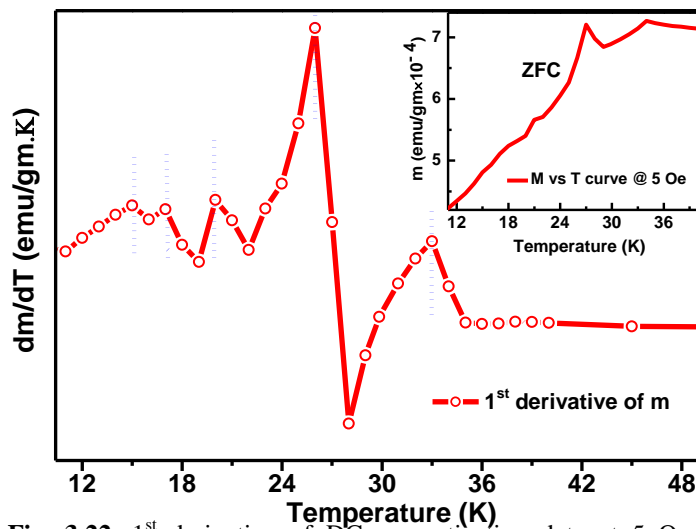


Fig. 3.22. 1st derivative of DC magnetization data at 5 Oe (shown in the inset), which shows clear signature of all magnetic transitions, especially at 16 K.

As discussed earlier, we see all the five magnetic transitions in our samples, in low magnetic field magnetization data. We show ZFC M vs T data along with the first derivative for an applied magnetic field of 5 Oe, in the inset and the main panel of Fig. 3.22, respectively. The ZFC and FC M vs T data along with second derivative for 100 Oe are also shown in Fig. 3.21. From Fig. 3.21, one could see a clear transition at 16 K (along with other four), which is also seen in Fig. 3.22. Through Figs. 3.21 and 3.22, we have not only validated our synthesis route for CTO sample but also observed all the magnetic transitions reported earlier for single crystals, by various groups. In the following, discussion on the observance of multiple magnetic transitions in CTO has been given.

Looking the data from high temperature side, the transition at ~ 34 K, also observed by Hudl et al. and Her et al. on their single crystal sample, is intrinsic to ceramic CTO.⁷⁷⁻⁷⁸ The remaining successive aforementioned low temperature magnetic transitions are studied by various authors on their single crystal as well as in powder samples using magnetic and neutron diffraction experiments.⁷⁵⁻⁸⁰ Only Wang et al.,⁸⁰ have discussed about multiple magnetic transitions observed in CTO and ascribed its possible origin to two magnetic networks Co1-Co4 and Co2-Co3-Co4 (detailed in next clause).⁸⁰ However, our observation of two possible additional Co-Co networks through structural analysis may provide structural origin for the additional magnetic transitions, as discussed in below.

3.3.2.2. Structural investigation for the insight into the magnetism

In order to understand multiple magnetic transitions, observed in CTO, we have carried out detailed structural investigations using VESTA (a 3D visualization) software¹³⁴ on Rietveld refined SXRD data. Rietveld analysis indicates that ceramic CTO adopts monoclinic crystal structure with C2/c space group as reported earlier⁷⁴⁻⁸⁰. A comparative table, consisting of lattice

parameters of CTO by various groups⁷⁴⁻⁸⁰ including our results, is presented in section 3.1. CTO exhibits complex magnetic behaviour at very low temperatures. Based on Rietveld refinement of neutron diffraction data, Wang et al.,⁸⁰ have reported the structure of CTO along [-101] direction by four layers A, B, C, D. Layers A and B represent Co3-Co2-Co5 (or 3-2-5) and Co1-Co4-Co4 (or 1-4-4) chains, respectively, where Co1, Co2, Co3, Co4 and Co5 represent crystallographically distinguishable Co atoms. Layers C and D can be obtained by a translation of A and B chain, respectively by $(a/2, b/2, 0)$. CTO unit cell can be obtained by translation of block or A, B, C, D layers along a-axis. Other layers (C and D) have not been mentioned further, neither their contribution to magnetic behaviour nor their assignment.⁸⁰ The authors have proposed that layer B possessing zig-zag Co1-Co4-Co4 chains, consist of IC moments, whereas layer A consists of simple AFM moment. Based on these results, the authors assigned IC transition at 26 K to zig-zag chain in layer B (1-4-4) and layer A (2-3-5) to second transition at ~ 18 K. However, their zero magnetic field phase diagram of CTO clearly shows four magnetic transitions below 30 K i.e. at 26 K, 21 K, 18 K and 16 K.⁸⁰ This suggests that networks corresponding to remaining magnetic transitions need to be identified. Therefore, we have made an attempt to identify other networks using SXRD to get insight into the origin of low temperature multiple magnetic transitions.

Fig. 3.23 shows a cross sectional (\perp to b axis) view of CTO structure, as obtained using VESTA tool based on Rietveld refined structure. Oxygen anions are not shown, for clarity following Wang et al.,⁸⁰ The interconnecting medium (oxygen) ions along with Co ions based chains / layers can be viewed easily through Fig. 3.23 and by layers A, B, C and D. The first two (A and B) layers show the reported Co-Co networks, while the third and fourth (C and D) layers show the additional ones. These are 2-3-5 (A), 1-4-4 (B), 2-3-4 (C) and 1-5-5 (D). As can be seen from

Fig. 3.23, layers A and B show the same chain as A and B as reported by Wang et al.,⁸⁰. The other two networks observed in the present work are very similar to A and B, but with Co4 (i.e. 2-3-4) and Co5 (i.e. 1-1-5) cations, which are crystallographically in octa- and tetrahedral coordinations, respectively. It is worth mentioning here that Wang et al., have not considered the pentahedral geometry (of Co3) and its possible implications to magnetism at all. These observations of layers like structure are in agreement with Wang et al.,⁸⁰. However, looking the structure from perpendicular direction, we find two additional chain (marked as C and D in Fig. 3.23).

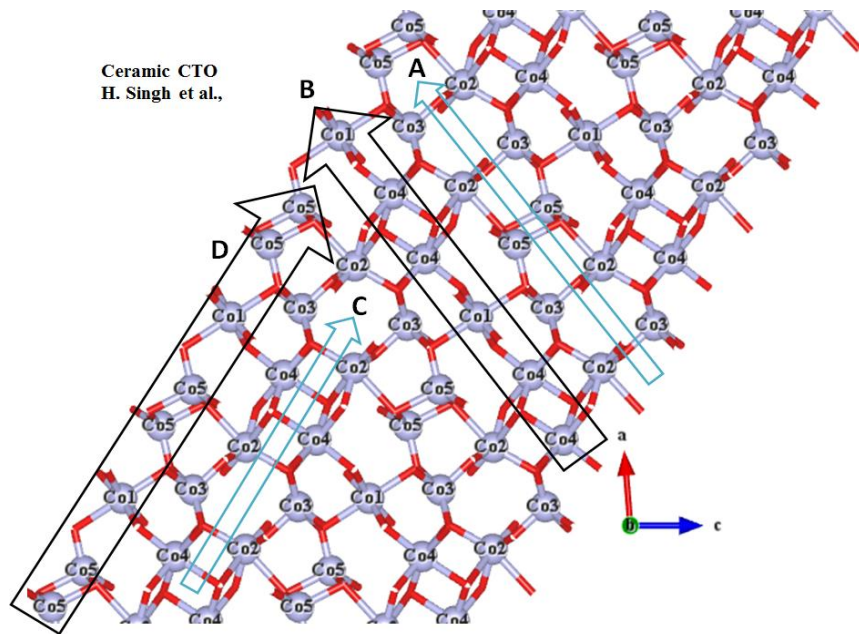


Fig. 3.23. Schematic drawing of the proposed Co-Co spins arrangements, for our ceramic CTO,⁹⁶ through layer A, B, C and D, respectively. These layers are Co2-Co3-Co5 (a), Co1-Co4 (b), Co2-Co3-Co4 (c) and Co1-Co5 (d), respectively. The Co ions lie in the ac plane, as in the earlier case of Wang et al.,⁸⁰

To validate our observation of two additional networks, we have compared our results with the reported structure of single crystal CTO.^{74,80} For this, we have generated the network like structure using VESTA from CTO.cif file.^{74,80} The obtained network is shown in Fig. 3.24. A comparison shows the presence of all the four networks in single crystal as well, validating our

observation. Therefore, our detailed structural analysis provides an origin for the observed multiple magnetic transitions in CTO at lower temperatures.

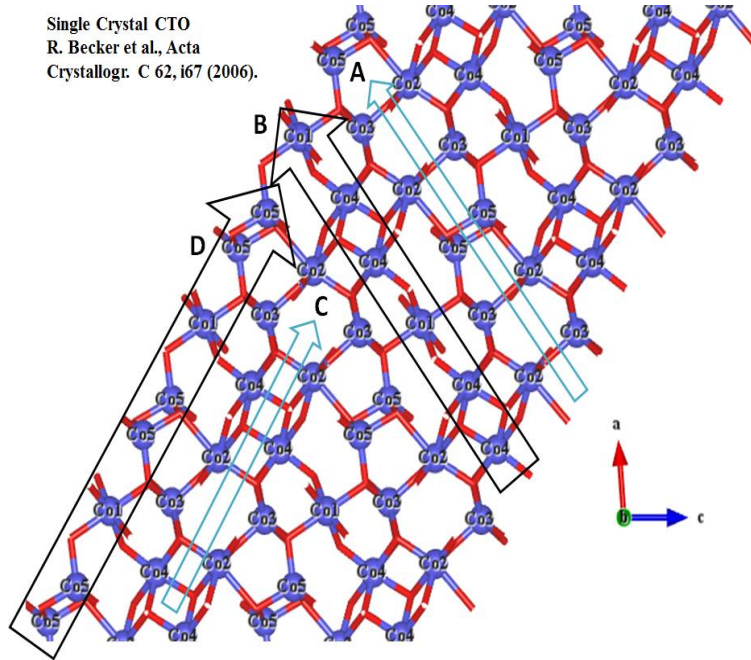


Fig. 3.24. Similar schematic drawing of the proposed Co-Co spins arrangements, for single crystal CTO⁸⁰ through layer A, B, C and D, respectively. These layers are Co2-Co3-Co5 (a), Co1-Co4 (b), Co2-Co3-Co4 (c) and Co1-Co5 (d), respectively.

Further, in the network 1-4-4, both the Co ions are in octahedral configurations, whereas in 1-5-5, Co5 is in tetrahedral. Similarly, 2-3-5 network consists of octa, penta, tetrahedral, whereas, 2-3-4 network consists of octa, penta, octahedral coordination. Also, in all the networks, Co-Co bond distances ($\sim 3 \text{ \AA}$) are much larger compared to Co-O distances ($\sim 2 \text{ \AA}$). Only Co5-Co5 ($\sim 2.75 \text{ \AA}$) or even Co3-Co4 ($\sim 2.85 \text{ \AA}$) pairs have lower bond lengths, which possibly makes these as a source for direct exchange. Rest of the bond lengths are $> 3 \text{ \AA}$, leading to a strong case for super-exchange or double exchange through oxygen. Furthermore, we observe typical bond angles of $\sim 90^\circ$ and 110° for Co4-O-Co4 and Co5-O-Co5, respectively, whereas, 105° to 130° for Co2-Co3-Co5 and 80° to 125° for Co2-Co3-Co4 networks. Accepted values of bond angles (TM-

O-TM) for AFM and FM interactions are 180° and 90° , respectively. The bond length must be as small as possible.²⁹⁻³⁰ Several reports²⁹⁻³⁰ indicate different values of bond angles, compared to the ones mentioned above. Hence, bond lengths and angles corresponding to these networks indicate various possible interactions, which further corroborate the observed complex magnetic structure.

Therefore, the presence of Co in five different polyhedral geometries with such large varieties of bond lengths and bond angles may lead to the observance of different crystal fields, which may contribute differently to the magnetic behaviour (as discussed in Chapter 1). Hence the observed complex magnetic ion networks may be responsible for the complex magnetic structure as well as multiple magnetic transitions in CTO. One of the implications of such complications in the magnetic behaviour is the observation of short range FM interactions in CTO, which is described in forthcoming paragraphs.

3.3.2.3. Bifurcation between FC and ZFC magnetization curves

Herein, nature and cause for the bifurcation at ~ 60 K between FC and ZFC magnetization curves (see Fig. 3.21) of ceramic CTO are discussed. We first establish FM interactions and then its short range nature. In general, this feature (bifurcation) may arise due to several reasons¹⁶⁴ including the opening up of hysteresis loops and a corresponding non-zero value for the coercivity (as temperature falls).¹⁶⁵ It may also possibly be due to the presence of FM clustering, termed as the Griffiths like FM clusters with nano-size domains.¹⁶⁶⁻¹⁷¹ The coexistence of magnetic interactions of opposite nature leading to complex magnetic behaviour has been seen in numerous magnetic systems.¹⁷¹⁻¹⁷⁷ Griffiths phase (GP) presents the competition between the FM and AFM interactions under random potential (due to disorder).¹⁶⁸⁻¹⁷⁰ Disorder sets in such a way that different values of exchange coupling (J) may be assigned randomly to different sites of the

lattice. This causes existence of short-range ordering of FM clusters when $T_C < T < T_{GP}$ (here, T_C represents the FM Curie temperature, whereas, T_{GP} is the Griffiths temperature at which the FM clusters begin to nucleate). The intermediate regime is known as GP. The Hallmark of GP is a sharp downturn in the inverse magnetic susceptibility data.¹⁶⁸⁻¹⁷⁰ This downturn in the behaviour of χ^{-1} (as a function of temperature) is an important observation that distinguishes GP from smeared phase transition because, the later gives rise to an upward curvature in χ^{-1} vs T above T_C , deviating from CW law.¹⁶⁸⁻¹⁷⁰ The softening (or disappearance) of the downturn in χ^{-1} vs T curve, with the increase in magnetic field is another typical signature of GP. The basic characteristic of GP regime is that above T_C there exists finite but nano size clusters with FM correlated spins.¹⁶⁶⁻¹⁷⁰ One of the possible causes for the appearance of FM clustering in AFM matrix is $Co^{2+} - O - Co^{3+}$ network, which may result in FM correlations. One may attribute this FM correlations to weak short range type as the long range FM $Co^{2+} - O - Co^{3+}$ networks are found less favorable from our first principles simulations leaving a possibility of local FM clustering (see section 3.2).^{96,163}

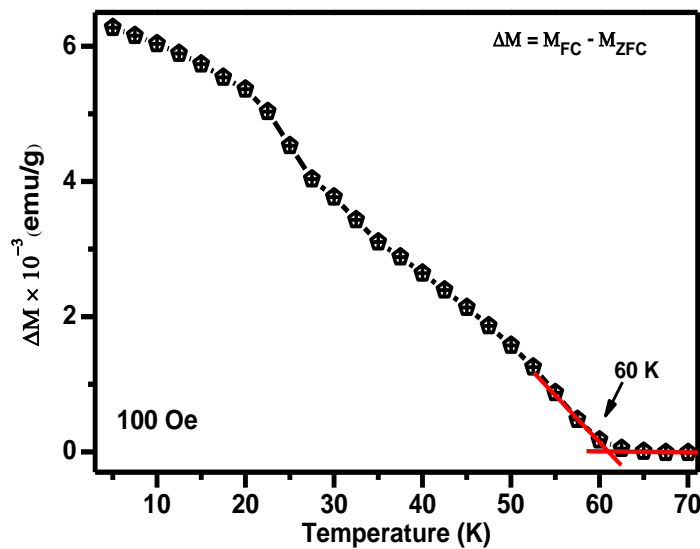


Fig. 3.25. It shows the magnetization difference of the corresponding FC and ZFC mode.

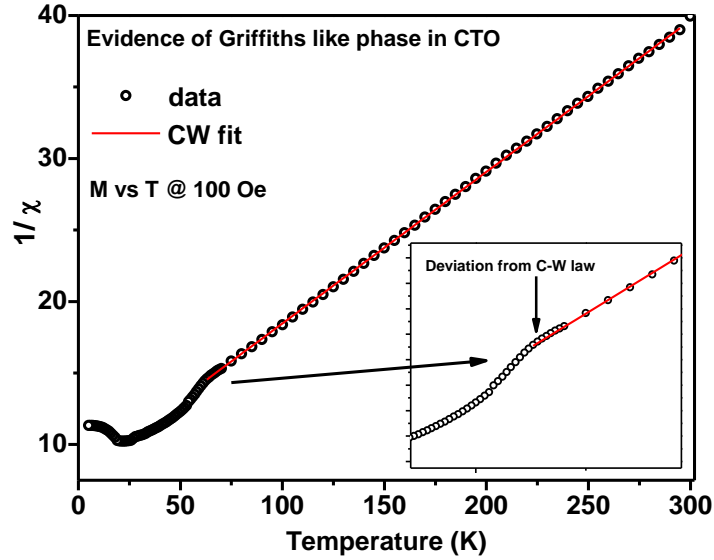


Fig. 3.26. Thermal dependence of inverse susceptibility (H/M) data of ceramic CTO taken at magnetic field of 100 Oe.

To elaborate the evidence of short range ferromagnetic correlations, we present the magnetization difference curve¹⁷⁸ and the down turn in the inverse susceptibility data¹⁶⁶⁻¹⁷⁰. These two curves are shown in Figs. 3.25 and 3.26, respectively. Magnetic hysteresis (which closes at higher fields ≥ 1000 Oe) at 300 K and 5 K are also plotted in Fig. 3.27. We plot the power law behaviour of $\chi^{-1} = (T-T_C^R)^{1-\beta}$, where we find $0 < \beta < 1$ and T_C^R (random ferromagnetic Curie temperature) = T_N , which is another characteristics of GP. The β values (see Fig. 3.28) for paramagnetic (β_{PM}) and GP (β_{GP}) phases are 0.003 and 0.342, respectively. This value of β_{GP} correspond to FM correlations, in agreements with our earlier first principles calculations (see section 3.2).^{96,163} FM interactions are also visible from the temperature-dependent difference between FC and ZFC magnetization ($M_{FC}-M_{ZFC}$) curves.¹⁷⁸ Fig. 3.25 shows $\Delta M (=M_{FC}-M_{ZFC})$ vs T curve taken at 100 Oe. The ferromagnetic characteristic transition temperature T_{FM} may be obtained by taking derivative of ($M_{FC}-M_{ZFC}$) with respect to temperature. The difference advantageously eliminates para- and diamagnetic contributions and indicates the presence of

hysteresis (if $\Delta M \neq 0$) leading to FM correlations.¹⁷⁸ However, this FM component appears only at very low fields and increases with decrease in magnetic fields, suggesting the presence of zero magnetic field magnetization. To investigate the same, we have plotted field dependent inverse susceptibility data for 100 Oe, 500 Oe and 1000 Oe in Fig. 3.29. We have re-plotted the M vs T and χ^{-1} for 100 Oe data for comparison.

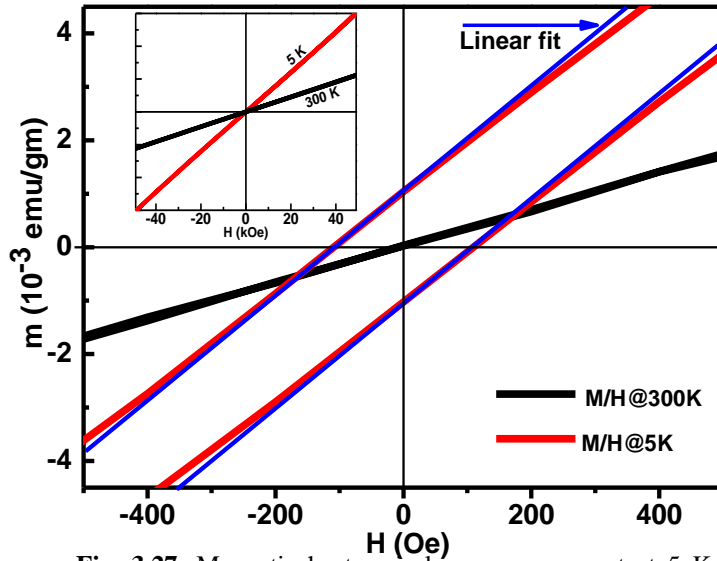


Fig. 3.27. Magnetic hysteresis loop measurement at 5 K and 300 K.

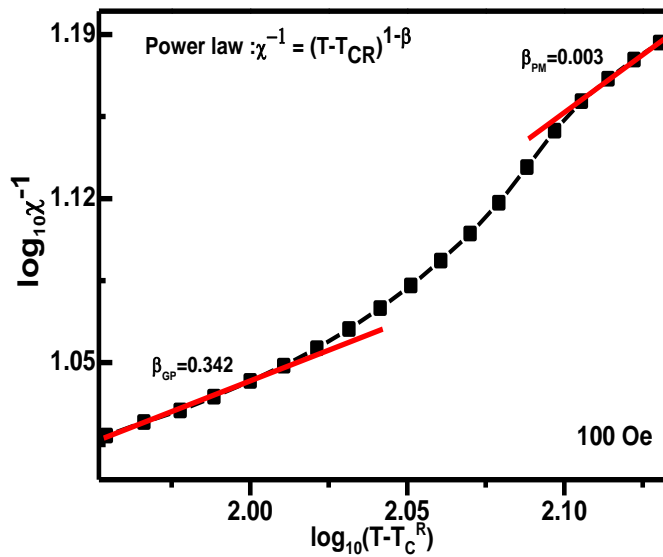


Fig. 3.28. This shows power law behavior of inverse susceptibility (H/M) data.

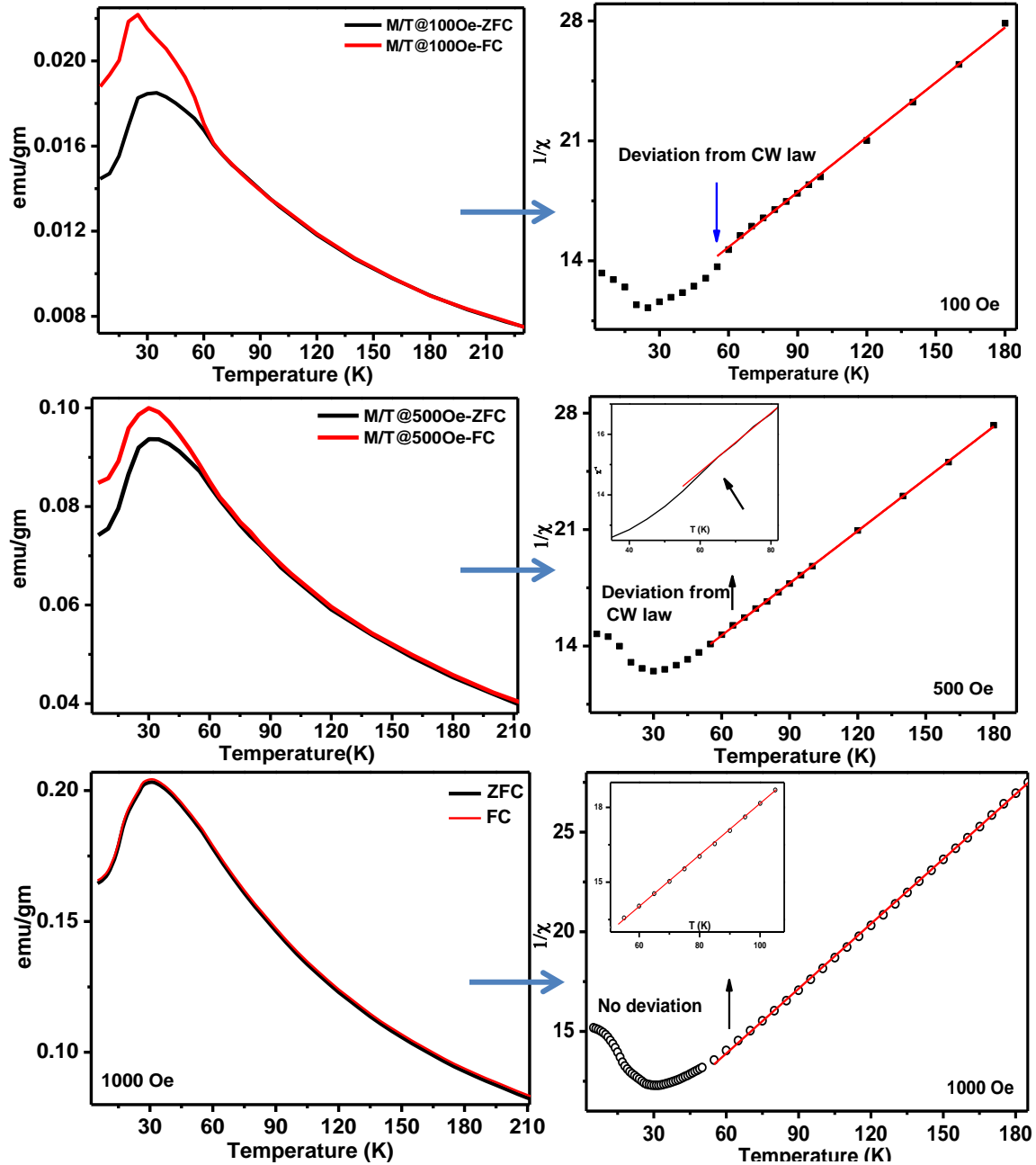


Fig. 3.29. Low field Magnetization data, both in ZFC and FC mode, taken subsequently at 100 Oe, 500 Oe and 1000 Oe. It clearly shows the suppression of deviation, as indicated by vertical arrows and insets.

It is clear from Fig. 3.29 that the deviation from CW behaviour, which is sufficiently strong at low field, suppresses with the increase in magnetic field. In the case of 500 Oe and 1000 Oe, we also plot enlarged χ^{-1} data to confirm suppression of the downturn. This feature has disappeared

at 1000 Oe data. This confirms GP.¹⁶⁶⁻¹⁷⁰ Therefore, we have evidenced ferromagnetic correlations in CTO, which is of short range nature and Griffiths like. We now discuss the investigation of magneto-electric and magneto-dielectric effects in CTO.

3.3.2.4. Investigation of Magneto-Electric (ME) and Magneto-Dielectric (MD) effects

To investigate ME and MD couplings in our ceramic CTO, we perform temperature and magnetic field dependent dielectric constant and pyroelectric current (and hence polarization) measurements. We have measured the dielectric constant, pyroelectric current and polarization in the magnetic fields of 0, 3 and 5 T. Fig. 3.30 shows dielectric constant as a function of temperature performed under above mentioned magnetic fields.

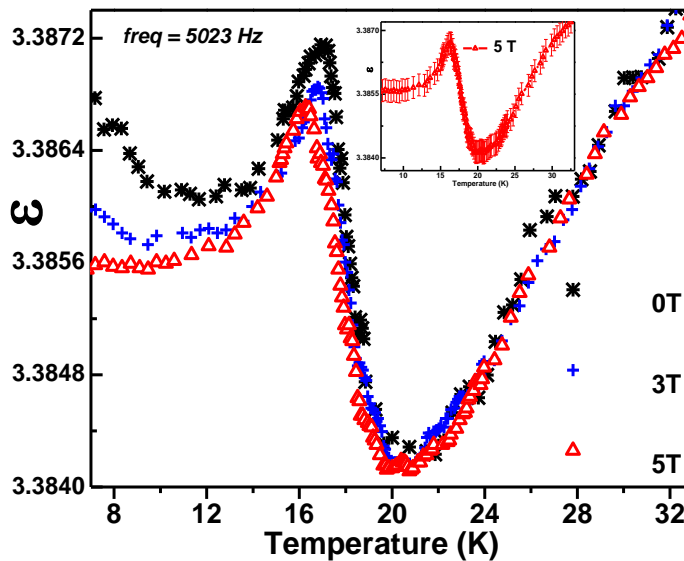


Fig. 3.30. Dielectric constant vs temperature profile at different magnetic fields. Inset shows the error bar of one of the representative dielectric data taken at 5 T.

In the inset of Fig. 3.30, we show dielectric constant as a function of temperature ϵ (T) with error bar. Before interpreting the data, we would like to mention few common features about dielectric constant. One normally observes lower value of dielectric constant for ceramic samples as compared to those for single crystals. This is because, in powder, one can measure the average

dielectric constant compared to a larger value measured in a preferred direction in single crystal. Also, as shown in Fig. 3.30, above 20 K, the dielectric constant for CTO shows a gradual decrease on cooling, typical feature of many insulating materials.¹⁷⁹ Below roughly 20 K, the dielectric constant increases with further cooling. The following features have been observed from Fig 3.30.

a) While cooling from room temperature to lower temperature, zero magnetic field dielectric constant data show a step anomaly at 18 K. It may be mentioned that temperature of dielectric anomaly, which may be taken as the first derivative of dielectric constant data with temperature just below 20 K, matches well with magnetic transition ($T_{N2} \sim 18$ K) in our sample, indicating a possible common origin for the two.

b) In literature¹⁸⁰, such sharp upturn in $\epsilon(T)$ has been correlated with the spontaneous polarization; e.g. in CuO and other type II multiferroic materials.¹⁸⁰ This leads us to infer that our sample should show spontaneous polarization below 18 K. Recent neutron diffraction data⁸⁰ also support our interpretation of spontaneous polarization below 18 K, quoting our work¹⁸¹ as an example.

c) The dielectric constant data on the application of magnetic fields show very interesting observations. Similar downturn is observed for $\epsilon(T)$ curves measured at 3 T and 5 T, well above 20 K, indicating no change in the dielectric constant data for $T > 20$ K.

d) Shift of T_2 ($\sim T_{N2}$) towards lower temperature below 20 K on the application of magnetic fields, confirm the magneto-electric coupling in CTO (see Fig. 3.31). The observation of lowering of T_2 with raising magnetic fields is also in accordance with the theoretical prediction by Toledano et al.,⁸⁰ applicable to single crystal. This may be an additional evidence for the correlation between T_2 in $\epsilon(T)$ curve and (T_{N2}) in $M(T)$ curve in CTO.

e) Following our magnetization measurement as a function of temperature at various magnetic fields, we show indication of Griffiths like phase, in addition to AFM majority phase (see section 3.3.2.3). Our dielectric measurements show decrease in the AFM transition temperature and also a decrease in magnitude of dielectric constant at high magnetic field. Both these are indications of AFM phase¹⁸²⁻¹⁸³.

f) Most importantly, we find dispersion in $\epsilon''(T)$ curve (i.e. reduction of the overall magnitude of dielectric constant below 18 K) as a function of applied magnetic field (see Fig. 3.31). We observe lower ϵ'' value for higher applied magnetic field for $T < 18$ K. This is an evidence of magneto-dielectric effect in CTO; being reported for the first time for this material.

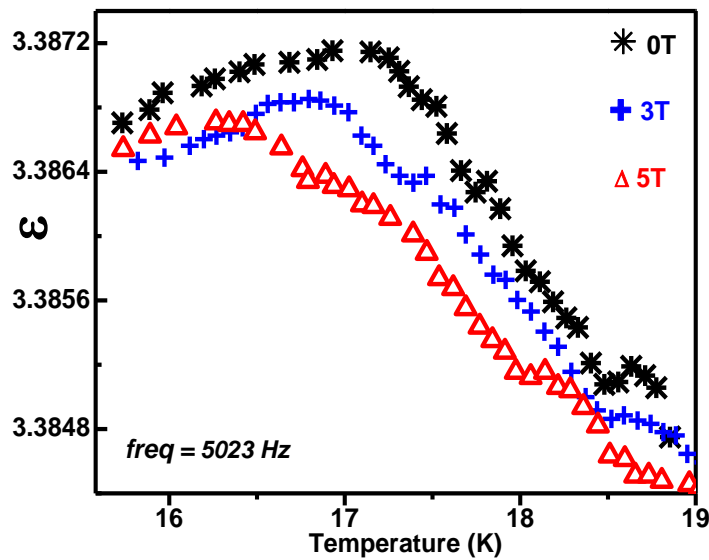


Fig. 3.31. Dielectric constant showing change in peak position towards lower temperature with the increase in magnetic field.

Furthermore, Figs. 3.32 and 3.33 show the thermal profile of pyroelectric current and derived polarization under 0, 3 and 5 T magnetic fields respectively. The pyroelectric current and corresponding polarization in the absence of magnetic field shows no observable anomaly within the experimental resolution. It may be noted that very well studied compound $\text{CaMn}_7\text{O}_{12}$, in

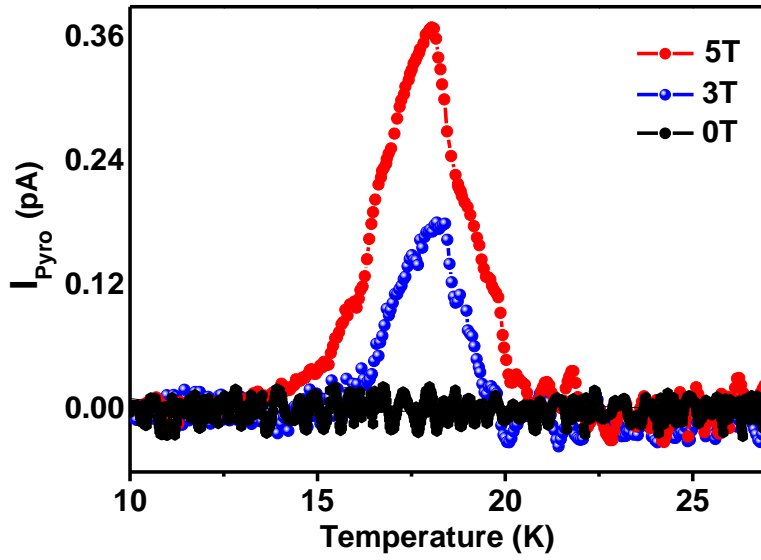


Fig. 3.32. Measured pyroelectric current as a function of temperature in the presence of 0, 3 and 5 T external field (poling field = 6.6 kV/cm).

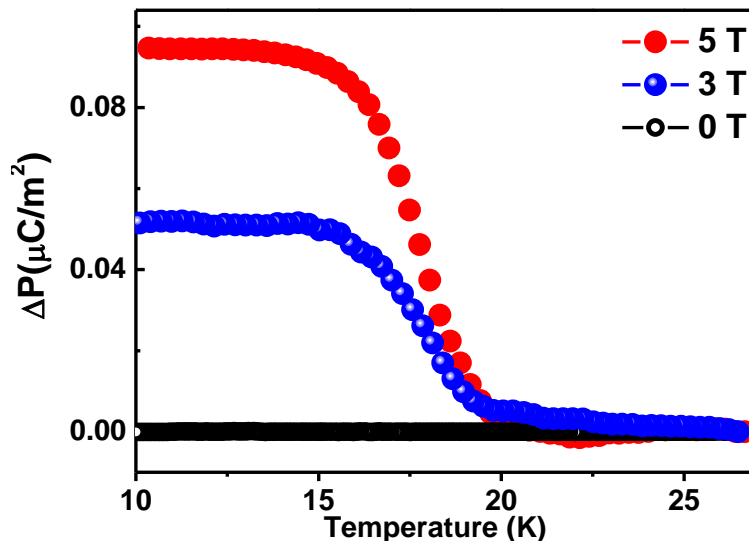


Fig. 3.33. Electrical polarization derived from pyroelectric current is plotted as a function of temperature in the presence of 0, 3 and 5 T external field.

single crystal form, exhibits polarization of $3000 \mu\text{C}/\text{m}^2$, whereas, in ceramic form its magnitude gets reduced by an order of magnitude to $\sim 300 \mu\text{C}/\text{m}^2$.¹⁸⁵⁻¹⁸⁶ In literature, this decrease in polarization (and hence dielectric constant) has been attributed to the ceramic nature of the

sample, as mentioned earlier in this chapter. It is worth mentioning that the emergence of pyroelectric current, polarization and sharp upturn in dielectric constant at identical temperatures is observed where magnetization ~ 18 K also shows downturn. Therefore, observable magnitude of ferroelectric polarization is perhaps a consequence of rearrangement of spin ordering due to the magnetic field. The ferroelectric phase transition temperature gradually shifts towards lower temperatures whereas the degree of polarization increases with application of magnetic field, which signifies magnetically coupled ferroelectricity. This is also observed in the temperature dependence of electronic specific heat (C_p) and ac magnetic susceptibility (χ') data at various magnetic fields by Her et al.⁷⁸ on their single crystal CTO. The magnitude of pyroelectric current and derived polarization increases monotonically with the strength of magnetic field. These observations i.e. opposite response of dielectric constant and polarization to magnetic fields (in our ceramic CTO) not only follow the same polarization behaviour as that of single crystal CTO studies,⁷⁷ but also show the similar trend as in the well-studied compound $\text{Ni}_3\text{V}_2\text{O}_8$.^{184,187} This may also suggest the possible origin for the observance of electrical polarization in CTO. Further, our polarization measurements derived from the pyroelectric current measurements verify the upward turn in dielectric constant around the 18 K occurs at the cost of spatial symmetry inversion in the presence of magnetic field.

The following inferences may be drawn from the magnetic field dependent dielectric and pyroelectric measurements. The nature of magneto-dielectric behaviour presents a generic response of magneto-electric coupling in CTO. The systematic response of thermal profile of dielectric constant at 0, 3 and 5 T magnetic fields suggests that the magnetic ground state alone is sufficient to break the spatial inversion symmetry. A qualitative analysis of all the collective experimental results suggests that the magneto-dielectric effect is originated as interdependent

response of magneto-electric effect. The intriguing interplay of dielectric constant and polarization (as evidenced through magneto-dielectric and magneto-electric couplings) at magnetic transition temperature with the application of magnetic field, is a characteristics of type-II multiferroic. This is because in such materials, intrinsic spin ordering in inhomogeneous non-collinear magnet provides driving force to spontaneously break spatial inversion symmetry.²¹ Our combined analyses indicate magnetically broken inversion symmetry leading to a possible spontaneous polarization. According to the prediction by Toledano et al.,⁸⁰ and a requirement of type II MF,³⁵ spontaneous electric polarization is also accompanied by spontaneous magnetization in the same phase III (< 20 K). Very weak hysteresis loop at 5 K i.e. in phase III (see Fig. 3.27) confirms the presence of a weak ferromagnetism in our CTO. In the same phase, our dielectric constant data also shows the ferromagnetic correlations below 18 K. Our observations based on above measurements indicate that our ceramic CTO is strongly coupled type II multiferroic material.

3.3.3. Conclusions

Temperature dependent DC magnetization measured at low and high magnetic fields reveals complicated magnetic structures and signature of all the magnetic transitions, observed earlier in neutron diffraction studies, are also retained in our ceramic CTO. Synchrotron XRD based structural analysis indicates two additional possible magnetic (Co-Co) networks. At low temperatures, weak FM interactions are developed as also evidenced through very weak hysteresis. This behavior is because of Griffiths like ferromagnetic clusters of nano size domains. The measured dielectric constant exhibits a steep upward turn at around 21 K and a well-defined peaked structure at 18 K (T_2). On further lowering in temperature and applying magnetic field, T_2 (H) along with overall magnitude of ϵ (T) decrease with increasing magnetic field indicating

several unresolved observations like FM correlations in phase III and spin-phonon coupling leading to magneto-dielectric effect in CTO. This further supports strong coupling between electric and magnetic orders in CTO.

To conclude this chapter, single phase ceramic Co_3TeO_6 (CTO) is synthesized via conventional solid state reaction route by taking *off-stoichiometric* Co_3O_4 and TeO_2 and two step calcination in air. CTO structure crystallizes in monoclinic C2/c space group, which is understood as due to the formation of low symmetry CoTeO_4 intermediate phase. Spectroscopic characterizations using XANES and XPS show mixed oxidation state of Co (Co^{2+} and Co^{3+} , both in high spin), which can be due to wider variations in bond lengths and bond angles as elucidated using Rietveld refinement on structural data. The high spin states of both Co^{2+} and Co^{3+} is further supported by pre-edge XANES data, high field magnetization data (wherein CW fit gives higher magnetic moment as compared to that reported for single crystal CTO) and first principles *ab-initio* calculations. It has been established that possible charge imbalance due to different oxidation states of Co-ions may be compensated by Te-cation vacancies. Further, we have observed only two magnetic transitions ($T_{N1} \sim 26$ K and $T_{N2} \sim 18$ K) in high field magnetization data. This observation is in disagreement with low field DC magnetization data, which shows all the five magnetic transitions. This suggests CTO has complex magnetic structures at low magnetic field, which may be due to the fact that CTO possesses low symmetry structure. In addition, we observe bifurcation (~ 60 K) in the ZFC and FC magnetization curves at lower magnetic fields ($H < 500$ Oe) and its disappearance under higher (≥ 1000 Oe) magnetic fields, indicating possible zero magnetic field magnetization. Magnetic hysteresis (M vs H) data also shows very weak hysteresis loop at very low temperatures, which has been attributed to the presence of Griffiths like phase in CTO, suggesting short range FM nano domains in AFM matrix. Both FM

and AFM interactions can arise due to the mixed valence of Co leading to the network $\text{Co}^{2+}\text{-O-}\text{Co}^{3+}$ (normally favours FM interactions) and $\text{Co}^{2+}\text{-O-}\text{Co}^{2+}$ or $\text{Co}^{3+}\text{-O-}\text{Co}^{3+}$ (favours AFM interactions). Observance of multiple magnetic transitions is understood to have origin in the structure of CTO and is further correlated with the four structural networks observed. This is because, various polyhedral configurations of Co ions experience different crystal fields leading to their different electronic/spin configurations. This is in dis-agreement with the observation of only two networks reported in literature, based on their neutron diffraction data. Temperature and magnetic field dependent dielectric constant and polarization measurements show the possibility of spontaneous electrical polarization in CTO. The response of dielectric constant with magnetic field confirms the magneto-dielectric coupling. Our magnetic, polarization and dielectric measurements show spontaneous electrical polarization as well as spontaneous magnetization at low temperatures and hence a possible magneto-electric coupling. Also, combined dielectric, pyroelectric and polarization measurements suggest that the ground state of CTO may possess spontaneous symmetry breaking even in the absence of magnetic field.

Chapter 4

Mn doped Co_3TeO_6

In the last chapter, we have presented a detailed investigation on CTO, a type II MF, which shows the ME coupling at very low temperatures. In this chapter, we attempt to enhance the temperature, by doping CTO system with Mn. From fundamental as well as application points of view, investigations are guided to achieve two major goals in MF materials; increasing the coupling among various ferroic orders and enhancing the transition temperature below which the coupling strength is significant.^{2-3,7-16} In addition, the understanding the mechanism of MF coupling is also important. Doping an existing MF with a suitable dopant as well as designing and developing new MF materials are major routes to attain the above mentioned goals.¹⁸⁸⁻¹⁸⁹ Undoubtedly, controlling the coupling of various ferroic orders and enhancing the transition temperature to room temperature are of immense interest.¹⁹⁰ Enhancement of these couplings at higher temperatures may possibly be achieved by various ways like internal chemical pressure and external perturbations etc.¹⁹¹⁻¹⁹³ Most of the existing materials show aforementioned couplings at very low temperatures.^{77-80,96}

With an aim to developing new functionalities in Co_3TeO_6 (CTO), we have partially replaced Co in CTO by two nearby transition metals: Fe and Mn. Substitution of Fe in CTO does not result in single phase material due to unstable structure of Fe_3TeO_6 .¹⁹⁴⁻¹⁹⁵ Our initial synthesis (not discussed further) and structural characterization (along with literature) of Fe doped CTO show the formation of Fe_2TeO_6 , a magneto-electric material, which is not a multiferroic.¹⁹⁴⁻¹⁹⁵ On the other hand, Mn doped CTO (CMTO) results in a single phase solid solution of CTO and MTO after a particular Mn concentration.^{91-92,100-102} For lower Mn concentration, two phase compound is observed.¹⁰⁰ As discussed in the previous chapter, CTO is low symmetry ($C2/c$) type II MF material, which shows complex magnetic structure with a sequence of AFM transitions at very low temperatures.^{77-80,95-99} MTO, on the other hand,

crystallizes in higher symmetry ($R\bar{3}$) and is a type I MF material, which exhibits AFM transition at approximately the same temperature as that of CTO.¹⁹⁶ MTO and CTO show AFM transitions at around 23 K and 26 K, respectively.^{77-80,198} In contrast, Mn doping in CTO enhances the AFM transition temperature to ~ 40 K (45 K in for our sample: at the same Mn concentration); even when the AFM transition temperatures of the end members are lower.^{91-92,100-101}

Rest of the chapter is organized in two sections. The preparation and characterization of $\text{Co}_{3-x}\text{Mn}_x\text{TeO}_6$ (CMTO); ($0 < x \leq 2$) solid solutions have been discussed in section 4.1. The section describes structural and spectroscopic characterizations of CMTO. The results obtained from these characterizations for CMTO samples are used to explain interesting magnetic properties, as discussed in section 4.2.

4.1. Structural and Spectroscopic Characterizations on $\text{Co}_{3-x}\text{Mn}_x\text{TeO}_6$

In this section, we describe growth of $\text{Co}_{3-x}\text{Mn}_x\text{TeO}_6$; ($0 < x \leq 2$) solid solutions using two step solid state reaction route as described for CTO. Synthesized CMTO in an optimized condition are characterized using SXRD and XANES techniques.

4.1.1. Introduction

As discussed above, present section of this chapter explores effect of Mn doping in CTO on structural and spectroscopic properties, leading to the anomalous magnetic behaviour in CMTO. Mn substitutions on Co sites in CTO may have several effects like **(i)** different ionic radii of Mn as compared to Co can modify the effective orbital overlap between the transition metals and thus modifying the exchange integral, **(ii)** probable mixing of variable oxidation states of Mn/Co may also influence the effective magnetic moment and magnetic interactions and **(iii)** chemical pressure may change electronic configuration, inter-atomic distances and local environment. As a result, changes in TM – oxygen (Co/Mn-O) bond lengths and their respective angles (TM-O-TM) along with variable oxidation states of Co and Mn greatly influence the magnetic properties of the compound.¹⁰⁰ Doped materials show properties quite different from the parent compounds. For example, interesting features like insulator-metal and FM-AFM transition are observed in the intermediate compounds $\text{LaMn}_{1-x}\text{Co}_x\text{O}_3$ ¹⁹⁷⁻¹⁹⁸ (absent in the end members). This led us to investigate $\text{Co}_{3-x}\text{Mn}_x\text{TeO}_6$ solid solutions. Several studies on various other solid solutions have also been reported e. g., $\text{Mn}_{3-x}\text{Cd}_x\text{TeO}_6$.¹⁹⁹⁻²⁰¹ However, the observance of combined ferromagnetism at higher temperature and enhanced anti-ferromagnetism at lower temperature has not been reported so far. The main contribution of the present work is the observance of high temperature (185 K) FM interactions and low temperature (45 K) AFM interactions in these solid solutions. We have also provided the explanation for the experimental observations, based on

structural and spectroscopic measurements. To address issues discussed above, we have carried out room temperature SXR and XANES studies. The detailed structural as well as spectroscopic studies provide information to understand and explore its probable correlation with observed as well as reported anomalous magnetic behavior of $\text{Co}_{3-x}\text{Mn}_x\text{TeO}_6$ ($0 \leq x \leq 2$) solid solutions.

4.1.2. Results and Discussion

4.1.2.1. Synchrotron X-ray diffraction study

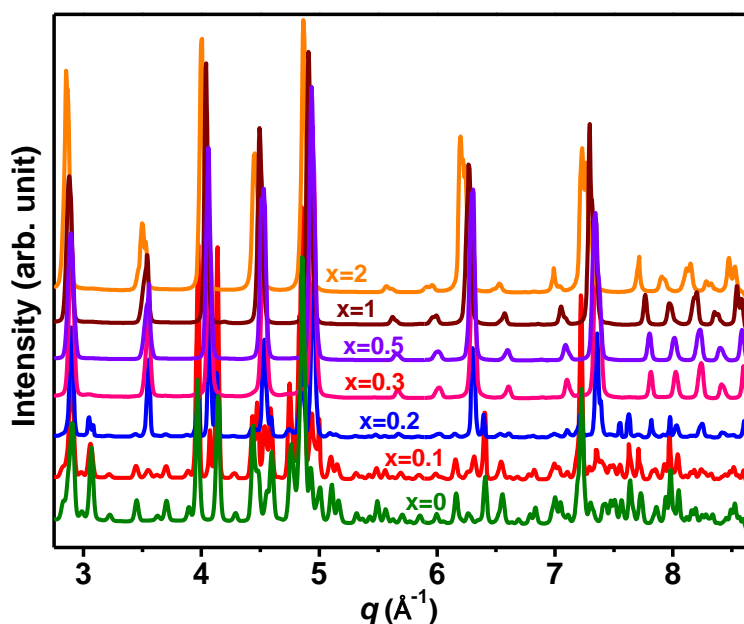


Fig. 4.1. Synchrotron X-ray diffraction patterns of $x = 0.0, 0.1, 0.2, 0.3, 0.5, 1$ and 2 compositions possessed either mixed ($C2/c$ and $R\bar{3}$) symmetry ($0.1, 0.2, 0.3$) or pure $R\bar{3}$ symmetry ($0.5, 1.0, 2.0$). Here $x = 0$ corresponds to pure CTO ($C2/c$) phase.

Polycrystalline samples of $\text{Co}_{3-x}\text{Mn}_x\text{TeO}_6$; ($x = 0.0, 0.05, 0.1, 0.2, 0.25, 0.3, 0.4, 0.5, 1, \text{ and } 2$) have been synthesized via conventional solid state reaction route using Co_3O_4 , Mn_3O_4 and TeO_2 reactants. Synthesis procedure is given in chapter 2. Fig. 4.1 shows SXR patterns of $\text{Co}_{3-x}\text{Mn}_x\text{TeO}_6$ for $x = 0, 0.1, 0.2, 0.3, 0.5, 1.0, \text{ and } 2.0$ collected at room temperature. A closer look at

the SXRD patterns reveals that patterns of samples with composition $x = 0.1, 0.2$ and 0.3 have some extra peaks as compared to those for $x = 0.5, 0.8, 1.0, 2.0, 3.0$. A comparison of the diffraction patterns of present CMTO samples with reported patterns of end members CTO and MTO; reveals that the composition with $x = 0.1, 0.2$ and 0.3 may be in a mixed phase of CTO and MTO (i.e. mixed $C2/c$ and $R\bar{3}$ symmetries). In addition, the SXRD pattern of $Co_{3-x}Mn_xTeO_6$ with $x = 0.05$ (not shown in Fig. 4.1) shows very weak reflections of MTO ($R\bar{3}$) phase. But the concentration of $R\bar{3}$ phase increases very rapidly with the increase in x . For example, for $x = 0.25$ (or even $x = 0.4$) $R\bar{3}$ phase dominates (see Fig. 4.2). Similarly for $x = 0.4$, minor additional reflections have been observed (inset of Fig. 4.2). The inset of Fig. 4.2 clearly indicate the complete crystallographic phase transition at $x = 0.5$.

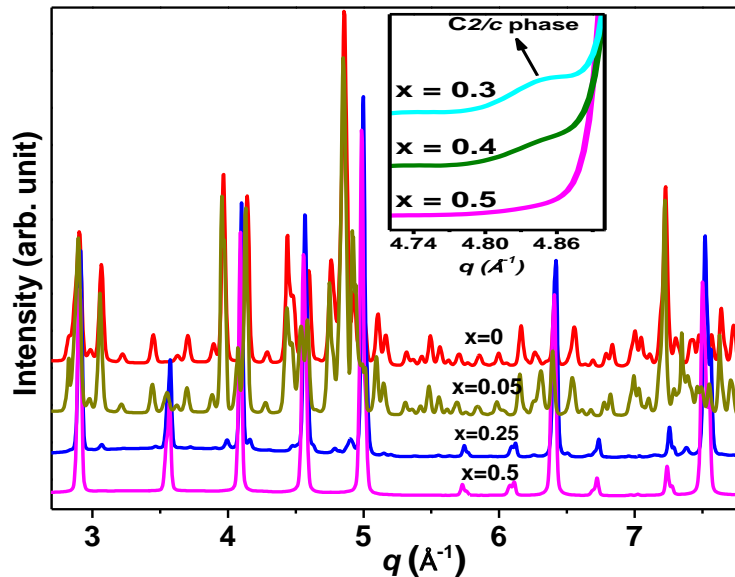


Fig. 4.2. Synchrotron XRD patterns of $Co_{3-x}Mn_xTeO_6$ with only $x = 0.0, 0.05, 0.25$ and 0.5 . Inset shows SXRD patterns for $x = 0.3, 0.4$ and 0.5 for q around ~ 4.8 , indicating mix phase behavior below 0.5 .

As mentioned earlier, ceramic CTO possesses monoclinic (space group $C2/c$) symmetry, whereas, MTO exhibits rhombohedral ($R\bar{3}$) symmetry.^{96,196} Visualized crystal structures of CTO

and MTO are presented in Fig. 4.3. While doping different concentrations of Mn in CTO, it has been found that for the lower doping concentration ($x < 0.5$), mixed phases of CTO (C2/c) and MTO ($R\bar{3}$) like symmetries co-exist.

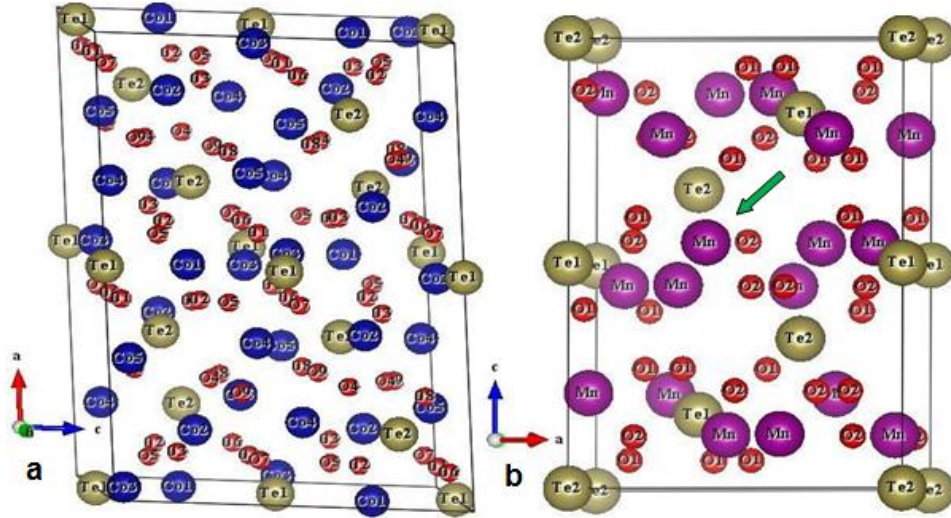


Fig. 4.3. (a) CTO, (b) MTO crystal structures with C2/c and $R\bar{3}$ symmetries, respectively. Red smaller circles represent oxygen atoms, blue and magenta circles represent Co and Mn atoms, respectively, while the large dark yellow circles show Te atomic positions (a, b, c axes are as indicated). Arrow in (b) shows a particular transition metal in oxygen environment.

In order to obtain the phase concentrations of $R\bar{3}$ and C2/c quantitatively, two phase Rietveld refinement has been done for all the samples with $x < 0.5$, where C2/c and $R\bar{3}$ phases with their (CTO and MTO) corresponding structural parameters have been used as initial guess.^{96,196} As discussed in chapter 2, during the structural refinement, a Pseudo- Voigt and linear interpolation function has been used to refine the peak shape and background, respectively. The instrumental broadening has been taken into account by refining SXRD pattern of LaB₆. Further, as discussed in chapter 3, Co in CTO occupies five different crystallographic sites; therefore Mn substitutions at Co site may have several possibilities of occupying a crystallographic site. On the other hand, MTO has comparatively simpler crystal structure (all Mn sites are equivalent).^{96,196} Two phase

Reitveld refinement is shown for the samples with $x = 0.1$ (Fig. 4.4 (a)), $x = 0.2$ (Fig. 4.4 (b)), $x = 0.25$ (Fig. 4.4 (c)), and $x = 0.3$ (Fig. 4.4 (d)). Two phase Rietveld refinement analysis shows the presence of $C2/c$ phase with percentage around 85%, 39% and 4% for $x = 0.1, 0.2$ and 0.3 , respectively in the mixed phase solid solutions.

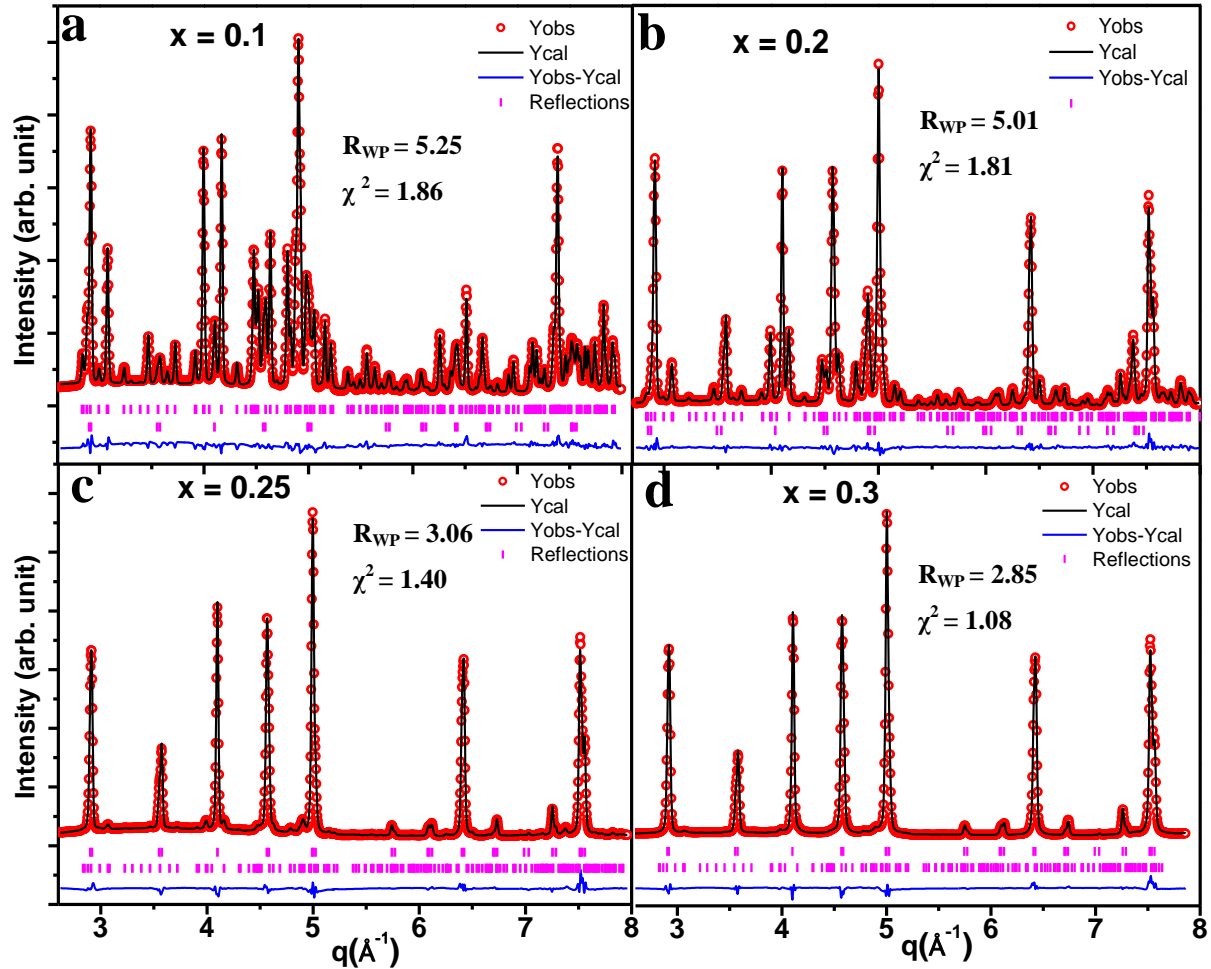


Fig. 4.4. Two phase Rietveld refinement for the composition $x =$ (a) 0.1, (b) 0.2, (c) 0.25 and (d) 0.3, wherein $C2/c$ and $R\bar{3}$ with their corresponding structural parameters have been taken as inputs. Red circle represent raw data, black solid line the Rietveld fit, blue vertical bar the Bragg reflections and zigzag magenta line the difference between observed and calculated intensities.

It is surprising that small ($< 17\%$) substitution of Co by Mn at A site, leads to the transformation of $C2/c$ (CTO) phase to $R\bar{3}$ phase. Even for smaller Mn substitutions, volume of $R\bar{3}$ phase is concentration disproportionate. Phase diagram obtained from Rietveld refinement (two phases

for $x < 0.5$ and single phase for $x \geq 0.5$, which is discussed in the next clause, indicates doping disproportionate concentration of $R\bar{3}$ phase for $x < 0.5$ (Fig. 4.4). Doping disproportionate amount of $R\bar{3}$ and $C2/c$ phase observed for $x < 0.5$ are due to the change in monoclinic phase to rhombohedral phase.²⁰²

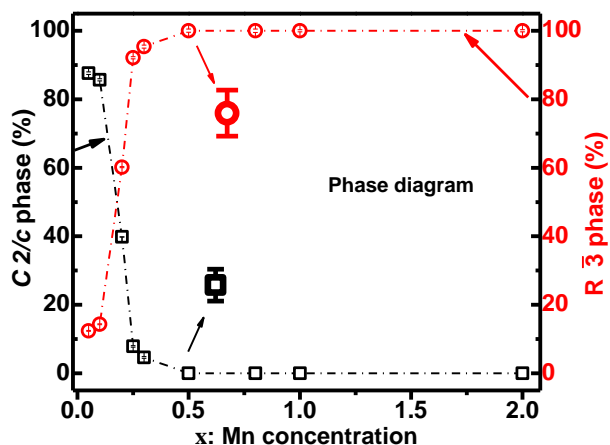


Fig. 4.5. Phase diagram obtained from Rietveld Refinement on the SXR data as a function of Mn concentration indicates mixed phases of $C2/c$ and $R\bar{3}$ for $x < 0.5$, while pure $R\bar{3}$ phase for $x \geq 0.5$. Enlarge data shows the representative error bar.

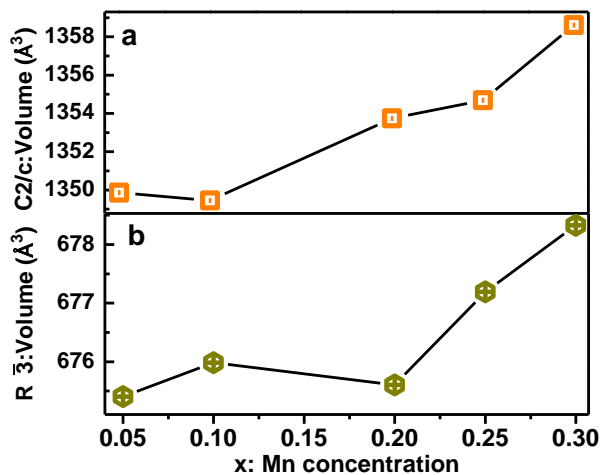


Fig. 4.6. (a) Variations of lattice parameters through volume per formula unit of $C2/c$ phase and (b) $R\bar{3}$ phase as a function of Mn concentrations for $x < 0.5$, error bars are within the symbols. Connecting solid lines are shown just to guide the eye.

Changes in the lattice parameters of both the phases with increasing Mn concentration for $x < 0.5$ have been estimated through the volume per formula unit (V/Z , Z is the formula unit). Volume per formula unit of $C2/c$ (CTO) and $R\bar{3}$ (MTO) phases are shown in Fig. 4.6, for $x < 0.5$. Here, Z is the ratio of number of atoms in the unit cell divided by number of atom in the chemical formula. The Rietveld refinement on SXRD data of mix phase samples shows overall increase in volume per formula unit (Fig. 4.6 (a) and (b)) with the increase in Mn concentration. However, the same shows a constant value till $x = 0.2$, followed by sharp increase beyond $x = 0.2$ for $R\bar{3}$ (Fig. 4.6 (b)). In literature, various considerations have been taken into account to explain the structural parameters variation on doping.^{104,203-205} One of the responsible factors can be different ionic radii of Mn and Co,²⁰³ which may result in internal stresses,¹⁰⁴ defects/impurities,²⁰⁴ and/or chemical pressure effect²⁰⁵. Above discussions suggest that a deeper understanding of the phase concentration variation of the mixed phase of $\text{Co}_{3-x}\text{Mn}_x\text{TeO}_6$ (for $x < 0.5$) is required. Present work emphasizes detailed studies on obtained single phase ($x \geq 0.5$) samples as discussed below.

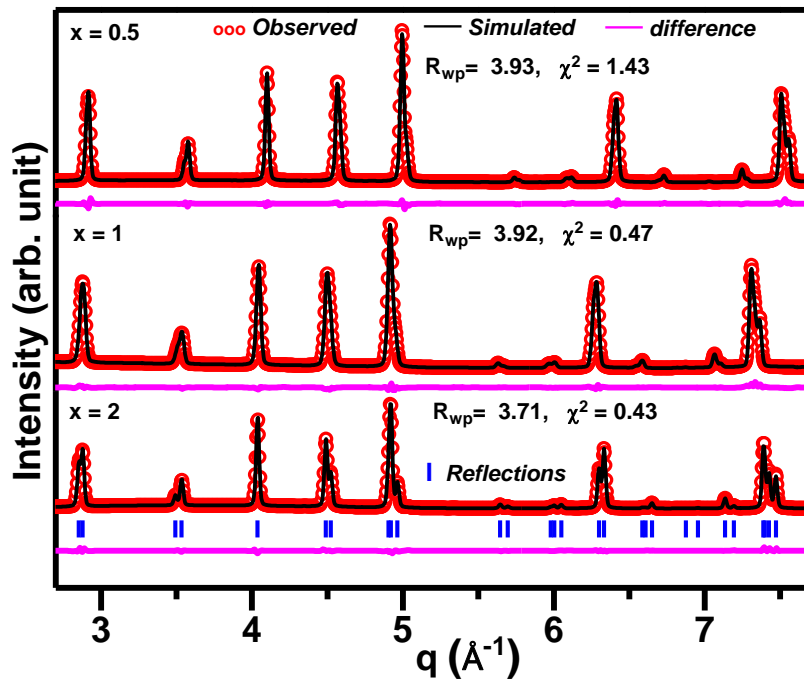


Fig. 4.7. Rietveld refinement of SXRD patterns for $x = 0.5, 1$ and 2 indicates the pure $R\bar{3}$ phase.

Table 4.1. Results of the Rietveld refinement of the crystal structure of the Mn doped CTO samples (here $x = 0.5, 1.0$ and 2.0 only) at room temperature using Synchrotron X-ray powder diffraction data using $R\bar{3}$ space group.

Phase		$x = 0.5$	$x = 1.0$	$x = 2.0$
a/Å		8.6398(3)	8.7117(1)	8.7964(3)
c/Å		10.4934(2)	10.5628(2)	10.6276(3)
Mn/Co	x/a	0.0413(1)	0.0421(3)	0.0409(1)
	y/b	0.2667(2)	0.26557(4)	0.2655(3)
	z/c	0.2101(3)	0.21215(3)	0.2119(2)
	B/A2	0.64(4)	0.18(3)	0.06(2)
Te1	x/a	0.0	0.0	0.0
	y/b	0.0	0.0	0.0
	z/c	0.5	0.5	0.5
	B	0.33(2)	0.06(3)	0.03(4)
Te2	x/a	0.0	0.0	0.0
	y/b	0.0	0.0	0.0
	z/c	0.0	0.0	0.0
	B	0.77(2)	0.03(2)	0.12(4)
O1	x/a	0.0323(3)	0.0295(1)	0.0289(2)
	y/b	0.2077(1)	0.1971(4)	0.1999(5)
	z/c	0.3983(1)	0.40034(2)	0.3996(2)
	B	0.37(2)	0.02(3)	0.38(3)
O2	x/a	0.1883(1)	0.1859(1)	0.1868(4)
	y/b	0.1667(2)	0.1614(1)	0.1601(1)
	z/c	0.1134(1)	0.1149(3)	0.1135(3)
	B	0.78(3)	0.21(2)	0.23(4)
Rp		3.93	3.92	3.71
Rwp		4.74	3.99	4.16
χ^2		1.43	0.47	0.74

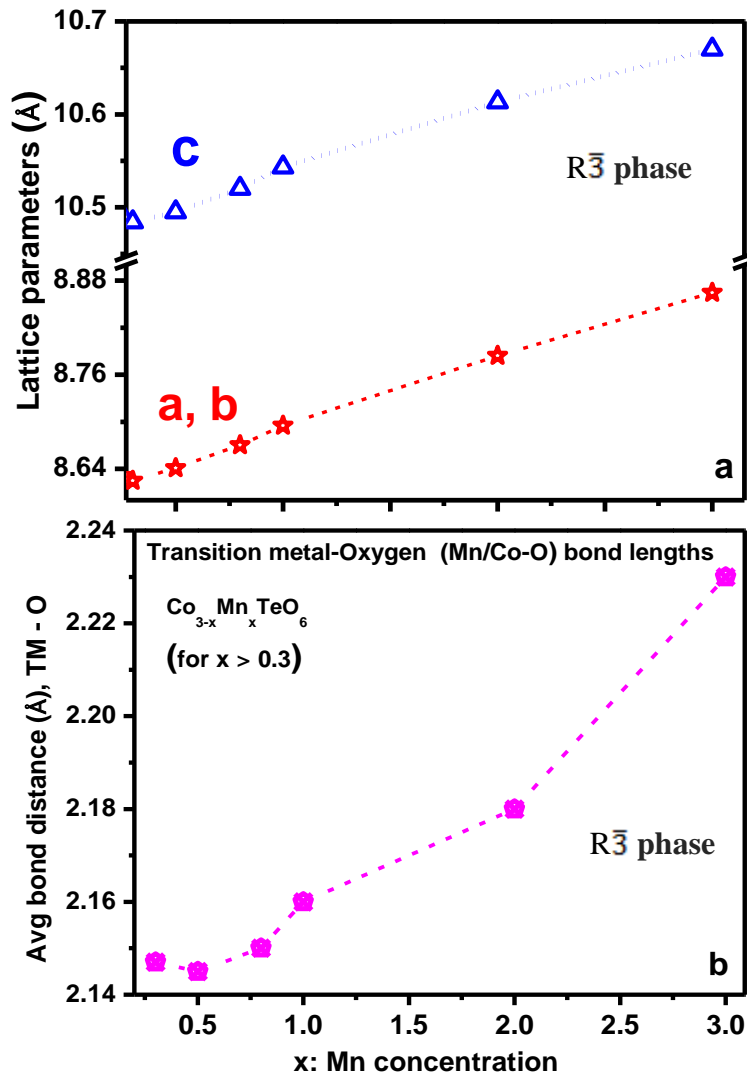


Fig. 4.8. (a) Variations of $R\bar{3}$ phase lattice parameters and (b) average transition metal-oxygen bond distances as a function of Mn concentration for $x \geq 0.5$ along with $x = 0.3$ within the error bars.

Rietveld refinement on SXRDR data of $\text{Co}_{3-x}\text{Mn}_x\text{TeO}_6$ with $x \geq 0.5$ reveals solid solutions with symmetry ($R\bar{3}$), the same as that of MTO. Representative experimental, calculated, and their difference SXRDR profiles are shown in Fig. 4.7 for $x = 0.5, 1$ and 2 . Rietveld refinement reveals octahedral Co/Mn cations sit at $18f$ Wyckoff site, assuming random distribution of Co/Mn. Both Te_1 and Te_2 occupy octahedral configuration $3b$ and $3a$, respectively. All the Rietveld refined parameters along with quality factors are included in Table 4.1 Rietveld refinement on samples

for $x \geq 0.5$ indicate almost linear increase in lattice parameters with increasing Mn concentration; attaining the values of MTO for $x = 3$ (shown in Fig. 4.8 (a)). Fig. 4.8 (b) shows variations in the average bond length as a function of Mn concentration (x) for single phase sample. Values corresponding to $x = 3$ has been incorporated from Ivanov et al., for comparisons.⁹¹⁻⁹²

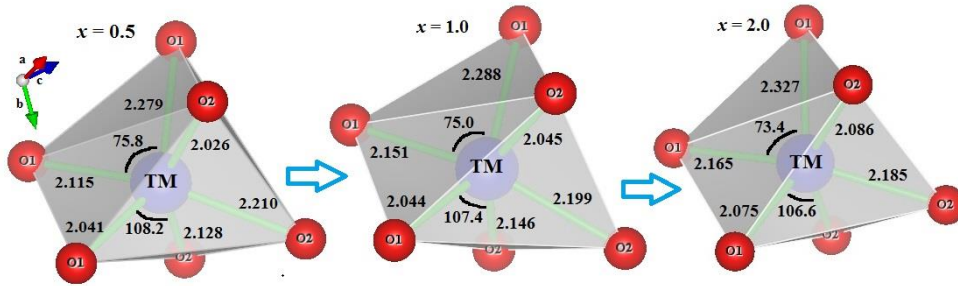


Fig. 4.9. Octahedral distortions for $x = 0.5, 1.0$ and 2.0 , obtained from Rietveld refined structure, clearly showing bond length (in Å) variations. Distortions in the bond distances can also be seen in the bond angles (O-TM-O) which vary from 75.8 to 73.4° in upper part and from 108.2 to 106.6° in the lower part as we go from $x = 0.5$ to $x = 2.0$. This particular TM has been shown by arrow in Fig. 4.3 (b).

On Mn doping, large changes (increase) in the lattice constants (about 0.15 \AA) has been observed. However, the change in lattice parameters is in agreement with those reported in various other compounds.⁹⁰⁻⁹⁴ In most of these systems, large change in lattice parameters has been attributed to large change in the ionic radii.,²⁰³ the apparent discrepancy, in this case, may also be solved by invoking mixed oxidation states of Mn and Co in $R\bar{3}$ phase (discussed below).

In order to investigate the effect of doping in the microstructure (bond length and bond angles) of CMTO, polyhedral investigation with the help of VESTA software on the Reitveld refined structure has been carried out. We plot the distorted octahedra depicting TM-O bond lengths and TM-O-TM bond angles as a function of Mn concentrations in Fig. 4.9. We observe considerably distorted Mn/CoO₆ octahedra, which are reflected in the variation of the TM-O bond distances as well as (O-TM-O) bond angles. On the other hand, Te-O octahedra (TeO₆; not shown here) are

less distorted. The TM-O bond lengths (Mn/Co-O) vary between 2.0414 (2) Å and 2.2793 (2) Å for $x = 0.5$ and 2.0751 (2) Å and 2.3273 (2) Å for $x = 2$. Co-Mn-O bond angles vary between 75.8° and 73.4° in upper part of the octahedra, whereas the same vary between 108.2° and 106.6° in the lower part, with increasing x from 0.5 to 2.0. Mn/CoO₆ octahedra seems to have been contracted as compared to those reported one by S. A. Ivanao et al.,⁹¹ as inferred from reduced bond lengths observed in this work.

The observation of contracted octahedra in these solid solutions, compared to those reported earlier, may be attributed to the presence of mixed valence TM ions (to be discussed later in this chapter). We argue that a more distorted octahedral in our samples may be because Co³⁺/Mn³⁺ - O bonds are smaller as compared to Co²⁺/Mn²⁺ - O bonds.¹⁴⁵ As the TM - TM bond lengths (Mn/Co-Mn/Co) range from 3.2171 (2) Å to 4.4522 (3) Å, which is quite large and thus may indicate that the exchange interaction is favored through nonmagnetic oxygen anions only.²⁹⁻³⁰ Smaller TM-O lengths increase the strength of super-exchange interaction which in turn increases the Neel temperature (T_N) (to be discussed in next section of this chapter). We observe bond angle variation in the upper part of the octahedra (shown in Fig. 4.9), proportional to Mn concentration, whereas, the variation in lower part is smaller. It may be mentioned that these bond length and angles are important factors for the interpretation of magnetic interactions in these solid solutions. The same values for $x = 3.0$ has been reported to be as 70.46° (upper one) and 104.0° (lower one).⁹¹ The other important parameters that influences the magnetic properties are the charge states and the spin states (high spin state for Mn and low/intermediate/high spin state for Co) of TMs. To study the average oxidation state of TMs, we have performed Mn and Co K-edge XANES measurements along with Te L₃ edge.

4.1.2.2. X-ray Absorption Near Edge Structure study

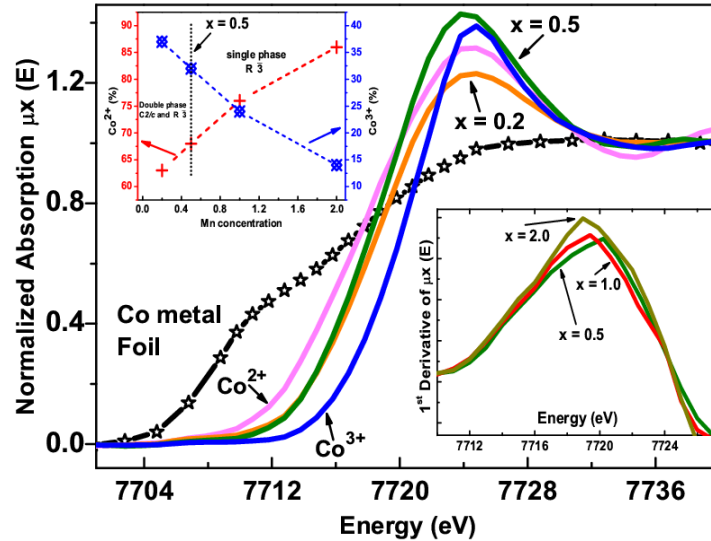


Fig. 4.10. Edge step normalized XANES spectra at Co K edge, which show gradual shift of main edge energy indicating increase of Co^{2+} concentration (right inset) with increase in Mn concentration using maxima in the first derivative of normalized absorption and the corresponding charge proportion (left inset).

XANES spectra at Co and Mn K-edges of $\text{Co}_{3-x}\text{Mn}_x\text{TeO}_6$ series have been measured along with standard references for Co [Co^{2+} (CoO), Co^{3+} (CoF₃)] and Mn [Mn^{2+} (MnCl₂), $\text{Mn}^{2.67+}$ (Mn₃O₄) and Mn^{3+} (Mn₂O₃)]. Edge step normalized XANES spectra for $\text{Co}_{3-x}\text{Mn}_x\text{TeO}_6$ series at Co K edge is shown in Fig. 4.10. Co K edge XANES spectra are similar for all the studied compositions. The spectra show a structured pre-edge region and the dominant peak called white line peak together with main rising edge in between the two.^{115,146} Here, we emphasize only the main edge of the XANES spectra, which is normally used for the estimation of average oxidation state of the sample. More details of interpretation of XANES spectra are given earlier (chapter 2). A close inspection of Fig. 4.10 reveals that the main edge energy corresponding to Co K edge for the solid solutions of $\text{Co}_{3-x}\text{Mn}_x\text{TeO}_6$ lie in between those of CoO and CoF₃ (see main panel, Fig. 4.10). It is also important to note that the peak positions (energy position) of 1st derivative

shifts towards lower energy with increasing x (right inset of Fig. 4.10), which suggests that *average* oxidation state gradually decreases with increasing Mn concentration. In order to estimate the relative concentration of Co^{2+} and Co^{3+} , we note main edge energy positions and use a simple linear combination formula as discussed earlier (chapters 2 and 3).

Quantitative phase composition analysis by LCF method on XANES data, using Athena software, has also been carried out.¹⁴⁸ Quantitative analysis using LCF and linear combination formula give the information about relative concentration of Co^{2+} and Co^{3+} in the corresponding solid solutions. For example, above mentioned combined analysis for $x = 0.2$ results in 37% Co^{3+} and 63% Co^{2+} with ~ 2.37 as an average valence state. The relative concentration is shown in left inset of Fig. 4.10. Further, with increasing $x \geq 0.5$ (only single phase), the relative ratio of $\text{Co}^{3+}/\text{Co}^{2+}$ start decreasing from ~ 0.4 for $x = 0.5$ to 0.2 for $x = 2.0$. However, maximum charge disproportion has been found at $x = 0.5$ (see left inset of Fig. 4.10). In a single phase material ($x \geq 0.5$), we observe that $\text{Co}^{3+}/\text{Co}^{2+}$ decreases monotonically with increasing x . This is in agreement with the average TM-O bond length data (in $R\bar{3}$ phase), which is found to be minimum at $x = 0.5$.

Similar to Co K-edge, edge step normalized XANES spectra for Mn K-edge (6539 eV) is shown in Fig. 4.11 (only a few XANES spectra presented for brevity). The shift in the main edge (rising edge) energy with doping concentration for selected samples is shown in the right inset of Fig 4.11. The left inset of Fig. 4.11 shows LCF fit for $x = 0.1$. It is clearly evident that the main edge energy for all the solid solution of $\text{Co}_{3-x}\text{Mn}_x\text{TeO}_6$ are red shifted (towards Mn^{2+} from Mn^{3+}) with increasing x (right inset of Fig 4.11). Qualitative analysis of the Mn K-edge shifts has been performed using main edge energies of standards reference samples such as MnCl_2 , Mn_3O_4 and Mn_2O_3 having formal valence states of Mn^{2+} , $\text{Mn}^{2.67+}$ and Mn^{3+} , respectively. Quantitative

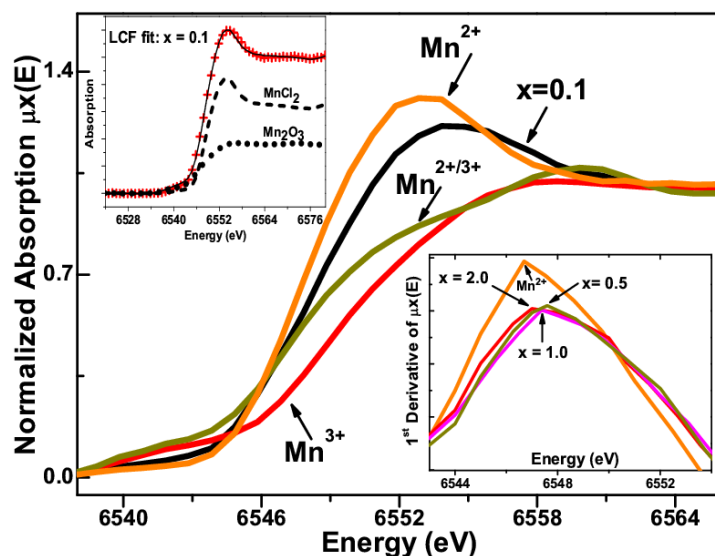


Fig. 4.11. Edge step normalized XANES spectra at Mn K edge for $x = 0.1$ and the corresponding LCF fit (right inset) along with gradual shift of main edge (raising edge) energy, via maxima in the first derivative, which indicates increase of Mn²⁺ concentration with increase in Mn concentration (left inset).

analysis for the oxidation state of Mn in $\text{Co}_{3-x}\text{Mn}_x\text{TeO}_6$ has also been performed on Mn K edge XANES spectra, similar to Co K-edge analysis. We obtain from the combined analysis (Linear Combination Fitting as well as linear combination formula) that the sample with $x = 0.1$ (left inset of Fig. 4.11) shows approximately 70% Mn²⁺ and 30% Mn³⁺ and thus ~ 2.30 as an average valence state of Mn. Moreover, with increase in x value, the ratio of Mn³⁺/Mn²⁺ decreases from ~ 0.26 for $x = 0.5$ to ~ 0.13 for $x = 2.0$ and show maximum at $x \sim 0.5$ in the concentration range $0.5 < x < 2$.

From the analysis of Co and Mn K edge XANES spectra, it is clear that both the transition metals are in mixed oxidation states of +2 and +3 in $\text{Co}_{3-x}\text{Mn}_x\text{TeO}_6$. This can be possible only if at least one of the following cases occur: a) Te is in average oxidation state of lower than +6, b) Te or TM vacancies, and c) excess interstitial oxygen. Further, in order to probe the Te oxidation state in $\text{Co}_{3-x}\text{Mn}_x\text{TeO}_6$ solid solutions, we have carried out Te L₃ edge XANES measurements.

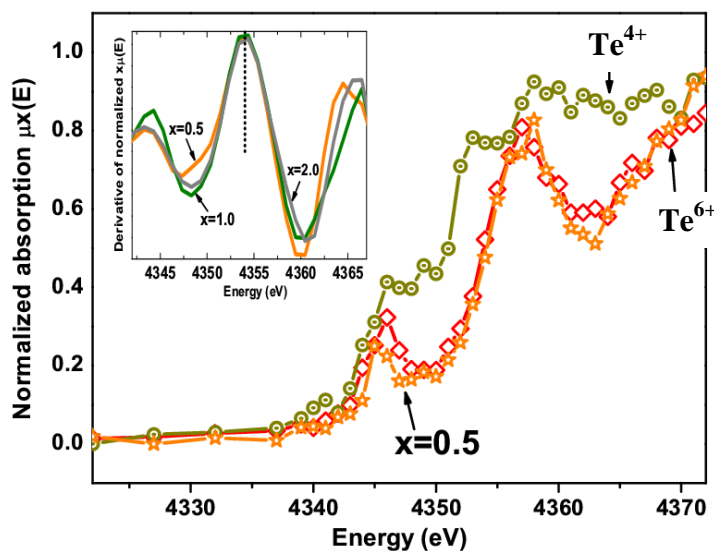


Fig. 4.12. Te L_3 edge XANES spectra of $x = 0.5$ sample (main panel), showing +6 oxidation state of Te in the corresponding solid solution. Here we have used two standards reference samples, TeO_2 for Te^{+4} state and $\text{Te}(\text{OH})_6$ for Te^{+6} oxidation states, respectively. Inset show 1st derivative for $x = 0.5, 1.0$ and 2.0 as a function of energy, indicating the same +6 oxidation state of Te in all the samples.

Here, we have considered only the compositions with $x = 0.5, 1.0$ and 2.0 . Fig. 4.12 shows comparison of Te L_3 -edge XANES spectra of $\text{Co}_{3-x}\text{Mn}_x\text{TeO}_6$ solid solution with two standard references for Te^{+6} ($\text{Te}(\text{OH})_6$) and Te^{+4} (TeO_2). From the main panel and inset of Fig. 4.12, we find that Te L_3 -edge XANES spectra for these samples coincide with that of the standard samples containing Te^{6+} state. Comparisons of these samples with two standards (Te^{4+} and Te^{6+}) confirm the +6 oxidation state of Te in $\text{Co}_{3-x}\text{Mn}_x\text{TeO}_6$, which is consistent with other reports.²⁰⁶ Therefore, XANES observations on Mn, Co and Te edges indicate the presence of either excess oxygen or cations vacancies in the $\text{Co}_{3-x}\text{Mn}_x\text{TeO}_6$ solid solutions.¹⁴⁹⁻¹⁵¹

Mathew et al., and Ivanov et al.,⁹¹⁻⁹² have recently reported magnetic properties (magnetic transition temperature) with change in Mn concentration in the $\text{Co}_{3-x}\text{Mn}_x\text{TeO}_6$. They have found that these solid solutions show comparatively higher AFM transition temperature as compared to the end members ($x=0$ and $x=3$). They were unable to correlate the structural changes with the

enhancement in the AFM transition temperatures. Our SXRD and XANES data, on the other hand, indicate possible structural correlation to the magnetic transition temperatures with change in Mn concentration. Mn doping at Co site and/or vice versa may affect the structure either through TM ion's size or by chemical pressure introduced into the lattice by doping. In $\text{Co}_{3-x}\text{Mn}_x\text{TeO}_6$, these changes are reflected in the Mn/Co-O bond distance as well as in O-TM-O bond angles (Fig. 4.9). In addition to the average TM-O bond distance, which shows a linear increase (for $x \geq 0.5$, Fig. 4.8) with increase in x , the present work reports, for the first time, that TM ions show mix valence in $\text{Co}_{3-x}\text{Mn}_x\text{TeO}_6$. Mn/Co mixed valency observed through XANES would induce different exchange interaction in the sense that super exchange through like spins ($\text{TM}^{2+/3+}\text{-O- TM}^{2+/3+}$) and double exchange between unlike spins ($\text{TM}^{2+/3+}\text{-O-TM}^{3+/2+}$).²⁰⁷⁻²¹⁰ Due to completely antiferromagnetic nature of magnetic order in CTO and MTO, it is likely that the similar magnetic order may exist in these solid solutions, as well.^{77,196} Though weak ferromagnetism in single crystal (which exhibits only single magnetic Co^{2+} ions) as well as ceramic CTO (which contains both Co^{2+} and Co^{3+} ions) has also been suggested using possible spin canting and double exchange, respectively.^{78,97} However, in the present case enhanced ferromagnetism may also be possible through the double exchange interaction ($\text{TM}^{2+/3+}\text{-O-TM}^{3+/2+}$).²⁰⁷⁻²¹⁰

4.1.3. Conclusions

In the above discussion, we have explained the structural and spectroscopic variations in CTO on Mn doping at Co sites using SXRD and XANES measurements. Changes in average TM-O bond lengths and average oxidation state of TM follow an interesting trend, as we increase Mn from $x = 0.5$ to $x = 3.0$. These changes may perturb the overlap integral of the magnetic interactions and hence the magnetic transition. Variable oxidation states of TM (both Co and Mn) may also give

rise to both FM and AFM magnetic transitions. In order to correlate the structural and spectroscopic changes with the magnetic properties, we present magnetic measurements on these solid solutions (only for $x \geq 0.5$) in the next section.

4.2. Magnetic Properties of $\text{Co}_{3-x}\text{Mn}_x\text{TeO}_6$; ($x = 0.5, 1 \text{ \& } 2$)

In this section, we describe DC magnetization studies on $\text{Co}_{3-x}\text{Mn}_x\text{TeO}_6$ (CMTO); ($x = 0.5, 1$ and 2) solid solutions. We observe not only near room temperature ferromagnetic interactions but also low temperature enhanced anti-ferromagnetic interactions for all the compositions. We explain the observed magnetic properties using our structural and spectroscopic studies, discussed in the previous section. Finally, we probe the insight into the complex magnetic behavior by network like structural analysis.

4.2.1. Introduction

The coexistence of magnetic interactions of opposite nature (well accepted phenomenon in colossal magneto-resistance) leading to complex magnetic behavior has been seen in numerous magnetic systems like manganites, cobaltites.^{171,174-177} Role of Griffiths phase like ferromagnetism in MF systems cannot be overemphasized. We show that the presence of such a phase in MFs can add to a great advantage. Properties corresponding to type II MF materials, which are of practical interest, are found only at very low temperatures except for a few systems.¹⁸⁰ Such materials with enhanced MF properties and coupling of various ‘ferro or antiferro’ magnetic orders along with FE at room temperature are some of the current activities. In this regard, many doped compounds become intrinsically inhomogeneous due to random distribution of cation’s sizes, valence/spin states and strong competition between different ordering tendencies. Compounds on doping, not only show the enhanced coupling at higher temperature but also the coexistence of more than one magnetic interaction, e. g. AFM and FM.^{197-198,100-101}

As described earlier, MTO and CTO show AFM transitions (T_N , the Neel temperature) at ~ 23 K and ~ 26 K, respectively.^{77,96,196} In this section, we show that Mn doping in CTO (CMTO) not

only enhances the AFM transition temperature^{91-92,100-101} but also show very high temperature ferromagnetism for all the aforementioned compositions.¹⁰⁰⁻¹⁰¹ In the following, we describe the underlying mechanism behind these phenomena in details.

4.2.2. Results and Discussion

4.2.2.1. Magnetic behavior of $Co_{3-x}Mn_xTeO_6$ ($x = 0.5, 1$ and 2)

Figs. 4.13 (a), (b) and (c) show temperature dependent magnetization for CMTO ($x = 0.5, 1.0,$ and 2.0) at 100 Oe. All these DC magnetization data have been recorded under ZFC and FC conditions, as in the case of CTO. We have also used constant magnetic fields of 10 kOe and 50 kOe during the magnetization measurements (to be discussed later). It is interesting to note that the observed magnetic behaviors for all the compositions are similar but much richer (more features) than those reported earlier.⁹¹⁻⁹² Looking from room temperature side, in Figs. 4.13 (a), (b) and (c), samples exhibit paramagnetic (PM) to FM like transition at a characteristic temperature T_C (Curie temperature) ~ 185 K, which is the same (within ± 2 K) for all the samples. This feature in the magnetization curve is followed by the AFM transitions at $T_N \sim 45$ K, 40 K and 30 K, for $x = 0.5, 1.0,$ and 2.0 Mn content, respectively. However, in literature,⁹¹⁻⁹² the reported transition for these solid solutions were AFM like and at temperatures ≤ 40 K. These values (reported earlier ~ 40 K and observed presently ~ 45 K) are much higher compared to the Neel temperatures observed in either of the compounds CTO (26 K) or MTO (23 K).^{77,96,196} To the best of our knowledge, no FM correlation has been reported in CMTO compounds.⁹¹⁻⁹² We observe FM like transition at $T \sim 185$ K along with bifurcation in ZFC and FC curves for all the samples (see Figs. 4.13 (a), (b) and (c)).

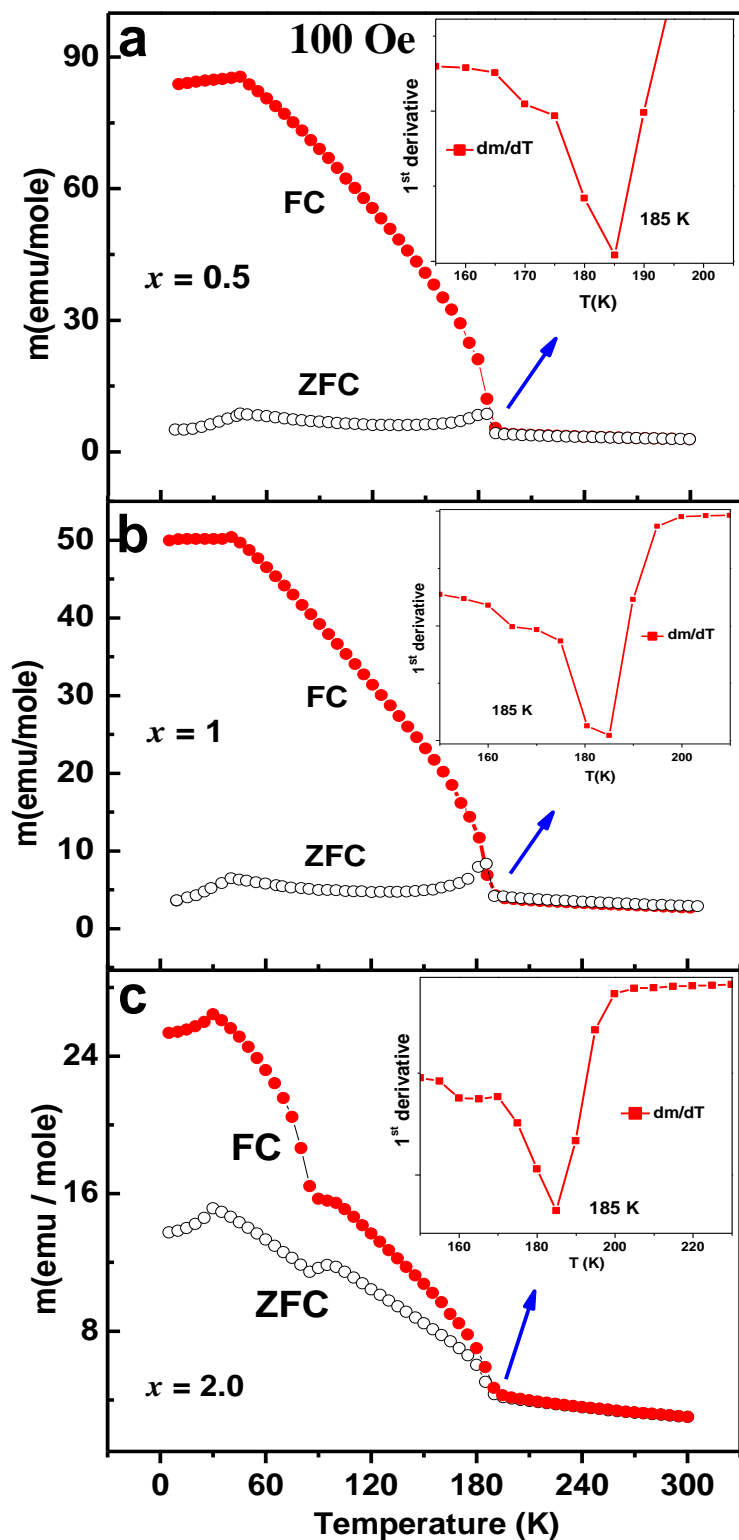


Fig. 4.13. (a), (b), (c) Low magnetic field DC magnetization in ZFC/FC protocol for $x = 0.5$, 1.0 and 2.0 indicates enhanced AFM transition (45 K, 40 K and 30 K) followed by induced ferromagnetic ordering at around 185 K. Insets show the dm/dT to assign exact Curie temperature.

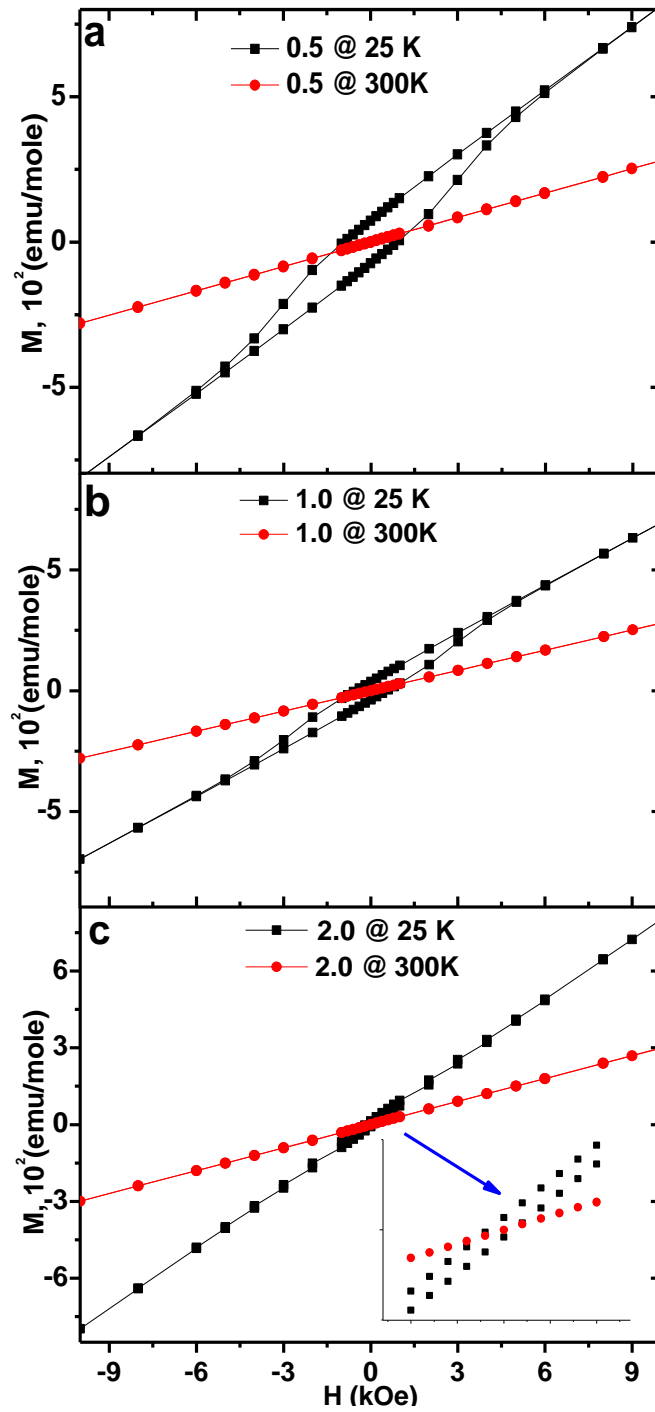


Fig. 4.14. (a), (b), (c): Corresponding magnetic hysteresis (M/H) measurements at 300 K and 25 K for all samples signify the paramagnetic behavior at room temperature and FM like at low temperature.

In literature,¹⁶⁴⁻¹⁶⁵ the bifurcation in FC–ZFC magnetization data has been attributed to the presence of a spin-glass, cluster-glass, super-PM behaviour etc. We attribute this feature to a PM to FM like transition. As discussed in section 3.3 of chapter 3 (for the case of CTO), the temperature derivative dm/dT of the field-cooled magnetic data visualizes the FM transition, and is shown in the inset of Figs. 4.13 (a), (b) and (c). The existence of FM correlations (along with its short range nature) below T_N , reported earlier for various other compounds,^{174,211-212} has been understood as the presence of FM correlation inside AFM matrix. The statement made during the analysis of magnetization data, is confirmed through the magnetic hysteresis data, as can be seen in Figs. 4.14 (a), (b) and (c). The PM state is confirmed by the reversible linear M-H curve at 300 K, and the persistence of FM nature from 185 K down to 10 K is revealed by the M-H loop. The loop does not show any signature of saturation up to 10 kOe, which indicates the presence of significant AFM contribution. In addition, the magnetic hysteresis loop at 25 K signifies the existence of ferromagnetism even below T_N , suggesting the coexistence of FM and AFM phases. The presence of FM correlations is also manifested through the CW fit of the inverse magnetic susceptibility χ^{-1} (H/M) data (see Fig. 4.15). It can be seen that all the χ^{-1} vs T curves follow CW law just above $T_{GP} \sim 190$ K (onset of downturn), with an effective magnetic moment, $\mu_{eff} \sim 8.97 - 9.42 \mu_B / f. u.$ and a PM negative Curie temperature, $\Theta_{CW} \sim 49.1$ K to 68.8 K for $x = 0.5$ to $x = 2.0$, respectively. Both values (μ_{eff} and Θ_{CW}) are significantly larger than the previous reports of Θ_{CW} (-ve) ranging from about 35 K to 45 K and $\mu_{eff} \sim 5.8 - 6.0 \mu_B / f. u.$ ⁹¹⁻⁹² In Table 4.2, we tabulate all the fitted parameters observed from CW fit for all x values. As we go from $x = 0.5$ to $x = 2.0$, Θ_{CW} increases while T_N decreases, indicating weakening of AFM interactions on Mn doping. Interestingly, the observed larger magnetic moment, which increases with Mn concentration, indicates FM cluster type interactions in our samples,²¹³ as discussed further.

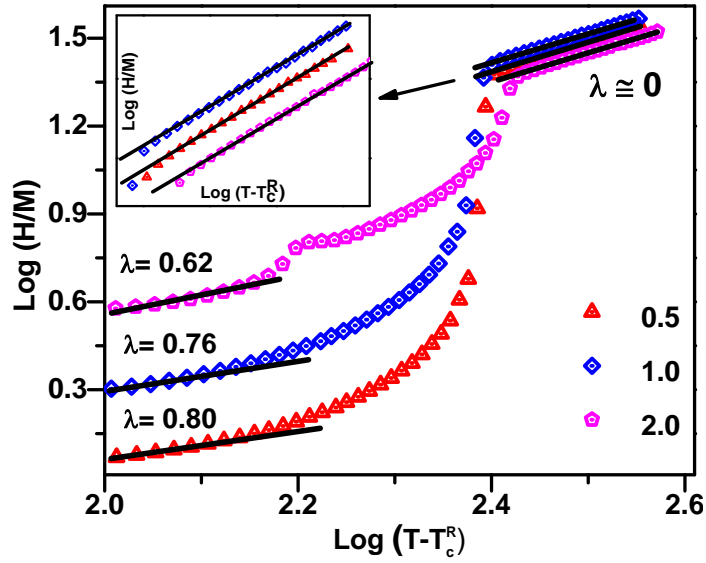


Fig. 4.15. FM correlations is manifested through the CW fit of the inverse magnetic susceptibility (H/M) data for CMTO ($x = 0.5, 1$ and 2) solid solutions, inset enlarge the linear part. Data has been offset along Y-axis for clarity.

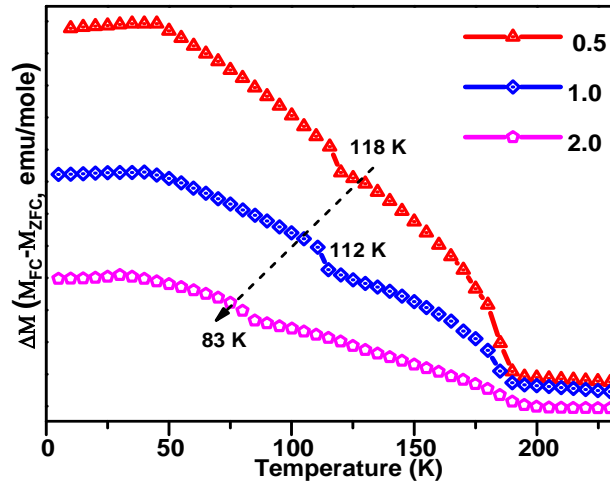


Fig. 4.16. Magnetization difference curve as a function of temperature for CMTO ($x = 0.5, 1$ and 2). This is just to show additional transitions at 118 K, 112 K and 83 K.

Table 4.2. Effective Bohr magneton (μ_{eff}) and λ values for both GP and PM phase obtained from fitted parameters (observed through CW fit) and modified CW law for CMTO. Maximum errors in μ_{eff} and λ are 0.06 and 0.005, respectively.

$x =$	0.5			1.0			2.0		
H (Oe)	100	10000	50000	100	10000	50000	100	10000	50000
μ_{eff} ($\mu_B/f.u.$)	8.97	9.14	9.25	9.03	9.22	9.33	9.42	9.67	9.83
λ_{PM}	0.002	0.003	0	0.004	0.003	0	0.003	0.004	0
λ_{GP}	0.80	0.29	-	0.76	0.244	-	0.62	0.145	-

Evidence of short range FM correlation is also presented through the down turn in the (log-log plot) inverse susceptibility data (a hallmark of GP)¹⁶⁸⁻¹⁷⁰ and magnetization difference curve,¹⁶⁹ and are shown in Fig. 4.15 and Fig. 4.16, respectively. Fig. 4.15 represents one of the main characteristics of GP i.e., it follows power law: $\chi^{-1} = (T-T_C^R)^{1-\lambda}$, where $0 < \lambda < 1$ and $T_C^R = T_N$. The λ values for paramagnetic (λ_{PM}) and Griffiths phase (λ_{GP}) are tabulated in Table 4.2. We find λ_{GP} increases with increasing x from 0.62 to 0.80 for the increase in x from $x = 0.5$ to $x = 2.0$. These values of λ_{GP} correspond to strong FM correlation in CMTO.¹⁶⁶⁻¹⁷⁰ One of the possible reasons for this ferromagnetic ordering is TM^{2+} -O- TM^{3+} networks (as a result of the replacement in TM^{2+} by TM^{3+} in TM^{2+} -O- TM^{2+} networks). This is because of coexistence of mixed oxidation states (+2 and +3) of Co and Mn, as described in section 4.2 of this chapter, and the fact that unlike spins favor FM interactions while like spins favor AFM interactions.²⁰⁷⁻²¹⁰

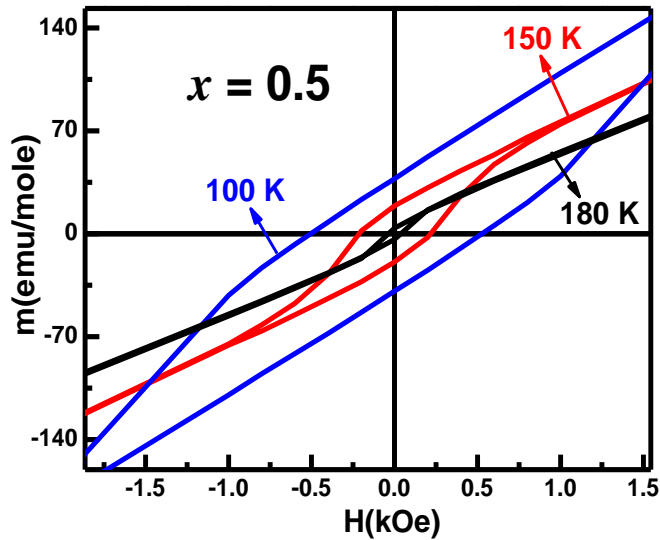


Fig. 4.17. Representative hysteresis loop for CMTO; $x = 0.5$ at 180 K, 150 K and 100 K.

Furthermore, the FM correlation is also clear from the magnetization difference ($M_{FC} - M_{ZFC}$) versus temperature plot. Fig. 4.16 shows the temperature-dependent $\Delta M = M_{FC} - M_{ZFC}$ curves at 100 Oe. This subtraction advantageously eliminates PM and diamagnetic contributions and

simultaneously indicates the presence of hysteresis (if $\Delta M \neq 0$).¹⁶⁹ The FM characteristic transition temperature T_{FM} may be obtained by taking $\frac{d}{dT}(M_{FC} - M_{ZFC})$ from the $(M_{FC}-M_{ZFC})$ versus temperature curve (Fig. 4.16). Fig. 4.16 shows one additional anomaly for each composition at around 118 K, 112 K and 85 K for $x = 0.5, 1.0$ and 2.0 , respectively. These transitions were not seen clearly in M vs T data. Representative magnetic hysteresis loops at 180 K, 150 K and 100 K for $x = 0.5$ (Fig. 4.17) indicate FM nature of these transitions. Moreover, the strength of FM correlation shows suppression with increase in magnetic field, similar to samples having GP.¹⁶⁶⁻¹⁷⁰

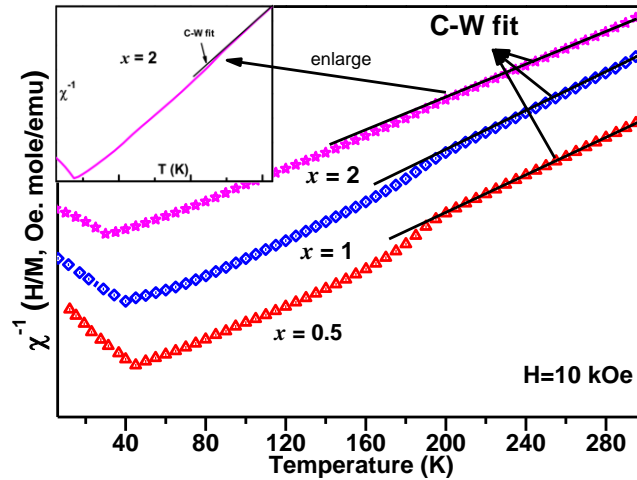


Fig. 4.18. Deviation of H/M curve from the CW law, the upper inset shows the enlarge data for $x = 2$. Main panel data is shifted in Y axis for clarity, corresponding values are not shown.

To further check, whether, the short-range FM correlations can be ascribed to GP; we have measured M vs T data and have plotted χ^{-1} (H/M) vs T for 10 kOe and 50 kOe, as shown in Figs. 4.18 and 4.19, respectively. According to GP, the downturn feature in χ^{-1} is expected to increase with decreasing field strength, at least for low H , where the susceptibility of the clusters is dominant. This behavior is clearly reflected in Fig. 4.18 (and Fig. 4.15). At higher fields, the contribution from PM matrix is significant. As a result, χ^{-1} vs T curve becomes almost linear in

GP region, as shown in Fig. 4.19. Similar downward turn (and the corresponding suppression) in χ^{-1} (T) has also been observed in several other compounds, and is attributed to GP, owing to the formation of nano size FM domains.¹⁶⁸⁻¹⁷⁰ Formation of nano-size Griffiths-like FM clusters has also been demonstrated by small-angle neutron scattering in $\text{Tb}_5\text{Si}_2\text{Ge}_2$.²¹⁴ Often, the same is reflected in the very large value of effective Bohr magneton, μ_{eff} and is discussed earlier in the current section.

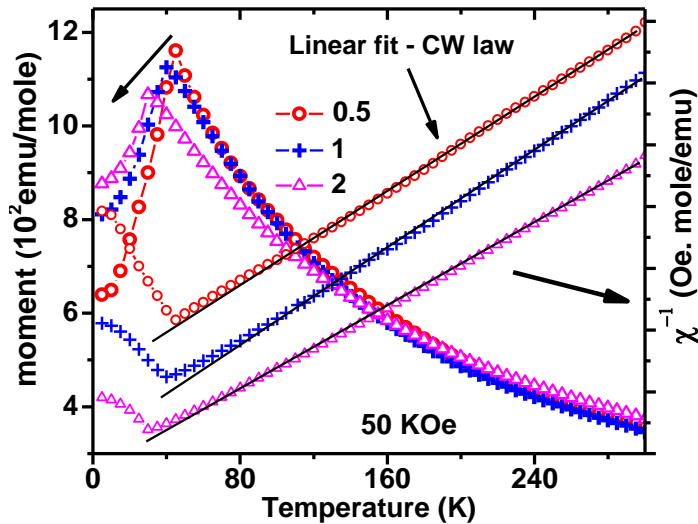


Fig. 4.19. Very high magnetic field χ (H/M) and χ^{-1} curve for CMTO, which signifies another characteristic of GP. The CW fit indicates absence of GP at 50 kOe.

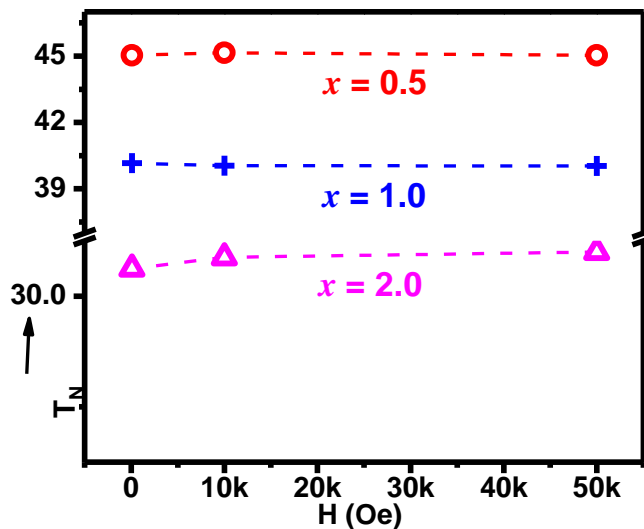


Fig. 4.20. Unaltered values of T_N at various magnetic fields for CMTO ($x = 0.5, 1$ and 2).

So far, we have illustrated the signatures of FM correlations along with its short-range nature in CMTO ($x = 0.5, 1$ and 2) solid solutions using M vs T and M vs H studies. This feature has been attributed to the FM nano phase embedded in AFM matrix, which is also called Griffiths phase. This is quite unusual because the same was not observed in previous investigations of CMTO.⁹¹⁻⁹² We attribute this GP like anomaly to the presence of mixed valence TM ions in our samples. Also, as the Mn content is changed, it modifies the H/M vs T curves very significantly and changes the value of λ_G (Table 4.2). The downturn feature of the H/M curve shows suppression, whereas, there is no change in AFM transition temperatures (T_N), as shown in Fig. 4.20, with the increase in the Co/Mn ratio. Our observations also support the absence of ferromagnetism in MTO, whereas a very weak presence of FM interactions in CTO.^{78,96} In the following, we study structural data in order to understand magnetic behaviour of CMTO samples.

4.2.2.2. Structural insight for the observed magnetic behavior

We present detailed structural studies in order to find its possible correlation to magnetic behavior presented in preceding paragraphs.⁹² Fig. 4.21 shows representative layer and equilateral triangular arrangements of Mn/Co (ions structure) of studied CMTO solid solution at room temperature for $x = 0.5$. Oxygen is not shown for the sake of clarity. First we show the polyhedral view of a representative R-3 structure for $x = 0.5$ (Fig. 4.21 (a)). Simplified unit cell of CMTO solid solution is displayed through Mn/Co ions in Fig. 4.21 (b). From the side view along a - or b - axis, a layer structure is observed (Fig. 4.21 (b)), and from the top view along c axis, an equilateral triangular arrangement of Mn/Co ions can be found (Fig. 4.21 (b)). Fig. 4.21 (c) (slightly tilted from Fig 4.21 (b)) show the equilateral triangles (length = 3.699 Å) consisting of Mn ions. Only few triangles are shown.

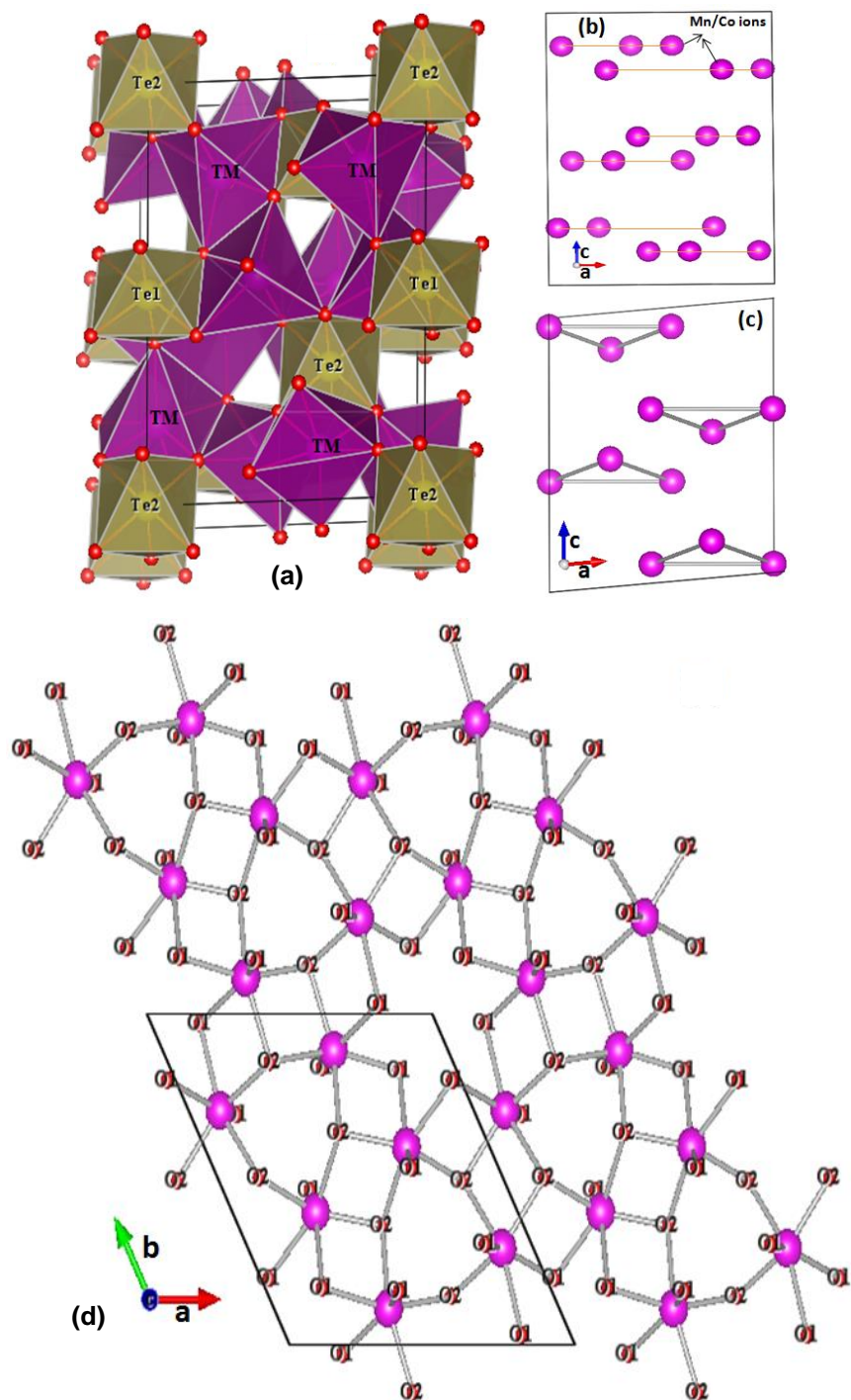


Fig. 4.21. (a) Polyhedral view along (010), (b) layered structure (side view from b -axis) of Mn/Co ions, (c) equilateral triangular arrangements (top view along b axis) of Mn/Co ions located at different layers, and (d) network type of structure through oxygen along c -axis (a - b plane).

These triangles belong to different layers. Furthermore, a network structure is also presented (Fig. 4.21 (d)) perpendicular to *c*-direction (*a*-*b* plane). The above analysis indicates that there are triangular cycles, which may be comprised of Mn/Co/Mn and Co/Mn/Co sites, stacked along *c* axis of the unit cell, very similar to the earlier observation by Ivanov et al.,⁹² predicted using neutron diffraction study. The connectivity of TM or Mn/Co cations with increasing Mn concentration shows a deviation from the ideal triangular lattice, distortions due to which are reflected in the displacements of TM ions from their initial sites.^{91-92,100,196} Further, to have an insight we have shown triangular structure in Fig 4.21 (d), similar to the one shown in literature based on neutron diffraction.⁹² It shows the possible cationic arrangements for this geometry along *c* axis, which can extend throughout the lattice through periodic translation. They are attached through O atoms which prefer to have either super exchange or double exchange interactions. Our earlier report¹⁰⁰ clearly elaborates the increasing nature of average bond distances and resulting distortion in the lattice decreases the magnetic interactions in these CMTO solid solutions.

Finally, we have discussed and demonstrated the origin of Griffiths-like anomaly in CMTO solid solutions. In the structural section, we speculate all the possible cause related to competing FM and AFM interactions. Comparison of the present CMTO samples with those reported by Ivanov et al., and Mathew et al.,⁹¹⁻⁹² reveals that because of mixed oxidation states in TM ions in our samples, there is a possibility of double exchange between unlike spins (e. g. $\text{Co}^{3+} - \text{O} - \text{Co}^{2+}$, $\text{Mn}^{3+} - \text{O} - \text{Mn}^{2+}$) favoring ferromagnetic interactions. However, few reports on other compounds contradict the conjecture that the the existence of Griffiths phase may not be because of mixed valance.²¹⁵ Also, the presence of $\text{Co}^{3+}/\text{Mn}^{3+}$ in the triangular lattice of Mn/Co/Mn and Co/Mn/Co, may lead to frustration and hence, spontaneously induce FM and or AFM

interaction, apart from major AFM interaction proposed earlier.⁹¹⁻⁹² This may cause disorder / magnetic inhomogeneity in CMTO samples leading to GP.¹⁶⁶⁻¹⁷⁰ Moreover, JT distortion (due to TM³⁺) can also induce GP like FM.¹⁶⁶⁻¹⁶⁸ But we do not consider JT effect in the present study because, out of the three known modes of octahedral distortions (breathing, basal plane and stretching modes), breathing mode (which can't be responsible for GP) is found in our CMTO samples.¹⁰⁰

4.2.3. Conclusions

We identify CMTO ($x = 0.5, 1$ and 2) solid solutions as a potential magnetic material having high temperature FM interactions, low temperature enhanced AFM interactions. This is demonstrated through detailed magnetization (M vs T and M vs H) studies. Inverse magnetic susceptibility vs temperature data provide clear indication of Griffiths like FM phase extended over large thermal region. This FM phase is robust against applied magnetic field. Both FM and AFM phases are sensitive to the content of Co/Mn ratio. We also attempt detailed structural studies in order to find its possible correlation to the magnetic behavior possessed by CMTO solid solutions.

To conclude this chapter, we have synthesized polycrystalline samples of $Co_{3-x}Mn_xTeO_6$ ($0 < x \leq 2$) using conventional two step solid state reaction route with Co_3O_4 , Mn_3O_4 and TeO_2 (in off-stoichiometric ratio). We have carried out structural and spectroscopic investigations in order to find the structural correlation with magnetic behaviour of these solid solutions as a function of Mn concentration using SXRD, XANES and magnetization studies. Structural studies using Rietveld refinement reveal $R\bar{3}$ structure for $x \geq 0.5$, whereas mixture of C2/c and $R\bar{3}$ phases for $x < 0.5$. For $x \geq 0.5$, increase in lattice parameters and average TM - O bond distances with increasing Mn concentration naturally corroborate with the observed as well as reported

magnetic behavior of enhanced AFM transition temperatures in CMTO. Analysis of XANES spectra at Co and Mn K-edges show mixed oxidation states of $\text{Co}^{2+}/\text{Co}^{3+}$ and $\text{Mn}^{2+}/\text{Mn}^{3+}$. Quantitative analysis of the oxidation state using Linear combination fit (LCF) indicates gradual increase in Co^{2+} and Mn^{2+} with increase in Mn concentration. Relative ratios of $\text{Co}^{3+}/\text{Co}^{2+}$ and $\text{Mn}^{3+}/\text{Mn}^{2+}$ are found to be maximum at around $x \sim 0.5$, where the corresponding $\langle\text{Co/Mn-O}\rangle$ bond lengths are minimum. Approximately at the same concentration, maximum T_N (~ 45 K) has been observed and could be correlated with the observed structural and spectroscopic results, which also show anomalous behavior in average bond lengths and charge ratio at $x \sim 0.5$. Further, we identify $\text{Co}_{3-x}\text{Mn}_x\text{TeO}_6$ ($x = 0.5, 1$ and 2) solid solutions as an interesting magnetic material having coexistence of high temperature ferromagnetic and enhanced low temperature antiferromagnetic transitions, demonstrated through detailed magnetization (M vs T and M vs H) studies. We believe such high temperature FM and low temperature enhanced AFM transition temperatures in CMTO would attract further research with an aim to achieving room temperature FM and low temperature AFM together with strong dielectric coupling. Our detail structural, spectroscopic and magnetic studies indicate that CMTO could be an important material for future technological application as well as fundamental research.

Chapter 5

Conclusions and Future Work

In this thesis, we have carried out structural and spectroscopic studies on TM based oxides and MFs.¹⁻³ TM and their complexes exhibit variety of structures and properties due to the unique nature of their outer shell *d*-electrons. These electrons in TMOs manifest themselves in many different ways leading to interactions among charge, spin, lattice and orbital degrees of freedom. These systems have also been proposed to be of great technological importance. For example ME MFs,²⁻³ which offer opportunities for applications in information storage, spin electronics, magneto-electronics and solar cells.⁴⁻¹⁷ A number of MFs possessing cationic and anionic non-stoichiometry are also useful in many other applications such as energy conversion, oxygen sensing, oxygen storage etc.¹⁸⁻²⁰

Recently, Co_3TeO_6 (CTO: a type-II MF material and the only low symmetry compound in A_3TeO_6 family; A= Cu, Mn, Co, Ni) has been reported to show favourable characteristic, which exhibits very interesting structural as well as low temperature MF properties. Its monoclinic crystal structure with multiple magnetic transitions (at very low temperatures) makes CTO very interesting from fundamental point of view. However, due to very complex crystal as well as magnetic structures, understanding of origin and of the magnetic transitions is still under debate. We have performed structural and spectroscopic studies in corroboration with magnetic, dielectric and polarization measurements in an attempt to understand underlying phenomena.

Single phasic ceramic CTO is synthesized using solid state reaction route. Rietveld refinement analysis on high resolution Synchrotron X-ray diffraction data suggests that only off-stoichiometric ratio of Co_3O_4 and TeO_2 reactants and two step solid state reaction route give rise to single phase of CTO. During synthesis, initial ingredient Co_3O_4 is found better than CoO in circumventing the intermediate Co_5TeO_8 or CoTeO_3 phases. Detailed growth reaction mechanism suggest formation of intermediate phase (CoTeO_4 : monoclinic symmetry), which on

calcinations leads to the formation of single phase of CTO (monoclinic symmetry). This may be due to the diffusion of unreacted high symmetry Co_3O_4 phase (Fd3m) into lower symmetry CoTeO_4 phase ($\text{P2}_1/\text{c}$) during the intermediate calcinations. Rietveld analysis show wider variations in bond lengths and bond angles in our ceramic sample compared to those reported in literature for single crystal as well as ceramic CTO, which may lead to the observance of additional possible cation valency. Thorough structural study suggests low symmetry structure of CTO. Implications of such lower symmetry structure (compared to other members of A_3TeO_6 family) are seen in its low temperature complex magnetic structure.

Spectroscopic characterizations using XANES and XPS show the mixed oxidation state (Co^{2+} and Co^{3+}) of Co in CTO. We attribute observed wider variations in bond lengths to the presence of mixed valence Co ions. Further, the analysis of pre-edge XANES spectra shows that both Co^{2+} and Co^{3+} are in high spin states. Curie-Weiss fit of the high field magnetization data, which show only two magnetic transitions ($T_{\text{N1}} \sim 26$ K and $T_{\text{N2}} \sim 18$ K), give higher magnetic moment compare to that reported for single crystal CTO. The observed value of magnetic moment support our observation of high spin mixed oxidation state of Co. This observation is also confirmed with first principles *ab-initio* calculations, which shows that the minimum energy configuration for the system remains for high spin states of Co^{2+} and Co^{3+} . Te L_3 -edge XANES and synthesis of CTO in oxygen deficient (vacuum and argon) conditions indicate that the plausible charge imbalance due to different oxidation states of the Co-cations may be compensated by Te-cation vacancy.

Low field magnetization data show all the five magnetic transitions (~ 34 K, 26 K, 21 K, 17.4 K and 16 K) in CTO, which indicates its complex magnetic ground state. It is important to note here that different groups have reported different set of magnetic transitions including two main

magnetic transitions ($T_{N1} \sim 26$ K and $T_{N2} \sim 17.4$ K) in CTO. This indicates that MF properties of CTO depend on the method of synthesis and thus understanding the growth mechanism is crucial, which may explain its complex magnetic structure. In addition, we observe bifurcation (~ 60 K) in the zero field cooled and field cooled magnetization curves at lower magnetic fields ($H < 500$ Oe) and its disappearance under higher (> 500 Oe) magnetic fields indicating the presence of zero field magnetization in CTO. Magnetic hysteresis data also show very weak hysteresis at very low temperatures. Analysis of the magnetic data (M vs T and M vs H) suggests the presence of Griffiths phase in CTO, showing short range ferromagnetic nano domains in an anti-ferromagnetic matrix. Weak ferromagnetic correlation may be explained through the mixed valence of Co ions due to the presence of $\text{Co}^{2+}\text{-O-Co}^{3+}$ networks (which favour ferromagnetic interactions) along with $\text{Co}^{2+}\text{-O-Co}^{2+}$ networks (which normally favour anti-ferromagnetic interactions).

Origin of multiple magnetic transitions is investigated by using room temperature structural (SXRD) data and their Rietveld refined structure of our ceramic as well as those of reported single crystal CTO. Our analyses indicate four structural networks, which may be correlated with aforementioned multiple magnetic transitions observed both in single crystal as well as in ceramic CTO. This is because, various polyhedral configurations of Co ions experience different crystal fields leading to their different electronic/spin configurations. This observation is in agreement with the observation of only two networks proposed by Wang et al., based on their low temperature neutron diffraction data.

Temperature and magnetic field dependent DC magnetization, dielectric constant and polarization (measured through pyroelectric current) measurements suggest the magneto-electric and magneto-dielectric couplings in CTO. Dielectric constant data shows a step anomaly at 18 K

(T_2 ; which is also T_{N2} observed in the magnetization data). Furthermore, shift of 18 K towards lower temperature and reduction of the overall magnitude of dielectric constant below 18 K on the application of magnetic fields confirm the magneto-electric and magneto-dielectric couplings in CTO. Together with these, the polarization measurements show the possibility of spontaneous electrical polarization in CTO. Lowering of T_2 (AFM transition temperature) on applying magnetic field indicates strong coupling between electric and magnetic orders. In this phase (at lower temperatures) weak magnetization is observed along with very weak hysteresis attributed to Griffiths like ferromagnetic clusters of nano size domains. Our results further indicate that ceramic CTO is a strongly coupled multiferroic material. These observations on our ceramic CTO not only investigate magneto-electric multi-ferroic behaviour but also show additional features such as magneto-dielectric and mixed valence Co (not reported so far).

Furthermore, in an effort to enhance the coupling strength and the temperature at which the material shows MF behavior, we have prepared $Co_{3-x}Mn_xTeO_6$; ($0 < x \leq 2$) solid solutions. Room temperature structural and spectroscopic investigations on these solid solutions as a function of Mn concentration using SXRD and XANES measurements, respectively, indicate disproportionate mixing of monoclinic (C2/c) and rhombohedral ($R\bar{3}$) structures for $x < 0.5$, while only $R\bar{3}$ phase for $x \geq 0.5$. Relative ratios of Co^{3+}/Co^{2+} and Mn^{3+}/Mn^{2+} decrease with increasing x (for $x \geq 0.5$). Interestingly, the ratios of Co^{3+}/Co^{2+} and Mn^{3+}/Mn^{2+} are found to be maximum at around $x \sim 0.5$, where the corresponding average $\langle Co/Mn-O \rangle$ bond length is minimum. Approximately at the same concentration, maximum T_N has been observed. These evidences are used to provide interpretation of the observed enhancement in the AFM transition to ~ 45 K for $x = 0.5$, whereas, the transition temperatures for the end member CTO ($x = 0$) and MTO ($x = 3$) are ~ 26 K.

Moreover, detailed analysis of the magnetic data (M vs T and M vs H) on CMTO solid solutions not only suggest enhancement in the AFM transition temperature to ~ 45 K but also show near room temperature ~ 185 K short-range robust FM correlation. Griffiths-like ferromagnetism exists over an extended temperature range (up to 185K) and is finite even for an applied magnetic field of 1 T, indicating its robustness. This may further be attributed to the observed anomalies in TM-O bond lengths as well as mixed charge states of TMs for $\text{Co}_{3-x}\text{Mn}_x\text{TeO}_6$.

Future work

a) Low temperature X-ray and neutron diffraction

It would be interesting to study low temperature SXRD as well as neutron diffraction and correlate possible anomalies in lattice parameters to the magnetic transitions in CTO as well as CMTO. These studies are expected to provide information on the nature of the magnetic transitions. For example, whether these transitions have structural origin or not?. By using low temperature evaluation of bond distances and other structural parameters, one may also provide a possible probe for spin lattice coupling in CTO and CMTO. Exact identifications of these transitions however would specially need detailed neutron diffraction measurements at low temperature.

b) Low temperature heat capacity measurements:

One of the interesting observations from this thesis work is the difference in high and low field magnetization data, wherein zero (low) magnetic field magnetic behaviour of CTO shows various multiple magnetic transitions compared to the only two magnetic transitions at higher magnetic fields. This is consistent with the magnetization data of single crystal CTO and various other compounds, reported in literature. To the best of our knowledge, the origin of this difference is not yet understood. Further, in order to find the origin of large variation in the

number of magnetic transitions observed by various groups as well as in the present study, we have planned for detail specific heat measurements. The temperature and the magnetic field dependence of the same measurement would also be a main goal.

c) TGA measurements under oxygen reduced condition ($> 600\text{ }^{\circ}\text{C}$)

In this thesis, we have reported results on CTO samples synthesized in oxygen deficient conditions to conclude that the TM charge excess cannot be explained by oxygen excess. This conclusion is based on an indirect way. For direct measurements, we had performed EDS measurements, however, it was not being conclusive. A direct measurement may be TGA/DTA or DSC of CTO in oxygen reduced environment, may be done to estimate oxygen concentration ($>600^{\circ}\text{C}$). As an origin of the enhanced multiferroicity in our ceramic samples as compared to reported single crystal, we have concluded that it may be cation vacancies which play role to the observed mixed valency in our samples and is not because of oxygen non-stoichiometry. As a further confirmation about the oxygen anion concentration, we have planned for performing TGA under oxygen reduced condition ($> 600\text{ }^{\circ}\text{C}$), as the future studies.

References:

1. C. N. R. Rao, A. Sundaresan and R. Saha, *J. Phys. Chem. Lett.* **3** (16), 2237 (2012).
2. H. Schmid, *Ferroelectrics* **162**, 317 (1994).
3. N. A. Hill, *J. Phys. Chem. B* **104**, 6694 (2000).
4. A. Kargol, L. Malkinski, and G. Caruntu, “Advanced Magnetic Materials” Dr. Leszek Malkinski (Ed.), ISBN: 978-953-51-0637-1, InTech, (2012).
5. S. R. Pattan, S. B. Pawar, U. D. Gharate and S. B. Bhawar, *Indian Drugs* **49**, 5 (2012).
6. E. Papisa, F. Rossia, M. Raspantib, I. D. Donnec, G. Colomboc, A. Milzanic, G. Bernardiniad and R. Gornatia, *Toxicol. Lett.* **189**, 253 (2009).
7. S. Fusil, V. Garcia, A. Barthélémy and M. Bibes, *Ann. Rev. of Mat. Res.* **44**, 91 (2014).
8. R. Ramesh, *Nature Mater.* **9**, 380 (2010).
9. S. A. Wolf, D. D. Awschalom, R. A. Buhrman, J. M. Daughton, S. Von Molnár, M. L. Roukes, A. Y. Chtchelkanova and D. M. Treger, *Science* **294**, 1488 (2001).
10. J. Mannhart and D. G. Schlom, *Science* **327**, 1607 (2010).
11. M. Gajek, M. Bibes, S. Fusil, K. Bouzehouane, J. Fontcuberta, A. Barthélémy and A. Fert, *Nature Mater.* **6**, 296 (2007).
12. A. Roy, R. Gupta and A. Garg, *Adv. in Cond. Matt. Phys.*, **2012**, 926290 (2012).
13. A. P. Pyatakov and A. K. Zvezdin, *Phys. Usp.* **55**, 557 (2012).
14. J. M. Slaughter, *Annu. Rev. Mater. Res.* **39**, 277 (2009).
15. R. Nechache, C. Harnagea, S. Li, L. Cardenas, W. Huang, J. Chakrabartty and F. Rosei, *Nature Photonics* **9**, 61 (2015).
16. M. A. Jalaja and S. Dutta, *Adv. Mat. Lett.* **6**, 7 (2015).
17. T. Choi Y. Horibe, H. T. Yi, Y. J. Choi, and S.W. Cheong, *Nat. Mater.* **9**, 253 (2010).
18. M. Mostovoy, *Nat. Mater.* **9**, 188 (2010).
19. J. Seidel, L. W. Martin, Q. He, Q. Zhan, Y.-H. Chu, A. Rother, M. E. Hawkrigde, P. Maksymovych, P. Yu, M. Gajek, N. Balke, S. V. Kalinin, S. Gemming, F. Wang, G. Catalan, J. F. Scott, N. A. Spaldin, J. Orenstein and R. Ramesh, *Nat. Mater.* **8**, 229 (2009).
20. J. Meyer, S. Hamwi, M. Kröger, T. Riedl and A. Kahn, *Adv. Mater.* **24**, 5408 (2012).
21. N. Izyumskaya, Y. Alivov and H. Morkoç, *Crit. Rev. in Sol. St. & Mat. Sci.* **34**, 89 (2009).

22. C. Yuan, H. Bin Wu, Yi Xie and X. W. D. Lou, *Angew. Chem. Int. Ed.* **53**, 1488 (2014).
23. S. Maekawa, T. Tohyama, S. E. Barnes, S. Ishihara, W. Koshibae, and G. Khaliullin, “Physics of Transition Metal Oxides” Springer, Berlin, (2004).
24. F. J. Morin, *Bell System Tech. J.* **37**, 1047 (1958).
25. N. B. Aetukuri, A. X. Gray, M. Drouard, M. Cossale, L. Gao, A. H. Reid, R. Kukreja, H. Ohldag, C. A. Jenkins, E. Arenholz, K. P. Roche, H. A. Dürr, M. G. Samant and S. S. P. Parkin, *Nature Physics* **9**, 661 (2013).
26. K. I. Kugel and D. I. Khomskii, *Sov. Phys. Usp.* **25** (4), (1982).
27. C. A. Marianetti, D. Morgan and G. Ceder, *Phys. Rev. B* **63**, 224304 (2001).
28. D. L. Wood and J. P. Remeika, *The Journal of Chemical Physics* **46**, 3595 (1967).
29. J. B. Goodenough, “Magnetism and Chemical Bond” Inter-science, New York, (1963).
30. W. Geertsma and D. Khomskii, *Phys. Rev. B* **54**, 3011 (1996).
31. J. C. Maxwell, *Philos. Trans. of the Royal Society of London* **155**, 459, (1865).
32. W. C. Röntgen, *Ann. Phys.* **271**, 264 (1888).
33. H. Schmid, *J. Phys.: Condens. Matter* **20**, 434201 (2008)
34. I. E. Dzyaloshinskii, *Sov. Phys. JETP* **10**, 628 (1959).
35. D.N. Astrov, *Sov. Phys. JETP* **13**, 729 (1961).
36. J. Wang J. B. Neaton, H. Zheng, V. Nagarajan, S. B. Ogale, B. Liu, D. Viehland, V. Vaithyanathan, D. G. Schlom, U. V. Waghmare, at el., *Science* **299**, 1719 (2003).
37. T. Kimura, T. Goto, K. Ishizaka, T. Arima and Y. Tokura, *Nature* **426**, 55 (2003).
38. M. Mostovoy, *Phys. Rev. Letts.* **96**, 067601 (2006).
39. S. Lee, M. T. F. Diaz, H. Kimura, Y. Noda, D. T. Adroja, S. Lee, J. Park, V. Kiryukhin, S.W. Cheong, M. Mostovoy and Je Geun Park, *Phys. Rev. B* **88**, 060103 (2013).
40. G. Catalan and J. F. Scott, *Advanced Materials* **21**, 2463 (2009).
41. D. Khomskii, *Physics* **2**, 20 (2009).
42. E. Giliolia and L. Ehm, *IUCrJ* **1**, 590 (2014).
43. N. C. Wen, M. I. Bichurin, S. Dong, D. Viehland and G. Srinivasan, *J Appl. Phys.* **103**, 031101 (2008).
44. Y. Zhang, L. Zheng, D. Chaoyong, M. Jing, L. Yuanhua and C. W. Nan, *Appl. Phys. Letts.* **92**, 152510 (2008).

45. M. Hambe, A. Petraru, N. A. Pertsev, P. Munroe, V. Nagarajan and H. Kohlstedt, *Adv. Funct. Mater.* **20**, 2436 (2010).
46. J. van den Brink and D. I. Khomskii, *J. Phys.: Condens. Matter* **20**, 434217 (2008).
47. Y. Miyamoto, S. Ishihara, M. Takada and N. Suzuki, *Sol. St. Commun.* **89**, 51 (1994).
48. N. Ikeda, K. Kohn, N. Myouga, E. Takahashi, H. Kitoh and S. Takekawa, *J. Phys. Soc. Japan* **69**, 1526 (2000).
49. B. V. Aken, T. T. M. Palstra, A. Filippetti and N. A. Spaldin, *Nature Mater.* **3**, 164 (2004).
50. R. Moessner and A. P. Ramirez, *Phys. Today* **59**, 24 (2006).
51. A. R. Bishop, A. B. Holder, S. Kamba and M. Maglione, *Phys. Rev. B* **81**, 064106 (2010).
52. C. M. Hurd, *Contemporary Physics*, **23**, 469 (1982).
53. I. Dzyaloshinskii, *J. Phys. Chem. Solid* **4**, 241 (1958).
54. H. Katsura, N. Nagaosa and A. V. Balatsky, *Phys. Rev. Lett.* **95**, 057205 (2005).
55. H. Wu, T. Burnus, Z. Hu, C. Martin, A. Maignan, J. C. Cezar, A. Tanaka, N. B. Brookes, D. I. Khomskii and L. H. Tjeng, *Phys. Rev. Lett.* **102**, 026404 (2009).
56. L. N. Bulaevskii, C. D. Batista, M. V. Mostovoy and D. I. Khomskii, *Phys. Rev. B* **78**, 024402 (2008).
57. J. H. Park, E. Vescovo, H. J. Kim, C. Kwon, R. Ramesh and T. Venkatesan, *Nature* **392**, 794 (1998).
58. J. F. Scott, *Nature Mater.* **6**, 256 (2007).
59. M. Bibes and A. Barthélémy, *Nature Mater.* **7**, 425 (2008).
60. M. Hambe, A. Petraru, N. A. Pertsev, P. Munroe, V. Nagarajan and H. Kohlstedt, *Adv. Funct. Mater.* **20**, 2436 (2010).
61. Garcia, V. M. Bibes, L. Bocher, S. Valencia, F. Kronast, A. Crassous, X. Moya, S. E. Vedrenne, A. Gloter, D. Imhoff, et al., *Science* **327**, 1106 (2010).
62. M. Gajek, M. Bibes, S. Fusil, K. Bouzehouane, J. Fontcuberta, A. Barthélémy and Albert Fert, *Nature Mater.* **6**, 297 (2007).
63. E. Y. Tsymlal and H. Kohlstedt, *Science* **313**, 181 (2006).
64. J. M. Hu, Z. Li, L. Q. Chen and C. W. Nan, *Nature Communications* **2**, 553 (2011).
65. C. W. Nan, M. I. Bichurin, S. Dong, D. Viehland and G. Srinivasan, *J. Appl. Phys.* **103**, 031101 (2008)

66. Y. Zhang, L. Zheng, D. Chaoyong, M. Jing, L. Yuanhua and C. W. Nan, *Appl. Phys. Letts.* **92**, 152510 (2008).
67. J. Gao, J. Das, Z. Xing, J. Li and D. Viehland, *J. Appl. Phys.* **108**, 084509 (2010).
68. J. Gao, L. Shen, Y. Wang, J. Li and D. Viehland, *J. Appl. Phys.* **109**, 074507 (2011).
69. D. D. Awschalom and M. E. Flatté, *Nature Phys.* **3**, 153 (2007).
70. A. Bhatnagar, A. R. Chaudhuri, Y. H. Kim, D. Hesse and M. Alexe, *Nat. Commun.* **4**, 2835 (2013).
71. C. A. F. Vaz, J. Hoffman, C. H. Ahn and R. Ramesh, *Adv. Mater.* **22**, 2900 (2010).
72. R. D. Johnson, L. C. Chapon, D. D. Khalyavin, P. Manuel, P. G. Radaelli and C. Martin, *Phys. Rev. Lett.* **108**, 067201 (2012).
73. W. Wang, J. Zhao, W. Wang, Z. Gai, N. Balke, M. Chi, Ho N. Lee, W. Tian, L. Zhu, X. Cheng, D. J. Keavney, et al., *Phys. Rev. Lett.* **110**, 237601 (2013).
74. R. Becker, M. Johnsson and H. Berger, *Acta Crystallogr. C* **62**, i67 (2006).
75. N. V. Golubko, V. Yu. Proidakova, G. M. Kaleva, S. A. Ivanov, A.V. Mosunov, S. Yu. Stefanovich, N. V. Sadovskaya, E. D. Politova and P. Nordblad, *Bull. Russ. Acad. Sci.: Phys.* **74**, 724 (2010).
76. S. A. Ivanov, R. Tellgren, C. Ritter, P. Nordblad, R. Mathieu, G. Andre, N. V. Golubko, E. D. Politova and M. Weil, *Mater. Res. Bull.* **47**, 63 (2012).
77. M. Hudl, R. Mathieu, S. A. Ivanov, M. Weil, V. Carolus, T. Lottermoser, M. Fiebig, Y. Tokunaga, Y. Taguchi, Y. Tokura and P. Nordblad, *Phys. Rev. B* **84**, 180404(R) (2011).
78. J. L. Her, C. C. Chou, Y. H. Matsuda, K. Kindo, H. Berger, K. F. Tseng, C. W. Wang, W. H. Li and H. D. Yang, *Phys. Rev. B* **84**, 235123 (2011).
79. W. H. Li, C. W. Wang, D. Hsu, C. H. Lee, C. M. Wu, C. C. Chou, H. D. Yang, Y. Zhao, S. Chang, J. W. Lynn and H. Berger, *Phys. Rev. B* **85**, 094431 (2012).
80. C. W. Wang, C. H. Lee, C. Y. Li, C. M. Wu, W. H. Li, C. C. Chou, H. D. Yang, J. W. Lynn, Q. Huang, A. B. Harris and H. Berger, *Phys. Rev. B* **88**, 184427 (2013).
81. A. B. Harris, *Phys. Rev. B* **85**, 100403 (R) (2012).
82. P. Toledano, V. Carolus, M. Hudl, T. Lottermoser, D. D. Khalyavin, S. A. Ivanov and M. Fiebig, *Phys. Rev. B* **85**, 214439 (2012).
83. J. Sikac and L. Jenskysky, *Collection Czechoslov. Chern. Comrnun.* **45**, (1980).

84. Y. N. Sokolov, K. K. Samplavskaya, M. K. Karapetyants, *Izv. Akad. Nauk SSSR, Neorg. Mater.* **3**, 560 (1977).
85. H. Kasper, *Z. Anorg. Allg. Chem.* **354**, 78 (1967).
86. J. Sloczynski, *Z. Anorg. Allg. Chem.* **438**, 287 (1978).
87. B. Raveau and Md. M. Seikh, “Cobalt Oxides: From Crystal Chemistry to Physics” First Edition, Wiley VCH Verlag GmbH and Co. KGaA (2012).
88. K. Grimaud, J. May, C. E. Carlton, Y. L. Lee, M. Risch, W.T. Hong, J. Zhou and Y. S. Horn, *Nat. Commun.* **4**, 2439 (2013).
89. M. E. Foglio and G. E. Barberis, *Brazilian Journal of Physics* **36**, 1A (2006).
90. S. A. Ivanov, P. Nordblad, R. Mathieu, R. Tellgren, C. Ritter, N. Golubko, E. D. Politova and M. Weil, *Mater. Res. Bull.* **46**, 1870 (2011).
91. R. Mathieu, S. A. Ivanov, P. Nordblad and M. Weil, *Eur. Phys. J. B.* **86**, 361 (2013).
92. S. A. Ivanov, R. Mathieu, P. Nordblad, C. Ritter, R. Tellgren, N. Golubko, A. Mosunov, E. D. Politova, M. Weil, *Mater. Res. Bull.* **50**, 42 (2014).
93. S. A. Ivanov, R. Mathieu, P. Nordblad, E. Politova, R. Tellgren, C. Ritter and V. Proidakova, *J. Magn. Magn. Mater.* **324**, 1637 (2012).
94. R. Mathieu, S. A. Ivanov, R. Tellgren and P. Nordblad, *Phys. Rev. B* **83**, 174420 (2011).
95. H. Singh, A. K. Sinha, S. M. Gupta, M. N. Singh, and H. Ghosh, Communicated.
96. H. Singh, H. Ghosh, T.V. Chandrasekhar Rao, A. K. Sinha and P. Rajput, *J. of Appl. Phys.* **116**, 214106 (2014).
97. H. Singh, H. Ghosh, T. V. Chandrasekhar Rao, G. Sharma, J. Saha and S. Patnaik, Communicated.
98. H. Singh, A. K. Sinha, H. Ghosh, M. N. Singh and A. Upadhyay, *AIP Conf. Proc.* **1665**, 060021 (2015).
99. H. Singh, G. Sharma, Haranath Ghosh, S. Patnaik, A. K. Sinha, EMF 2015, University of Porto, Portugal.
100. H. Singh, A. K. Sinha, H. Ghosh, M. N. Singh, P. Rajput, C. L. Prajapat, M. R. Singh and G. Ravikumar, *J. of Appl. Phys.* **116**, 074904 (2014).
101. Harishchandra Singh, H. Ghosh, C. L. Prajapat and M. R. Singh: Communicated.
102. H. Singh, A. K. Sinha, Haranath Ghosh, M. N. Singh and A. Upadhyay, ICAFM-2014, Thiruvananthapuram, Kerala, India.

103. R. K. Gupta A. K. Sinha B. N. Raja Sekhar, A. K. Srivastava, G. Singh and S. K. Deb, Appl. Phys. A. **103**, 13 (2011).
104. A. K. Sinha, R. K. Gupta and S. K. Deb, Appl. Phys A **108**, 607 (2012).
105. H. Singh, A .K. Sinha, M.N. Singh, P. Tiwari, D.M. Phase and S.K. Deb, J. of Physics and Chemistry of Solids **75**, 397 (2014).
106. A. K. Sinha, A. Sagdeo, Pooja Gupta, Anuj Upadhyay, Ashok Kumar, M.N. Singh, R.K. Gupta, S.R. Kane, A. Verma, and S. K. Deb, J. of Phys.: Conf. Series **425**, 072017 (2013).
107. S. Basu, C. Nayak, A. K. Yadav, A. Agrawal, A. K. Poswal, D. Bhattacharyya, S. N. Jha and N. K. Sahoo, J. of Phys.: Conference Series **493**, 012032 (2014).
108. S. K. Deb, Gurnam Singh, and P. D. Gupta, J. of Physics: Conf. Series **425**, 072009 (2013).
109. Website: <http://www.cat.gov.in/technology/accel/srul/beamlines/index.html>
110. B. D. Cullity, "Elements of X-Ray Diffraction" Addison-Wesley, Reading MA (1978) p. 233-247.
111. B. E. Warren, "X-ray Diffraction" Addison-Wesley, Reading, (1969).
112. A. P. Hammersley, S. O. Svensson, and A. Thompson, Nucl. Instrum. Methods A **346**, 312 (1994).
113. J. Rodriguez-Carvajal, Physica B **192**, 55 (1993).
114. R. A. Young, "The Rietveld Method" Oxford: University Press. (ISBN 0 19 855577 6) (1993).
115. J. C. Taylor, "Rietveld made easy: a practical guide to the understanding of the method and successful phase quantifications" Canberra: Sietronics Pty Ltd. (ISBN 0 9750798 0 8) (2001).
116. G. Bunker, "Introduction to XAFS Cambridge University Press" Cambridge, (2010).
117. F. de Groot, G. Vanko, and P. Glatzel, J. Phys. Condens. Matter **21**, 104207 (2009).
118. J. P. Rueff, L. Journel, P.-E. Petit, and F. Farges, Phys. Rev. B **69**, 1 (2004).
119. T. Yamamoto, X-Ray Spectrum. **37**, 572 (2008).
120. D. Cabaret, Y. Joly, H. Renevier, and C. R. Natoli, J. Synchrotron Rad. **0495**, 258 (1999).
121. P. K. Patel, K. L. Yadav, H. Singh, A.K. Yadav, J. Alloys & Comp. **591**, 224 (2014).
122. G. Vankó, F. M. F. de Groot, S. Huotari, R. J. Cava, T. Lorenz, and M. Reuther, arXiv:0802.2744 (2008).

123. M. Kusunoki, O. T. ki, T. Matsushita, H. Oyanagi, and Y. Inoue, *J. Biochem.* **108**, 566 (1990).
124. A. J. Berry, H. S. C. O'Neill, K. D. Jayasuriya, S. J. Campbell and G. J. Foran, *American Mineralogist.* **560**, 967 (2003).
125. O. Durmeyer, J. P. Kappler, E. Beaurepaire, J. M. Heintz, and M. Drillon, *J. Phys.: Condens. Matter* **2**, 6127 (1990).
126. G. Sankar, P.R. Sarode and C.N.R. Rao, *Chemical Physics* **76**, 435 (1983).
127. F. Bridges, C. H. Booth. G. H. Kwei, J. J. Neumeier and G. A. Sawatzky, *Phys. Rev. B* **61**, R9237 (2000).
128. E. R. Aluri and A. P. Grosvenor, *Phys. Chem. Chem. Phys.***15**, 10477 (2013).
129. C. D. Wagner, W. M. Riggs, L. E. Davis, J. F. Moulder, G. E. Muilenberg (Ed.), "Handbook of X-ray Photoelectron spectroscopy" Perkin-Elmer, Physics Electronics Division 6509, Flying Cloud Drive, Eden Prairie, Minnesota 553444 USA (1992).
130. A. K. Bakshi, S.N. Jha, L. Olivi, D.M. Phase, R.K. Kher and D. Bhattacharyya, *Nucl. Instrum. Methods Phys. Res. B* **264**, 109 (2007).
131. J. Isasi, *Journal of Alloys and Compounds* **322**, 89 (2001).
132. X. Zhu, Z. Wang, X. Su and P. M. Vilarinhopaula, *ACS Appl. Mater. Interfaces* **6**, 11326 (2014).
133. X. Su, A. Wu and P. Vilarinho, *Scr. Mater.* **67**, 927 (2012).
134. K. Momma and F. Izumi, *J. Appl. Crystallogr.* **44**, 1272 (2011).
135. C. A. F. Vaz, D. Prabhakaran, E. I. Altman and V. E. Henrich, *Phys. Rev. B* **80**, 155457 (2009).
136. T. Mizokawa, Y. Morita, T. Sudayama, K. Takubo, I. Yamada, M. Azuma, M. Takano and Y. Shimakawa, *Phys. Rev. B* **80**, 125105 (2009).
137. J. F. Mouller, W. F. Stickie, P. E. Sobol, K. D. Bomben, "Handbook of X-ray Photoelectron Spectroscopy", Perkin-Elmer, Physics Electronics Division, Eded Prairie 1992.
138. W. E. Sartz Jr., K. J. Wynne and D. M. Hercules, *Anal. Chem.* **43**, 1884 (1971).
139. Y. Ikedo, J. Sugiyama, H. Nozaki, H. Itahara, J. H. Brewer, E. J. Ansaldo, G. D. Morris, D. Andreica and A. Amato, *Phys. Rev. B* **75**, 054424 (2007).

140. L. G. Bai, M. Pravica, Y. S. Zhao, C. Park, Y. Meng, S. Sinogeikin and G. Shen, *J. Phys.: Condens. Matter* **24**, 435401 (2012).
141. P. Sahoo, H. Djieutedjeu and P. Poudeu., *J. Mater. Chem. A* **1**, 15022 (2013).
142. J. Chen, Y. Chin, M Valldor, Z. Hu, J. Lee, S. Haw, N. Hiraoka, H. Ishii, C. Pao, K. Tsuei, J. Lee, H. Lin, L. Jang, A. Tanaka, C. Chen and L. H. Tjeng, *J. Am. Chem. Soc.* **136**, 1514 (2014).
143. Z. Hu, H. Wu, M. W. Haverkort, H. H. Hsieh, H. J. Lin, T. Lorenz, J. Baier, A. Reichl, I. Bonn, C. Felser, A. Tanaka, C.T. Chen and L. H. Tjeng, *Phys. Rev. Lett.* **92**, 20 (2004).
144. C. T. Chen, L. H. Tjeng, J. Kwo, H. L. Kao, P. Rudolf, F. Sette and R. M. Fleming, *Phys. Rev. Lett.* **68**, 2543 (1992).
145. K. Sano and Y. Ono, *J. Phys. Soc. Jpn.* **72**, 1847 (2003).
146. S. Kimura, Y. Maeda, T. Kashiwagi, H. Yamaguchi, M. Hagiwara, S. Yoshida, I. Terasaki and K. Kindo, *Phys. Rev. B* **78**, 180403(R) (2008).
147. N. Hollmann, M. W. Haverkort, M. Benomar, M. Cwik, M. Braden and T. Lorenza, *Phys. Rev. B* **83**, 174435 (2011).
148. J. Park, S. Cho, J. Jeong and G. Jeong, *Bull. Korean Chem. Soc.* **21**, 973 (2000).
149. F. de Groot, G. Vanko and P. Glatzel, *J. Phys.: Condens. Matter* **21**, 104207 (2009).
150. M. C. Sanchez J. Garcia, J. Blasco, G. Subias and J. P. Cacho, *Phys. Rev. B* **65**, 144409 (2002).
151. B. Ravel and M. Newville, *J. Synchrotron Rad.* **12**, 537 (2005).
152. A. A. Taskin, A. N. Lavrov and A. Yoichi, *Phys. Rev. B* **71**, 134414 (2005).
153. L. Malavasi, C. Ritter, M. C. Mozzati, C. Tealdi, M. S. Islam, C. B. Azzoni and G. Flor, *J. of Solid State Chemistry* **178**, 2042 (2005).
154. H. Eisaki, N. Kaneko, D. L. Feng, A. Damascelli, P. K. Mang, K. M. Shen, Z. X. Shen and M. Greven, *Phys. Rev. B* **69**, 064512 (2004).
155. M. Sikora, Cz. Kapusta, K. Knížek, Z. Jiráček, C. Autret, M. Borowiec, C. J. Oates, V. Procházka, D. Rybicki and D. Zajac, *Phys. Rev. B* **73**, 094426 (2006).
156. G. Vankó, J. Rueff, Z. Németh and A. Shukla, *Phys. Rev. B* **73**, 024424 (2006).
157. O. Haas, R. P. W. J. Struis and J. M. McBreen, *J. Solid State Chem.* **177**, 1000 (2004).
158. A. Chainani, M. Mathew and D. D. Sharma, *Phys. Rev. B* **46**, 9976 (1992).
159. H. Ikeno, T. Mizoguchi and I. Tanaka, *Phys. Rev. B* **83**, 155107 (2011).

160. S. Medling, Y. Lee, H. Zheng, J. F. Mitchell, J. W. Freeland, B. N. Harmon and F. Bridges, *Phys. Rev. Lett.* **109**, 157204 (2012).
161. J. Clark, M. D. Segall, C. J. Pickard, P. J. Hasnip, M. J. Probert, K. Refson, and M. C. Payne, *Zeitschrift fuer Kristallographie* **220**, 567 (2005).
162. P. Perdew, K. Burke and M. Ernzerhof, *Phys. Rev. Lett.* **77**, 3865 (1996).
163. Z. W. Ouyang, V. K. Pecharsky, K. A. Gschneidner, D. L. Schlagel and T. A. Lograsso, *Phy. Rev. B* **74**, 094404 (2006).
164. D. Kumar and A. Banerjee, *J. Phys.: Condens. Matter* **25**, 216005 (2013).
165. D. J. Goossens, K. F. Wilson, M. James, A. J. Studer and X. L. Wang, *Phys. Rev. B* **69**, 134411 (2004).
166. R. B. Griffiths, *Phys. Rev. Lett.* **23**, 17 (1969).
167. A. J. Bray and M. A. Moore, *J. Phys. C* **15**, L765 (1982); A. J. Bray, *Phys. Rev. Lett.* **59**, 586 (1987).
168. M. B. Salamon, P. Lin and S. H. Chun, *Phys. Rev. Lett.* **88**, 197203 (2002).
169. M. B. Salamon and S. H. Chun, *Phys. Rev. B* **68**, 014411 (2003).
170. A. K. Pramanik and A. Banerjee, *Phys. Rev. B* **81**, 024431 (2010).
171. W. Jiang, X. Z. Zhou, G. Williams, Y. Mukovskii and K. Glazyrin, *Phys. Rev. B* **76**, 092404 (2007); **77**, 064424 (2008).
172. K. Grimaud, J. May, C. E. Carlton, Y. L. Lee, M. Risch, W.T. Hong, J. Zhou and Y. S. Horn, *Nature Communications* **4**, 2439 (2013).
173. M. E. Foglio and G. E. Barberis, *Brazilian Journal of Physics* **36**, 1A (2006).
174. D. J. Goossens, K. F. Wilson, M. James, A. J. Studer and X. L. Wang, *Phys. Rev. B* **69**, 134411 (2004).
175. Y. Shimada, S. Miyasaka, R. Kumai and Y. Tokura, *Phys. Rev. B* **73**, 134424 (2006).
176. A. Moreo, S. Yunoki and E. Dagotto, *Science* **283**, 2034 (1999).
177. E. Dagotto, "Nanoscale Phase Separation and Colossal Magnetoresistance" Springer, New York, (2002).
178. N. Theodoropoulou, A. F. Hebard, M. E. Overberg, C. R. Abernathy, S. J. Pearton, S. N. G. Chu and R. G. Wilson, *Phys. Rev. Lett.* **89**, 107203 (2002).
179. A. P. Ramirez, M. A. Subramanian, M. Gardel, G. Blumberg, D. Li, T. Vogt and S. M. Shapiro, *Solid State Commun.* **115**, 217 (2000).

180. T. Kimura, T. Goto, H. Shintani, T. Arima and Y. Tokura, *Nature* **426**, 6 (2003).
181. H. Singh, H. Ghosh, T. V. C. Rao, G. Sharma, J. Saha and S. Patnaik, “Spontaneous electric polarization and Magneto-dielectric coupling in ceramic multiferroic Co_3TeO_6 ” arXiv:1309.6417[cond-mat.mtrl-sci] (2013).
182. G. Lawes, T. Kimura, C. M. Varma, M. A. Subramanian, N. Rogado, R. J. Cava and A. P. Ramirez, *Progress in Solid State Chemistry* **37**, 40 (2009).
183. A. Dixit, G. Lawes and A. B. Harris, *Phys. Rev. B* **82**, 024430 (2010).
184. G. Lawes, A. B. Harris, T. Kimura, N. Rogado, R. J. Cava, A. Aharony, O. E. Wohlman, T. Yildirim, M. Kenzelmann, C. Broholm and A. P. Ramirez, *Phys. Rev. Lett.* **95**, 087205 (2005).
185. R. D. Johnson, L. C. Chapon, D. D. Khalyavin, P. Manuel, P. G. Radaelli and C. Martin, *Phys. Rev. Lett.* **108**, 067201 (2012).
186. J. Sannigrahi, S. Chattopadhyay, D. Dutta, S. Giri and S. Majumdar, *J. Phys.: Condens. Matter* **25**, 246001 (2013).
187. A. K. Singh, D. Jain, V. Ganesan, A. K. Nigam and S. Patnaik, *Europhysics Letters* **86**, 57001 (2009).
188. I. N. Apostolova, A. T. Apostolov S. G. Bahoosh and J. M. Wesselinowa, *J. Appl. Phys.* **113**, 203904 (2013).
189. J. F. Scott, *NPG Asia Materials.* **5**, e72 (2013).
190. L. Wang, D. Wang, Q. Cao, Y. Zheng, H. Xuan, J. Gao and Y. Du, *Sci. Rep.* **2**, 223 (2012).
191. N. N. Hur, S. Park, P. A. Sharma, S. Guha and S. W. Cheong, *Nature* **429**, 392 (2004).
192. E. M. Choi, A. Kursumovic, O. J. Lee, J. E. Kleibeuker, A. Chen, W. Zhang, H. Wang, and J. L. M. Driscoll, *ACS Appl. Mater. Interfaces* **6** (17), 14836 (2014).
193. J. Hellsvik, M. Balesieri, T. Usui, A. Stroppa, A. Bergman, L. Bergqvist, D. Prabhakaran, O. Eriksson, S. Picozzi, T. Kimura and J. Lorenzana, *Phys. Rev. B* **90**, 014437 (2014).
194. A. van der Lee and R. Astier, *J. of Solid State Chemistry* **180**, 1243 (2007).
195. J. Wang, J. A. C. Santana, N. Wu, C. Karunakaran, J. Wang, P. A. Dowben and C. Binek, *J. Phys.: Condens. Matt.* **26**, 055012 (2014).
196. S. A. Ivanov, P. Nordblad, R. Mathieu, R. Tellgren, C. Ritter, N. Golubko, E. D. Politova, and M. Weil *Mater. Res. Bull.* **46**, 1870 (2011).
197. P. Schiffer, A. P. Ramirez, W. Bao and S. W. Cheong, *Phys. Rev. Lett.* **75**, 3336 (1995).

198. M. Sikora, K. Knizek, C. Kapusta and P. Glatzel, *J. Appl. Phys.* **103**, 07C907 (2008).
199. R. Mathieu, S. A. Ivanov, R. Tellgren and P. Nordblad, *Phys. Rev. B* **83**, 174420 (2011).
200. S. A. Ivanov, R. Mathieu P. Nordblad, E. Politova, R. Tellgren, C. Ritter and V. Proidakova, *J. of Magnetism and Magnetic Materials* **324**, 1637 (2012).
201. S. Ivanov, P. Nordblad, R. Mathieu, R. Tellgren, E. Politova and G. André, *European Journal of Inorganic Chemistry* **2011**, 30 (2011).
202. S. Z. Karazhanov, P. Ravindran, P. Vajeeston, A. G. Ulyashin, H. Fjellvag and B. G. Svensson, *J. Phys.: Condens. Matter* **21**, 485801 (2009).
203. R. D. Shannon, *Acta Crystallogr. A* **32**, 751 (1976).
204. A. Z. Simoes, A. H. M. Gonzalez, A. A. Cavalheiro, M. A. Zaghete, B. D. Stojanovic and J. A. Varela, *Ceramics International*. **28**, 265 (2002).
205. J. Park, S. Lee, M. Kang, K. Jang, C. Lee, S. V. Streltsov, V. V. Mazurenko, M. V. Valentyuk, T. Kamiyama and J. G. Park, *Phys. Rev. B.* **82**, 054428 (2010).
206. N. Jiang and C. H. John Spence, *Phys. Rev. B* **70**, 184113 (2004).
207. N. Hollmann, M. W. Haverkort, M. Benomar, M. Cwik, M. Braden and T. Lorenz, *Phys. Rev. B.* **83**, 174435 (2011).
208. R. Zhao, K. Jin, Z. Xu, H. Guo, Le Wang, Chen Ge, H. Lu and G. Yang, *Appl. Phys. Lett.* **102**, 122402 (2013).
209. S. Sonoda, I. Tanaka, H. Ikeno, T. Yamamoto, F. Oba, T. Araki, Y. Yamamoto, K. Suga, Y. Nanishi, Y. Akasaka, K. Kindo and H. Hori, *J. Phys.: Condens. Matter* **18**, 4615 (2006).
210. T. Harada, I. Ohkubo, M. Lippmaa, Y. Matsumoto, M. Sumiya, H. Koinuma and M. Oshima, *Rap. Res. Lett.* **5**, 34 (2011).
211. L. D. Yao, W. Zhang, F. Y. Li, C. Q. Jin and R. C. Yu, *J. Appl. Phys.* **103**, 063909 (2008).
212. R. C. Flores, N. S. Bingham, M. H. Phan, M. A. Torija, C. Leighton, V. Franco, A. Conde, T. L. Phan, S. C. Yu and H. Srikanth, *J. Phys.: Condens. Matter* **26**, 286001 (2014).
213. D. Bhoi, N. Khan, A. Midya, M. Nandi, A. Hassen, P. Choudhury and P. Mandal, *J. Phys. Chem. C* **117**, 16658 (2013).
214. C. Magen, P. A. Algarabel, L. Morellon, J. P. Araujo, C. Ritter, M. R. Ibarra, A. M. Pereira and J. B. Sousa, *Phys. Rev. Lett.* **96**, 167201 (2006).
215. A. Karmakar, S. Majumdar, S. Kundu, T. K. Nath and S. Giri, *J. Phys.: Condens. Matter* **25**, 066006 (2013).

